

AD-A138 468

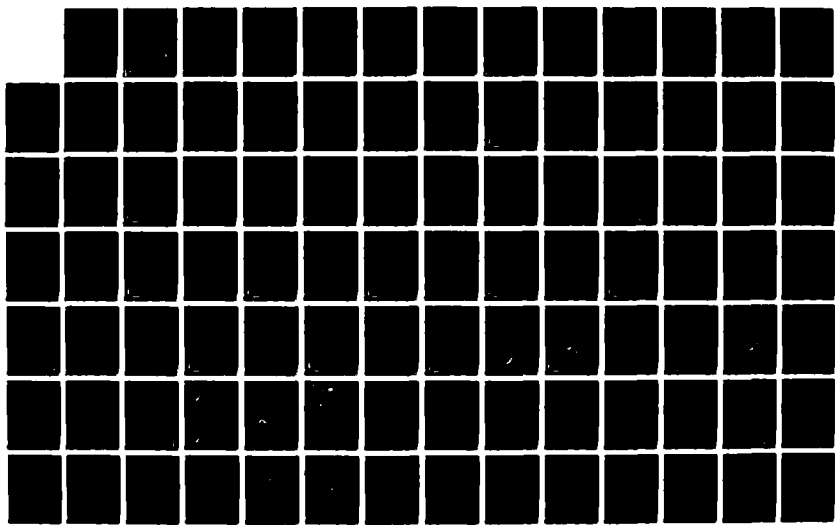
LINEAR AND NONLINEAR FINITE ELEMENTS(U) BOSTON UNIV MA
DEPT OF MATHEMATICS I FRIED DEC 83 BU-1-84
N00014-76-C-0036

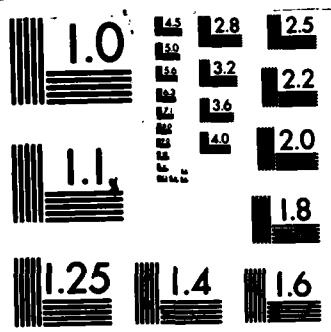
1/3

UNCLASSIFIED

F/G 12/1

NL





MICROCOPY RESOLUTION TEST CHART
NATIONAL BUREAU OF STANDARDS-1963-A

DTIC FILE COPY

ADA138468

Linear and Nonlinear Finite Elements*

Date:

Isaac Fried**

Boston University
Department of Mathematics
Boston, Mass. 02215

Dec 9 1983

0036
S DTIC
ELECTE
FEB 6 1984

* Final Report to the Office of Naval Research for Contract No. ONR-N00014-76 C-~~0036~~

** Professor

This document has been approved
for public release and sale; its
distribution is unlimited.

84 02 6 084

1. Introduction

This report reviews the work of the principal investigator as published in the following scientific papers:

1. I. Fried, Nonlinear finite element analysis of the thin shell of revolution. Submitted for publication to CMAME (1983).
2. I. Fried, Orthogonal trajectory accession to the nonlinear equilibrium curve. Submitted for publication to CMAME (1983).
3. I. Fried, On unconditionally stable implicit time integration methods in elastodynamics and heat transfer. Submitted for publication to CMAME (1983).
4. I. Fried, Reflections on the computational approximation of elastic incompressibility. Computers & Structures 17, 161-168 (1983).
5. I. Fried, Nonlinear finite element computation of the equilibrium stability and motion of the extensional beam and ring. CMAME 38, 29-44 (1983).
6. I. Fried, Finite element computation of large elastic deformations. Proceedings of the Bruxel Conference on the Mathematics of Finite Elements and Applications, MEFLAP IV, J.R. Whiteman, Editor, Academic Press, 143-159 (1982).
7. I. Fried, Finite element computation of large rubber membrane deformations. IJNME 18, 653-660 (1982).
8. I. Fried, Large deformation static and dynamic finite element analysis of extensible cables. Computers & Structures 15, 315-319 (1982).
9. I. Fried, Stability and equilibrium of the straight and curved elasta-finite element computation. CMAME 28, 49-61 (1981).

10. I. Fried, Nonlinear finite element computation of the equilibrium and stability of the circular plate. IJNME 17, 1427-1440 (1981).
11. I. Fried, Meaningful existence of finite element solutions to off-limit problems. CMAME 22, 229-240 (1980).
12. I. Fried, Irregular finite element meshes in elastodynamics. IJNME 15, 626-628 (1980).
13. I. Fried, On the optionality of the pointwise accuracy of the finite element solution. IJNME 15, 451-476 (1980).
14. I. Fried, Accuracy of string element mass matrix. CMAME 20, 317-321 (1979).
15. I. Fried and J. Metzler, SOR vs. conjugate gradients in a finite element discretization. IJNME 12, 1329-1342 (1978).
16. I. Fried and J. Metzler, Conjugate gradient solution of a finite element elastic problem with high Poisson ratio. CMAME 15, 83-84 (1978).
17. I. Fried and J. Metzler, Displacement, strain and stress error nodal lines in finite elements. Computers & Structures 9, 335-339 (1978).
18. I. Fried and D.S. Malkus, Energy error in the elastic solution when an incompressible solid is assumed compressible. In Formulation and Computational Algorithms, K.J. Bathe et al., Editors, MIT Press 131-139 (1976).

Information For
GRAXI

1. TAB
2. Announced
3. Justification

By _____
Distribution/ _____
Availability Codes _____

Dist	Avail and/or Special
A-1	

2. Overview

This section reviews the papers listed in Section 1 in ascending order:

1. Energy error....: The computational problems arising in the finite element simulation of incompressibility have occupied the author's attention since 1975. The purpose of this paper is to show that, at least energetically, the exact solution to the linear three dimensional elastic problem depends continuously on Poisson's ratio ν . This means that taking ν close to one half theoretically guarantees a close analytic solutions to the incompressible state. This is also the basis for the residual energy balancing technique. Computational difficulties concerning convergence and conditioning are discussed in entry 4. of Sec. 1.

2. Displacement, strain and stress error nodal lines....: The paper shows computationally the existence of nodal lines in two dimensional finite elements on which the error between the computed solution and the exact one is zero.

3. Conjugate gradient solution....: Iterative methods for the solution of the large stiffness equation set up with finite elements has some distinct advantages (and admittedly disadvantages) over direct methods. Iterative methods do not require the explicit assembly of the global stiffness matrix and can operate on the element data and connectivity information only and are therefore immune to the numbering of the nodes and the ordering of the elements. They may require the minimum of data, as only one element if the elements repeat, and naturally take advantage of symmetries and repeating eigenvalues.

The paper describes the application of the conjugate gradients method to the solution of three dimensional elastic problem with Poisson's number that may be close to 0.5. Scaling of the global stiffness matrix is shown to be highly effective.

4. SOR vs. conjugate gradients...: The method of successive over relaxation has achieved great popularity in mathematical circles for the iterative solution of linear systems of equations. Its main drawback is that it requires an elusive factor for its success. It is shown on a two dimensional heat conduction problem discretized with finite elements that even with the optimal factor ω SOR does not do appreciably better than the conjugate gradient method. A slight change in the optimal ω causes SOR to lose to CG by a wide margin.

5. Accuracy of string element...: Various mass distributions are discussed for the string element mass matrix.

6. On the optimality...: The finite element method produces solutions that are energy optimal. The paper shows that the theoretical predictions for the pointwise optimality of the finite element solution are correct. Essentially in two dimensional second order problems the asymptotic displacement error for linear elements is

$$\max|u - \hat{u}| = ch^2 \ln \frac{1}{h}$$

where u is the exact solution \hat{u} the computed, h the element diameter, and c a constant.

The paper argues that the asymptotic error estimate is impractical since when h is large c is still a function of it and $c(h) \ln \frac{1}{h}$ does not behave like $\ln \frac{1}{h}$. One must go up to thousands of elements to be able to numerically discover the $\ln(\frac{1}{h})$ in the error estimate.

7. Irregular finite element meshes...: The paper discusses some basic problems in optimal arrangement of finite element meshes in the simple context of the string problem. Setting up a truly optimal mesh of finite elements is a

very difficult task even in the simplest of problems and all one can hope is for an adaptive, or iterative, procedure for the mesh improvement. The paper discusses the mass matrix only and makes the following interesting conclusions:

- a. The optimal mass matrix is optimal only for a uniform mesh. Small deviation from uniformity causes drastic accuracy losses with this element.
- b. With first order elements the grading of the mesh is in opposite directions for the lumped and the consistent mass matrices. The consistent mass matrix is also insensitive to mesh grading.
- c. With quadratic elements and a consistent mass matrix the mesh grading is opposite to that for the linear element, and the problem becomes more sensitive to mesh variation.

8. Meaningful existance...: Considered are problems that are theoretically off limits for the finite element method such as problems with an unlimited energy, with a discontinuous solution, and with redundant boundary conditions. It is argued that the finite element solution in all these cases is still useful.

9. Nonlinear...circular plate...: Gauss integration of the nonquadratic total potential energy of the circular plate is used to derive the element tangent stiffness matrix and element gradient for the large deformation analysis of the plate. Computations are made for the plate under lateral load and post critical rim thrust.

10. Stability and equilibrium...curved elastica...: A slope formulation of the elastica is discretized with quadratic finite elements. The element tangent stiffness matrix and element gradient are written in a form that is easily programmable for use with the Newton-Raphson solution of the nonlinear stiffness

equation. Load and stiffness correction solution methods are also considered and the importance of averaging the iterates is demonstrated. Very large deformations of straight and bent elastics are computed.

11. Large deformation...cables...: To extend the possible boundary conditions and to be able to include inertia loads the cable is assumed extensible. A quadratic-quadratic large displacement element is formulated through discreet sampling of the total potential energy. Various static and dynamic cable problems are solved and the difficulties in computing the tension from the constitutive equation is pointed out. An experiment with a falling cable shows excellent agreement with the computer model.

12. Finite element...rubber membrane...: Numerical sampling of the total potential energy is used to derive the quadratic element tangent stiffness and element gradient for the largely deformed axisymmetrical, Mooney, rubber membrane. Computations are made for the stretched and inflated disc, the inflated torus, and the bulging tube under internal pressure. The convergence of the Newton-Raphson method near a critical point is discussed.

13. Finite element...large elastic deformation...: Creation of the element tangent stiffness matrix and element gradient for the computation of large elastic deformation is discussed. The procedure does not require the elements to be small in the sense of approximating an arc, and is otherwise analogous to the linear finite element method except that the Newton-Raphson (or its modification) method must be called to solve the nonlinear stiffness equation.

14. Nonlinear...equilibrium...extensional beam...: The element data for the large deformation analysis of the curved extensible rod are given. Numerical tests are done with the element to compute the large deflection of a cantilever,

the pressing of a ring by polar forces, the deformation of a circular ring by external pressure; the motion of simply supported and free beams, the vibration of the ring, and the bending of a cantilever by a follower force.

15. Reflections on...elastic incompressibility...: Introduction of incompressibility into the finite element model is still of great current interest. It is argued that the gradual increase of the bulk modulus coupled with a mesh refinement is the most sensible thing to do both from the theoretical as well as the practical point of view.

16. On Unconditionally stable...: Unconditionally stable explicit time integration methods are of the greatest interest in the finite element analysis of elastodynamics and heat transfer. Several such algorithms have recently been published. It is shown that the time and space errors become coupled and that the space mesh reduction may cause a disastrous loss of accuracy.

17. Orthogonal trajectory...: The Riks-Wempner method for correcting the equilibrium equation is modified to remove the need for an explicit load-displacement constraint.

18. Nonlinear...shell of revolution...: A cubic-cubic element is developed for the large deformation analysis of the axisymmetrical shell of revolution. Explicit formulas are given for the element tangent stiffness matrix and element gradient. The bending of a thin spherical shell under the combined action of polar forces and a surface pressure is computed. The high computational price of the Newton-Raphson method is noted.

3. Papers

6. K. S. Chen, "A Certain Type of Ill-Conditioned Stiffness Matrix," *AIAA J.* 11, 100-100 (1973).

7. D. J. Nayler, "Stresses in Nearly Incompressible Materials by Finite Elements with Application to the Calculation of Excess Pure Tensions," *Int. J. Num. Meth. Eng.* 8, 413-460 (1974).

8. J. H. Argyris, P. C. Drumm, T. Angelopoulos, B. Michal, "Large Natural Strains and Some Special Difficulties Due to Non-Linearity and Incompressibility in Finite Elements," *Comp. Meth. Appl. Mech. Eng.* 4, 219-310 (1974).

9. L. R. Herrmann, "Elasticity Equations for Incompressible and Nearly Incompressible Materials by a Variational Theorem," *AIAA J.* 3, 1000-1000 (1965).

10. P. Tong, "An Assumed Stress Hybrid Finite Element Method for an Incompressible and Near-incompressible Material," *Int. J. Solids Struct.*, 455-480 (1980).

11. G. Tricomi, "Applications of the Finite Element Method to the Stress Analysis of Materials Subject to Creep," *Dissertation, University of Wales* (1971).

12. W. Griffler, "Mechanische Theorie," *Bibliographisches Institut, Mannheim* (1969).

13. H. Leipholz, "Einführung in die Elastostatiktheorie," *G. Braun, Berlin* (1969).

ENERGY ERROR IN THE ELASTIC SOLUTION WHEN AN INCOMPRESSIBLE SOLID IS ASSUMED COMPRESSIBLE

Iacob Fried and David S. Mallett

Introduction

In the finite element solution of the elastic problem when Poisson's ratio ν is nears one-half or the solid approaches incompressibility one of the following mishaps occurs: either the approximation ability of the element reduces to null or the condition of the stiffness matrix increases without bound [1, 2]. To avoid these computational difficulties in the analysis of (nearly) incompressible solids Poisson's ratio should be increased to 1/2 gradually [3, 4] with the mesh refinement in such a way as to balance the discretization error with the compressibility error resulting from the change in ν in order to maximally reduce the condition number of the stiffness matrix. To do this it is necessary to know the energy error committed in the compressibility assumption and it is the purpose of this paper to estimate this error.

Basic Equations

Consider the common isotropic elastic problem [5]

$$\nabla^2 u_1 + \frac{m}{m-1} \frac{\partial \sigma}{\partial x_1} + \frac{F_1}{G} = 0 , \quad 1 = 1, 2, 3 \text{ in } D \quad (1)$$

$$\sigma = \frac{\partial \sigma_1}{\partial x_1} + \frac{\partial \sigma_2}{\partial x_2} + \frac{\partial \sigma_3}{\partial x_3} \quad (2)$$

with boundary conditions

$$U = (u_1^0, u_2^0, u_3^0) \text{ on } \tilde{S}_1 \quad (3)$$

$$\mathbf{T} = (T_1, T_2, T_3) \text{ and } \mathbf{q}_1 =$$

(4)

where $\mathbf{U} = (u_1, u_2, u_3)$ is the Cartesian displacement vector, $\mathbf{F} = (F_1, F_2, F_3)$ the body force vector, and $\mathbf{T} = T(T_1, T_2, T_3)$ the surface traction vector.

The shear and direct strains are related to the displacement \mathbf{U}

$$e_{ij} = \frac{\partial u_i}{\partial x_j} + \frac{\partial u_j}{\partial x_i}, \quad i,j = 1,2,3, \quad (5)$$

Hooke's law for the isotropic solid is of the form

$$q_1 = \sigma_{ij} \left(e_{ij} + \frac{\alpha - 1}{2} \right), \quad q_2 = \sigma_{12}, \quad q_3 = \frac{\partial \sigma_{12}}{\partial x_1}, \quad i,j = 1,2,3. \quad (6)$$

Giving the shear modulus and $\alpha = 1/\nu$ the inverse of Poisson's ratio ν , the traction \mathbf{T} on any surface with unit normal $\mathbf{n} = (n_1, n_2, n_3)$ is given in terms of the stresses by

$$T_1 = q_1 n_1 + q_2 n_2 + q_3 n_3. \quad (7)$$

The total potential energy $\Pi(\mathbf{U})$ associated with the elastic boundary value problem described by equations (1), (2), (3), and (4) is written as

$$\Pi(\mathbf{U}) = E(\mathbf{U}, \mathbf{U}) - \int_{\Omega} (T_1 u_1 + T_2 u_2 + T_3 u_3) d\Omega - \int_{\Gamma} (T_1 n_1 + T_2 n_2 + T_3 n_3) d\Gamma, \quad (8)$$

where the internal elastic energy $E(\mathbf{U}, \mathbf{U})$ is explicitly given by

$$K = \frac{2}{3} \frac{m+1}{m-3}. \quad (14)$$

$$E(\mathbf{U}, \mathbf{U}) = \int_{\Omega} \left[\frac{1}{2} \frac{m+1}{m-3} e^2 + \frac{1}{3} [(e_{11} - e_{22})^2 + (e_{22} - e_{33})^2 + (e_{33} - e_{11})^2] \right. \\ \left. + \frac{1}{2} (e_{12}^2 + e_{23}^2 + e_{31}^2) \right] dx \quad (9)$$

and in which G was set equal to 1.

Denoting by U the solution to the compressible elastic problem the principle of minimum potential energy can be stated as

$$\pi(U) = \min_V \Pi(V) \quad (10)$$

minimization being carried out over the class of functions V which satisfy equation (3) and for which $E(V, V) < \infty$.

In the case of an incompressible solid with $\nu = 1/2$ (in 2D) the pressure p

$$p = \frac{1}{3} (\sigma'_{11} + \sigma'_{22} + \sigma'_{33}), \quad (11)$$

where $(')$ refers to the incompressible state, needs to be introduced and the stress-strain relation becomes with a unit shear modulus G

$$q'_i = 2e'_{ii} + p, \quad q'_{ij} = e'_{ij}, \quad i,j = 1,2,3 \quad (12)$$

leading to the equilibrium equations

$$\nabla^2 u'_i + \frac{\partial p}{\partial x_i} + F'_i = 0, \quad i = 1,2,3. \quad (13)$$

It is found useful to introduce the constant

Compressibility Error

The principal result of this paper is given in the following theorem.

Theorem: Let U be the elastic solution of a compressible solid with $m < 2$, and U' be the solution to the same problem but with an incompressible material for which $m = 2$. Then,

$$E(U - U', U - U') \leq \frac{1}{K} \int_D p^2 dx . \quad (15)$$

Concerning the dependence on K inequality (15) is optimal.

For the proof the potential $\Psi(U)$ is introduced

$$\begin{aligned} \Psi(U) = \int_D \left\{ \frac{1}{2} [(\epsilon_{11} - \epsilon_{22} - \epsilon_{11}' + \epsilon_{22}')^2 + (\epsilon_{22} - \epsilon_{33} - \epsilon_{22}' + \epsilon_{33}')^2 \right. \\ \left. + (\epsilon_{33} - \epsilon_{11} - \epsilon_{33}' + \epsilon_{11}')^2] \right\} dx \\ + \frac{1}{2} \left[(\epsilon_{12} - \epsilon_{12}')^2 + (\epsilon_{23} - \epsilon_{23}')^2 + (\epsilon_{31} - \epsilon_{31}')^2 \right] \\ + \frac{1}{K} (p - u')^2 \} dx . \quad (16) \end{aligned}$$

This potential is minimized by the same displacement state U that minimizes $\Psi(U)$ in equation (8). This is so because $\Psi(U)$ is merely $\Psi(U)$ plus a constant term which is independent of U . Indeed, squaring the terms in the integrand of (8) transforms it into

$$\begin{aligned} \Psi(U) = E(U, U) + \int_D \left[\epsilon_{11}^2 + \epsilon_{22}^2 + \epsilon_{33}^2 + \frac{1}{2} (\epsilon_{12}'^2 + \epsilon_{23}'^2 + \epsilon_{31}'^2) \right] dx \\ - \int_D p u' dx + \frac{1}{K} \int_D p^2 dx - \frac{1}{2} \int_D [(\epsilon_{11}\epsilon_{11}' + \epsilon_{22}\epsilon_{22}' + \epsilon_{33}\epsilon_{33}') dx \\ - \int_D (\epsilon_{12}\epsilon_{12}' + \epsilon_{23}\epsilon_{23}' + \epsilon_{31}\epsilon_{31}') dx . \quad (17) \end{aligned}$$

Adding and subtracting $\epsilon_{11}'^2 + \epsilon_{22}'^2 + \epsilon_{33}'^2$ from the integrand of the fourth integral in equation (17), and adding and subtracting $\epsilon_{12}'^2 + \epsilon_{23}'^2 + \epsilon_{31}'^2$ from the integrand of the last integral in equation (17) while using the fact that $u' = 0$, transforms $\Psi(U)$ further into

$$\begin{aligned} \Psi(U) = E(U, U) - \int_D \left[\epsilon_{11}^2 + \epsilon_{22}^2 + \epsilon_{33}^2 + \frac{1}{2} (\epsilon_{12}'^2 + \epsilon_{23}'^2 + \epsilon_{31}'^2) \right] dx \\ + \frac{1}{2K} \int_D p^2 dx - \int_D p(u - u') dx \\ - 2 \int_D [\epsilon_{11}'(\epsilon_{11} - \epsilon_{11}') + \epsilon_{22}'(\epsilon_{22} - \epsilon_{22}') + \epsilon_{33}'(\epsilon_{33} - \epsilon_{33}')] dx \\ - \int_D [\epsilon_{12}'(\epsilon_{12} - \epsilon_{12}') + \epsilon_{23}'(\epsilon_{23} - \epsilon_{23}') + \epsilon_{31}'(\epsilon_{31} - \epsilon_{31}')] dx . \quad (18) \end{aligned}$$

Integration by parts of the integral including $p(u - u')$ in equation (18) yields

$$\begin{aligned} - \int_D p(u - u') dx = \int_D [p_{,1}(u_1 - u_1') + p_{,2}(u_2 - u_2') + p_{,3}(u_3 - u_3')] dx \\ - \int_S p(u - u') n_1 + (u_2 - u_2') n_2 + (u_3 - u_3') n_3 dS \quad (19) \end{aligned}$$

in which $()_{,1} = \partial/\partial x_1$, and where $n = (n_1, n_2, n_3)$ is a unit normal on S . Substituting in equation (19) $p_{,1}$ from the equilibrium equations

$$\begin{aligned} -p_{,1} = F_1 + 2\epsilon_{11}'(1 + \epsilon_{12}'^2 + \epsilon_{23}'^2 + \epsilon_{31}'^2) \\ -p_{,2} = F_2 + 2\epsilon_{22}'(2 + \epsilon_{12}'^2 + \epsilon_{23}'^2 + \epsilon_{13}'^2) \\ -p_{,3} = F_3 + 2\epsilon_{33}'(3 + \epsilon_{31}'^2 + \epsilon_{23}'^2) \end{aligned} \quad (20)$$

Integration by parts and addition of the resulting form of equation (19) back to $\Psi(U)$ results in the cancellation of the last two integrals in equation (18) and $\Psi(U)$ becomes now

$$\begin{aligned} \Phi(\mathbf{U}, \mathbf{U}') = & E(\mathbf{U}, \mathbf{U}) - \int_D \left[c_{11}^2 + c_{22}^2 + c_{33}^2 + \frac{1}{2} (c_{12}^2 + c_{23}^2 + c_{31}^2) \right] dx \\ & + \frac{1}{K} \int_D p^2 dx \\ & - \int_D (T_1(u_1 - u'_1) + T_2(u_2 - u'_2) + T_3(u_3 - u'_3)) dx \\ & - \int_S (u_1 - u'_1) \partial u_1 + 2c_{11}^* u_1^* + c_{12}^* u_2^* + c_{13}^* u_3^* \\ & + (u_2 - u'_2) \partial u_2 + 2c_{22}^* u_2^* + c_{23}^* u_3^* + c_{12}^* u_1^* \\ & + (u_3 - u'_3) \partial u_3 + 2c_{33}^* u_3^* + c_{31}^* u_1^* + c_{23}^* u_2^*) dS . \end{aligned} \quad (21)$$

The boundary integral vanishes on S_1 , since there $\mathbf{U}' = \mathbf{U}^* = \mathbf{U}^*$. On S_2 , $T = (T_1, T_2, T_3)$ is prescribed and hence due to equations (7) and (12) becomes

$$\Phi(\mathbf{U}) = E(\mathbf{U}) - E(\mathbf{U}') + \frac{1}{K} \int_D p^2 dx \quad (22)$$

as claimed before.

The potential (Φ) in equation (16) can be concisely written as

$$\Phi(\mathbf{U}) = |\mathbf{U} - \mathbf{U}'|^2_1 + \frac{1}{K} \mathbf{k} \cdot \mathbf{p} \cdot \left| \mathbf{p} - \frac{1}{K} \mathbf{p} \right|_0^2 , \quad (23)$$

where the subscripts 0 and 1 refer to the order of differentiation in the integrands. Since \mathbf{U} minimizes $E(\mathbf{U})$

$$\Phi(\mathbf{U}) \leq \Phi(\mathbf{U}') \quad (24)$$

and, therefore,

$$|\mathbf{U} - \mathbf{U}'|^2_1 + \frac{1}{K} \mathbf{k} \cdot \mathbf{p} \cdot \left| \mathbf{p} - \frac{1}{K} \mathbf{p} \right|_0^2 \leq \frac{1}{K} \mathbf{k} \cdot \mathbf{p} \cdot \left| \mathbf{p} \right|_0^2 . \quad (25)$$

Or

$$\left| \mathbf{p} - \frac{1}{K} \mathbf{p} \right|_0^2 \leq \frac{1}{K^2} \mathbf{k} \cdot \mathbf{p} \cdot \left| \mathbf{p} \right|_0^2 - \frac{2}{K} |\mathbf{U} - \mathbf{U}'|_1^2 , \quad (26)$$

which upon taking the square root on both sides becomes

$$\left| \mathbf{p} - \frac{1}{K} \mathbf{p} \right|_0 \leq \left(\frac{1}{K^2} \mathbf{k} \cdot \mathbf{p} \cdot \left| \mathbf{p} \right|_0^2 - \frac{2}{K} |\mathbf{U} - \mathbf{U}'|_1^2 \right)^{1/2} . \quad (27)$$

But since

$$\left| \mathbf{p} - \frac{1}{K} \mathbf{p} \right|_0 \geq \left| \mathbf{p} \right|_0 - \frac{1}{K} \mathbf{k} \cdot \mathbf{p} \cdot \left| \mathbf{p} \right|_0 , \quad (28)$$

it follows that

$$\left| \mathbf{p} \right|_0 \leq \left(\frac{1}{K^2} \mathbf{k} \cdot \mathbf{p} \cdot \left| \mathbf{p} \right|_0^2 - \frac{2}{K} |\mathbf{U} - \mathbf{U}'|_1^2 \right)^{1/2} + \frac{1}{K} \mathbf{k} \cdot \mathbf{p} \cdot \left| \mathbf{p} \right|_0 . \quad (29)$$

Squaring both sides of (29), dropping the cross term, and retreating the displacement term leads to

$$|\mathbf{U} - \mathbf{U}'|^2_1 + \frac{1}{K} \mathbf{k} \cdot \mathbf{p} \cdot \left| \mathbf{p} \right|_0^2 \leq \frac{1}{K} \mathbf{k} \cdot \mathbf{p} \cdot \left| \mathbf{p} \right|_0^2 , \quad (30)$$

which is

$$E(\mathbf{U} - \mathbf{U}', \mathbf{U} - \mathbf{U}') \leq \frac{1}{K} \int_D p^2 dx \quad (31)$$

corresponding to equation (16).

Optimality of Error Estimate

To prove that, concerning K , the error estimate in equation (31) is optimal it is sufficient to come up with an example where equation (31) is sharp. An appropriate case is that of a hollow sphere [6]

holding an internal unit pressure. In the incompressible case the radial displacement u^r and the pressure p are given by

$$u^r = -\frac{A}{r}, \quad A = \frac{a^3 b^3}{4(p_0 - a)}, \quad p = \frac{a^3}{b^3 - a^3}, \quad (32)$$

where r is the radial coordinate, and a and b the inner and outer radii, respectively. In the compressible case

$$u^r = -\frac{A}{r} + \frac{1}{K} \nabla p \quad (33)$$

from which it results that

$$\nabla p = (u^r, u^z, u^y) = \frac{1}{r} \frac{1}{K} \nabla^2 p \quad (34)$$

assuming unit volume. This shows that the dependence of the error estimate (31) on K is sharp at least up to a multiplicative constant independent of ν .

Acknowledgment

This research was supported by NSF Grant GK 42363 and ONR contract No. 07-2320-0004, to both of which the authors are grateful.

References

1. L. Fried, Bounds on the Extremal Eigenvalues of the Finite Element Matrices and Mass Matrices and Their Spectral Condition Number, J. Sound and Vibration 22, 407-418 (1972).
2. L. Fried, Influence of Poisson's Ratio on the Condition of the Finite Matrix, J. Solids Structures 9, 223-239 (1973).

DISPLACEMENTS, STRAIN AND STRESS ERROR NODAL LINES IN FINITE ELEMENTS†

ISAAC FRIED

Department of Mathematics, Boston University, Boston, MA 02215, U.S.A.

and

J. A. METZLER

Department of Mathematics, Drew University, Madison, NJ 07940, U.S.A.

(Received 11 September 1977; received for publication 1 December 1977)

Abstract—Numerical experiments show that the error in the computed finite element solution and its derivatives vanish on typical error nodal lines inside each finite element. A theoretical explanation is given to this phenomenon, which was previously discovered for distinct, special points. Systematic classification of these lines for different element types and problems appears to be a worthy undertaking.

INTRODUCTION

Since the original observation by Barlow[1] that the finite element stresses computed in rectangular elements at the Gauss points are superior in accuracy, there have been reports on different such special points in rectangles[2] and triangles[3]. Using the best energy fit technique[4], whereby minimization of the error in the energy is carried out over a single typical element with an assumed polynomial exact solution that assures a globally admissible finite element solution, it is shown here that there are *entire lines* (surfaces in space) inside the element on which accuracy is superior and hence the variety of observed special points.

These nodal lines depend on the element, original problem and eventually location, as shown theoretically and numerically in this paper.

POISSON'S EQUATION

Here the finite element solution δ is obtained from the minimization of

$$\pi(\delta) = \frac{1}{2} \int_D (\delta_x^2 + \delta_y^2 - 2/\delta) dx dy \quad (1)$$

or equivalently

$$\pi(\delta) - \pi(u) = \frac{1}{2} \int_D [(u_x - \delta_x)^2 + (u_y - \delta_y)^2] dx dy \quad (2)$$

where u and δ are the exact solution and the finite element trial function, respectively.

For the bilinear, rectangular finite element $\delta = a_0 + a_1x + a_2y + a_3xy$, $-1 \leq x, y \leq 1$, inside each element and accordingly the choice $u = a_0x^2 + a_1xy + a_2y^2$ is made. Minimization of (2) yields $a_1 = 0$, $a_2 = 0$ and $a_3 = a$, such that $\delta = a_0 + a_3xy$. Equating u_x , u_y with δ_x , δ_y , produces $a_{0x} = 0$, and $a_{0y} = 0$, and the errors $\delta_{u_x} = u_x - \delta_x$, and $\delta_{u_y} = u_y - \delta_y$, are changing signs on the lines $x = 0$ and $y = 0$, respectively. Choosing the free

parameter $a_0 = 0$ makes the finite element solution the interpolate to the quadratic, meaning that it is extendable over neighboring elements. Also, since any smooth solution is, by Taylor's theorem, almost a polynomial inside each element, it is expected of the errors to change signs on $x = 0$ and $y = 0$ in general. One is also tempted to conjecture (as was done in [4]) that the best place to compute δ is at the nodes. Numerical experiments, however, refute this, at least in the bilinear case.

For the biquadratic element $\delta = a_0 + a_1x + a_2y + a_3x^2 + a_4xy + a_5y^2 + a_6x^2y + a_7x^2y^2 + a_8x^3y^2$, $-1 \leq x, y \leq 1$, and consequently the choice $u = a_0x^3 + a_1x^2y + a_2xy^2 + a_3y^3$ is made. Similar arguments lead here to the conclusion that δ_{u_x} changes signs along the lines $x = \pm\sqrt{1/3}$ and δ_{u_y} along $y = \pm\sqrt{1/3}$. For δ_{u_z} one is again led to expect the best accuracy at the nodes.

To numerically observe all this and to see the effects of numerical integration, the equation $u_{xx} + u_{yy} + 1 = 0$ is solved in a square region with $u = 0$ on its boundary. Finite element calculations are carried out with bilinear and biquadratic elements (because of symmetry only one quarter is considered.) The error nodal lines of δ_{u_x} and δ_{u_y} for a 7×7 mesh of bilinear elements and the shaded element as in Fig. 1(a), are shown in Figs. 1(b) and (c). Figures 1(d) and (e) show the nodal lines of δ_{u_x} and δ_{u_y} for the biquadratic element (3×3 mesh and an element at the middle of the quadrant), with exact integration and a 2×2 (broken line) Gauss integration scheme. If δ_x or δ_y are computed at the Gauss point then the 2×2 integration results, as can be seen from Table 1, in a certain loss of accuracy.

PLATE BENDING

Here one is called to minimize (Poisson's ratio $\nu = 0$): The potential energy

$$\pi(\delta) = \frac{1}{2} \int_D (\delta_{xx}^2 + \delta_{yy}^2 + 2\delta_{xy}^2 - 2/\delta) dx dy \quad (3)$$

or

$$\pi(\delta) - \pi(u) = \frac{1}{2} \int_D (u_{xx}^2 - \delta_{xx}^2) + (u_{yy}^2 - \delta_{yy}^2) + 2(u_{xy} - \delta_{xy})^2 dx dy. \quad (4)$$

*Research supported by the Office of Naval Research ONR-N00014-76-C-036.

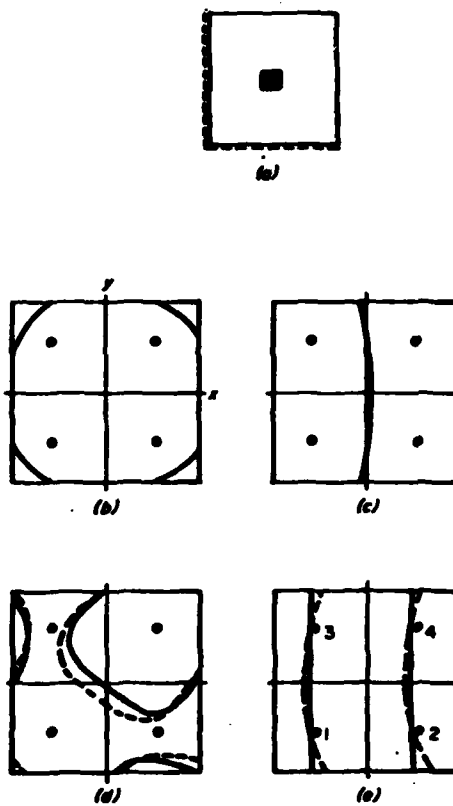


Fig. 1. Fixed square membrane discretized with rectangular elements. Nodal lines for δu (b) and δu , (c) in case of a mesh of bilinear elements as in (a). The nodal lines in (d) and (e) are for δu and δu , respectively, for exact and a 2×2 Gauss scheme (broken line), and a 3×3 mesh of biquadratic elements as in Fig. 3(e). The marked points \odot are Gauss points.

Table 1. Values of $\delta u_s = \delta_s - \delta_s$ at the four Gauss points in Fig. 1(e) for a biquadratic element and a 3×3 mesh discretizing a uniformly loaded membrane. Once for exact (3×3) and once for a 2×2 Gauss integration Scheme

Point	δu_s	
	3×3	2×2
1	-0.35d-4	-0.61d-4
2	-0.45d-4	0.20d-3
3	-0.12d-4	-0.33d-3
4	0.84d-2	0.25d-3
max(δu_s)	0.31d-2	0.40d-2

In the case of the bicubic, rectangular element

$$\delta = \sum a_i x^i y^j \quad i < 3, j < 3, -1 \leq x, y \leq 1 \quad (5)$$

and accordingly the choice for u falls upon

$$u = a_0 x^4 + a_1 x^3 y + a_2 x^2 y^2 + a_3 x y^3 + a_4 y^4, \quad -1 \leq x, y \leq 1. \quad (6)$$

Once more the best energy fit is the interpolate such that

$$\delta = -a_0 x^2 - a_4 y^2 + 2a_0 x^3 + 2a_4 y^3 + a_1 x^3 y + a_2 x^2 y^2 + a_3 x y^3 \quad (7)$$

and

$$\delta u = \frac{1}{4} a_0 (x+1)(x-1)^2 + \frac{1}{4} a_4 (y+1)(y-1)^2 \quad (8)$$

$$\delta u_x = \frac{1}{4} a_0 x (x+1)(x-1) \quad (9)$$

$$\delta u_{xx} = a_0 (3x^2 - 1) \quad (10)$$

$$\delta u_{yy} = a_4 (3y^2 - 1) \quad (11)$$

$$\delta u_{xy} = a_4 (3y^2 - 1) \quad (12)$$

with δu_{xy} being identically zero. Thus the nodal lines for δu_x are $x = -1, x = 0$ and $x = 1$. Those of $\delta u_y, y = -1, y = 0$ and $y = 1$, while δu_{xx} and δu_{yy} change sign on the lines that pass through the Gauss points $(\pm \sqrt{3}/3, \pm \sqrt{3}/3)$ and parallel to the x and y axes, respectively.

Figure 2(a)-(d) shows the experimental error nodal lines for δu , δu_x , δu_y , and δu_{xy} in case of a simply supported plate uniformly loaded and discretized as in Fig. 2(e).

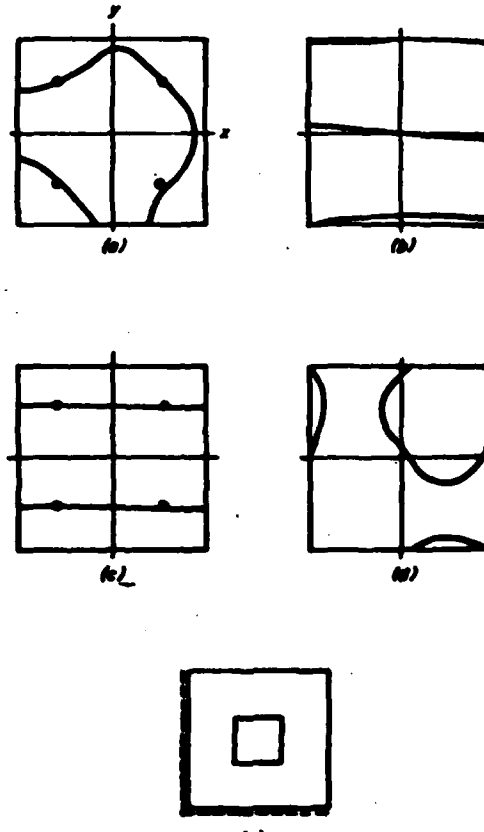


Fig. 2. Nodal lines of δu (a), δu_x (b), δu_y (c) and δu_{xy} (d) in case of a simply supported square plate uniformly loaded and discretized by a 3×3 mesh (e) of bicubic elements (nodal values a_0, a_1, a_2, a_3, a_4). The marked points \odot are Gauss points.

Table 2. Rotating sphere with biquadratic elements. Relative errors of strains at the twenty-five points in Fig. 3(a). Integration with 3×3 Gauss integration points and $\nu = 0.3$

Point	$\delta e_x/e_0$	$\delta e_y/e_0$	$\delta e_z/e_0$	$\delta \gamma/\gamma$
1	-0.102d-00	-0.111d-02	-0.232d-01	0.277d-00
2	-0.304d-01	-0.119d-01	-0.554d-01	0.467d-01
3	-0.764d-01	-0.110d-02	-0.666d-01	-0.457d-01
4	-0.634d-01	0.148d-01	-0.681d-01	0.740d-01
5	-0.542d-01	0.109d-02	-0.410d-01	0.329d-00
6	-0.257d-01	0.108d-03	-0.174d-01	0.219d-00
7	-0.113d-01	-0.105d-01	-0.498d-01	-0.764d-02
8	0.506d-02	0.136d-02	-0.666d-01	-0.987d-01
9	0.218d-01	0.191d-01	-0.593d-01	0.188d-01
10	0.306d-01	0.470d-02	-0.321d-01	0.270d-00
11	0.220d-01	-0.264d-03	-0.170d-01	0.204d-00
12	0.336d-01	-0.116d-01	-0.481d-01	-0.308d-01
13	0.516d-01	0.270d-03	-0.543d-01	-0.125d-00
14	0.682d-01	0.187d-01	-0.734d-01	-0.400d-02
15	0.723d-01	0.151d-02	-0.387d-01	0.255d-00
16	-0.199d-01	-0.717d-03	-0.193d-01	0.255d-00
17	-0.126d-01	-0.129d-01	-0.477d-01	-0.435d-02
18	0.551d-02	-0.820d-03	-0.492d-01	-0.109d-00
19	0.206d-01	0.106d-01	-0.119d-00	0.240d-01
20	0.137d-01	-0.204d-02	-0.533d-01	0.309d-00
21	-0.975d-01	0.306d-03	-0.159d-01	0.345d-00
22	-0.999d-01	-0.118d-01	-0.448d-01	0.534d-01
23	-0.853d-01	0.143d-02	-0.538d-01	-0.644d-01
24	-0.835d-01	0.237d-01	-0.125d-01	0.840d-01
25	-0.120d-00	0.166d-02	-0.459d-01	0.403d-00

Table 3. Same as Table 2 but with 3×3 Gauss integration points $\nu = 0.45$

Point	$\delta e_x/e_0$	$\delta e_y/e_0$	$\delta e_z/e_0$	$\delta \gamma/\gamma$
1	-0.112d-00	-0.519d-02	0.130d-01	0.244d-00
2	-0.325d-01	-0.170d-01	-0.835d-02	0.466d-01
3	-0.558d-01	-0.362d-02	-0.427d-02	-0.344d-01
4	-0.398d-01	0.155d-01	0.201d-00	0.713d-01
5	-0.319d-10	-0.502d-02	-0.109d-01	0.296d-00
6	-0.704d-01	-0.257d-02	0.222d-01	0.197d-00
7	-0.370d-01	-0.146d-01	-0.885d-03	-0.222d-02
8	-0.475d-03	0.233d-03	-0.735d-02	-0.821d-01
9	0.258d-01	0.219d-01	-0.223d-02	0.222d-01
10	0.387d-01	-0.902d-03	0.121d-00	0.244d-00
11	-0.449d-01	-0.164d-02	0.266d-01	0.192d-00
12	-0.123d-01	-0.150d-01	0.308d-02	-0.194d-01
13	0.372d-01	-0.476d-03	-0.680d-02	-0.185d-00
14	0.718d-01	0.219d-01	-0.201d-01	0.272d-02
15	0.909d-01	-0.664d-02	-0.457d-00	0.234d-00
16	-0.653d-01	-0.799d-03	0.270d-01	0.245d-00
17	-0.413d-01	-0.157d-01	0.584d-02	0.814d-02
18	0.284d-02	-0.143d-02	-0.711d-02	-0.887d-01
19	0.502d-01	0.219d-01	-0.233d-01	0.292d-01
20	0.719d-01	-0.144d-01	-0.116d-00	0.285d-00
21	-0.112d-00	0.159d-02	0.297d-01	0.331d-00
22	-0.102d-00	-0.137d-01	0.707d-02	0.628d-01
23	-0.702d-01	0.103d-02	-0.102d-01	-0.679d-01
24	-0.452d-01	0.293d-01	-0.322d-01	0.238d-01
25	-0.618d-01	-0.111d-01	-0.933d-01	0.371d-00

ELASTICITY

As an example in elasticity, consider the rotating thick spherical shell for which analytic solution to compare with the approximate is available[5] (refers to this paper in the Appendix). The spherical strains[6] are too involved for a theoretical prediction as in the preceding section and analysis is confined to the numerical. Of

interest here is the dependence of the nodal lines on the order of numerical integration and Poisson's ratio ν .

Figures 3(a)-(d) shows the nodal lines for the strain error δe_x , δe_y , δe_z and the shear $\delta \gamma$, for a 3×3 mesh of biquadratic elements and the shaded element in Fig. 3(e). Figure 3 refers to a 3×3 Gauss integration scheme and $\nu = 0.3$.

Table 4. Same as Table 2 but with 2×2 Gauss integration points and $\nu = 0.3$

Point	$\delta u/u_0$	$\delta v_0/u_0$	$\delta w_0/u_0$	θ/γ
1	0.369d+00	0.796d-02	-0.483d-01	0.371d+00
2	-0.573d-01	-0.100d-01	-0.537d-01	0.991d-01
3	-0.549d+00	-0.394d-02	0.308d-01	-0.407d-01
4	-0.616d-01	0.157d-01	-0.820d-01	0.285d-01
5	0.284d+00	0.123d-01	-0.193d-01	0.236d+00
6	0.617d+00	0.198d-02	-0.133d-01	0.219d+00
7	-0.320d-02	-0.875d-02	-0.452d-01	-0.664d-02
8	-0.320d+00	0.276d-02	-0.585d-01	-0.964d-01
9	0.190d-01	0.196d-01	-0.665d-01	0.222d-01
10	0.714d+00	0.399d-02	-0.368d-01	0.274d+00
11	0.296d-01	-0.236d-02	-0.195d-02	0.158d+00
12	0.489d-01	-0.102d-01	-0.466d-01	-0.572d-01
13	0.645d-01	0.361d-02	-0.790d-01	-0.127d+00
14	0.555d-01	0.187d-01	-0.913d-01	0.224d-01
15	0.226d-01	-0.641d-02	-0.769d-01	0.310d+00
16	-0.740d+00	0.855d-03	-0.384d-01	0.261d+00
17	0.121d-01	-0.120d-01	-0.599d-01	-0.794d-02
18	0.504d+00	-0.870d-03	-0.325d-01	-0.116d+00
19	-0.780d-02	0.180d-01	-0.251d+00	0.213d-01
20	-0.149d+01	-0.220d-02	-0.117d+00	0.317d+00
21	-0.132d+01	0.977d-02	-0.108d+00	0.475d+00
22	-0.655d-01	-0.115d-01	-0.794d-01	0.110d+00
23	0.836d+00	-0.527d-02	0.275d-01	-0.777d-01
24	-0.129d+00	0.225d-01	-0.102d+02	0.140d-01
25	-0.365d+01	0.216d-01	-0.113d+00	0.291d+00

Table 5. Same as Table 2 but with 2×2 Gauss integration points and $\nu = 0.45$

Points	$\delta u/u_0$	$\delta v_0/u_0$	$\delta w_0/u_0$	θ/γ
1	0.275d+01	0.455d-01	-0.124d+00	0.690d+00
2	-0.510d-01	-0.123d-01	-0.369d-01	0.285d+00
3	-0.134d+01	-0.287d-01	0.122d+00	-0.329d-01
4	-0.483d-01	0.195d-01	751d+00	-0.169d+00
5	0.235d+01	0.813d-01	0.275d+00	-0.169d+00
6	0.181d+01	0.173d-02	-0.135d-01	0.191d+00
7	-0.127d-02	-0.100d-01	-0.279d-01	-0.658d-02
8	-0.899d+00	0.313d-01	0.763d-02	-0.867d-01
9	0.100d+01	0.252d-01	0.168d+00	0.264d+01
10	0.102d+01	0.623d-02	-0.206d+00	0.342d+00
11	0.114d+01	-0.232d-01	0.374d-01	-0.514d+01
12	0.291d+01	-0.127d-01	-0.263d-01	-0.152d+00
13	0.451d+01	0.173d-01	-0.579d-01	-0.114d+00
14	0.430d+01	0.203d-01	0.333d-01	0.121d+00
15	0.224d+01	-0.597d-01	0.288d+01	0.471d+00
16	-0.236d+01	0.768d-03	-0.362d-01	0.237d+00
17	0.533d-02	-0.151d-01	-0.340d-01	-0.736d-02
18	0.196d+01	-0.190d-02	-0.367d-02	-0.106d+00
19	-0.682d-02	0.257d-01	0.798d-01	0.199d+01
20	-0.470d+01	-0.153d-02	0.231d+00	0.289d+00
21	-0.432d+01	0.553d-01	-0.166d+00	0.913d+00
22	-0.310d+01	-0.147d-01	-0.466d-01	0.349d+00
23	0.327d+01	-0.399d-01	0.367d-01	-0.738d-01
24	-0.142d+00	0.310d-01	0.333d-01	-0.239d+00
25	-0.136d+02	0.100d+00	-0.381d+00	-0.211d+00

Tables 2-5 list the relative errors at the twenty-five points in Fig. 3(a), for 2×2 and 3×3 Gauss integration schemes, and $\nu = 0.3$ and $\nu = 0.45$. It is evident from these tables that as ν approaches 0.5 and with a low integration scheme(7) it becomes imperative to look for

the strains (stresses) at points on the nodal lines lest they become dimensionally wrong.

The excellence of the strains at the special points helps to explain the success of Reissner's principle with independent stress fields sampled at the integration points.

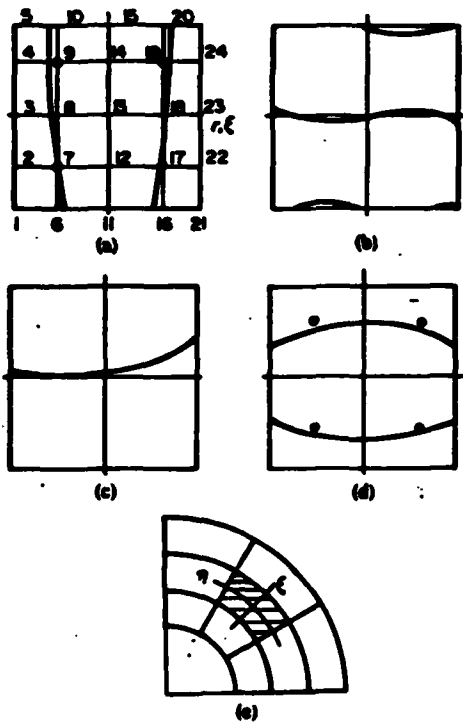


Fig. 3. Nodal lines of the strain errors δe , (a), δe_0 , (b), δe_{10} and δe , (d) in case of a revolving hollow elastic sphere discretized with a 3×3 mesh of biquadratic elements (e). This case is with a 3×3 Gauss integration scheme and $\nu = 0.3$. The marked points \bullet are Gauss points.

REFERENCES

1. G. Strang and G. J. Fix, *An Analysis of the Finite Element Method*, Section 3.4. Prentice-Hall, New Jersey (1973).
2. O. C. Zienkiewicz, Isoparametric element forms in finite element analysis. In *Lectures on Finite Element Methods in Continuum Mechanics* (Edited by J. T. Oden and E. R. de Arantes e Oliveira), pp. 379-414. University of Alabama Press (1973).
3. T. Moon, Experiences with orthogonal polynomials and "best" numerical integration formulas on a triangle; with particular reference to finite element approximations. *ZAMM* 54 501-508 (1974).
4. I. Fried, Finite element method: accuracy at a point. *Quart. Appl. Math.* 19-161 (1974).
5. M. A. Goldberg, V. A. Salerno and M. A. Sadowsky, Stress distribution in a rotating spherical shell of arbitrary thickness. *J. Appl. Mech.* 127-131 (1961).
6. A. E. H. Love, *The Mathematical Theory of Elasticity*, 4th Edn, Section 22. Dover, New York (1944).
7. I. Fried, Finite element analysis of incompressible material by residual energy balancing. *Int. J. Solids Structures* 10, 993-1002 (1975).

APPENDIX

In Ref. [5] eqn (3) should read

$$\sigma_R = [-4\nu + (-3 + 10\nu)\mu^2 + 3(1 - 2\nu)\mu^4]\mu^2.$$

Equation (8) should have been

$$B_0 = -\frac{2(7 - 5\nu)}{5\nu^2} \frac{1 - \alpha^2}{1 - \alpha^4} B_1.$$

CONJUGATE GRADIENT SOLUTION OF A FINITE ELEMENT ELASTIC PROBLEM WITH HIGH POISSON RATIO *

Isaac FRIED

*Boston University, Department of Mathematics,
Boston, Massachusetts 02215, USA*

and

J.A. METZLER

Drew University, Madison, New Jersey 07940, USA

Received 6 February 1978

Introduction

The conjugate gradients method has been shown [1] to be an attractive technique for the solution of the linear algebraic system that is produced by finite elements. It has been noticed however [2] that convergence depends on the eigenvalue spread in the global stiffness matrix, and that an ill-conditioned system leads to poor convergence. Scaling has been shown to improve the performance of the conjugate gradient method in plate problems. In the present paper this method is applied to an elastic problem to study its functioning in the presence of high Poisson ratios that cause a deterioration [3] in the condition of the global stiffness matrix. It is also shown here that scaling has a considerable beneficial effect on the convergence of conjugate gradients also in this case.

1. The elastic problem and its discretization

We propose to use conjugate gradients to solve the problem of a rotating hollow elastic sphere [4] discretized with finite elements. Because of symmetry only a quarter of the sphere need be considered, and we divide the arc and radius into N_e equal parts to form a mesh with N_e^2 "square" finite elements. A biquadratic interpolation is adopted over each element, which is thus associated with nine nodal points.

2. Numerical computations

Actual numerical computations were carried out with $N_e = 4, 5, 6$ and 7 elements per side, once

* Work supported by ONR contract No. ONR-N00014-76-C-36.

without scaling and once with the global stiffness matrix K symmetrically scaled so that $K_{11} = 1$. The algorithm was terminated in each case when the change in the quadratic form $\pi(x) = \frac{1}{2}x^t Kx - x^t f$ which is minimized reached the machine accuracy. The results of these numerical computations are listed in the tables below. Notice in these tables the substantial savings with scaling. The following notation will be used:

ν Poisson's ratio

N_e number of elements per side

N size of the linear system

N_{it} number of iterations required for convergence

$N_e = 7, N = 450$

not scaled			scaled		
ν	N_{it}	N_{it}/N	ν	N_{it}	N_{it}/N
0.0	421	0.936	0.0	158	0.351
0.1	426	0.947	0.1	158	0.351
0.2	452	1.000	0.2	165	0.367
0.3	484	1.076	0.3	183	0.407
0.4	587	1.304	0.4	225	0.500
0.45	738	1.640	0.45	292	0.649
0.475	964	2.142	0.475	395	0.878

$N_e = 6, N = 338$

not scaled			scaled		
ν	N_{it}	N_{it}/N	ν	N_{it}	N_{it}/N
0.0	344	1.018	0.0	135	0.399
0.1	350	1.036	0.1	138	0.408
0.2	359	1.062	0.2	141	0.417
0.3	376	1.112	0.3	157	0.464
0.4	447	1.322	0.4	191	0.565
0.45	581	1.719	0.45	247	0.731
0.475	744	2.201	0.475	333	0.985

$N_e = 5, N = 242$

not scaled			scaled		
ν	N_{it}	N_{it}/N	ν	N_{it}	N_{it}/N
0.0	272	1.124	0.0	113	0.467
0.1	269	1.111	0.1	114	0.471
0.2	276	1.140	0.2	119	0.492
0.3	298	1.231	0.3	128	0.529
0.4	351	1.450	0.4	156	0.645
0.45	440	1.818	0.45	205	0.847
0.475	546	2.256	0.475	264	1.091

$N_e = 4, N = 162$

not scaled			scaled		
ν	N_{it}	N_{it}/N	ν	N_{it}	N_{it}/N
0.0	194	1.198	0.0	87	0.537
0.1	194	1.198	0.1	90	0.556
0.2	198	1.222	0.2	94	0.580
0.3	212	1.309	0.3	103	0.636
0.4	242	1.494	0.4	122	0.753
0.45	296	1.827	0.45	153	0.944
0.475	364	2.247	0.475	193	1.191

References

- [1] I. Fried and J.A. Metzler, The conjugate gradient method with finite elements. Proceedings of the Second IMACS International Symposium on Computer Methods for Partial Differential Equations (June 1977).
- [2] R.L. Fox and E.L. Stanton, Developments in structural analysis by direct energy minimization. AIAA J. 6 (1968) 1036-1042.
- [3] I. Fried, Finite element analysis of incompressible material by residual energy balancing. Int. J. Solids and Structs. 14 (1975) 461-466.
- [4] M.A. Goldberg, V.A. Salerno and M.A. Sadowsky. Stress distribution in a rotating spherical shell of arbitrary thickness. J. Appl. Mech. 28 (1961) 127-131.

SHORT COMMUNICATIONS

SOR vs. CONJUGATE GRADIENTS IN A FINITE ELEMENT DISCRETIZATION

ISAAC FRIED¹

Boston University, Department of Mathematics, Boston, Massachusetts, U.S.A.

AND

JIM MEIJER²

Drew University, Department of Mathematics, Madison, New Jersey, U.S.A.

SUMMARY

Successive Overrelaxation and Conjugate Gradients are used to solve the linear algebraic system set up with finite elements for the discretization of a plane, linear, heat conducting problem. It is numerically shown that even with the optimal overrelaxation factor SOR is hardly superior to CG which is decisively simpler to program.

INTRODUCTION

Even though finite elements are being accepted now as the most appropriate way to discretize problems which can be formulated variationally, the question of how to solve the resulting algebraic systems is yet much in debate. The large computational packages have almost exclusively adopted direct methods of solution based on Gauss elimination and triangular factorization. The reasons for this choice are many: the need to solve the same system with different right hand vectors, the direct method's small sensitivity to round off errors and their termination in a finite number of steps. Direct methods suffer, however, from the disadvantage that they operate on a two-dimensional array which in the case of finite elements is sparse but with no distinct sparseness pattern. As a result the effort to make direct methods efficient becomes a considerable programming exercise to avoid zero operations that depend also on the numbering of the nodal points.

Iterative methods are subtler to apply; one has to know when to stop them and their efficiency is a hidden function of the properties of the global stiffness matrix. On the other hand their programming is considerably simpler than that of direct methods and the sparseness of the matrix can be accounted for in an uncomplicated way since they do not operate on a two-dimensional array but rather require as a basic operation only the multiplication of a vector by a matrix.

Among iterative methods, Successive Overrelaxation has received extensive coverage¹ in the context of finite difference equations. For some reason, Conjugate Gradients² never became that prominent. This method, however, is technically very well suited^{3,4} to solve the finite element algebraic equations. Although both of these methods suffer from truncation and

¹ Associate Professor

² Assistant Professor

Research supported by Office of Naval Research Contract No. ONR N00014-76-C-036

round-off errors, it is the author's experience that this is not a serious problem unless the system is particularly ill-conditioned. In the cases where this is a problem, the author recommends scaling of the type described in References 3, 4.

In this paper we apply both SOR and CG to a two-dimensional stationary heat conduction problem discretized with finite elements and show that even under optimal conditions, that in fact rarely materialize, SOR converges only slightly faster than the more conveniently programmed CG.

SUCCESSIVE OVERRELAXATION

Let us recall the SOR algorithm. We wish to solve the linear algebraic system

$$\mathbf{K}\mathbf{x} = \mathbf{f} \quad (1)$$

and with positive definite and symmetric \mathbf{K} , which we decompose in the form

$$\mathbf{K} = \mathbf{D} + \mathbf{L} + \mathbf{L}^T \quad (2)$$

where \mathbf{D} is (block) diagonal and \mathbf{L} the remaining strictly lower triangular matrix. We write now

$$[\mathbf{D} + \omega\mathbf{L}]\mathbf{x}_1 = [\omega\mathbf{L}^T + (1 - \omega)\mathbf{D}]\mathbf{x}_0 + \omega\mathbf{f} \quad (3)$$

in which ω is the overrelaxation factor. The successive overrelaxation scheme in equation (3) has the iteration matrix

$$\mathbf{L}_{\omega} = [\mathbf{D} + \omega\mathbf{L}]^{-1} = \omega\mathbf{L}^T + (1 - \omega)\mathbf{D} \quad (4)$$

and the basic problem of SOR is to locate the optimal ω that minimizes the spectral radius $\rho(\mathbf{L}_{\omega})$ of the matrix \mathbf{L}_{ω} . No sure way exists to find the optimal ω , which is the greatest flaw of SOR especially in view of the fact that the efficiency of the method strongly depends on ω .

CONJUGATE GRADIENTS

Here the algebraic system in equation (1) is solved by

$$\mathbf{r}_0 = \mathbf{f} - \mathbf{K}\mathbf{x}_0, \quad \mathbf{p}_0 = \mathbf{r}_0$$

$$\alpha_i = \mathbf{p}_i^T \mathbf{r}_i / \mathbf{p}_i^T \mathbf{K} \mathbf{p}_i$$

$$\mathbf{x}_{i+1} = \mathbf{x}_i + \alpha_i \mathbf{p}_i$$

$$\mathbf{r}_{i+1} = \mathbf{r}_i - \alpha_i \mathbf{K} \mathbf{p}_i$$

$$\beta_i = \mathbf{r}_{i+1}^T \mathbf{r}_{i+1} / \mathbf{r}_i^T \mathbf{r}_i$$

$$\mathbf{p}_{i+1} = \mathbf{r}_{i+1} + \beta_i \mathbf{p}_i$$

No elusive factor is needed in this algorithm and the only matrix vector multiplication that appears in it is \mathbf{Kp} . How to carry out this algorithm with finite elements is discussed in Reference 3. What we want to do here is only to compare the two algorithms on a given realistic problem.

TEST CASE

Figure 1 shows half the cross section of a double barrelled steam pipe of which *abcdef* is a line of symmetry. The larger bore *bc* carries steam at a constant temperature 500°F while the

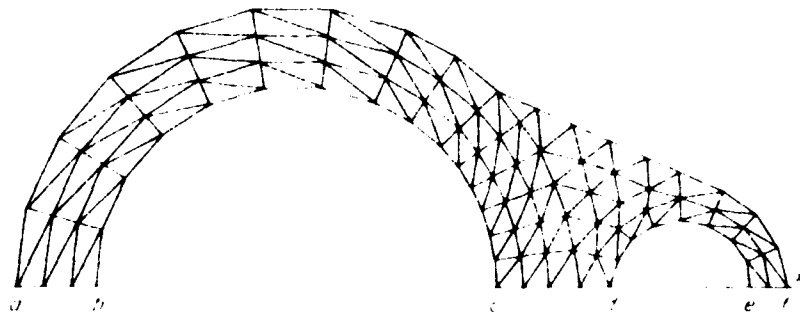


Figure 1

smaller is designed to house a thermometer and we assume the arch be insulated. Heat is lost from the outer surface af of the manifold by radiation. The cross section is divided into 140 triangular elements with the temperature taken to be linear over each one of them. This discretization gives rise to 99 unknown temperature values at the vertices of all elements.

The iteration matrix L_ω in equation (4) was set up and its spectral radius $\rho(L_\omega)$ computed as a function of ω and plotted in Figure 2. It is seen that the optimal ω , ω_{opt} is 1.69. Next the heat conduction problem was solved first with CG and then with SOR using this ω_{opt} . To compare the convergence in both cases the iterated temperature at point f , T_f is plotted in Figure 3 versus the number of iterations N_ω . When ω_{opt} is used in SOR it is seen to be slightly faster

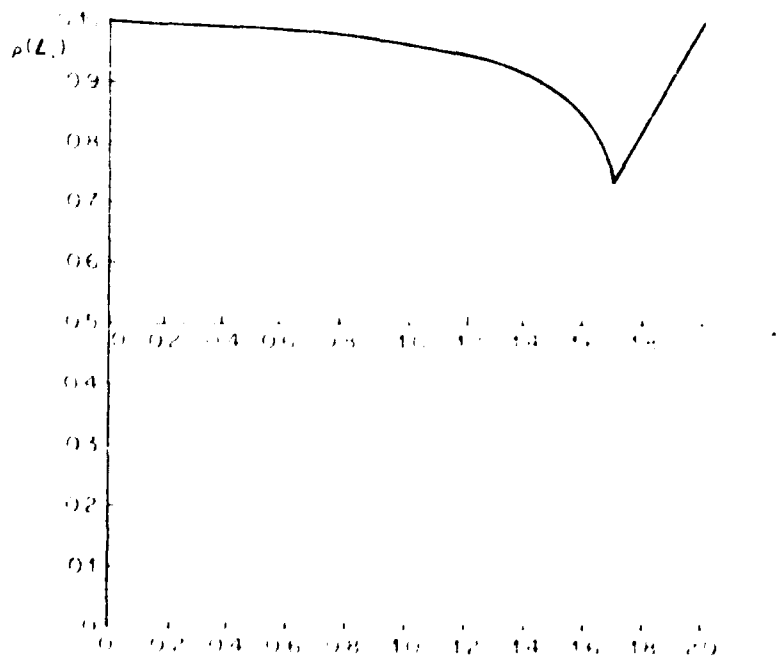


Figure 2

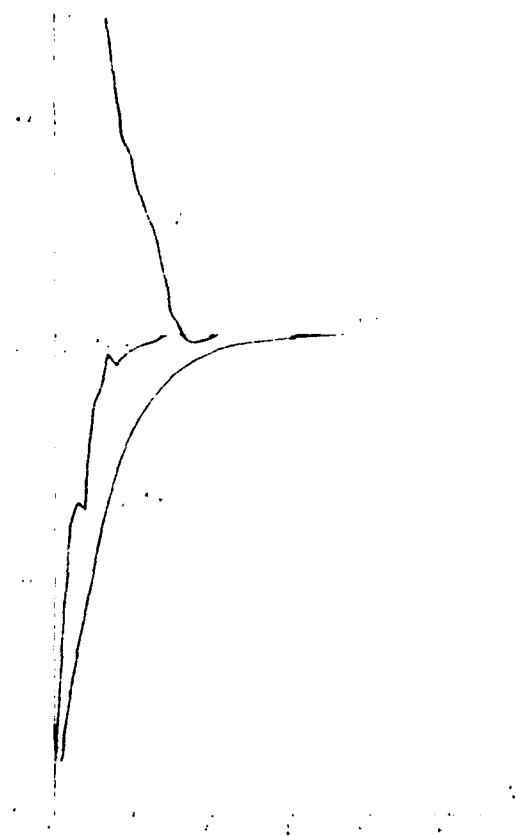


FIGURE 3

than CG but with the non-optimal $\alpha = 1.6$ the efficiency of SOR declines dramatically relative to CG.

REFERENCES

1. R. S. Varga, *Matrix Iterative Analysis*, Prentice-Hall, Englewood Cliffs, N.J., 1962.
2. M. R. Hestenes and E. Stiefel, 'Methods of Conjugate Gradients for solving linear systems', *NBS J. Research* **49**, 409-436 (1952).
3. I. Fried and L. M. Meidner, 'The Conjugate Gradient method with finite elements', *Proc. 2nd IMACS Int. Symp. Computer Meth. for Partial Diff. Equ.*, Lehigh University, 1971.
4. R. T. Fox and F. T. Stanton, 'Developments in structural analysis by direct energy minimization', *AIAA J.* **6**, 1636-1642 (1968).
5. A. I. Yeltsev and M. I. S. Hirst, 'The solution of structural equilibrium equations by the Conjugate Gradient method with particular reference to plane stress analysis', *Int. J. Num. Meth. Engng.* **3**, 349-360 (1971).
6. H. F. Kausche, 'Application of Conjugate Gradient Process in Finite-Element calculation of non-Linear Structures', *Zentralblatt für Angewandte Mechanik und Mechanik*, **54**, 183-86 (1974).

Copy available to DTIC does not permit fully legible reproduction

ACCURACY OF STRING ELEMENT MASS MATRIX

Isaac FRIED*

Department of Aeronautical Engineering, Technion—Israel Institute of Technology, Haifa, Israel

Received 12 February 1979

Revised 9 March 1979

Various element mass matrices are considered for the two-nodal-point string element. From finite difference arguments it is known that an optimal element mass matrix exists – equal to half the sum of the lumped and consistent mass matrices – which causes an error of only $O(h^4)$ in the computed natural frequencies instead of the $O(h^2)$ that is obtained with the consistent matrix. It is shown here that nonuniformity in the mesh destroys this optimality and has also an adverse effect on the accuracy of the frequencies computed with the lumped element mass matrix.

1. Uniform mesh

Let us write the element stiffness matrix k_e and element mass matrix m_e for the two-nodal-point string element as

$$k_e = \frac{1}{h} \begin{bmatrix} 1 & -1 \\ -1 & 1 \end{bmatrix}, \quad m_e = \frac{1}{2} h \begin{bmatrix} \alpha & 1-\alpha \\ 1-\alpha & \alpha \end{bmatrix}, \quad (1)$$

where the element size h may vary from element to element. When $\alpha = 2/3$ and $\alpha = 1$, m_e in eq. (1) becomes the (variationally) consistent and lumped element mass matrix, respectively. According to the minimax principle [1] all the natural frequencies computed with the consistent m_e are above the corresponding exact ones, and the error in them is $O(h^2)$.

We are interested in studying the effect of α on the accuracy of the computed natural frequencies of the fixed string with the hope of discovering an optimal α . We shall do it by finding a closed form expression for the approximate natural frequencies of the fixed string. Assembly of two neighbouring elements produces the finite difference equation for the j th node:

$$-u_{j-1} + 2u_j - u_{j+1} = \frac{1}{2} \hat{\lambda} h^2 [(1-\alpha)u_{j-1} + 2\alpha u_j + (1-\alpha)u_{j+1}], \quad (2)$$

where $\hat{\omega} = \sqrt{\hat{\lambda}}$ is the approximate natural frequency, where $j = 1, 2, \dots, N$, and $h = 1/(N+1)$. Eq. (2) is solved by $u_j = cz^j$, which when substituted in eq. (2) leads to the characteristic

*On leave from Department of Mathematics, Boston University, Boston, Massachusetts, USA.
Research supported by the Office of Naval Research Contract No. ONR-N00014-76-C-036.

equation for z :

$$z^2 - 2bz + 1 = 0, \quad b = \frac{1 - \alpha\mu}{1 + \mu(1 - \alpha)}, \quad \mu = \frac{1}{2} \hat{\lambda} h^2, \quad (3)$$

or

$$z = b \pm \sqrt{b^2 - 1}. \quad (4)$$

Since the eigenfunctions of the fixed string are trigonometric functions, we expect the roots of the characteristic eq. (3) to be complex. The condition for this is that $b^2 - 1 < 0$, or

$$0 < \mu(2\alpha - 1) < 2, \quad (5)$$

assuming that $2\alpha - 1 > 0$. We know [1] that the eigenvalues $\hat{\lambda}$ of the global system $\mathbf{K}\mathbf{u} = \hat{\lambda}\mathbf{M}\mathbf{u}$ are bounded by the eigenvalues of the element system

$$\mathbf{k}_e \mathbf{u}_e = \hat{\lambda}_e^e \mathbf{m}_e \mathbf{u}_e \quad (6)$$

such that

$$\min_e \{\hat{\lambda}_1^e\} \leq \hat{\lambda} \leq \max_e \{\hat{\lambda}_n^e\} \quad (7)$$

where $\hat{\lambda}_1^e$ and $\hat{\lambda}_n^e$ are the first (lowest) and n th (highest) eigenvalues of eq. (6). Here, with \mathbf{k}_e and \mathbf{m}_e given in eq. (1) $\hat{\lambda}_1^e = 0$ with the corresponding element eigenvector $\mathbf{u}_e^1 = [1, 1]$, and $\hat{\lambda}_2^e = 4/[(2\alpha - 1)h^2]$ with the corresponding element eigenvector $\mathbf{u}_e^2 = [1, -1]$. Hence, according to eq. (7), $0 \leq \mu \leq 2/(2\alpha - 1)$. But $\mu = 2/(2\alpha - 1)$ occurs only when the string is free-free for the global eigenvector $\mathbf{u}^t = [1, -1, 1, -1, \dots]$. Fixation of the end points reduces the maximal natural frequency to $\mu < 2/(2\alpha - 1)$, and z in eq. (4) is indeed complex. Because the free term in the characteristic eq. (3) equals 1, $|z| = 1$, and we may write the complex conjugate roots of this equation as $z = \cos \theta \pm i \sin \theta$. Then $u_i = c_1 e^{i\theta} + c_2 e^{-i\theta}$, $i = \sqrt{-1}$, or $u_i = c_1 \cos j\theta + c_2 \sin j\theta$, $j = 0, 1, 2, \dots, N+1$. The end condition $u_0 = 0$ is satisfied with $c_1 = 0$, and the end condition $u_{N+1} = 0$ with

$$(N+1)\theta = \pi, 2\pi, \dots, n\pi. \quad (8)$$

The j th entry in the n th eigenvector therefore becomes

$$(u_n)_j = \sin \frac{n j \pi}{N+1}. \quad (9)$$

From eq. (4) we have that $\cos \theta = b$, or

$$\mu = \frac{1 - \cos \theta}{1 + (\alpha - 1)(1 - \cos \theta)}, \quad (10)$$

which (with the identity $1 - \cos \theta = 2 \sin^2 \frac{1}{2}\theta$) simplifies into

$$\hat{\omega}h = \frac{2 \sin \frac{1}{2}\theta}{[1 + 2(\alpha - 1) \sin^2 \frac{1}{2}\theta]^{1/2}}. \quad (11)$$

Expansion of the right-hand side of eq. (11) in terms of θ yields the following error expression for $\hat{\omega}$:

$$\frac{\hat{\omega}}{\omega} - 1 = -\frac{1}{24}(6\alpha - 5)\theta^2 + O(\theta^4). \quad (12)$$

When $\alpha = 4/6$ (i.e. when m_e is consistent) and when $\alpha = 6/6$ (i.e. when m_e is lumped), the error in the computed frequencies is $O(h^2)$. But when $\alpha = 5/6$, the error (according to eq. (12)) decreases to $O(h^4)$ (see [2], [3]). In view of this we shall term m_e with $\alpha = 5/6$ *optimal*. It is interesting that the optimal element mass matrix is obtained from the physical lumping method [4] by considering half the element mass uniformly distributed and another half lumped at the ends.

Fig. 1 compares the frequency errors for the different choices of α in m_e in eq. (1) for the complete spectrum $0 \leq \xi = \frac{1}{2}n\pi h \leq \frac{1}{2}\pi$.

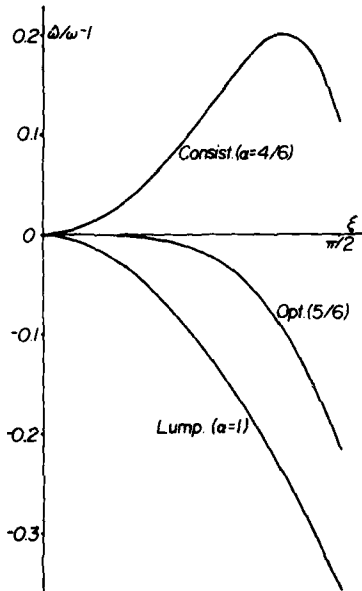


Fig. 1. Frequency error curves for the fixed string.

2. Nonuniform mesh

Accuracy predictions obtained by finite difference arguments over a uniform mesh are susceptible to deterioration when the mesh is not uniform. To see what happens to the

accuracy of the frequencies of the fixed string computed with the various element mass matrices m_e , we numerically solve the string eigenproblem:

$$\begin{aligned} u'' + \omega^2 u = 0, \quad & 0 < x < \frac{1}{2}, \\ u(0) = u'(\frac{1}{2}) = 0 \end{aligned} \tag{13}$$

for the fundamental frequency ω_1 .

According to eq. (13) u'' is proportional to u , suggesting a nonuniform mesh with elements near $x = 0$ larger than those near $x = \frac{1}{2}$. We decide to grade the elements according to

$$h_j = \epsilon \sin^{-1/2} \frac{\pi j}{2(N+1)}, \quad j = 1, 2, \dots, N+1, \tag{14}$$

where ϵ is fixed by the condition that $h_1 + h_2 + \dots + h_{N+1} = \frac{1}{2}$. The graded mesh thus obtained is shown in fig. 2 for the case of 12 elements ($N_e = N + 1 = 12$).

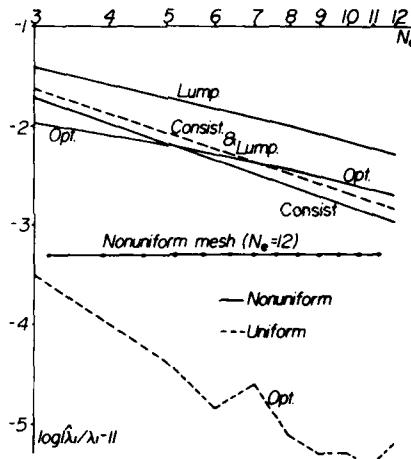


Fig. 2. Convergence of the fundamental frequency $\hat{\lambda}_1$ in a fixed string that is discretized with (a) a uniform mesh (---) and (b) a nonuniform mesh (—).

Computation of the fundamental frequency $\hat{\omega}_1^2 = \hat{\lambda}_1$ is now carried out first with a uniform mesh, and the error reduction with the number of elements N_e is indicated in fig. 2 by a broken line. As predicted in the previous section, the magnitudes of the error in λ_1 computed with the lumped and consistent mass matrices are nearly equal. The optimal m_e produces a far more accurate λ_1 with a faster diminishing error. The erratic convergence of $\hat{\lambda}_1$ computed with the optimal m_e (as seen in fig. 2) is due to round-off errors, the calculation being carried out on a computer with about 8 significant digits.

The nonuniform mesh, graded according to eq. (14), produces a slightly more accurate $\hat{\lambda}_1$ when the consistent m_e is used. On the other hand, the effect of nonuniformity on the accuracy of $\hat{\lambda}_1$ computed with the optimal m_e is devastating. Superconvergence is not only wiped out, but the error in $\hat{\lambda}_1$ is not even proportional to N_e^{-2} in the range $N_e \leq 12$.

The grading rule (14) that is based on variational error estimates produces also a less accurate $\hat{\lambda}_1$ with the lumped m_e . It is observed, however, that to improve $\hat{\lambda}_1$ with the lumped m_e the mesh should be with smaller elements near the ends than in the middle.

References

- [1] I. Fried, Numerical solution of differential equations (Academic Press, New York, 1979).
- [2] R.H. MacNeal, The NASTRAN theoretical manual, Level 15 (NASA SP221(01), Apr. 1972).
- [3] G.L. Goudreau and R.L. Taylor, Evaluation of numerical methods in elastodynamics, Comp. Meths. Appl. Mech. Eng. 2 (1973) 67-79.
- [4] J.H. Argyris and P.C. Dunne, Non-linear and post-buckling analysis of structures, in: K.J. Bathe, J.T. Oden and K. Wunderlich (eds.), Proceedings of the U.S.-Germany symposium: Formulation and computational algorithms in finite element analysis (1977) 525-571.

SHORT COMMUNICATIONS

ON THE OPTIMALITY OF THE POINTWISE ACCURACY OF THE FINITE ELEMENT SOLUTION[†]

ISAAC FRIED[‡]

Department of Aeronautical Engineering, Technion-Israel Institute of Technology, Haifa, Israel

SUMMARY

Closed form finite element solutions are obtained for the uniformly loaded membrane in R^n , $n = 2, 3$ discretized with first-order elements. It is verified on this model that the pointwise error in the displacement is $O(h^2 \log 1/h)$. Slopes converge pointwise at the optimal rate $O(h)$.

INTRODUCTION

Since the finite element solution is obtained by the minimization of the total potential energy, this solution is optimal in the energy norm. If the element shape functions include a complete polynomial of order p , then the error in the finite element solution to second-order (membrane) problems is $O(h^p)$. Energetically, this is the best approximation achievable with piecewise polynomials of order p . But what about the *pointwise* error in the finite element solution? The best pointwise displacement error possible with elements of order p is $O(h^{p+1})$. Recently, Scott¹ showed that for the two-dimensional membrane the pointwise error in the computed solution \hat{u} is actually

$$\max |u - \hat{u}| = \begin{cases} O(h^2 \log 1/h), & p = 1 \\ O(h^{p+1}), & p \geq 2 \end{cases} \quad (1)$$

Nitsche² showed that with linear element the pointwise error is $O(h^2 \log 1/h)$ also in three dimensions.

Here the uniformly loaded membrane problem in R^n , $n = 2, 3$

$$\begin{aligned} -r^{1-n}(r^{n-1}u')' &= 2n, & 0 < r < 1 \\ u'(0) &= u(1) = 0 \end{aligned} \quad (2)$$

that is solved by $u = 1 - r^2$ is considered (see also Reference 3). With the total potential energy

$$\pi(u) = \int_0^1 (\frac{1}{2}u'^2 - 2nu)r^{n-1} dr \quad (3)$$

a finite element solution \hat{u} , consisting of piecewise linear elements, is obtained from equation (1) in a closed form. It is verified from this solution that, in fact, asymptotically $\|u - \hat{u}\|_\infty = O(h^2 \log 1/h)$. Slopes converge, according to the present computational model, at the optimal rate $\|u' - \hat{u}'\|_\infty = O(h)$, both in two and three dimensions.

[†] Research supported by the Office of Naval Research, Contract No. ONR-N00014-76-C-036.

[‡] Associate Professor, on leave from Boston University, Department of Mathematics.

CIRCULAR MEMBRANE

Discretization is performed with $N = 1/h$ linear elements. With $n = 2$, the total potential energy in equation (3) provides the element stiffness matrix k_e and element load vector f_e as

$$k_e = \frac{1}{2}(2e-1) \begin{bmatrix} 1 & -1 \\ -1 & 1 \end{bmatrix}, \quad f_e = \frac{3}{3}h^2 \begin{bmatrix} 3e-2 \\ 3e-1 \end{bmatrix} \quad (4)$$

from which the global data

$$K = \frac{1}{2} \begin{bmatrix} 1 & -1 & & & & & \\ -1 & 4 & -3 & & & & \\ & -3 & 8 & -5 & & & \\ & & -5 & 12 & -7 & & \\ & & & \ddots & \ddots & \ddots & \\ & & & & \ddots & \ddots & \ddots \end{bmatrix}, \quad f = \frac{2}{3}h^2 \begin{bmatrix} 1 \\ 6 \\ 12 \\ 18 \\ \vdots \\ \vdots \end{bmatrix} \quad (5)$$

is assembled. Because of the regular structure of K and f the global system $K\hat{u} = f$ is readily solved to yield

$$\hat{u}_i = \frac{4}{3}h^2 \sum_{j=i}^N \frac{j^3 - (j-1)^3}{j^2 - (j-1)^2}, \quad i = 1, 2, \dots, N \quad (6)$$

but

$$\frac{j^3 - (j-1)^3}{j^2 - (j-1)^2} = \frac{3j^2 - 3j + 1}{2j-1} = \frac{1}{4} \left(6j - 3 + \frac{1}{2j-1} \right) \quad (7)$$

and consequently equation (6) becomes

$$\hat{u}_i = 1 - r_i^2 + \frac{1}{3}h^2 \sum_{j=i}^N \frac{1}{2j-1} \quad (8)$$

where $r_i = h(i-1)$. Figure 1 traces the error distribution $u - \hat{u}$, where $u = 1 - r^2$ and \hat{u} is linearly interpolated inside the element from the computed nodal values \hat{u}_i in equation (8), over a seven-element mesh. The maximum pointwise error occurs at $r=0$ (i.e. $i=1$, $r_i=0$) and

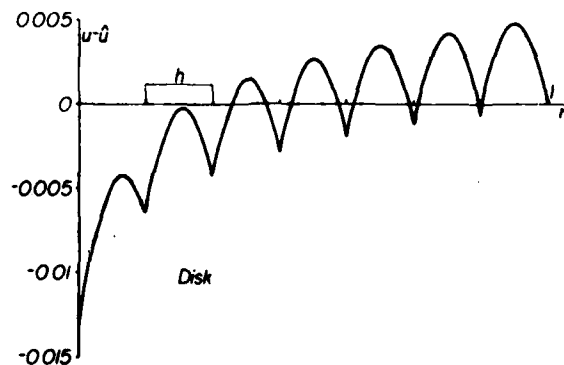


Figure 1. Error distribution $u - \hat{u}$ over a seven linear elements discretization of the uniformly loaded circular membrane

equation (8) provides the error expression

$$\max |u - \hat{u}| = \frac{1}{3} N^{-2} \sum_{j=1}^N \frac{1}{2j-1} \quad (9)$$

As N increases, the sum in equation (9) grows like $\log N$, and it may be written as

$$\|u - \hat{u}\|_\infty = \frac{1}{3} c(N) N^{-2} \log N \quad (10)$$

where $c(N)$ is graphed in Figure 2. The coefficient $c(N)$ converges to the value $\frac{1}{2}$ but so slowly as to make the asymptotic estimate $\|u - \hat{u}\|_\infty = O(N^{-2} \log N)$ of only remote practical usefulness.

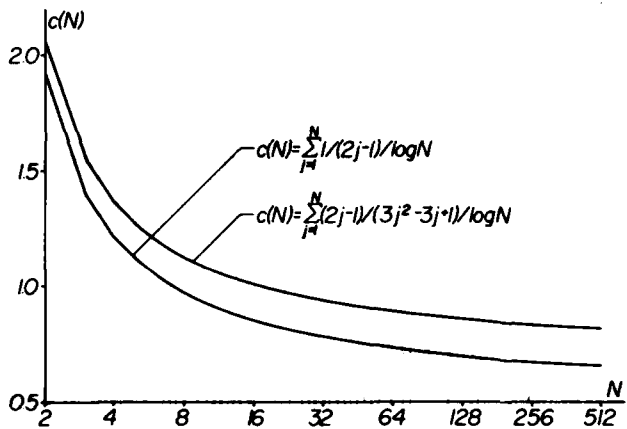


Figure 2. Coefficients $c(N)$ for error expressions (10) and (22)

First-order elements provide only a constant computed slope inside each element, and here

$$\hat{u}' = h^{-1}(\hat{u}_{j+1} - \hat{u}_j) = -\frac{4}{3}h \frac{3j^2 - 3j + 1}{2j - 1} \quad (11)$$

Figure 3 traces the error distribution $u' - \hat{u}'$ over the same seven-element mesh. It is seen that the slope error changes sign inside each element so that there is a point inside each element at which $u' - \hat{u}' = 0$. The exact slope inside the j th element may be written as

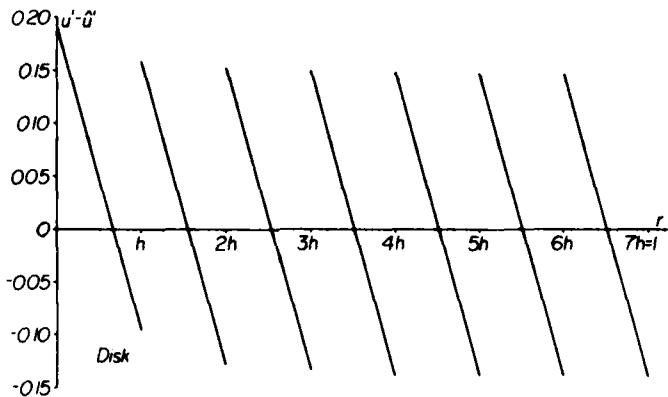
$$u' = -2r = -2h(j-1+\xi), \quad 0 \leq \xi \leq 1 \quad (12)$$

and the condition $u' = \hat{u}'$ yields the special points

$$\xi_j = \frac{1}{2} + \frac{1}{6} \frac{1}{2j-1} \quad (13)$$

At the centre of the j th element

$$u' - \hat{u}' = \frac{h}{6j-3} \quad (14)$$

Figure 3. Circular membrane, slope error distribution $u' - \hat{u}$

and when $j = (N + 1)/2$, for instance, $u' - \hat{u}' = \frac{1}{3}N^{-2}$; superconvergence takes place. The maximum error in u' is at $r = 0$, and

$$\max |u' - \hat{u}'| = \frac{4}{3}h \quad (15)$$

Slopes converge pointwise at the optimal rate $O(h)$.

SPHERICAL MEMBRANE

With $n = 3$, the total potential energy in equation (3) yields the element data for the first-order element as

$$k_e = \frac{1}{3}h(3e^2 - 3e + 1) \begin{bmatrix} 1 & -1 \\ -1 & 1 \end{bmatrix}, \quad f_e = \frac{1}{2}h^3 \begin{bmatrix} 6e^2 - 8e + 3 \\ 6e^2 - 4e + 1 \end{bmatrix} \quad (16)$$

maths grids

from which the global data

$$K = \frac{h}{3} \begin{bmatrix} 1 & -1 & & & \\ -1 & 8 & -7 & & \\ & -7 & 26 & -19 & \\ & & -19 & 56 & -37 \\ & & & -37 & 98 & -61 \\ & & & & \ddots & \ddots \\ & & & & & \ddots \end{bmatrix}, \quad f = \frac{1}{2}h^3 \begin{bmatrix} 1 \\ 14 \\ 50 \\ 110 \\ 124 \\ \vdots \end{bmatrix} \quad (17)$$

is assembled.

A closed-form solution to $K\hat{u} = f$ is readily obtained and at the i th node

$$u_i = \frac{1}{3}h^2 \sum_{j=i}^N \frac{j^4 - (j-1)^4}{j^3 - (j-1)^3} \quad (18)$$

But

$$\frac{j^4 - (j-1)^4}{j^3 - (j-1)^3} = \frac{4j^3 - 6j^2 + 4j - 1}{3j^2 - 3j + 1} = \frac{1}{3} \left(-2 + 4j + \frac{2j-1}{3j^2 - 3j + 1} \right) \quad (19)$$

and consequently, equation (18) becomes

$$\hat{u}_i = 1 - r_i^2 + \frac{1}{2} h^2 \sum_{j=i}^N \frac{2j-1}{3j^2 - 3j + 1} \quad (20)$$

Figure 4 traces the error $u - \hat{u}$, where $u = 1 - r^2$ and where \hat{u} is linearly interpolated from the nodal values \hat{u}_i given in equation (18), over a seven-element discretization. The largest

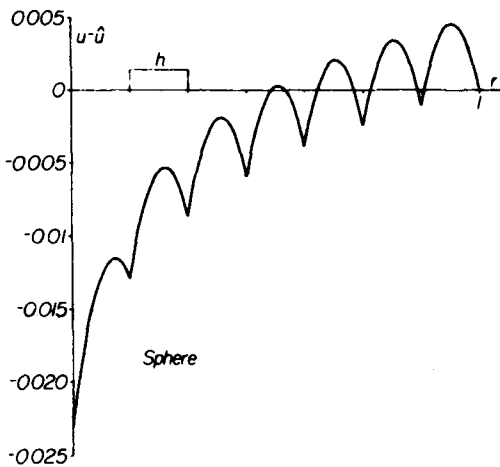


Figure 4. Sphere, displacement error distribution $u - \hat{u}$

pointwise error in u occurs at $r = 0$ (i.e. $i = 1$), and according to equation (20)

$$\|u - \hat{u}\|_\infty = \frac{1}{2} h^2 \sum_{j=1}^N \frac{2j-1}{3j^2 - 3j + 1} \quad (21)$$

Again, equation (21) is written as

$$\|u - \hat{u}\|_\infty = \frac{1}{2} c(N) N^{-2} \log N \quad (22)$$

where $c(N)$ is graphed in Figure 2. As $N \rightarrow \infty$, $c(N) \rightarrow 2/3$, but so slowly as to make the asymptotical error estimate $\|u - \hat{u}\|_\infty = O(N^{-2} \log N)$ of theoretical interest only.

The computed slope inside each element is here

$$h^{-1}(\hat{u}_{i+1} - \hat{u}_i) = -\frac{3}{2} h \frac{j^4 - (j-1)^4}{j^3 - (j-1)^3} \quad (23)$$

and the error distribution $u' - \hat{u}'$ is graphed in Figure 5. Change of sign of $u' - \hat{u}'$ takes place, also here, inside each element and the error nodal points for $u' - \hat{u}'$ are at

$$\xi_i = \frac{1}{2} \frac{6j^2 - 4j + 1}{6j^2 - 6j + 2} \quad (24)$$

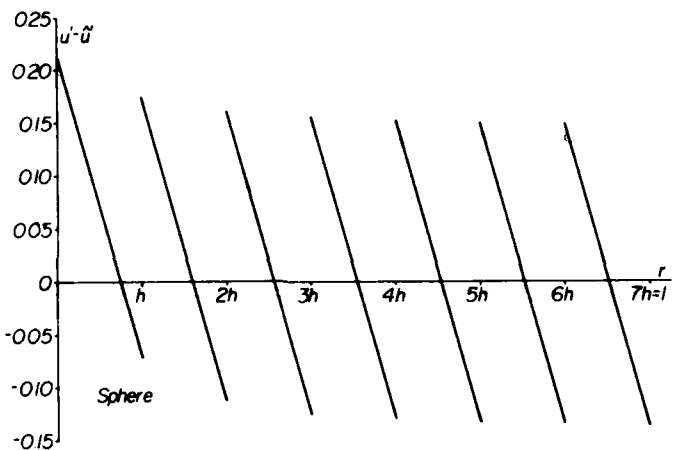


Figure 5. Sphere, slope error distribution $u' - \hat{u}'$

The maximum of $|u' - \hat{u}'|$ occurs at $r = 0$, and

$$\max |u' - \hat{u}'| = \frac{3}{2}h \quad (25)$$

Also in three dimensions the computed slopes converge pointwise at the optimal rate $O(h)$.

REFERENCES

1. R. Scott, 'Optimal L_∞ estimates for the finite element method on irregular meshes', *Math. Comp.*, **30**, 681-697 (1976).
2. J. Nitsche, ' L_∞ convergence of finite element approximation', *Proc. Rome Conf. on Mathematical Aspects of Finite Element Methods* (Eds. A. Dold and B. Eckmann), Springer-Verlag; *Lecture Notes in Math.*, **606**, 261-274 (1977).
3. D. Jespersen, 'Ritz-Galerkin methods for singular boundary value problems', *SIAM J. Numer. Anal.*, **15**, 813-834 (1978).

IRREGULAR FINITE ELEMENT MESHES IN ELASTODYNAMICS[†]

ISAAC FRIED[‡]*Department of Aeronautical Engineering, Technion-Israel Institute of Technology, Haifa, Israel*

SUMMARY

Grading rules for consistent and lumped elements are opposite. Optimal mass matrices on finite difference considerations are very sensitive to mesh grading. Sensitivity of the solution accuracy to the mesh ratio increases with element order.

FIRST ORDER ELEMENT

First we shall solve the string eigenproblem

$$\begin{aligned} u'' + \lambda u &= 0, \quad 0 \leq x \leq 1 \\ u(0) = u(1) &= 0 \end{aligned} \quad (1)$$

with an irregular mesh of first-order elements. The element stiffness matrix k_e and the element mass matrix m_e of the linear element are

$$k_e = \frac{1}{h} \begin{bmatrix} 1 & -1 \\ -1 & 1 \end{bmatrix}, \quad m_e = \frac{1}{2}h \begin{bmatrix} \alpha & 1-\alpha \\ 1-\alpha & \alpha \end{bmatrix} \quad (2)$$

When $\alpha = \frac{1}{3}$ and $\alpha = 1$, m_e becomes variationally consistent, and lumped, respectively. When $\alpha = \frac{5}{6}$, m_e becomes optimal—the accuracy of λ computed with a uniform mesh of these elements increases¹ from $O(h^2)$ to $O(h^4)$.

Suppose we are interested in the first eigenvalue $\lambda_1 = \pi^2$ of equation (1) with the corresponding eigenfunction $u = \sin \pi x$. In the consistent formulation the energy error² in the e th element is proportional to $h_e |u''|$, where h_e is the element size. Hence, the optimally graded mesh is here with small elements near the centre of the string where u'' is large, and with large elements near the ends of the string where u'' is small.

To observe more precisely the dependence of the discretization accuracy of λ_1 on the mesh grading the string is divided into N_e finite elements symmetrically graded according to

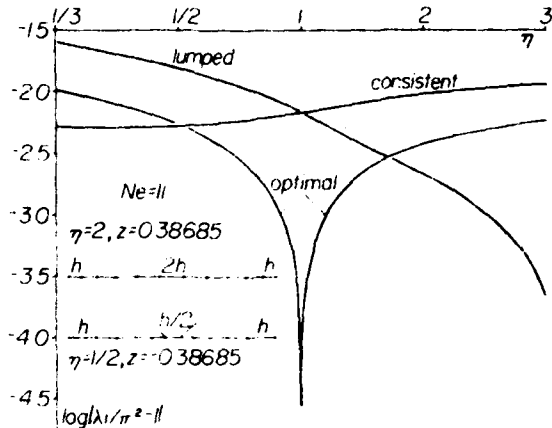
$$h_e = h e^z, \quad e = 1, 2, \dots, (N_e + 1)/2 \quad (3)$$

where z is changed to achieve various mesh ratios η

$$\eta = [\frac{1}{2}(N_e + 1)]^z \quad (4)$$

For instance, for $\eta = 2$, $z = 0.38685$ while for $\eta = \frac{1}{2}$, $z = -0.38685$. These element size distributions are graphically shown in Figure 1.

[†] Research supported by the Office of Naval Research Contract No. ONR-N00014-76-C-036.
[‡] Associate Professor, on leave from Boston University, Department of Mathematics.

Figure 1. Accuracy of λ_1 computed with first-order elements

The fundamental eigenvalue λ_1 of the string is now computed with the consistent, lumped and optimal m_e in equation (2) for different values of the mesh ratio η , and the results of this computation are shown in Figure 1. As predicted, with the consistent m_e , the optimal mesh ratio η is less than 1 and is seen to be close to one-third. It is interesting, however, that with our grading rule (3) the accuracy of the computed λ_1 does not change much between $\eta = 3$ and $\eta = \frac{1}{3}$. A computational procedure to automatically grade the mesh is not likely to prove profitable here. We further note in Figure 1 that with the lumped m_e , grading of the mesh should be done in the other direction, with larger elements near the centre rather than near the ends. Mesh grading based on variational arguments will lead with a lumped mass matrix to a loss of accuracy. The optimal element mass matrix is extremely accurate when the mesh is uniform but its accuracy drastically drops³ with departure from mesh regularity.

QUADRATIC ELEMENT

How do matters change when quadratic elements are used to discretize equation (1)? To find out we use the element matrices

$$k_e = \frac{1}{6h} \begin{bmatrix} 7 & -8 & 1 \\ -8 & 16 & -8 \\ 1 & -8 & 7 \end{bmatrix}, \quad m_e = \frac{h}{15} \begin{bmatrix} 4 & 2 & 1 \\ 2 & 16 & 2 \\ -1 & 2 & 4 \end{bmatrix}, \quad m'_e = \frac{1}{12}h \begin{bmatrix} 1 & & \\ & 4 & \\ & & 1 \end{bmatrix} \quad (5)$$

for quadratic elements of size $2h$. In equation (5), k_e denotes the element stiffness matrix, m_e the consistent element mass matrix, and m'_e the corresponding lumped matrix.

With the consistent formulation, the error in the e th element is proportional to $h_e^2 |u''|$. But here $|u''| = \pi^2 |\cos \pi x|$ and hence the optimal mesh is with large consistent elements near the centre of the string and with small elements near the ends.

Because of their high order, three of the quadratic elements are sufficient for reasonable accuracy in λ_1 . They are symmetrically graded, as shown in Figure 2, and the mesh ratio η is again increased from one-third to 3. Figure 2 verifies the theoretical prediction of optimal $\eta > 1$. The gain in accuracy between $\eta = \frac{1}{3}$ and $\eta = 3$ is greater here than with the first-order elements but is still not so great as to justify an expensive computational procedure to locate the optimal η .

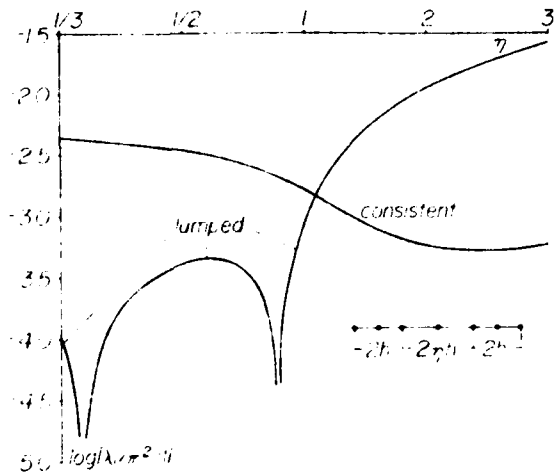


Figure 2. Accuracy of λ_1 computed with quadratic elements

With the lumped m_e , the grading direction is once more opposite to the consistent; $\eta > 1$ causes a loss in the computed λ_1 . Also, with the lumped m_e , the error in λ_1 may change sign and hence the horns on the error curve for this element.

REFERENCES

1. R. H. MacNeal, *The NASTRAN Theoretical Manual*, level 15, NASA SP221(01), April 1972.
2. I. Fried, *Numerical Solution of Differential Equations*, Academic Press, 1979.
3. I. Fried, 'Accuracy of string element mass matrix', to appear in *Comp. Meth. Appl. Mech. Eng.*

MEANINGFUL EXISTENCE OF FINITE ELEMENT SOLUTIONS TO OFF-LIMIT PROBLEMS

Isaac FRIED*

Department of Aeronautical Engineering Technion - Israel Institute of Technology Haifa, Israel

Received 30 March 1979

Revised manuscript received 15 June 1979

Problems for which the variational principle of minimum potential energy breaks down, and are therefore formally unsuitable for a finite element analysis, are shown to possess, nevertheless, a useful discrete solution.

1. Introduction

Finite elements are at their best [1], [2] in problems that possess a true minimum or maximum variational principle. For then the energy convergence of the finite element solution is generally proved, and the numerical stability of the discrete algebraic system set up with finite elements is guaranteed for general mesh layouts. There are boundary value problems of physical significance and interest for which the variational principle breaks down because of boundless energy in the solution or because an analytic solution does not even exist for these problems. These problems are theoretically off-limits for the finite element method in as much as the theoretical support of the method does not cover them. Energy convergence - even pointwise convergence - as discussed in the literature, becomes meaningless, for how does one measure convergence to a solution that does not exist? Nevertheless, conventional finite element discretization of such problems produce discrete solutions that improve, in some sense, with the refinement of the mesh, and are therefore entirely useful.

Some simple examples are solved in closed form or numerically in the following text to demonstrate that the usefulness of finite elements is retained in these marginal areas where the analytic solution or the variational principle totters. Hopefully, more light is shed thereby and understanding deepen on the twin prime theoretical questions of existence and convergence of the finite element solution when viewed from the discrete point of view.

2. Circular membrane under a point load

Operationally this axisymmetrical problem is formulated as:

$$\begin{aligned} -(ru')' &= 0, & 0 < r < 1, \\ -ru'(0) &= 1, & u(1) = 0, \end{aligned} \tag{1}$$

*Associate Professor, on leave from Boston University, Department of Mathematics.
Research supported by the Office of Naval Research Contract No. ONR-N00014-76-C-036.

and

$$u(r) = \log(1/r). \quad (2)$$

The energy stored in a unit membrane axisymmetrically deflected is

$$E[u] = \frac{1}{2} \int_0^1 u'^2 r dr, \quad (3)$$

which is infinite for the logarithmic u in eq. (2). Let u now be any continuous function that satisfies the condition $u(1) = 0$. Formally, the total potential energy of the point-loaded membrane (1) thus deflected is

$$\pi(u) = E[u] - u(0). \quad (4)$$

To approximately solve problem (1) with finite elements by minimizing $\pi(u)$ in eq. (4), a uniform mesh of N linear finite elements is laid upon the membrane. From $E[u]$ in eq. (3) an element stiffness matrix k_e is derived in the form

$$k_e = \frac{1}{2} (2e - 1) \begin{bmatrix} 1 & -1 \\ -1 & 1 \end{bmatrix}, \quad e = 1, 2, \dots, N, \quad (5)$$

and the discrete total potential energy is assembled according to eq. (4). Minimization of $\pi(u)$ with respect to the nodal variables, under the restriction that $u(1) = 0$, produces the algebraic system $K\hat{u} = f$ for the nodal unknown vector \hat{u} , where the global stiffness matrix K and the load vector f are

$$K = \frac{1}{2} \begin{bmatrix} 1 & -1 & & & & \\ -1 & 4 & -3 & & & \\ & -3 & 8 & -5 & & \\ & & -5 & 12 & -7 & \\ & & & -7 & 16 & -9 \\ & & & & \ddots & \ddots \end{bmatrix}, \quad f = \begin{bmatrix} 1 \\ 0 \\ 0 \\ 0 \\ 0 \\ \vdots \end{bmatrix}. \quad (6)$$

The closed-form solution of $K\hat{u} = f$ yields

$$u_i = \sum_{j=1}^N \frac{2}{2j-1}, \quad i = 1, 2, \dots, N, \quad (7)$$

for the i th node and $\hat{u}_{N+1} = 0$. At the center $r = 0$ ($i = 1$) of the membrane where the point force acts

$$\hat{u}_1 = \sum_{j=1}^N \frac{2}{2j-1} \cong \log N. \quad (8)$$

Even without a closed-form solution an assiduous analyst performing numerical computations with a succession of refined finite element meshes will soon discover that \hat{u}_i keeps ever increasing with N , and that correspondingly the discrete total potential energy keeps ever dropping as N is increased.

Away from the singular point $r = 0$ pointwise convergence of the finite element piecewise linear solution \hat{u} to $u = \log(1/r)$ takes place with the increase of N . Consider, for example, the point $r = 1/2$ ($i = N/2 + 1$, N even). At this point $u(1/2) = \log 2$ and, according to eq. (7),

$$\hat{u}\left(\frac{1}{2}\right) = 2 \left(\frac{1}{N+1} + \frac{1}{N+3} + \frac{1}{N+5} + \cdots + \frac{1}{N+N-1} \right). \quad (9)$$

To elicit the rate of convergence of the series in eq. (9), it is helpful to notice that

$$\int_{\rho}^1 \frac{1}{\rho} d\rho = \int_{\rho}^1 \frac{2}{(\rho^2)} d\rho = \log r \quad (10)$$

so that

$$\int_{1/2}^1 \frac{2}{(\rho^2)} d\rho = \log 2. \quad (11)$$

Numerical integration in eq. (11) produces the series of eq. (9). Indeed, if $\frac{1}{2} \leq \rho \leq 1$ is divided into $N/2$ equal intervals, then at each node thus created $\rho_i = \frac{1}{2} + (i-1)/N$ ($i = 1, 2, \dots, \frac{1}{2}N + 1$). Within each interval $(\rho^2)' = (N+2i-1)/N$, and the contribution of each interval to the integral in eq. (11) is $2/(N+2i-1)$. Summation readily produces eq. (9). Numerical differentiation and integration arguments lead to the conclusion that this sum converges $O(N^{-2})$ to $\log 2$. The same conclusion could have been reached using the trapezoidal rule on the first integral of eq. (10).

Fig. 1 compares the computed \hat{u} with the exact $u = \log(1/r)$ for $N = 10$. At the origin the approximation is of course bad, but away from it agreement between the computed \hat{u} and the theoretical u rapidly becomes excellent.

Once our ideal analyst has noticed the singular behavior of \hat{u} near the origin, he knows that he should change to a nonuniform mesh of finite elements for higher computational efficiency. We suppose him endowed with broad knowledge and deep understanding of the method of finite elements and its theoretical intricacies. Consequently, to decide the mesh grading, he sets out to estimate the curvature of u . This he does by computing $|\hat{u}''|$, where

$$\hat{u}''_i = N^2(u_{i-1} - 2u_i + u_{i+1}), \quad i = 2, 3, \dots, N. \quad (12)$$

In more complex situations \hat{u}'' may be computed from the computer output. Here eq. (7) leads to the formula

$$\hat{u}''_i = \frac{4N^2}{(2i-1)(2i-3)}, \quad i = 2, 3, \dots, N, \quad (13)$$

indicating the sensibility of a much finer mesh nearer $r = 0$ than near $r = 1$.

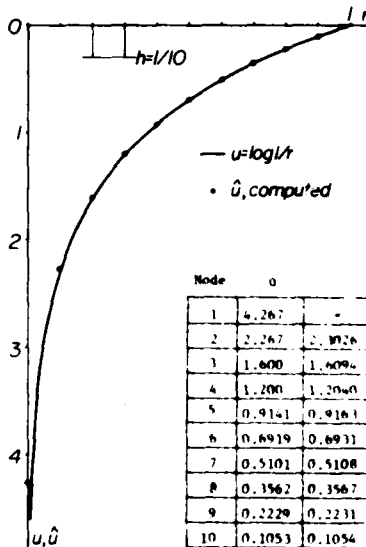


Fig. 1. Point-loaded circular membrane discretized with 10 linear finite elements.

When the mesh is nonuniform, then at the i th node

$$\hat{u}_i = 2 \sum_{j=1}^N \frac{r_{j+1} - r_j}{r_{j+1} + r_j}, \quad (14)$$

where $r_1 = 0$ and $r_{N+1} = 1$, and in fact as grading becomes steeper, or $r_{i+1}/r_i \gg 1$, \hat{u}_i approaches a growth proportional to N . The rule $r_j = \epsilon(j-1)^\alpha$, $1 = \epsilon N^\alpha$, for instance, yields for the specific $\alpha = 4$ the computed central deflection

$$\hat{u}_1 = 2 \left(1 + \frac{15}{17} + \frac{65}{97} + \frac{175}{337} + \frac{369}{881} + \dots \right) \quad (15)$$

instead of eq. (8).

Energy convergence of the singular membrane problem of this section, excluding the neighborhood of the singularity, can be proved also generally by the standard finite element arguments. Corresponding to K in eq. (6) the global flexibility matrix is given here by

$$K_y = \left[2 \sum_{k=i}^N \frac{1}{2k-1} \right]^{-1}, \quad j \geq i, \quad (16)$$

which means that removing the force from the origin and fixing it at node i does not change the solution \hat{u}_j for $j \geq i$, while \hat{u}_j remains constant for $j \leq i$. The analytical solution u behaves the same way since $-ru' = 1$ is true not only for $r = 0$ but for all r . Now u is regular inside all the finite elements, and consequently the full rate of convergence of the finite element approximation to our original solution, excluding the singular origin, takes place.

Table 1. Computed finite element approximation \hat{u} to the deflection of a square membrane with a central unit force

x	y	$\hat{u}, N_{es} = 20$	$\hat{u}, N_{es} = 60$	Analytical
0.05	0.03	0.27531 E-2	0.27375 E-2	0.27357 E-2
0.10	0.10	0.11015 E-1	0.10956 E-1	0.10949 E-1
0.15	0.15	0.24840 E-1	0.24714 E-1	0.24699 E-1
0.20	0.20	0.44456 E-1	0.44243 E-1	0.44217 E-1
0.25	0.25	0.70505 E-1	0.70177 E-1	0.70138 E-1
0.30	0.30	0.10451 E0	0.10399 E0	0.10383 E0
0.35	0.35	0.14994 E0	0.14810 E0	0.14890 E0
0.40	0.40	0.21592 E0	0.21333 E0	0.21312 E0
0.45	0.45	0.33650 E0	0.32429 E0	0.32337 E0
0.50	0.50	0.72346 E0	0.89016 E0	∞

Such simple explicit reasoning does not apply to the square membrane problem with a point force at (ξ, η)

$$\begin{aligned} u_{xx} + u_{yy} + \delta(\xi, \eta) &= 0, & 0 < x < 1, 0 < y < 1, \\ u &= 0 & \text{on the boundary,} \end{aligned} \quad (17)$$

for which Green's function [3] is

$$G(x, y, \xi, \eta) = \frac{4}{\pi^2} \sum_{i,j=1}^{\infty} \frac{\sin i\pi x \sin j\pi y \sin i\pi\xi \sin j\pi\eta}{i^2 + j^2}, \quad (18)$$

including a singularity $0(\log 1/r)$ around (ξ, η) .

To observe the behavior of the finite element solution to eq. (17), the square with a unit point force at $\xi = \eta = \frac{1}{2}$ is discretized with N_{es} bilinear elements, and the discrete problem is solved twice, once with 20 elements per side ($N_{es} = 20$) and then with 60 elements per side ($N_{es} = 60$). Table 1 compares the computed results with those given by eq. (18). An addition of about one significant digit with the mesh refinement is evident. Next the serious analyst sets out to compute \hat{u}_{xx} , \hat{u}_{yy} , and \hat{u}_{xy} to better lay a nonuniform mesh of elements, triangular perhaps, around the singular point, but we are not yet prepared to follow him that far.

3. Spherical membrane under point load

Eq. (1) changes here into

$$\begin{aligned} -(r^2 u')' &= 0, & 0 < r < 1, \\ -r^2 u'(0) &= 1, & u(1) = 0, \end{aligned} \quad (19)$$

and

$$u = \frac{1}{r} - 1. \quad (20)$$

The total potential energy corresponding to boundary value problem (19) is

$$\pi(u) = \frac{1}{2} \int_0^1 u'^2 r^2 dr - u(0), \quad (21)$$

where u is continuous and $u(1) = 0$. From $\pi(u)$ an element stiffness matrix is derived in the form

$$k_e = \frac{1}{3N} (3e^2 - 3e + 1) \begin{bmatrix} 1 & -1 \\ -1 & 1 \end{bmatrix}, \quad (22)$$

where N denotes the number of equal finite elements in the discretization. Following the standard finite element procedure produces the algebraic system $\mathbf{K}\hat{\mathbf{u}} = \mathbf{f}$, where

$$\mathbf{K} = \frac{1}{3N} \begin{bmatrix} 1 & -1 & & & & \\ -1 & 8 & -7 & & & \\ & -7 & 26 & -19 & & \\ & & -19 & 56 & -37 & \\ & & & -37 & 98 & -61 \\ & & & & \ddots & \end{bmatrix}, \quad \mathbf{f} = \begin{bmatrix} 1 \\ \vdots \\ \vdots \end{bmatrix} \quad (23)$$

and

$$\hat{u}_i = 3N \sum_{j=i}^N \frac{1}{j^3 - (j-1)^3} = N \sum_{j=i}^N \frac{3}{3j^2 - 3j + 1}. \quad (24)$$

At the center

$$\hat{u}_1 = N \sum_{j=1}^N \frac{3}{3j^2 - 3j + 1} = 3.915 N \quad (25)$$

since the sum of the infinite series $\sum 1/j^2$ has a limit. Again, as the mesh of finite elements is refined, the computed central deflection \hat{u}_i keeps ever increasing, and with it the energy stored in the membrane.

Away from the origin, pointwise convergence of the computed \hat{u} to the exact $u = 1/r - 1$ takes place. Consider for instance the point $r = \frac{1}{2}$ ($i = N/2 + 1$, N even) at which $u = 1/(1/2) - 1 = 1$. At this point

$$u\left(\frac{1}{2}\right) = N \sum_{j=1,2N+1}^N \frac{3}{j^3 - (j-1)^3}. \quad (26)$$

The convergence of the sum in eq. (21) to $u(1/2) = 1$ can be proved by differentiation and integration arguments, as has been done for the circular membrane of the previous section, from the equation

$$u(r) = \frac{1}{r} - 1 = \int_1^r \frac{1}{\rho^2} d\rho = \int_1^r \frac{3}{(\rho^3)^2} d\rho, \quad (27)$$

or in particular from

$$u\left(\frac{1}{2}\right) = \int_{1/2}^1 \frac{3}{(r^3)'} dr. \quad (28)$$

Division of the interval $\frac{1}{2} \leq r \leq 1$ into $N/2$ equal segments and the performance of the numerical differentiation of r^3 and then a midpoint numerical integration of $3/(r^3)'$ produces the sum in eq. (26). Convergence of $\hat{u}\left(\frac{1}{2}\right)$ to the value 1 occurs at the rate of N^{-2} . Fig. 2 compares the computed \hat{u} and the exact $u = 1/r - 1$ when $N = 10$.

All the above discussion assumes a uniform mesh which is very inefficient here since

$$\hat{u}_i'' = 18N^3 \frac{i^2 - 1}{[i^3 - (i-1)^3][(i-1)^3 - (i-2)^3]} \quad (29)$$

A much finer mesh near $r = 0$ is called for than near $r = 1$. With such a mesh

$$\hat{u}_i = 3 \sum_{j=i}^N \frac{r_{j+1} - r_j}{r_{j+1}^2 + r_{j+1}r_j + r_{j+1}^2}, \quad r_1 = 0, r_{N+1} = 1 \quad (30)$$

or, when $r_j = \epsilon(j-1)^\alpha$ and $\epsilon N^\alpha = 1$,

$$\hat{u}_i = 3N^\alpha \sum_{j=i}^N \frac{j^\alpha - (j-1)^\alpha}{j^{2\alpha} + j^\alpha(j-1)^\alpha + (j-1)^{2\alpha}}, \quad (31)$$

and for large N

$$\hat{u}_1 = c(\alpha)N^\alpha, \quad (32)$$

where $c(1) = 3.91$, $c(2) = 3.64$, $c(3) = 3.38$, $c(4) = 3.20$ and $c(5) = 3.10$.

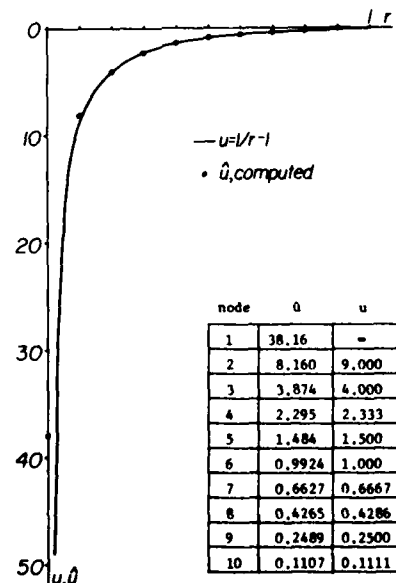


Fig. 2. Point-loaded spherical membrane discretized with 10 linear finite elements.

4. String under point torque

Consider a string of unit length with two equal but opposite forces P acting on it at the points $\frac{1}{2} - \epsilon$ and $\frac{1}{2} + \epsilon$, and such that $2\epsilon P = M$, where M is a constant moment. When $\epsilon \rightarrow 0$, the deflection of this string becomes

$$\begin{aligned} u(x) &= -Mx & 0 \leq x < \frac{1}{2}, \\ u(x) &= -M(x-1) & \frac{1}{2} < x \leq 1, \end{aligned} \quad (33)$$

and at $x = \frac{1}{2}$ the string deflection becomes multivalued: $u(\frac{1}{2} - 0) = -\frac{1}{2}M$ and $u(\frac{1}{2} + 0) = \frac{1}{2}M$. The energy needed to thus deform the string is infinite.

Our hypothetical analyst ignores this last unpleasant fact about string energy, and, being an ardent admirer of the method of finite elements sets out to solve it numerically by this technique.

Associated with the present string problem is the total potential energy

$$\pi(u) = \frac{1}{2} \int_0^1 u'^2 dx - Mu' \left(\frac{1}{2} \right). \quad (34)$$

Because u' is needed at the point $x = \frac{1}{2}$, cubic C^1 finite elements suggest themselves for the discretization. What results from such a computation is graphically shown in figs. 3 and 4 for a 20-element mesh and $M = 1$. Close to the center, where the torque enters, the computed displacement function oscillates severely over some two or three elements (over each side) as it tries to adapt to the discontinuity. Outside this internal boundary layer the oscillations rapidly subside, and \hat{u} and u agree excellently. Figs. 3 and 4 unmistakably suggest a

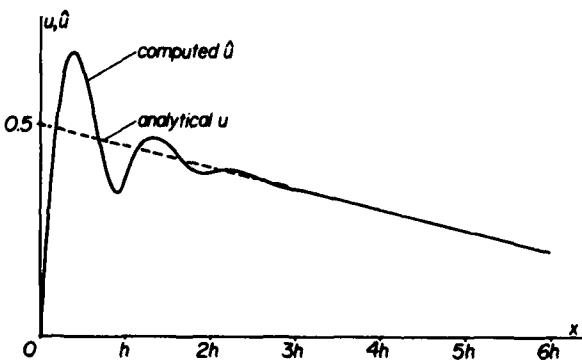


Fig. 3. String under central point torque discretized with 20 cubic C^1 finite elements (computed and analytical displacements shown for the right half of the string).

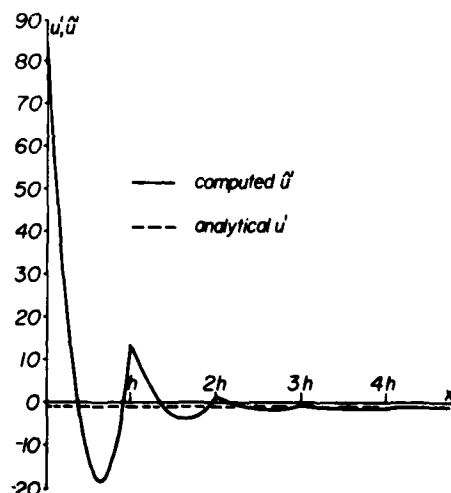


Fig. 4. String of fig. 3 (computed and analytical slopes shown for the right half of the string).

nonuniform mesh of finite elements with larger elements near the ends of the string and much smaller elements near the singular point $x = \frac{1}{2}$. A repeated computation with such a mesh will reveal that the boundary layer is mesh-dependent, and, as the elements close to $x = \frac{1}{2}$ become smaller, it shrinks. The oscillations, it is concluded, are spurious and are caused by a discontinuity of u at $x = \frac{1}{2}$ with infinite slope and hence infinite energy.

5. Point displacement given to a membrane

Suppose that the unloaded axisymmetrical membrane is given a unit central displacement. The resulting deflection u of the membrane is determined by the solution of

$$-(ru')' = 0, \quad 0 < r < 1, \quad (35)$$

$$u(0) = 1, u(1) = 0,$$

$$u(r) = c_1 \log(1/r) + c_2, \quad (36)$$

where c_1 and c_2 are to be fixed by the boundary conditions $u(0) = 1$ and $u(1) = 0$. But it is impossible here to satisfy both of them. The condition $u(1) = 0$ is met with $c_2 = 0$, but there is no nonzero c_1 that makes $u(0) = 1$. According to the linear, small deflection theory of the membrane the central displacement given to the membrane is not transmitted; the boundary value problem (35) has no solution.

But what if one uses the total potential energy

$$\pi(u) = \frac{1}{2} \int_0^1 u'^2 r dr, \quad u(0) = 1, u(1) = 0, \quad (37)$$

to construct a finite element solution to eq. (35)? Here the problem is not infinite energy. In fact, $\pi(u)$ in eq. (37) is bounded from below by zero, and this limit can be approached as closely as one wishes with

$$u = 1 - r^\alpha, \quad \alpha > 0 \quad (38)$$

which satisfies both end conditions $u(0) = 1$ and $u(1) = 0$. Introduction of u of eq. (38) into $\pi(u)$ of eq. (37) results in

$$\pi(u) = \frac{1}{4} \alpha, \quad (39)$$

and $\pi(u) \rightarrow 0$ as $\alpha \rightarrow 0$.

Standard finite element approximation of $\pi(u)$ in eq. (37) with a uniform mesh of linear elements produces the linear algebraic system $K\hat{u} = f$ with

$$K = \begin{bmatrix} 4 & -3 & & & \\ -3 & 8 & -5 & & \\ & -5 & 12 & -7 & \\ & & -7 & 16 & -9 \\ & & & -9 & 20 & -11 \end{bmatrix}, \quad f = \begin{bmatrix} 1 \\ \\ \\ \\ \end{bmatrix} \quad (40)$$

and

$$\hat{u}_i = \frac{s_i}{s_0}, \quad i = 1, 2, \dots, N-1, \quad u_0 = 1, u_N = 0, \quad (41)$$

where

$$s_i = \sum_{j=i}^N \frac{1}{2j+1}. \quad (42)$$

At $r = \frac{1}{2}$ ($i = N/2$, N even)

$$\hat{u}\left(\frac{1}{2}\right) = \sum_{j=(N+1)/2}^N \frac{1}{2j+1} / \sum_{j=0}^{N/2} \frac{1}{2j+1} \cong \frac{\frac{1}{2} \log 2}{\frac{1}{2} \log N}, \quad (43)$$

and $\hat{u}\left(\frac{1}{2}\right) \rightarrow 0$ as $N \rightarrow \infty$.

To check the need and amount of mesh grading, \hat{u}_i in eq. (41) is used to compute $\hat{u}''_i = N^{-2}(\hat{u}_{i-1} - 2\hat{u}_i + \hat{u}_{i+1})$; this yields

$$\hat{u}''_i = \frac{N^{-2}}{S_0} \frac{2}{4i^2 - 1}, \quad i = 1, 2, \dots, N-1. \quad (44)$$

It is inferred from \hat{u}'' that a more efficient finite element model is achieved with a finer mesh close to $r = 0$ rather than close to $r = 1$.

Fig. 5 shows the computed deflection of the membrane discretized with 10 and 100 finite elements, once uniformly distributed and then graded according to the element size formula $h_i = ej^4$. It does not escape our vigilant analyst's eye that the central deflection imparted to the membrane does little to disturb the rest of it.

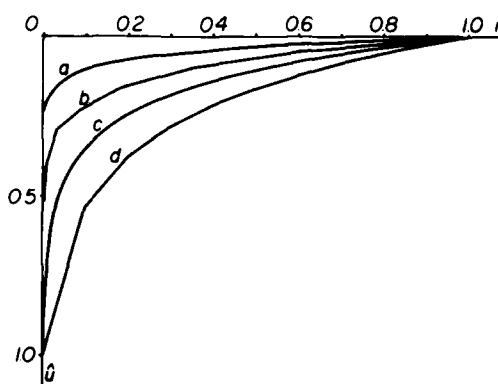


Fig. 5. Centrally displaced circular membrane. Curve (a) for $N = 100$, $h_i \propto j^4$; (b) for $N = 10$, $h_i \propto j^4$; and curves (c) and (d) for a uniform mesh with $N = 100$ ($h = 1/100$) and $N = 10$ ($h = 1/10$), respectively.

6. Overdetermined fixed string problem

A string that is fixed at its ends is discretized with cubic C^1 finite elements. Approximate solution of this problem through the minimization of the total potential energy includes the requirement that the finite element trial function satisfy the zero displacement provision at both ends. Suppose that an additional constraint is put on the finite element trial function, namely that also the slopes vanish at the end points. Both analytically and physically this additional boundary condition is meaningless; the string cannot resist a torque. The addition of the zero slope conditions merely implies a slope discontinuity at the ends. It is whatever results from the correct boundary conditions when approached from the interior, but then suddenly becoming zero over the end supports.

To observe the behavior of a finite element solution subject to the additional boundary condition of zero slopes, the string is discretized with 20 cubic C^1 elements, and a point load is applied to it at the center. At this point C^1 continuity is not enforced on the trial function to allow it to duplicate the slope discontinuity over the point force. At the end points, however, the finite element trial function is made to satisfy both conditions of zero displacement and zero slope.

Figs. 6 and 7 show the results of this computation for half (for symmetry reasons) the string. Near the end point $x = 0$ the computed slope \hat{u}' oscillates wildly inside a boundary layer of some 2 elements and then settles close to the exact solution $u' = 1$. The computed displacement, on the other hand, suffers permanent damage from $\hat{u}'(0) = 0$, that is it is transmitted all the way to the interior of the string.

But we have no doubt that our numerical analyst, who is by now a seasoned veteran of many a difficult computational struggle, will soon discover that the boundary layer effect is spurious and is due to the redundant imposition of $\hat{u}'(0) = 0$.

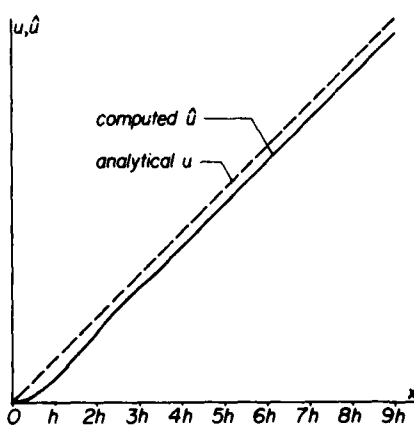


Fig. 6. Displacements of fixed string discretized with 10 cubic C^1 finite elements. Overdetermined boundary condition of zero slope at $x = 0$.

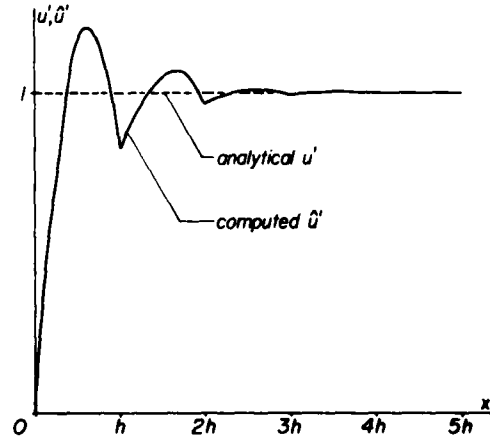


Fig. 7. Slopes of string of fig. 6.

References

- [1] J.H. Argyris, Computers and mechanics, in: W.T. Koiter (ed.), *Theoretical and applied mechanics* (1976) 261–302.
- [2] I. Fried, *Numerical solution of differential equations* (Academic Press, 1979).
- [3] R. Courant and D. Hilbert, *Methoden der mathematischen physik* (Springer, 1931) 333–335.

NONLINEAR FINITE ELEMENT COMPUTATION OF THE EQUILIBRIUM AND STABILITY OF THE CIRCULAR PLATE[†]

ISAAC FRIED[‡]*Boston University, Department of Mathematics, Boston, Massachusetts, U.S.A.*

INTRODUCTION

Numerical, reduced, integration¹ of the total potential energy is used to derive the element tangent vectors and matrices for the largely deflected circular plate.² All the element data is expressed in terms of few numerical element vector and matrices, and in a form convenient for standard assembly and use in the Newton-Raphson, or other iterative solution methods.

Actual numerical computations are carried out to study the bending of the circular plate under the action of a lateral load and a rim thrust that exceeds the critical value.

A brief numerical study is made of the discretization accuracy.

ELEMENT VECTORS AND MATRICES

Consider a unit circular plate largely bent³ under the action of a distributed lateral load f and an edge compression p . The total potential energy of the deflected plate can be written as

$$\begin{aligned} \pi(u, w) = & \frac{1}{2} \int_0^1 \left[\frac{1}{12} \left(w''^2 + \frac{1}{r^2} w'^2 \right) + \left(\frac{u}{r} \right)^2 \right] r dr \\ & + \frac{1}{2} \int_0^1 (u' + \frac{1}{2} w'^2)^2 r dr - \int_0^1 f w r dr + pu(1) \end{aligned} \quad (1)$$

where u and w denote the inplane and lateral displacements, respectively, and where $(\cdot)' = d/dr$.

In the finite element discretization of $\pi(u, w)$, we choose to interpolate w cubically with the beam shape functions. Because u is differentiated only once in $\pi(u, w)$, we correspondingly interpolate u quadratically, and decide to numerically integrate $\pi(u, w)$ with two Gauss points, that exactly integrate w''^2 and u'^2 .

A typical finite element (see Figure 1) extends between $r = r_1$ and $r = r_3$, is with three nodal points—two end points and one central—and is associated with the nodal values vector

$$u_e^1 = (u_1, w_1, \frac{1}{2} h w'_1, u_2, u_3, w_3, \frac{1}{2} h w'_3) \quad (2)$$

where $h = r_3 - r_1$. To prepare for the numerical integration of the total potential energy the typical element is mapped to the standard interval $-1 \leq \xi \leq 1$ by $r = \frac{1}{2}(1-\xi)r_1 + \frac{1}{2}(1+\xi)r_2$ so that $dr = \frac{1}{2}h d\xi$. We denote differentiation with respect to ξ by $(\cdot)'$ and have that $(\cdot)' = 2/h(\cdot)''$.

¹ Research supported by the Office of Naval Research under Contract ONR NOOO14-76C-036.

[‡] Professor

For a typical interior element we have now that

$$\begin{aligned}\pi_e(u, w) = & \int_{-1}^1 (\frac{1}{3}h^{-3}r\bar{w}^2 + \frac{1}{12}r^{-1}h^{-1}\bar{w}^2 + \frac{1}{4}hr^{-1}u^2) d\xi \\ & + h^{-3} \int_{-1}^1 (hu + \bar{w}^2)^2 r d\xi - \frac{1}{3}h \int_{-1}^1 hr d\xi\end{aligned}\quad (3)$$

Interpolation of u and w inside the typical element is formally written as

$$u = u_e^\top \varphi(\xi) \quad w = u_e^\top \psi(\xi) \quad (4)$$

where u_e is the element nodal values vector of equation (2) and where the shape functions vectors φ and ψ are here

$$\varphi^T(\xi) = [\frac{1}{3}\xi(\xi-1), 0, 0, 1-\xi^2, \frac{1}{3}\xi(\xi+1), 0, 0] \quad (5)$$

and

$$\psi^T(\xi) = \frac{1}{4}[0, 2+3\xi+\xi^3, 1-\xi-\xi^3+\xi^5, 0, 0, 2+3\xi-\xi^3, -1+\xi+\xi^2+\xi^3]$$

where, we recall $-1 \leq \xi \leq 1$.

Next we substitute u and w in equation (4) into $\pi_e(u, w)$ in equation (3) and numerically integrate it by sampling the integrand at the two Gauss points $\xi_1 = -\sqrt{3}/3$ and $\xi_2 = \sqrt{3}/3$, to have

$$\begin{aligned}\pi_e(u_e) = & \sum_{j=1}^2 [\frac{1}{3}h^{-3}r_j\bar{w}_j^2 + \frac{1}{12}r_j^{-1}h^{-1}\bar{w}_j^2 + \frac{1}{4}hr_j^{-1}u_j^2 \\ & + h^{-3}(hu_j + \bar{w}_j^2)^2 r_j - \frac{1}{3}hr_j f_j w_j]\end{aligned}\quad (6)$$

where the subscript $j = 1, 2$ refers to the two integration points $\xi_1 = -\sqrt{3}/3$ and $\xi_2 = \sqrt{3}/3$. The values of u_j , w_j , \bar{u}_j , \bar{w}_j , and f_j are computed from equation (4) as

$$u_j = u_e^\top \varphi_j \quad w_j = u_e^\top \psi_j \quad \bar{u}_j = u_e^\top \dot{\varphi}_j \quad \bar{w}_j = u_e^\top \dot{\psi}_j \quad f_j = u_e^\top \ddot{\psi}_j \quad (7)$$

with the numerical element vectors φ_j , ψ_j , $\dot{\varphi}_j$, $\dot{\psi}_j$, and $\ddot{\psi}_j$

$$\begin{aligned}\varphi_{1,2}^T &= \frac{1}{6}(1 \pm \sqrt{3}, 0, 0, 4, 1 \mp \sqrt{3}, 0, 0) \\ \dot{\varphi}_{1,2}^T &= \frac{1}{6}(\mp 2\sqrt{3}, 0, 0, \pm 4\sqrt{3}, \mp 2\sqrt{3}, 0, 0) \\ \psi_{1,2}^T &= \frac{1}{8}(0, 9 \pm 4\sqrt{3}, 3 \pm \sqrt{3}, 0, 0, 9 \mp 4\sqrt{3}, -3 \pm \sqrt{3}) \\ \dot{\psi}_{1,2}^T &= \frac{1}{6}(0, -3, \pm \sqrt{3}, 0, 0, 3, \mp \sqrt{3}) \\ \ddot{\psi}_{1,2}^T &= \frac{1}{2}(0, \mp \sqrt{3}, -1 \mp \sqrt{3}, 0, 0, \pm \sqrt{3}, 1 \mp \sqrt{3})\end{aligned}\quad (8)$$

where the upper sign of $\sqrt{3}$ belongs to $j = 1$, ($\xi_1 = -\sqrt{3}/3$), and the lower to $j = 2$, ($\xi_2 = \sqrt{3}/3$).

From equation (6) we obtain the element gradient g_e by differentiation with respect to u_e

$$\begin{aligned}g_e = \frac{\partial \pi_e}{\partial u_e} = & \sum_{j=1}^2 [\frac{1}{3}h^{-3}r_j\bar{w}_j\ddot{\psi}_j + \frac{1}{12}r_j^{-1}h^{-1}\bar{w}_j\dot{\psi}_j + \frac{1}{4}hr_j^{-1}u_j\dot{\varphi}_j \\ & + 2h^{-3}r_j(hu_j + \bar{w}_j^2)(h\dot{\varphi}_j + 2\bar{w}_j\dot{\psi}_j) - \frac{1}{3}hr_j f_j \psi_j]\end{aligned}\quad (9)$$

since $\partial u_j / \partial u_e = \varphi_j$, $\partial \bar{u}_j / \partial u_e = \dot{\varphi}_j$, etc. Or

$$g_e = \sum_{j=1}^2 (a_j \ddot{\psi}_j + b_j \dot{\psi}_j + c_j \psi_j + d_j \dot{\varphi}_j + e_j \varphi_j) \quad (10)$$

with

$$\begin{aligned} a_i &= \frac{3}{8}h^{-3}r_i\ddot{w}_i - b_i + \frac{1}{6}h^{-1}r_i^{-1}\dot{w}_i + 4h^{-3}r_i\ddot{w}_i(h\dot{u}_i + \dot{w}_i^2) \\ c_i &= -\frac{1}{2}hr_if_i - d_i - 2h^{-3}r_i(h\dot{u}_i + \dot{w}_i) - e_i - \frac{1}{6}hr_i^{-1}u_i \end{aligned} \quad (11)$$

Further differentiation of π_e with respect to u_i produces the element tangent stiffness matrix

$$k_{ii} = \frac{\partial g_e}{\partial u_i} = \frac{\partial^2 \pi_e}{\partial u_i^2} = \sum_{j=1}^3 [a_j(\ddot{\phi}_j\ddot{\phi}_i^3 + b_j\dot{\phi}_j\dot{\phi}_i^2 + c_j(\dot{\phi}_j\dot{\phi}_i^3 + \dot{\phi}_i\dot{\phi}_j^2) + d_j\dot{\phi}_j\dot{\phi}_i^3 + e_j\dot{\phi}_i\dot{\phi}_j^2)] \quad (12)$$

with

$$\begin{aligned} a_j &= \frac{3}{8}h^{-3}r_j & b_j &= \frac{1}{6}h^{-1}r_j^{-1} + 12h^{-3}r_j\ddot{w}_j^2 + 4h^{-3}r_j\dot{u}_j \\ c_j &= 4h^{-3}r_j\ddot{w}_j & d_j &= 2h^{-3}r_j & e_j &= \frac{1}{6}hr_j^{-1} \end{aligned} \quad (13)$$

Now the element gradient g_e and the element stiffness matrix k_{ii} are routinely assembled into the global g and K , the essential boundary conditions are introduced into them; the thrust p , that appears in equation (1), is added to g at the entry that corresponds to $u(1)$; and the nonlinear stiffness equation $g(u)=0$ is iteratively solved for u with the Newton-Raphson method according to

$$u_1 = u_0 - K_{11}^{-1}g_0 \quad (14)$$

where the subscripts 0 and 1 refer to the before and after values of u and g .

When we are satisfied that the iterative process in equation (14) has settled on an equilibrium configuration u_1 , we turn to decide its stability by computing the eigenvalue of $K(u_1)$; if they are all positive the equilibrium configuration is stable, while if some are negative the solution is unstable.

LATERAL LOAD

To numerically observe the performance of the discretization procedure that led to g_e in equation (10) and k_{ii} in equations (12), they are taken to compute the deflection of the uniformly loaded (i.e. $f = \text{const.}$), clamped (i.e. $w(1) = w'(1) = 0$) circular plate with an immovable (i.e. $u(1) = 0$) edge. Figure 1 shows the improvement in the accuracy in the central deflection $w(0)$, when $f = 10$, with the number of elements N_e . Curve (a) of Figure 1 refers to a linear interpolation of u , and (b) to a quadratic. In both cases w is interpolated cubically. Extrapolation to the limit leads to the conclusion that with a linear u the relative error in $w(0)$ is $0.46N_e^{-2.2}$, while a quadratic u drops the error in $w(0)$ to $0.068N_e^{-3.3}$.

Table I shows the convergence of the Newton-Raphson method, starting with the displacement vector $u = 0$, when $f = 10$, $N_e = 7$, and the displacements u and w are interpolated quadratically and cubically, respectively.

POSTCRITICAL THRUST

For a unit circular, simply-supported plate of zero ν the critical rim thrust is conveniently written⁴ as $p_c = \alpha^2/12$, where $\alpha = 1.8412$ ($\alpha^2 = 3.99$) is the smallest root of the Bessel function equation $J'_1(\alpha) = 0$.

Figure 2 describes the computed behaviour of this plate, bent by the combined action of a lateral uniformly distributed load f and a rim thrust p that exceeds p_c . When $f > 0$ the unstable

Table I. Convergence of the central deflection $w(0)$ with the Newton-Raphson method

Cycles	$w(0)$
1	1.874962
2	1.394681
3	1.182066
4	1.143467
5	1.142294
6	1.142293

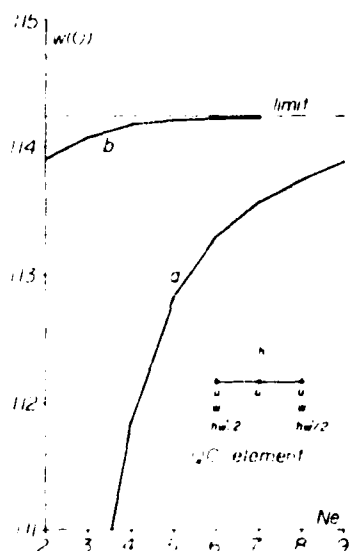


Figure 1. Uniformly loaded ($f = 10$) clamped circular plate with an immovable edge. Computed central deflection for an increased number of finite elements N_e .

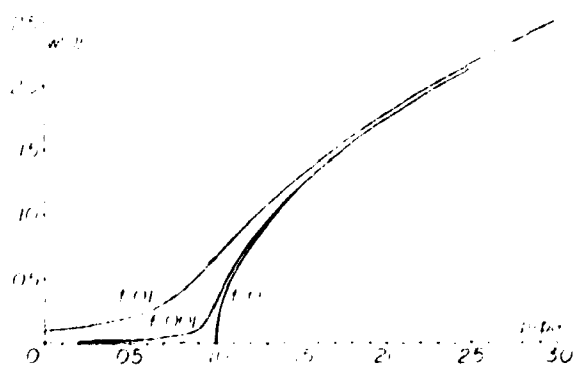


Figure 2. Deflection-load curve for a simply-supported circular plate bent by a lateral force f and an edge thrust p . Five quadratic-cubic element discretization.

solution $w = 0$ for $p = p_{cr}$ is absent and a zero initial guess can be chosen for the Newton-Raphson solution. The thrust p is then increased stepwise with the last computed configuration serving as an initial guess for the next iteration. When $f = 0$ a non-zero initial guess must be used but the computational procedure proceeds otherwise as before to produce the typical bifurcation curve of reference 5.

At the bifurcation point $p = p_{cr}$, K^{-1} becomes non-computable but since the present procedure is global (non-incremental) the problem of crossing such a point does not arise here. One computes the equilibrium configuration of the plate for any loading, regardless of its history. Extrapolating from $p > p_{cr}$ we find for $f = 0$ that near $p = p_{cr}$, $w(0) = 1.91(1 - p/p_{cr})^{1/2}$.

REFERENCES

1. I. Fried, *Numerical Solution of Differential Equations*, Academic Press, New York and London, 1979.
2. N. Perrone and R. Kao, 'A general nonlinear relaxation iteration technique for solving nonlinear problems in mechanics', *J. Appl. Mech.*, 371-376, June (1971).
3. E. Reissner, 'On finite deflections of circular plates', *Proc. Symp. Appl. Math.*, 1, 213-219 (1949).
4. S. Timoshenko and S. Woinowsky-Kreiger, *Theory of Plate and Shells*, McGraw-Hill, New York, 1969, pp. 391-393.
5. K. O. Friedrichs and J. J. Stoker, 'Buckling of the circular plate beyond the critical thrust', *J. Appl. Mech.*, 7-14, March (1942).

STABILITY AND EQUILIBRIUM OF THE STRAIGHT AND CURVED ELASTICA-FINITE ELEMENT COMPUTATION*

Isaac FRIED

Boston University, Department of Mathematics, Boston, MA 02215, USA

Received 1 October 1980

Revised manuscript received 20 February 1981

1. Introduction

The elastica [1, 2] is one of the humblest useful elastic systems that can realistically undergo very large displacements with small strain and assume multiple stable and unstable equilibrium configurations under equal loading. Its total potential energy is concise, yet irrational in the displacements requiring approximate computations for a finite element modeling [3-6].

We find the elastica a compelling practical example to recount the use of discrete integration techniques [7] to derive nonlinear finite elements [8].

2. Planar elastica

Consider the unit inextensional elastica of fig. 1 that obeys the Bernoulli-Euler law

$$M = \alpha\theta', \quad \theta' = d\theta/ds, \quad (1)$$

which linearly relates the bending moment M and the curvature θ' , $\alpha = IE$, E being the modulus of elasticity and I the cross sectional moment of inertia.

In its bent state $\theta = \theta(s)$ the elastica possesses a total potential energy

$$\pi(\theta) = \int_0^1 (\frac{1}{2}\alpha\theta'^2 - fy + gx) ds - Py(1) + Qx(1) - M\theta(1). \quad (2)$$

Or with $f = \tilde{f}'$, $g = \tilde{g}'$, $\tilde{f}(1) = \tilde{g}(1) = 0$, and since $x' = \cos \theta$, $y' = \sin \theta$, $x(0) = y(0) = \theta(0) = 0$, $\pi(\theta)$ becomes

$$\pi(\theta) = \int_0^1 [\frac{1}{2}\alpha\theta'^2 + \sin \theta(\tilde{f} - P) + \cos \theta(Q - \tilde{g})] ds - M\theta(1). \quad (3)$$

*Research supported by the Office of Naval Research under contract ONR-N00014-76C-036.

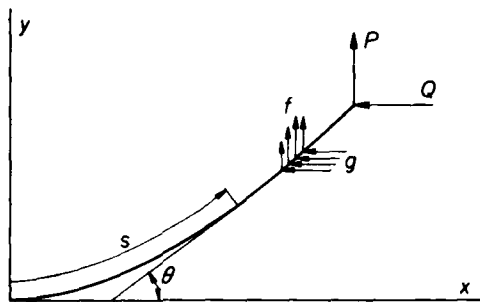


Fig. 1. Loaded elastica.

In this paper we shall consider only the simpler case of

$$\pi(\theta) = \int_0^1 \left(\frac{1}{2} \theta'^2 - P \sin \theta + Q \cos \theta \right) ds, \quad (4)$$

for which the admissible θ is continuous and satisfies the fixed end condition $\theta(0) = 0$.

Eq. (3) allows the expression of the total potential energy in terms of y . Indeed, since $y'' = \theta' \cos \theta$, eq. (4) may be written as

$$\pi(y) = \int_0^1 \left[\frac{1}{2} \frac{y''^2}{1-y'^2} + Q(1-y'^2)^{1/2} \right] ds - Py(1), \quad (5)$$

where $y \in C^1$ and $y(0) = y'(0) = 0$.

When the deflection of the elastica is known beforehand to remain moderate an intermediate, simpler, theory is possible based on the approximations

$$(1-y'^2)^{-1} = 1 + y'^2 + y'^4, \quad (1-y'^2)^{1/2} = 1 - \frac{1}{2}y'^2 - \frac{1}{8}y'^4 \quad (6)$$

that change eq. (5) to

$$\pi(y) = \frac{1}{2} \int_0^1 [y''^2(1+y'^2) - Qy'^2(1+\frac{1}{4}y'^2)] ds - Py(1). \quad (7)$$

3. Finite elements

Approximate computation of the total potential energy in eqs. (4), (5) and (7) with piecewise polynomial interpolations and a discrete Gauss sampling of the energy density function leads to a rational, efficient and automatic procedure for the generation of high order nonlinear finite elements.

We shall first apply this technique to $\pi(\theta)$ in eq. (4) which we intend to discretize with

three-nodal-point, quadratic elements. We have reason to believe that a two point Gauss integration of each element, that exactly integrates θ'^2 is most efficient here. A higher integration scheme is costlier and contributes but little towards improving the accuracy of the computed shape. Only raising the interpolation order of θ over the element would require a corresponding increase in the order of the integration scheme.

Interpolation of θ over the element is formally expressed by

$$\theta = \theta_e^t \phi, \quad (8)$$

where $\theta_e^t = (\theta_1, \theta_2, \theta_3)$ is the element nodal values vector, and where

$$\phi^t = [\frac{1}{2}\xi(\xi - 1), 1 - \xi^2, \frac{1}{2}\xi(\xi + 1)], \quad -1 \leq \xi \leq 1 \quad (9)$$

is the shape functions vector.

Let the typical element be of size h (not $2h$) such that $ds = \frac{1}{2}h d\xi$, $\theta' = 2h^{-1}\dot{\theta}$, where $(\cdot)' = d/d\xi$. Two point Gauss integration of $\pi(\theta)$ for this element produces the approximate element total potential energy

$$\pi_e = \frac{1}{2}h \sum_{j=1}^2 4h^{-2}\dot{\theta}_j^2 - P \sin \theta_j + Q \cos \theta_j, \quad (10)$$

in which the index $j = 1, 2$ refers to the two Gauss points $\xi_1 = -\sqrt{3}/3$ and $\xi_2 = \sqrt{3}/3$ respectively. The values of θ_j and $\dot{\theta}_j$ are computed from eq. (8) as

$$\theta_j = \theta_e^t \phi(\xi_j), \quad \dot{\theta}_j = \theta_e^t \dot{\phi}(\xi_j). \quad (11)$$

We prefer the briefer notation $\phi_j = \phi(\xi_j)$ and $\dot{\phi}_j = \dot{\phi}(\xi_j)$ and have from eq. (9) that

$$\begin{aligned} \phi_1^t &= \frac{1}{6}(1 + \sqrt{3}, 4, 1 - \sqrt{3}), & \phi_2^t &= \frac{1}{6}(1 - \sqrt{3}, 4, 1 + \sqrt{3}), \\ \dot{\phi}_1^t &= \frac{1}{6}(-2\sqrt{3} - 3, 4\sqrt{3}, -2\sqrt{3} + 3), & \dot{\phi}_2^t &= \frac{1}{6}(2\sqrt{3} - 3, -4\sqrt{3}, 2\sqrt{3}, 2\sqrt{3} + 3), \end{aligned} \quad (12)$$

which we record once and for all.

From π_e in eq. (10) we derive the element gradient

$$g_e = \frac{\partial \pi_e}{\partial \theta_e} = \sum_{j=1}^2 2h^{-1}\dot{\theta}_j \dot{\phi}_j - \frac{1}{2}h(P \cos \theta_j + Q \sin \theta_j) \phi_j \quad (13)$$

and the element tangent stiffness matrix (the element Hessian)

$$k_e = \frac{\partial g_e}{\partial \theta_e} = \frac{\partial^2 \pi_e}{\partial \theta_e^2} = \sum_{j=1}^2 2h^{-1}\dot{\phi}_j \dot{\phi}_j^t - \frac{1}{2}h(Q \cos \theta_j - P \sin \theta_j) \phi_j \phi_j^t, \quad (14)$$

and have here that

$$\begin{aligned}\dot{\phi}_1 \phi_1^t + \dot{\phi}_2 \phi_2^t &= \frac{1}{6} \begin{bmatrix} 7 & -8 & 1 \\ -8 & 16 & -8 \\ 1 & -8 & 7 \end{bmatrix}, \\ \phi_1 \phi_1^t &= \frac{1}{18} \begin{bmatrix} 2+\sqrt{3} & 2(1+\sqrt{3}) & -1 \\ 2(1+\sqrt{3}) & 8 & 2(1-\sqrt{3}) \\ -1 & 2(1-\sqrt{3}) & 2-\sqrt{3} \end{bmatrix}, \\ \phi_2 \phi_2^t &= \frac{1}{18} \begin{bmatrix} 2-\sqrt{3} & 2(1-\sqrt{3}) & -1 \\ 2(1-\sqrt{3}) & 8 & 2(1+\sqrt{3}) \\ -1 & 2(1+\sqrt{3}) & 2+\sqrt{3} \end{bmatrix}. \end{aligned} \quad (15)$$

An entirely analogous procedure is applied to $\pi(y)$ in eq. (5), except that now y is interpolated cubically over the interval $0 \leq \xi \leq 1$ that covers an element of size h . Once more we write $y = y_e^t \phi$ with the element nodal values vector $y_e^t = (y_1, \dot{y}_1, y_2, \dot{y}_2)$ and with the element shape functions vector

$$\phi^t = (1 - 3\xi^2 + 2\xi^3, \xi - 2\xi^2 + \xi^3, 3\xi^2 - 2\xi^3, -\xi^2 + \xi^3), \quad (16)$$

from which $\dot{\phi}$ and $\ddot{\phi}$ are computed.

A two point Gauss integration that exactly evaluates the integral of y''^2 appears to be most efficient here too. These two points are in the interval $0 \leq \xi \leq 1$ at $\xi_1 = \frac{1}{6}(3 - \sqrt{3})$, and $\xi_2 = \frac{1}{6}(3 + \sqrt{3})$, and with equal weights $w_1 = w_2 = \frac{1}{2}$. Consequently π_e of eq. (5) becomes

$$\pi_e = \frac{1}{2}h \sum_{j=1}^2 \frac{1}{2}h^{-4} \ddot{y}_j^2 (1 - h^{-2} \ddot{y}_j^2)^{-1} + Q(1 - h^{-2} \ddot{y}_j^2)^{1/2}, \quad (17)$$

where

$$\dot{y}_j = y_e^t \dot{\phi}_j, \quad \ddot{y}_j = y_e^t \ddot{\phi}_j$$

and

$$\dot{\phi}_{1,2}^t = (-1, \pm\sqrt{3}/6, 1, \mp\sqrt{3}/6), \quad \ddot{\phi}_{1,2}^t = (\mp 2\sqrt{3}, -1 \mp \sqrt{3}, \pm 2\sqrt{3}, 1 \mp \sqrt{3}), \quad (18)$$

where the upper sign of $\sqrt{3}$ belongs to $j = 1$ and the lower to $j = 2$.

From π_e in eq. (17) we have that

$$g_e = \partial \pi_e / \partial y_e = \sum_{j=1}^2 a_j \ddot{\phi}_j + b_j \dot{\phi}_j, \quad (19)$$

with

$$a_j = \frac{1}{2}h^{-3} \ddot{y}_j (1 - h^{-2} \ddot{y}_j^2)^{-1}, \quad b_j = \frac{1}{2}h^{-5} \dot{y}_j \ddot{y}_j (1 - h^{-2} \ddot{y}_j^2)^{-2} \quad (20)$$

and

$$k_e = \frac{\partial g_e}{\partial y_e} = \frac{\partial^2 \pi_e}{\partial y_e^2} = \sum_{j=1}^2 a_j \ddot{\phi}_j \ddot{\phi}_j^t + b_j (\dot{\phi}_j \ddot{\phi}_j^t + \ddot{\phi}_j \dot{\phi}_j^t) + c_j \dot{\phi}_j \dot{\phi}_j^t, \quad (21)$$

with

$$\begin{aligned} a_j &= \frac{1}{2} h^{-3} (1 - h^{-2} \dot{y}_j^2)^{-1}, & b_j &= h^{-5} \dot{y}_j \ddot{y}_j (1 - h^{-2} \dot{y}_j^2)^{-2}, \\ c_j &= \frac{1}{2} h^{-5} \ddot{y}_j (1 - h^{-2} \dot{y}_j^2)^{-2} + 2 h^{-7} \dot{y}_j^2 \ddot{y}_j^2 (1 - h^{-2} \dot{y}_j^2)^{-3} \\ &\quad - \frac{1}{2} Q h^{-1} [(1 - h^{-2} \dot{y}_j^2)^{-1/2} + h^{-2} \dot{y}_j^2 (1 - h^{-2} \dot{y}_j^2)^{-3/2}]. \end{aligned} \quad (22)$$

For the intermediate theory of eq. (7) we have in the same way that

$$\pi_e = \frac{1}{4} \sum_{j=1}^2 h^{-3} \dot{y}_j^2 (1 + h^{-2} \dot{y}_j^2) - Q h^{-1} \dot{y}_j^2 (1 + \frac{1}{4} h^{-2} \dot{y}_j^2), \quad (23)$$

then

$$g_e = \sum_{j=1}^2 a_j \ddot{\phi}_j + b_j \dot{\phi}_j, \quad (24)$$

with

$$a_j = \frac{1}{2} h^{-3} \ddot{y}_j (1 + h^{-2} \dot{y}_j^2), \quad b_j = \frac{1}{2} h^{-5} \dot{y}_j^2 \ddot{y}_j - \frac{1}{2} Q h^{-1} \dot{y}_j (1 + \frac{1}{4} h^{-2} \dot{y}_j^2) - \frac{1}{8} Q h^{-3} \dot{y}_j^3, \quad (25)$$

and

$$k_e = \sum_{j=1}^2 a_j \ddot{\phi}_j \ddot{\phi}_j^t + b_j (\dot{\phi}_j \ddot{\phi}_j^t + \ddot{\phi}_j \dot{\phi}_j^t) + c_j \dot{\phi}_j \dot{\phi}_j^t, \quad (26)$$

with

$$\begin{aligned} a_j &= \frac{1}{2} h^{-3} (1 + h^{-2} \dot{y}_j^2), & b_j &= h^{-5} \dot{y}_j \ddot{y}_j, \\ c_j &= \frac{1}{2} h^{-5} \ddot{y}_j^2 - \frac{1}{2} Q h^{-1} (1 + \frac{1}{4} h^{-2} \dot{y}_j^2) - \frac{3}{8} Q h^{-3} \dot{y}_j^3. \end{aligned} \quad (27)$$

Notice that

$$\frac{1}{2} h^{-3} \sum_{j=1}^2 \ddot{\phi}_j \ddot{\phi}_j^t = k = h^{-3} \begin{bmatrix} 12 & 6 & -12 & 6 \\ 6 & 4 & -6 & 2 \\ -12 & -6 & 12 & -6 \\ 6 & 2 & -6 & 4 \end{bmatrix} \quad (28)$$

is the element stiffness matrix of the linear beam.

4. Computations

To locate the extremum points of the global total potential energy we routinely assemble all the element gradients g_e into the global g , delete the entries of g that correspond to the fixed points, add the tip work terms, and set out to solve the nonlinear stiffness equation $g = 0$.

If we choose the Newton-Raphson method for the iterative solution of $g = 0$, then the tangent global stiffness matrix K is also assembled from all the element k_e and the solution proceeds with

$$\mathbf{y}_1 = \mathbf{y}_0 - K_0^{-1} g_0, \quad (29)$$

starting with some initial guess that determines the particular solution converged upon.

We may decide that to update K^{-1} at each step is too expensive and use instead a fixed K^{-1} over several steps then update it, reducing thereby the Newton-Raphson method into one of many linear successive substitution schemes. When and precisely how to do all this is too bewildering to contemplate now.

When we are satisfied that the iterations have converged to an equilibrium configuration \mathbf{y}_∞ we decide its stability by computing the (lowest) eigenvalues of $K(\mathbf{y}_\infty)$. If they are all positive the total potential energy is minimal at \mathbf{y}_∞ and this solution is stable, if, however, some are negative \mathbf{y}_∞ lies on a saddle point of $\pi(\mathbf{y})$ and this configuration is unstable.

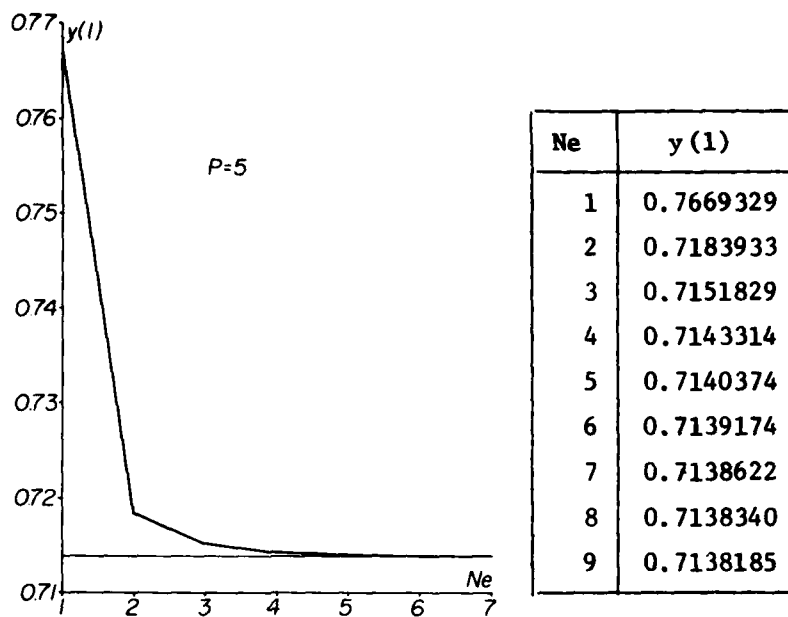
To observe the actual behavior of the derived elements with respect to the discretization accuracy and the performance of the Newton-Raphson method we undertake to compute the deflection of the elastica given in eq. (5) and eqs. (18)-(21), with $Q = 0$. Table 1 lists the iterative improvement in the tip deflection $y(1)$ for a Newton-Raphson computation with $P = 1.5$, that started with $y_0(s) = 0$. Four cycles produce here a wholly acceptable solution.

When P is increased beyond 1.5 the Newton-Raphson method suddenly ceases to converge from a zero initial guess. A closer initial form is needed then to start the iterative procedure, or one may reach the equilibrium states of the elastica for $P > 1.5$ with a stepwise increase of P using the computed deflection under the lower load as an initial guess for the next Newton-Raphson iteration. One is thus presented with the choice of small load increments with fewer corrections (incremental method [9, 10]) or large load increments with more corrections (global method). The solution reached with the incremental procedure depends on the chosen loading history, while the solution reached with the global method depends on the initial guess.

Fig. 2 traces the computed tip deflection $y(1)$ of the elastica loaded with $p = 5$, $Q = 0$, as it is

Table 1
Convergence of the end deflection $y(1)$, computed with the Newton-Raphson method, for a cantilever beam tip loaded with a force $P = 1.5$ and discretized with four cubic elements

Cycles	$y(1)$	Cycles	$y(1)$	Cycles	$y(1)$
1	0.500000	3	0.4124599	5	0.4109928
2	0.4337216	4	0.4109994	6	0.4109928

Fig. 2. Convergence of tip deflection $y(1)$ with number, Ne , of cubic C^1 finite elements.

improved in accuracy with the number of finite elements Ne used in the discretization. Extrapolation to the limit with the data in fig. 2 discloses that $| \text{error in } y(1) | = 0.1 Ne^{-3.75}$.

When the same elastica problem is solved with the element g_e and k_e of eqs. (13) and (14) we get for $Ne = 3, 4, 5, 6, 7$ the corresponding tip angles $\theta = 1.2149992, 1.2152510, 1.2153196, 1.2153444, 1.2153549$; and interpolation to the limit has it that the $| \text{error in } \theta(1) | = 0.03 Ne^{-4}$.

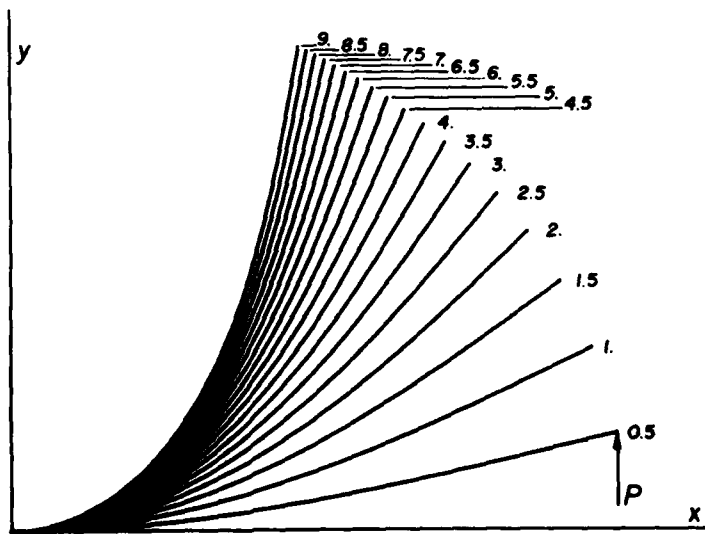


Fig. 3. Stable equilibrium states of the elastica.

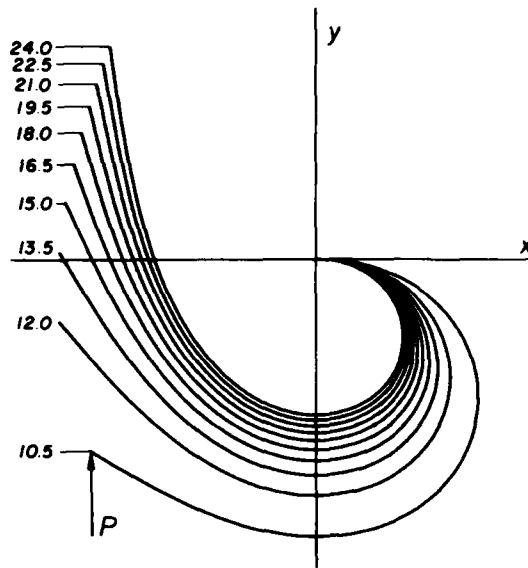


Fig. 4. Stable equilibrium states of the elastica.

A seven element discretization of the elastica with g_e and k_e of eqs. (13) and (14) is used to compute the stable and unstable equilibrium configurations shown in figs. 3, 4 and 5. Fig. 6 traces the variation of λ_1^K , the lowest eigenvalue of the global stiffness matrix K , with the force P for the equilibrium configurations of figs. 3, 4, and 5. The positive branches of fig. 6 correspond to stable equilibrium states, while the negative branch corresponds to unstable states.

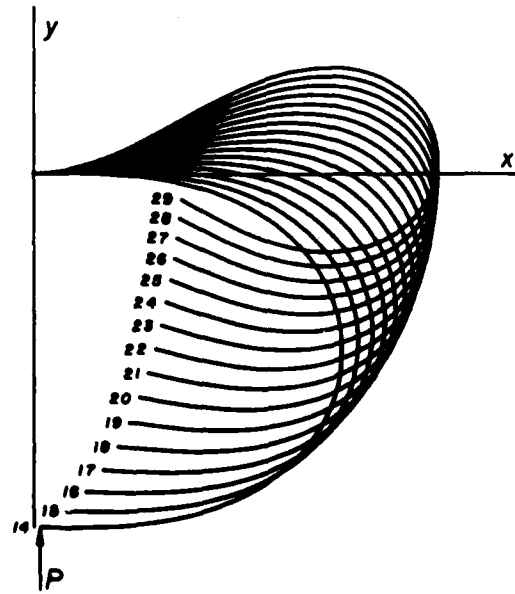


Fig. 5. Unstable equilibrium states of the elastica.

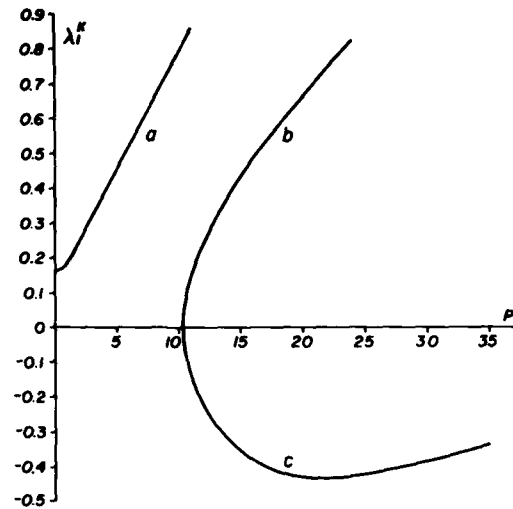


Fig. 6. Lowest eigenvalue λ_1^K of the global stiffness matrix K for the elastica in: (a) fig. 3, (b) fig. 4, 6, and (c) fig. 5.

5. Load correction stiffness

Circumstances may arise in which the nonlinearity is sufficiently small to warrant a simpler successive substitution scheme in the form of load or matrix correction for the solution of the nonlinear stiffness equation instead of the costlier Newton-Raphson scheme with its involved, ever reconstructed, tangent stiffness matrix.

The intermediate theory of eq. (7) with $Q = 0$ illustrates this. Eqs. (24), (25) and (28) allow us to write the element stiffness equation

$$ky_e = -\frac{1}{2}h^{-5} \sum_{i=1}^2 \ddot{y}_i \ddot{y}_i (\dot{y}_i \ddot{\phi}_i + \ddot{y}_i \dot{\phi}_i) \quad (30)$$

to be assembled into the global stiffness equation, $Ky = f(y)$, K being the linear, y free, global stiffness matrix, and $f(y)$ the displacement dependent load vector. Successive substitutions is attempted for the solution of $Ky = f(y)$ in the form of a load correction procedure

$$y_1 = K^{-1}f(y_0), \quad (31)$$

where K^{-1} need be formed only once.

But in its original form (31) successive substitutions performs unsatisfactorily. To understand why suppose that we start the corrections with $y_0 = 0$ and compute y_1 which is actually the solution to the completely linearized problem. If the elastic system has the property that it becomes stiffer with larger displacements then y_1 is much too large and consequently $f(y_1)$ is drastically reduced, to produce in the next iteration a too small y_2 . Repeated iterations produces then a sequence of computed y_0, y_1, \dots that wildly oscillate about the true solution.

We propose to dampen these oscillations with the averaging that replaces y_1 by $(y_1 + y_0)/2$, or change eq. (31) to

$$y_1 = \frac{1}{2}(y_0 + K^{-1}f_0). \quad (32)$$

Fig. 7 shows the progress of the computed tip deflection $Y(1)$ in a cantilever bent by a tip force $P = 2$, with successive load corrections, without (a) and with (b) averaging. Without averaging load correction is useless.

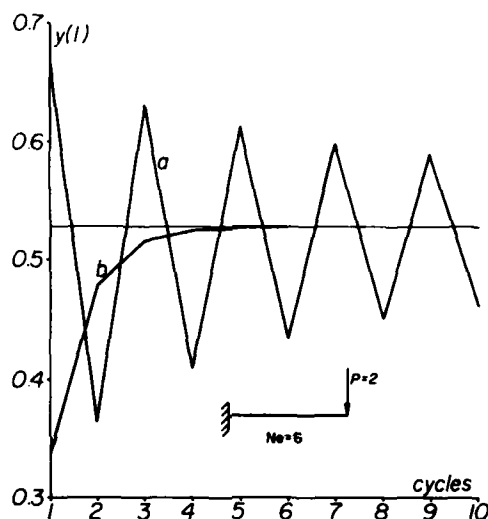


Fig. 7. Load correction solution of the stiffener equation; (a) without averaging, and (b) with averaging.

6. Curved elastica

When the elastica is initially curved to the form $\theta_0 = \theta_0(s)$ Bernoulli-Euler's law of eq. (1) becomes $M = \alpha(\theta - \theta_0)'$, and as a result $\pi(\theta)$ of eq. (4) changes into

$$\pi(\theta) = \int_0^1 [\frac{1}{2}\alpha(\theta' - \theta_0')^2 - P \sin \theta + Q \cos \theta] ds, \quad (33)$$

or after integration by parts

$$\pi(\theta) = \int_0^1 (\frac{1}{2}\alpha\theta'^2 + \alpha\theta_0''\theta - P \sin \theta + Q \cos \theta) ds - \alpha\theta_0'(1)\theta(1). \quad (34)$$

For the circular arch, in which $\theta_0'' = 0$, $\pi(\theta)$ is reduced to

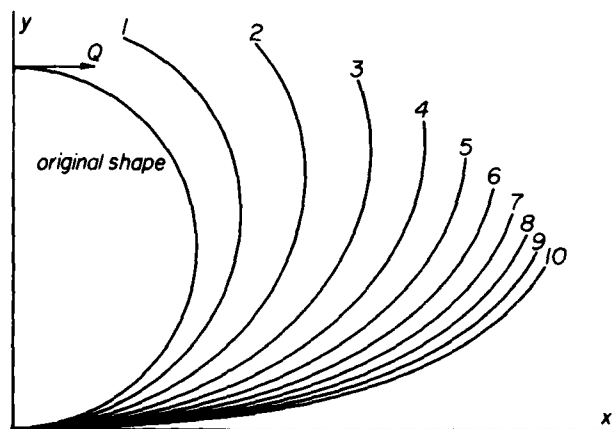


Fig. 8. Opening of a circular C-spring.

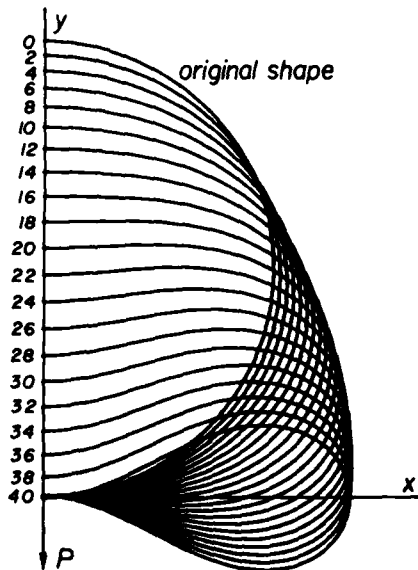


Fig. 9. Bending of a circular ring.

$$\pi(\theta) = \int_0^1 \left(\frac{1}{2} \alpha \theta'^2 - P \sin \theta + Q \cos \theta \right) ds - \alpha \theta'_0(1) \theta(1) \quad (35)$$

as for the elastica with an end moment.

We use eq. (35), with $\alpha = 1$ to compute the bending of a circular ring by two equal and opposite forces P , and the opening of a circular C-spring by the forces Q . Figs. 8 and 9 show the equilibrium states of the ring bent under a sequence of increasing forces. These figures compare well with the results obtained by other means [11-14].

7. Spatial elastica

To describe the position and twist of the neutral line of the elastica in space [1, 2] we need three parameters (angles) θ, φ, ψ , and have that

$$x' = \sin \theta \cos \psi, \quad y' = \sin \theta \sin \psi, \quad z' = \cos \theta, \quad (36)$$

where $\theta = 0$ corresponds to the shape of the free elastica along the z -axis.

Bernoulli-Euler's law becomes here

$$M_1 = \alpha \kappa_1, \quad M_2 = \beta \kappa_2, \quad T = \gamma \tau, \quad (37)$$

where the curvatures κ_1, κ_2 and the twist τ are given in terms of θ, φ, ψ as

$$\begin{aligned} \kappa_1 &= \theta' \sin \phi - \psi' \sin \theta \cos \phi, \\ \kappa_2 &= \theta' \cos \phi + \psi' \sin \theta \sin \phi, \quad \tau = \phi' + \psi' \cos \theta \end{aligned} \quad (38)$$

and the total potential energy of the elastica becomes

$$\pi(\theta, \phi, \psi) = \frac{1}{2} \int_0^1 (\alpha \kappa_1^2 + \beta \kappa_2^2 + \gamma \tau^2) ds - Px(1) - Qy(1) - Rz(1), \quad (39)$$

where P, Q and R are end forces in the x -, y - and z -directions, respectively.

Finite element models for the space elastica are derived from $\pi(\theta, \phi, \psi)$ as before.

References

- [1] A.E. Love, *A Treatise on the Mathematical Theory of Elasticity* (Dover Publications, New York, 4th ed., 1944) Ch. 18, 19.
- [2] M. Born, *Stabilität der elastischen Linie in Ebene und Raum*, Inaugural-Dissertation, Göttingen, 1906.
- [3] Y. Tada and G. Lee, Finite element solution to an elastica problem of beams, *Internat. J. Numer. Meths. Engrg.* 2 (1970) 229–241.
- [4] T.Y. Yang, Matrix displacement solution to elastica problems of beams and frames, *Internat. J. Solids Structures* 9 (1973) 829–842.
- [5] W.F. Schmidt, Nonlinear bending of beams using the finite element method, *Comput. and Structures* 8 (1977) 153–158.
- [6] R.D. Wood and O.C. Zienkiewicz, Geometrically nonlinear finite element analysis of beams, frames, arches and axisymmetric shells, *Comput. and Structures* 7 (1977) 725–735.
- [7] I. Fried, *The Numerical Solution of Differential Equations* (Academic Press, New York, 1979).
- [8] J.H. Argyris et al., Finite element method – the natural approach, *Comput. Meths. Appl. Mech. Engrg.* 17/18 (1979) 1–106.
- [9] J.A. Stricklin, W.A. Von Riesemann, J.R. Tillerson and W.E. Haisler, Static geometric and material nonlinear analysis, in: J.T. Oden et al., eds., *Advances in Computational Methods in Structural Mechanics and Design* (UAH Press, 1972) pp. 301–324.
- [10] Y. Yamada, Incremental formulation for problems with geometric and material nonlinearities, in: J.T. Oden et al., eds., *Advances in Computational Methods in Structural Mechanics and Design* (UAH Press, 1972) pp. 325–355.

- [11] R. Frisch-Fay, The deformation of elastic circular rings, *Aus. J. Appl. Sci.* 11 (1960) 329–340.
- [12] P. Seide, Postbuckling behavior of circular rings with two or four concentrated loads, *Internat. J. Nonlinear Mech.* 8 (1973) 169–178.
- [13] A. Shinohara and M. Hara, Large deflection of a circular C-shaped spring, *Internat. J. Mech. Sci.* 21 (1979) 179–186.
- [14] L.T. Watson and C.Y. Wang, A homotopy method applied to elastica problems, *Internat. J. Solids Structures* 17 (1981) 29–37.

LARGE DEFORMATION STATIC AND DYNAMIC FINITE ELEMENT ANALYSIS OF EXTENSIBLE CABLES[†]

ISAAC FRIED[‡]

Boston University, Department of Mathematics, Boston, MA 02215, U.S.A.

(Received 22 June 1981; received for publication 23 August 1981)

Abstract—Approximate numerical integration of the element total potential energy with polynomial interpolation of the displacements creates high order nonlinear, extensible, cable finite elements. Successful computations of static and dynamic large displacement cable problems are carried out with the element.

INTRODUCTION

Gauss integration of the element total potential energy routinely generates high order nonlinear extensible cable finite elements for any energy density function with no need for simplifications [1]. Assembly of the element matrices and the Newton-Raphson solution of the global nonlinear stiffness equation follows the linear finite element procedure.

High order elements are more efficient in static problems and indispensable in motion [2] problems. Physical discretization with rod linkages [3-6] can be expected to perform well only in equilibrium problems of cables with low curvature.

For cable dynamic problems with multidirectional accelerations it is computationally convenient [7] to assume independent x and y displacements that may cause extension. Near inextensibility is achieved with a high elastic constant.

Large axial stiffness gives rise to strong oscillations in the computed strain within each element. But, as in the incompressible elements [8], also here the strain and tension computed at the Gauss sampling points are accurate.

INFLATED BALLOON

To fix ideas and make comparisons we shall first computationally solve the static problem of a balloon lifted at the end of a long inextensional ideal cable as in Fig. 1. Buoyancy and wind drag provide the end forces P and Q on the cable that is otherwise assumed unaffected by the air.

Equilibrium of the unit length cable is expressed by

$$\begin{aligned} \frac{d}{ds}(\rho \sin \theta) &= 0 \\ \frac{d}{ds}(\rho \cos \theta) + \rho g &= 0 \end{aligned} \quad 0 \leq s \leq 1 \quad (1)$$

where ρ denotes the mass per unit length, and where $\rho = \rho(s)$ is the tension. At the elevated end of the cable the boundary conditions prevail

$$\begin{aligned} \tan \theta &= P/Q \\ \rho^2 &= P^2 + Q^2. \end{aligned} \quad (2)$$

[†]Supported by the Office of Naval Research through contract ONR-N00014-76C-0036.
[‡]Professor.

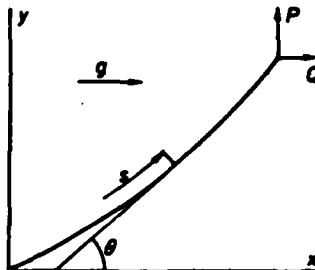


Fig. 1. End lifted cable.

Integration of eqns (1) yields, with the boundary conditions of eqn (2)

$$\rho^2 = P + [\alpha(1-s) + Q]^2 \quad (3)$$

and

$$\tan \theta = \frac{P}{\alpha(1-s) + Q} \quad (4)$$

where $\alpha = \rho g$. Inextensibility relates x and y to θ through

$$\frac{dx}{ds} = \cos \theta \text{ and } \frac{dy}{ds} = \sin \theta \quad (5)$$

and consequently, after another integration we have that

$$z = \sqrt{\left[\left(\frac{P}{\alpha}\right)^2 + \left(1 + \frac{Q}{\alpha}\right)^2\right]} - \sqrt{\left[\left(\frac{P}{\alpha}\right)^2 + \left[(1-s) + \frac{Q}{\alpha}\right]^2\right]} \quad (6)$$

and

$$y = \frac{P}{\alpha} \ln \frac{1 + \frac{Q}{\alpha} + \sqrt{\left[\left(\frac{P}{\alpha}\right)^2 + \left(1 + \frac{Q}{\alpha}\right)^2\right]}}{1 - s + \frac{Q}{\alpha} + \sqrt{\left[\left(\frac{P}{\alpha}\right)^2 + \left(1 - s + \frac{Q}{\alpha}\right)^2\right]}} \quad (7)$$

To prepare for a finite element model we need the total potential energy

$$U(x, y) = -\alpha \int_0^1 x ds + Py(1) - Qz(1) \quad (8)$$

of the inextensible cable, which with $d(xy) = x \, ds + s \, dx$ and with eqn (5) can be written in terms of θ only:

$$\pi(\theta) = c \int_0^1 (s-1) \cos \theta \, ds - \int_0^1 (P \sin Q + Q \cos \theta) \, dx. \quad (9)$$

An inextensile cable element, with θ nodal values only, can be readily derived from $\pi(\theta)$ in eqn (9). However, with an eye on dynamic problems and for greater generality we prefer to allow axial stretching and the corresponding additional elastic energy.

In terms of x and y the tensile strain is

$$\epsilon = (x^2 + y^2)^{1/2} - 1 \quad (10)$$

where $(\cdot)' = d/ds$, and for Hook material the extra term

$$\pi(x, y) = \frac{1}{2} c \int_0^1 \epsilon^2 \, ds \quad (11)$$

is added to the total potential energy in eqn (8). Addition of the elastic energy in eqn (11) permits an axial elongation of about $1/c$.

FINITE ELEMENTS

We now describe the development of a three-nodal point cable element with a quadratic-quadratic interpolation of x and y over it, and a two Gauss point integration of the element total potential energy. Inside each element the coordinates of the displaced cable, x and y are interpolated from the corresponding nodal values by

$$x = u_e^T \phi \text{ and } y = u_e^T \psi \quad (12)$$

where the nodal values vector

$$u_e^T = (x_1, y_1, x_2, y_2, x_3, y_3) \quad (13)$$

and where the Lagrange interpolation (shape) functions are

$$\phi^T = \frac{1}{2} [\xi(\xi-1), 0, 2(1-\xi^2), 0, \xi(\xi+1), 0] \quad (14)$$

$$\psi^T = \frac{1}{2} [0, \xi(\xi-1), 0, 2(1-\xi^2), 0, \xi(\xi+1)] \quad (15)$$

for $-1 \leq \xi \leq 1$.

With $s = s_2 + \xi h$, $ds = h \, d\xi$, $x' = h^{-1} \dot{x}$, and $y' = h^{-1} \dot{y}$, where $(\cdot)' = d/d\xi$, the total potential energy of a typical element becomes

$$\pi_e = -ch \int_{-1}^1 x \, d\xi + \frac{1}{2} ch \int_{-1}^1 [h^{-1}(x^2 + y^2)^{1/2} - 1] \, d\xi. \quad (16)$$

A two point Gauss integration of π_e in eqn (16) requires the evaluation of the energy density function at $\xi = \pm\sqrt{3}/3$ and its summation with equal unit weights. Hence π_e of eqn (16) becomes approximately

$$\pi_e = h \sum_{j=1}^2 -z_j + \frac{1}{2} c(h^{-1}(x_j^2 + y_j^2)^{1/2} - 1)^2 \quad (17)$$

with $j = 1, 2$ referring to the two Gauss points $\xi_1 = -\sqrt{3}/3$ and $\xi_2 = \sqrt{3}/3$. The values of x , y , \dot{x} , and \dot{y} at the Gauss points, namely x_j , y_j , \dot{x}_j , and \dot{y}_j , needed in eqn (17) are computed from eqns (11)-(13) as $x_j = u_e^T \phi_j$, $y_j = u_e^T \psi_j$, $\dot{x}_j = u_e^T \dot{\phi}_j$, and $\dot{y}_j = u_e^T \dot{\psi}_j$, where $\phi_j = \phi(\xi_j)$ and $\psi_j = \psi(\xi_j)$, etc. Actually

$$\begin{aligned} \phi_{1,2} &= \frac{1}{6} (1 \pm \sqrt{3}, 0, 4, 0, 1 \mp \sqrt{3}, 0) \\ \psi_{1,2} &= \frac{1}{6} (0, 1 \pm \sqrt{3}, 0, 4, 0, 1 \mp \sqrt{3}) \\ \dot{\phi}_{1,2} &= \frac{1}{6} (\mp 2\sqrt{3} - 3, 0, \pm 4\sqrt{3}, 0, \mp 2\sqrt{3} + 3, 0) \\ \dot{\psi}_{1,2} &= \frac{1}{6} (0, \mp 2\sqrt{3} - 3, 0, \pm 4\sqrt{3}, 0, \mp 2\sqrt{3} + 3) \end{aligned} \quad (18)$$

in which the upper sign of $\sqrt{3}$ belongs to $j = 1$ and the lower to $j = 2$.

The element gradient g_e and the element tangent stiffness matrix k_e are derived from the element total potential energy π_e in eqn (17) through repeated differentiation with respect to the element nodal values vector u_e :

$$g_e = \frac{\partial \pi_e}{\partial u_e} \text{ and } k_e = \frac{\partial g_e}{\partial u_e} = \frac{\partial^2 \pi_e}{\partial u_e^2} \quad (19)$$

so that

$$g_e = h \sum_{j=1}^2 -\phi_j + c(1 - \delta_j^{-1/2}) z_j \quad (20)$$

where

$$\delta_j = x_j^2 + y_j^2 \text{ and } z_j = x_j \phi_j + y_j \psi_j \quad (21)$$

and

$$k_e = ch \sum_{j=1}^2 (1 - \delta_j^{-1/2})(\phi_j \phi_j^T + \psi_j \psi_j^T) - \delta_j^{-3/2} z_j z_j^T. \quad (22)$$

COMPUTATIONS AND COMPARISONS

In the finite element computation of the cable's equilibrium an initial configuration guess vector u_0 is made, g_e and k_e are computed with this guess and are assembled into the global g_0 and K_0 . Essential boundary conditions (here $x(0) = y(0) = 0$) are imposed upon g_0 and K_0 as in the linear case and an improved configuration u_1 is computed with the Newton-Raphson method according

$$\text{to } u_1 = u_0 - K_0^{-1} g_0 \quad (23)$$

until convergence to u_1 . Stability of the computed equilibrium configuration is decided by testing for the positive definiteness of K_0 .

Figure 2 shows the computed cable configuration of Fig. 1 for $Q = 0$ and $P = 0.01, 0.05, 0.10, 0.15, 0.20, \dots, 0.90$, for a seven element discretization and $c = 100$. When P is small the cable tip behavior is nearly singular since it must rotate almost locally to $\theta = \pi/2$ in order to tangentially meet the vertical force. An enormous tip curvature is created thereby (which might in practice negate the pure cable assumption and force us to consider also the effects of bending at the tip) and

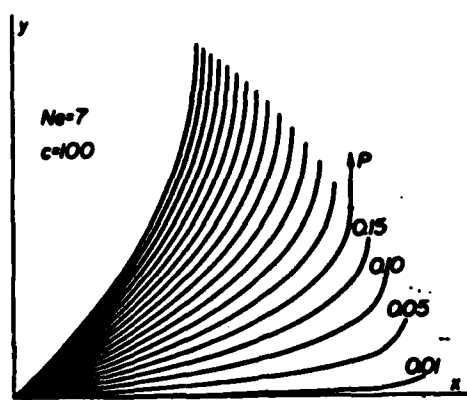


Fig. 2. Seven element computation of the lifted cable.

local misbehavior of the discrete model. Improvement in the computed tip rotation is noticed in Fig. 3 as the number of elements in the discretization is increased from seven to fifteen. Still, a uniform mesh is highly wasteful for small tip loads where small elements are needed only near the lifted end but where larger ones would suffice for the rest of the cable. As the cable is lifted higher the balloon end high curvature disappears and a uniform mesh becomes appropriate.

Table 1 sums up the convergence of the tip rise $y(1)$ due to end forces $P = 0.1$ and $Q = 0$, computed with the Newton-Raphson method for a 15 element discretization. The initial guess for the Newton-Raphson method was taken to be $x_0 = 0.9$ s, $y_0 = 0.3$ s, and all the computations were carried out in single precision (about 7 significant digits).

Table 2 shows the improvement in the computed end rise $y(1)$ with the number N_e of elements, for $P = 0.1$, $Q = 0$ and $c = 100$.

As for the tension, p it can be computed either from the first of eqns (1), which asserts that $p = P/\sin \theta$, or from Hook's law $p = ce$, where the strain e is given, in terms of x and y , in eqn (10). Figure 4 shows the computed strain e inside each of the seven finite elements for $c = 100$, and $P = 0.1, 0.3, 0.5, \dots, 1.1$.

Violent strain oscillations are observed for small values of P in the elements close to the lifted end. At the Gauss integration points the strain is, however, always accurate as can be seen in Table 3.

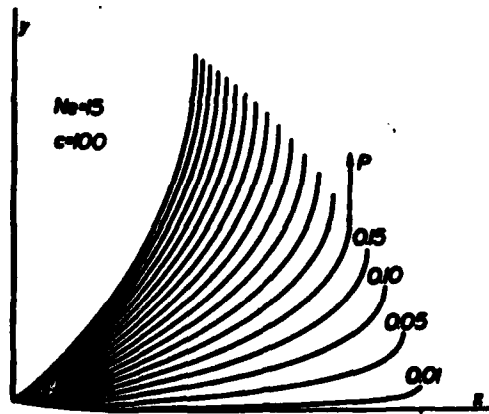


Fig. 3. Fifteen element computation of the lifted cable.

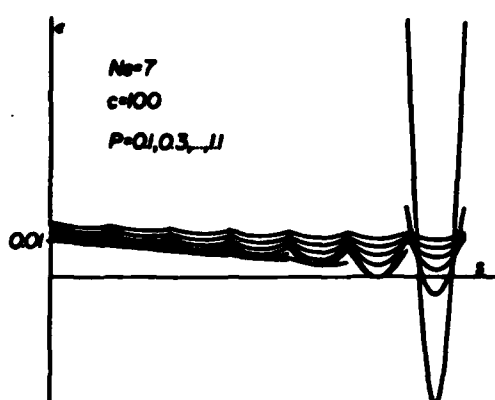


Fig. 4. Computed strain distribution.

Table 1. Convergence of the Newton-Raphson method

NR	$c = 100$	$c = 500$
1	0.320960	0.318679
2	0.347846	0.303435
3	0.301185	0.303387
4	0.301155	0.300195
5	0.300025	0.300037
6	0.300025	0.300025
Exact inextensible		
0.2998223		

Table 2. Discretization accuracy improvement of $y(1)$ with the number of N_e of finite elements

N_e	$y(1)$
3	0.304379
4	0.303113
5	0.302077
6	0.301475
7	0.301136
8	0.300992
9	0.300909
10	0.300866
11	0.300843
12	0.300834
13	0.300829
14	0.300825
15	0.300824

REVOLVING CABLE

Another relevant interesting problem is to determine the configuration and stability of a hanging cable that revolves around an axis parallel to its rest position.

If the eccentricity of the axis of revolution is e then the additional element total potential energy arising from an angular velocity ω is

$$\omega_e = -\rho \omega^2 h \int_{-1}^1 \left(\frac{1}{2} y^2 + ey \right) da. \quad (20)$$

Or numerically integrated

$$\tau_{ei} = -\rho \omega^2 h \sum_{j=1}^2 \left(\frac{1}{2} y_j^2 + cy_j \right). \quad (25)$$

Consequently an additional element gradient and element stiffness matrix

$$g_e = -\rho \omega^2 h \sum_{j=1}^2 (y_j + c) \phi_j \quad (26)$$

and

$$k_e = -\rho \omega^2 h \sum_{j=1}^2 \phi_j \phi_j^T \quad (27)$$

need be taken into account.

Figure 5 shows a series of computed, unstable, equilibrium configurations of the string ($\rho = 1$) for $c = 0.02$ and $\omega^2 = 2.5i + 2$, $i = 1, 2, 3, \dots, 20$; discretization being done with seven elements.

CABLE DYNAMICS

With u denoting the cable's global vector of nodal unknowns its equation of motion is written as

$$g(u) + M\ddot{u} = 0 \quad (28)$$

in which g is the global total potential energy gradient, and M the global mass matrix. A step by step integration of eqn (28) starting with the initial position u_0 and velocity \dot{u}_0 is performed with Newmark's method [2],

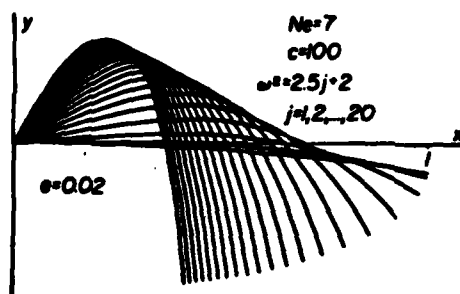


Fig. 5. Unstable configurations of revolving cable.

here

$$u_1 = u_0 + \tau \dot{u}_0 - \frac{1}{2} \tau^2 M^{-1} g_0$$

$$\dot{u}_1 = \dot{u}_0 - \frac{1}{2} \tau M^{-1} (g_0 + g_1) \quad (29)$$

for a time interval τ .

A lumped element mass matrix [2] for the nodal values arrangement in eqn (13)

$$m_e = \frac{h}{3} \text{ diag. } [1, 1, 4, 4, 1, 1] \quad (30)$$

is used to assemble M .

As an example we shall compute the free fall of a chain originally fixed between two horizontal points and then released at one end. At rest the shape of the hanging chain is parametrically given by

$$x = \frac{P}{a} \left[\sqrt{\left[1 + \left(\frac{a}{2P} \right)^2 \right]} - \sqrt{\left[1 + \left(\frac{a}{2P} \right)^2 (1-2s)^2 \right]} \right] \quad (31)$$

and

$$y = \frac{P}{a} \ln \frac{\frac{a}{2P} + \sqrt{\left[1 + \left(\frac{a}{2P} \right)^2 \right]}}{\frac{a}{2P} (1-2s) + \sqrt{\left[1 + \left(\frac{a}{2P} \right)^2 (1-2s)^2 \right]}} \quad (32)$$

so that

$$x\left(\frac{1}{2}\right) = \frac{P}{a} \left[\sqrt{\left[1 + \left(\frac{a}{2P} \right)^2 \right]} - 1 \right] \quad (33)$$

and

$$y(1) = 2 \frac{P}{a} \ln \left(\frac{a}{2P} + \sqrt{\left[1 + \left(\frac{a}{2P} \right)^2 \right]} \right). \quad (34)$$

Our particular case is for $a/(2P) = 1$, or $x(1/2) = 0.207$ and $y(1) = 0.881$.

Figure 6 traces the position of the chain at each $1/10$ of a second for computations carried on with $\tau = 1/1000$, $N_e = 15$, and $c = 100$. Figure 7 shows the same falling chain traced from a video camera film of an actual chain.

Table 3. Computed strains at the Gauss points

Element	s	Incompressible		$E/\sin \theta$	α
		exact	from 9		
5	0.8141E+00	0.2111E+00	0.2107E+00	0.2110E+00	
	0.8536E+00	0.1781E+00	0.1778E+00	0.1783E+00	
6	0.8930E+00	0.1536E+00	0.1534E+00	0.1537E+00	
	0.9192E+00	0.1285E+00	0.1284E+00	0.1284E+00	
7	0.9474E+00	0.1130E+00	0.1129E+00	0.1130E+00	
	0.9659E+00	0.8910E+00	0.8909E+00	0.8909E+00	

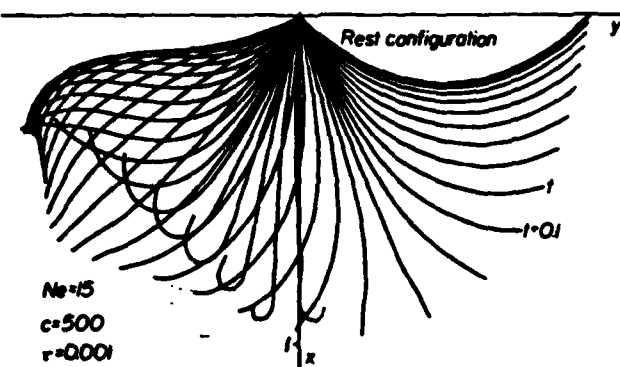


Fig. 6. Stations in a falling cable.

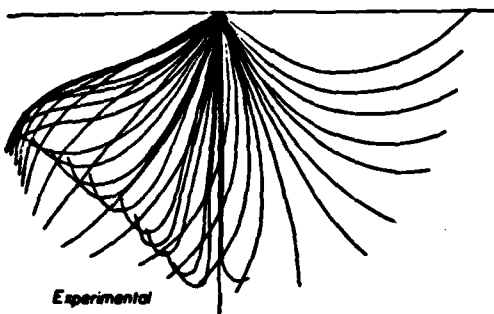


Fig. 7. Experimental counterpart to Fig. 6.

but taken at not equally spaced time intervals. It is remarkable that the computation agrees with reality even about such fine details as the curling up of the free end that takes place while the chain flings back across the vertical line.

REFERENCES

1. W. M. Henghold and J. J. Russell, Equilibrium and natural frequencies of cable structures (a nonlinear finite element approach). *Comput. Structures* 6, 267-271 (1976).
2. I. Fried, *Numerical Solution of Differential Equations*. Academic Press, New York (1979).
3. J. M. Winget and R. L. Huston, Cable dynamics—a finite segment approach. *Comput. Structures* 6, 475-480 (1976).
4. M. L. Gambhir and B. DeV. Batchelor, Parametric study of free vibration of tagged cables. *Comput. Structures* 8, 641-648 (1978).
5. J. Pietrzak, Matrix formulation of static analysis of cable structures. *Comput. Structures* 11, 327-335 (1980).
6. G. R. Monforton and N. M. El-Hakim, Analysis of truss-cable structures. *Comput. Structures* 11, 327-335 (1980).
7. E. J. Routh, *Dynamics of a System-of Rigid Bodies*, Chap. 13. Dover Publications, New York (1905).
8. D. J. Naylor, Stresses in nearly incompressible materials for finite elements with application to the calculation of excess pore pressure. *Int. J. Num. Meth. Engng* 8, 443-460 (1974).

FINITE ELEMENT COMPUTATION OF LARGE RUBBER MEMBRANE DEFORMATIONS

ISAAC FRIED[†]

Boston University, Department of Mathematics, Boston, Massachusetts, U.S.A.

INTRODUCTION

The stretched and inflated rubber membrane problem^{1,2} abounds in realistic examples of elastic systems that may undergo extremely large deformations far beyond anything a linear theory can handle. Geometric and material nonlinearities sufficiently complicate the situation for the analytic answer to its equilibrium question to become impossible even for membranes of the simplest geometry.

Rubber is conveniently characterized by an energy density function and it comes natural to apply variational methods,^{3,4} including finite elements,⁵⁻¹⁰ to the approximate computation of its deformation.

Piecewise polynomial approximation of the displacements, coupled with an element-by-element discrete integration of the total potential energy, promises to be the most general and efficient technique for the solution of the rubber membrane problem. Being a finite element method this solution technique is highly programmable and includes accuracy and efficiency controls through high order elements and a finer mesh.

In this paper we derive in detail the element gradient and element tangent stiffness matrix for the axisymmetric, Mooney, rubber membrane, including a quadratic-quadratic interpolation of the displacements and a two-point Gauss integration of the element total potential energy. Such a discretization procedure is, evidently, indifferent to the complexity of the energy density function and may be extensively applied to other¹¹⁻¹³ than Mooney materials.

We employ the quadratic element to compute the inflated and stretched shapes of the disc, the torus, and the tube, for which other comparative computational and experimental results are plentiful.¹⁴⁻²⁵ These numerical examples are made to check the correctness of the formulation, to exhibit the versatility of the finite element technique, and to study the accuracy of the element. The convergence of the Newton-Raphson method near a critical point is scrutinized.

AXISYMMETRIC MEMBRANE

With reference to Figure 1, let the generating curve of the undeformed membrane be described in the (r, z) plane through $r = r(s)$ and $z = z(s)$, where s denotes arc length. Under the action of applied forces and prescribed displacements the point (r, z) moves to the deformed location (x, y) . An arc element, originally ds is stretched thereby to ds^* , and the membrane thickness t shrinks to t^* .

[†] Professor. Research supported by the Office of Naval Research with Contract ONR-N00014-76C-0036.

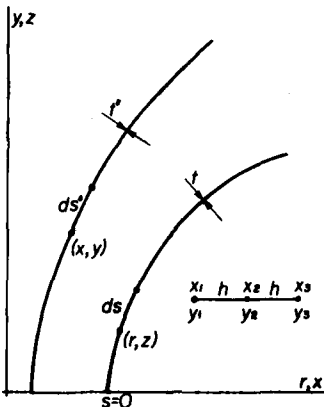


Figure 1. Undeformed and deformed element of arc on the generating curve of an axisymmetrical membrane

The energy density function of the rubber membrane is ultimately expressed in terms of the three principal stretch ratios

$$\lambda_1 = \frac{ds^*}{ds}, \quad \lambda_2 = \frac{2\pi x}{2\pi r}, \quad \lambda_3 = \frac{t^*}{t} \quad (1)$$

and if the deformation is volume preserving

$$\lambda_1 \lambda_2 \lambda_3 = 1 \quad (2)$$

Since $ds^* = (dx^2 + dy^2)^{1/2}$, equations (1) and (2) become

$$\lambda_1 = (x'^2 + y'^2)^{1/2}, \quad \lambda_2 = \frac{x}{r}, \quad \lambda_3 = \frac{1}{\lambda_1 \lambda_2} \quad (3)$$

where $(\)' = d/dx$.

Here we follow the common, rather realistic, assumption of an incompressible Mooney membrane, inflated under the pressure p , for which the total potential energy is of the form

$$\pi(x, y) = 2\pi\mu t \left\{ \int_0^l [(I_1 - 3) + \alpha(I_2 - 3)] r ds + \frac{1}{2} \frac{p}{\mu t} \int_0^l x^2 y' ds \right\} \quad (4)$$

where μ and α are material constants (when $\alpha = 0$ the material is modernistically named neo-Hookean), and where I_1 and I_2 are the strain invariants

$$\left. \begin{aligned} I_1 &= \lambda_1^2 + \lambda_2^2 + \lambda_3^2 \\ I_2 &= \lambda_1^2 \lambda_2^2 + \lambda_2^2 \lambda_3^2 + \lambda_3^2 \lambda_1^2 \end{aligned} \right\} \lambda_3 = 1/\lambda_1 \lambda_2 \quad (5)$$

Henceforth we shall replace, for typographical brevity, $p/\mu t$ by p , and we shall take $2\pi\mu t = 1$.

FINITE ELEMENTS

A typical three-nodal-point element is shown in Figure 1. Inside each such element x and y are interpolated quadratically by

$$x = u_e^T \phi, \quad y = u_e^T \psi \quad (6)$$

where the element nodal values vector $u_e^T = (x_1, y_1, x_2, y_2, x_3, y_3)$, and where the shape function vectors ϕ and ψ are here

$$\begin{aligned}\phi^T &= [\frac{1}{2}\xi(\xi-1), 0, 1-\xi^2, 0, \frac{1}{2}\xi(\xi+1), 0] \\ \psi^T &= [0, \frac{1}{2}\xi(\xi-1), 0, 1-\xi^2, 0, \frac{1}{2}\xi(\xi+1)]\end{aligned}\quad (7)$$

in which $-1 \leq \xi \leq 1$.

From $s = s_2 + h\xi$ it follows that $ds = h d\xi$, or $x' = h^{-1}\dot{x}$, $y' = h^{-1}\dot{y}$, where $(\cdot)' = d/d\xi$. Two-point Gauss integration over each element of the approximate $\pi(x, y)$ is sufficient to remove from the element all spurious mechanisms and artificial instabilities while assuring high computational efficiency. In the interval $-1 \leq \xi \leq 1$ the two Gauss points are at $\xi_1 = -\sqrt{3}/3$ and $\xi_2 = \sqrt{3}/3$, with the equal weights $w_1 = w_2 = 1$.

The element total potential energy π_e is expressed in terms of seven element integrals

$$\pi_e = J_1 + J_2 + J_3 + \alpha(J_4 + J_5 + J_6) + \frac{1}{2}pJ_7 \quad (8)$$

numerically integrated as

$$\begin{aligned}J_1 &= \int_e \lambda_1^2 r ds = h^{-1} \int_{-1}^1 (\dot{x}_i^2 + \dot{y}_i^2) r d\xi = h^{-1} \sum_{i=1}^2 r_i (\dot{x}_i^2 + \dot{y}_i^2) \\ J_2 &= \int_e \lambda_2^2 r ds = h \int_{-1}^1 r^{-1} x_i^2 d\xi = h \sum_{i=1}^2 r_i^{-1} x_i^2 \\ J_3 &= \int_e \lambda_1^{-2} \lambda_2^{-2} r ds = h^3 \int_{-1}^1 r^3 (\dot{x}_i^2 + \dot{y}_i^2)^{-1} x_i^{-2} d\xi = h^3 \sum_{i=1}^2 r_i^3 x_i^{-2} (\dot{x}_i^2 + \dot{y}_i^2)^{-1} \\ J_4 &= \int_e \lambda_1^2 \lambda_2^2 r ds = h^{-1} \int_{-1}^1 r^{-1} x_i^2 (\dot{x}_i^2 + \dot{y}_i^2) d\xi = h^{-1} \sum_{i=1}^2 r_i^{-1} x_i^2 (\dot{x}_i^2 + \dot{y}_i^2) \\ J_5 &= \int_e \lambda_1^{-2} r ds = h^3 \int_{-1}^1 r (\dot{x}_i^2 + \dot{y}_i^2)^{-1} d\xi = h^3 \sum_{i=1}^2 r_i (\dot{x}_i^2 + \dot{y}_i^2)^{-1} \\ J_6 &= \int_e \lambda_2^{-2} r ds = h \int_{-1}^1 x_i^{-2} r^3 d\xi = h \sum_{i=1}^2 r_i^3 x_i^{-2} \\ J_7 &= \int_e x_i^2 y_i' ds = \int_{-1}^1 x_i^2 \dot{y}_i d\xi = \sum_{i=1}^2 x_i^2 \dot{y}_i^2\end{aligned}\quad (9)$$

where the subscript $j = 1, 2$ refers to the two Gauss points $\xi_1 = -\sqrt{3}/3$ and $\xi_2 = \sqrt{3}/3$. Also, in equation (9) $r_j = r(s_j)$ and

$$x_j = u_e^T \phi_j, \quad y_j = u_e^T \psi_j, \quad \dot{x}_j = u_e^T \dot{\phi}_j, \quad \dot{y}_j = u_e^T \dot{\psi}_j \quad (10)$$

after setting $\phi_j = \phi(\xi_j)$. From equation (7) we get the numerical vectors

$$\begin{aligned}\phi_{1,2}^T &= \frac{1}{6}(1 \pm \sqrt{3}, 0, 4, 0, 1 \mp \sqrt{3}, 0) \\ \dot{\phi}_{1,2}^T &= \frac{1}{6}(\mp 2\sqrt{3} - 3, 0, \pm 4\sqrt{3}, 0, \mp 2\sqrt{3} + 3, 0) \\ \psi_{1,2}^T &= \frac{1}{6}(0, \mp 2\sqrt{3} - 3, 0, \pm 4\sqrt{3}, 0, \mp 2\sqrt{3} + 3)\end{aligned}\quad (11)$$

where the upper sign of $\sqrt{3}$ belongs to Gauss point 1 and the lower sign of $\sqrt{3}$ belongs to Gauss point 2.

Differentiation of π_e , given by equations (8) and (9), with respect to u_e produces the element gradient

$$g_e = \frac{\partial \pi_e}{\partial u_e} = \sum_{i=1}^2 a_i \dot{\phi}_i + b_i \dot{\psi}_i + c_i \phi_i \quad (12)$$

with

$$\begin{aligned} a_i &= 2r_i x'_i (1 - \lambda_{1i}^{-4} \lambda_{2i}^{-2}) (1 + \alpha \lambda_{2i}^2) \\ b_i &= 2r_i y'_i (1 - \lambda_{1i}^{-4} \lambda_{2i}^{-2}) (1 + \alpha \lambda_{2i}^2) + \frac{1}{2} p x_i^2 \\ c_i &= 2h \lambda_{2i} (1 - \lambda_{1i}^{-2} \lambda_{2i}^{-4}) (1 + \alpha \lambda_{1i}^2) + h p x_i y'_i \end{aligned} \quad (13)$$

Further differentiation of g_e with respect to u_e produces the element tangent stiffness matrix

$$\begin{aligned} k_e = \frac{\partial g_e}{\partial u_e} = \frac{\partial^2 \pi_e}{\partial u_e^2} &= \sum_{i=1}^2 a_i \dot{\phi}_i \dot{\phi}_i^T + b_i \dot{\psi}_i \dot{\psi}_i^T + c_i \phi_i \phi_i^T \\ &+ d_i (\phi_i \dot{\phi}_i^T + \dot{\phi}_i \phi_i^T) + e_i (\phi_i \dot{\psi}_i^T + \dot{\psi}_i \phi_i^T) + f_i (\dot{\phi}_i \dot{\psi}_i^T + \dot{\psi}_i \dot{\phi}_i^T) \end{aligned} \quad (14)$$

where

$$\begin{aligned} a_i &= 2h^{-1} r_i \left(1 - \frac{y_i'^2 - 3x_i'^2}{\lambda_{2i}^2 \lambda_{1i}^6} \right) (1 + \alpha \lambda_{2i}^2) \\ b_i &= 2h^{-1} r_i \left(1 - \frac{x_i'^2 - 3y_i'^2}{\lambda_{2i}^2 \lambda_{1i}^6} \right) (1 + \alpha \lambda_{2i}^2) \\ c_i &= 2h r_i^{-1} (1 + 3\lambda_{1i}^{-2} \lambda_{2i}^{-4}) (1 + \alpha \lambda_{1i}^2) + h p y'_i \\ d_i &= 4x'_i \lambda_{2i} (\alpha + \lambda_{1i}^{-4} \lambda_{2i}^{-4}) \\ e_i &= 4y'_i \lambda_{2i} (\alpha + \lambda_{1i}^{-4} \lambda_{2i}^{-4}) + p x_i \\ f_i &= 8h^{-1} r_i x'_i y'_i \lambda_{1i}^{-6} \lambda_{2i}^{-2} (1 + \alpha \lambda_{2i}^2) \end{aligned} \quad (15)$$

The element gradient g_e and the element tangent stiffness matrix k_e are linear combinations of the numerical vectors $\phi_i, \dot{\phi}_i$ and ψ_i , and the numerical matrices $\phi_i \phi_i^T, \psi_i \psi_i^T, \phi_i \psi_i^T, \psi_i \phi_i^T + \dot{\phi}_i \phi_i^T, \phi_i \dot{\psi}_i^T + \psi_i \phi_i^T$ and $\dot{\phi}_i \dot{\psi}_i^T + \dot{\psi}_i \phi_i^T$. To compute the displacement dependent coefficients $a_i, b_i, c_i, d_i, e_i, f_i$ of these combinations, u_e is picked out from the global displacement vector u and is introduced into equation (10) to yield, again with the aid of the numerical vectors $\phi_i, \dot{\phi}_i$ and ψ_i , the values of x_i, y_i, \dot{x}_i and \dot{y}_i . These values are used to compute the stretch ratios $\lambda_{1i}^2 = x_i'^2 + y_i'^2$ and $\lambda_{2i}^2 = x_i'^2/r_i^2$, where $x_i' = h^{-1} \dot{x}_i$ and $y_i' = h^{-1} \dot{y}_i$, with which the coefficients in equations (13) and (15) are finally computed.

Once g_e and k_e are formed the finite element assembly procedure follows for the nonlinear case precisely as in the linear: an initial global displacement u_0 is made, all g_e and k_e are computed for it and routinely assembled into the global g and K , the essential boundary conditions are introduced into g and K , and u_0 is improved into u_1 with the Newton-Raphson method

$$u_1 = u_0 - K^{-1}(u_0)g(u_0) \quad (16)$$

until convergence to u_∞ .

The lower eigenvalue spectrum of $K(u_\infty)$ indicates the stability of the computed solution. All positive eigenvalues mean that u_∞ is at a minimum point of the total potential energy and

is therefore stable. Some negative eigenvalues mean a saddle point of $\pi(x, y)$ and unstable equilibrium.

COMPUTATIONS

Finite elements prove themselves best through hard work. We put our element to the work of computing the deformations of a disc, a torus and a tube.

First the disc. It is originally described by $r(s) = s$, $z(s) = 0$, $0 \leq s \leq 1$, its edge is stretched to $x = 1.1$, $y = (0)$, and a pressure p is applied to its face. The purpose of this initial stretching is to endow the membrane with a linear solution and consequently an easier application of the Newton-Raphson method with a zero initial guess.

At the outset we assess the accuracy that our element can provide in order for the future computations to be correct but not overly expensive. We compute the polar rise $y(0)$ of the disc ($\alpha = 0.1$) caused by a pressure $p = 5$. The disc is substantially deformed under this value of p , and for a uniform mesh of N_e finite elements we have that corresponding to $N_e = 1, 2, 3, 4, 10$, $y(0) = 1.2546, 1.4278, 1.4299, 1.4304, 1.4304$. Five finite elements assure reasonable accuracy in the displacements.

Our next concern is with the performance of the Newton-Raphson method. To form an idea as to how this method works we compute $y(0)$ that results from $p = 5$, with an initial zero guess and a ten-element discretization. Newton-Raphson's method successively computes $y(0) = 2.31875, 1.44782, 1.44302, 1.43059, 1.43040, 1.43040$; and four cycles are sufficient for a six-digit accuracy. These computations are carried out in a single precision with some six significant digits. Double precision could have saved us one cycle.

Close to a critical point where K is singular the Newton-Raphson method slows down, as we shall see soon.

Figure 2 shows the inflated disc for a pressure that increases at a step of one between $p = 1$ and $p = 7$. Corresponding to these pressures are the polar stretch ratios $\lambda_0 = 1.144, 1.233,$

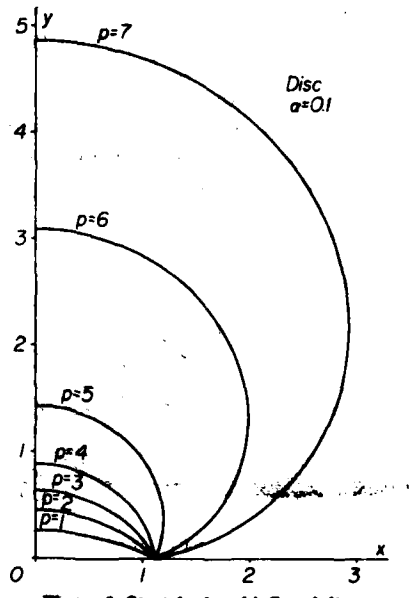


Figure 2. Stretched and inflated disc

Loss of stability in a stretched and inflated right tube ($\alpha = 0$) through bulging is shown in Figure 4. Simulation of the bulging is achieved by pulling out the central circumference of the tube and holding it fixed. A pressure is then introduced into the tube that is left to inflate until the slope at the central grip point becomes parallel to the y -axis.

REFERENCES

1. J. E. Adkins and R. S. Rivlin, 'Large elastic deformations of isotropic materials, IX the deformation of thin shells', *Phil. Trans. R. Soc., sec. A*, **505**-531 (1952).
2. L. R. G. Treloar, *The Physics of Rubber Elasticity*, 2nd edn, Oxford Univ. Press, 1958.
3. M. Levinson, 'The application of the principle of stationary potential energy to some problems in finite elasticity', *J. Appl. Mech.* **37**, 656-660 (1965).
4. J. T. Tielking and W. W. Feng, 'The application of the minimum potential energy principle to nonlinear axisymmetrical membrane problems', *J. Appl. Mech.*, 491-496 (1974).
5. J. T. Oden, *Finite Elements of Nonlinear Continua*, McGraw-Hill, 1972, p. 223.
6. J. H. Argyris, H. Balmer, J. Dotsiris, P. Dunne, M. Haase, M. Muller and D. Scharpf, 'Finite element method—the natural approach', *Compt. meth. Appl. Mech. Eng.* **17/18**, 1-106 (1979).
7. S. Cescotto and G. Fonder, 'A finite element approach for large strains of nearly incompressible rubber-like materials', *Int. J. Solids Struct.* **15**, 589-605 (1979).
8. R. C. Barta, 'Finite plane strain deformations of rubberlike materials', *Int. J. num. Meth. Engng.* **15**, 145-160 (1980).
9. A. R. Johnson, 'Finite element analysis of axisymmetric rubber membranes', *Ph.D. thesis*, Boston Univ. (1981).
10. P. B. Lindley, 'A finite element program for the plane-strain analysis of rubber', *J. Strain Anal.* **10**, 25-31 (1975).
11. A. J. Carmichael and H. W. Holdaway, 'Phenomenological elastomechanical behavior of rubber over wide ranges of strain', *J. Appl. Phys.* **32**, 159-166 (1961).
12. W. W. Klingbeil and R. T. Shield, 'Some numerical investigations on empirical strain energy functions in large axisymmetric extensions of rubber membranes', *ZAMP*, **15/39**, 608-629 (1964).
13. P. D. S. Verma and O. H. Rana, 'Radial deformations of a plane sheet containing a circular hole or inclusion', *Int. J. Non-Lin. Mech.* **13**, 223-232 (1978).
14. A. H. Corneliusen and R. T. Shield, 'Finite deformation of elastic membranes with application to the stability of an inflated and extended tube', *Arch. Rational. Mech. Anal.* **17**, 273-304 (1961).
15. J. J. Stoker, 'Elastic deformation of thin cylindrical sheets', in *Progress in Applied Mechanics* (Ed. D. C. Drucker), Macmillan, New York, 1963, pp. 179-188.
16. P. F. Jordan, 'Stresses and deformations of the thin-walled pressurized torus', *J. Aerosp. Sci.* **29**, 213-225 (1962).
17. J. L. Sanders, Jr. and A. A. Liepins, 'Toroidal membrane under internal pressure', *AIAA J.* **1**, 2105-2110 (1963).
18. A. D. Kydonieas, 'The finite inflation of an elastic toroidal membrane', *Int. J. Engng Sci.* **15**, 477-494 (1967).
19. H. O. Foster, 'Very large deformations of axially symmetrical membranes made of Neo-Hookean materials', *Int. J. Engng Sci.* **5**, 95-117 (1967).
20. A. D. Kydonieas and A. J. M. Spencer, 'The finite inflation of an elastic toroidal membrane of circular cross section', *Int. J. Engng Sci.* **15**, 367-391 (1967).
21. L. J. Hart-Smith and J. D. C. Crisp, 'Large elastic deformations of thin rubber membranes', *Int. J. Engng Sci.* **5**, 1-24 (1967).
22. A. D. Kydonieas and A. J. M. Spencer, 'Finite axisymmetric deformation of an initially cylindrical elastic membrane', *Q. J. Mech. Appl. Math.* **20**, 88-95 (1969).
23. W. H. Yang and W. W. Feng, 'On axisymmetrical deformations of nonlinear membranes', *J. Appl. Mech.* **37**, 1002-1011 (1970).
24. J. Mercier, J. Fremau and A. Rocha, 'Large deformations and stresses of a thin highly elastic toroidal shell under internal pressure', *Int. J. Solids Struct.* **6**, 1233-1241 (1970).
25. R. Benedict, A. Wineman and W. H. Yang, 'The determination of limiting pressure in simultaneous elongation and inflation of nonlinear elastic tubes', *Int. J. Solids Struct.* **15**, 241-249 (1979).

FINITE ELEMENT COMPUTATION OF
LARGE ELASTIC DEFORMATIONS

Isaac Fried

Institute of Technology

1. INTRODUCTION

Approximate Gaussian quadrature of the total potential energy[2] is showing great promise to become a universal means for the set up of nonlinear finite elements. As in the linear case also here all the numerically integrated finite elements are expressed in terms of few numerical vectors and matrices and in a form convenient for standard assembly and use in the Newton-Raphson method.

Detailed derivation and actual computation is included in this paper for the element gradient and stiffness matrices of the largely deformed beam, ring, circular plate and rubber membrane.

2. BEAM AND RING

Our starting point for the unit elasticity [8], shown in Fig. 1, is its total potential energy

$$\pi(\psi) = \int_0^1 \left(\frac{1}{2} EI (\psi'^2 - \psi \sin \theta + 0 \cos \theta)^2 + P \sin \theta + 0 \cos \theta \right) ds = M(1) \quad (2.1)$$

for which the admissible ψ is continuous and satisfies the fixed end condition $\psi(0)=0$.

Initial curvature in the form $\psi = \psi(s)$ alters the total potential energy of (2.1) into

$$\pi(\psi) = \int_0^1 \left(\frac{1}{2} EI (\psi'^2 - \psi \sin \theta + 0 \cos \theta)^2 + P \sin \theta + 0 \cos \theta \right) ds \quad (2.2)$$

where the end moment M is assumed absent. After integration by parts

FOLLOWING

Reproduced from
best available copy.

PAGE'S

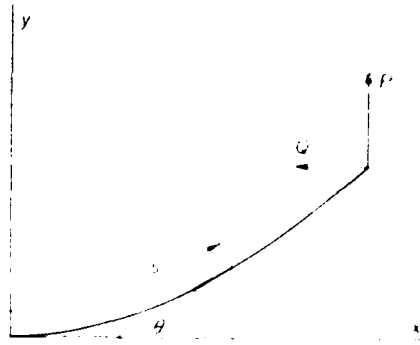


FIG. 1. Tip loaded elastica.

$$\pi(v) = \int_0^1 \left(\frac{1}{2} EI v'^2 + EI^{\frac{1}{2}} v'' \right) ds - Ps \sin v + q \cos v ds - EI^{\frac{1}{2}}(1) - C_1 \quad (2.3)$$

and for the circular ring $v'' = 0$ so that

$$\pi(v) = \int_0^1 \left(\frac{1}{2} EI v'^2 - Ps \sin v + q \cos v \right) ds - EI^{\frac{1}{2}}(1) - C_1 \quad (2.4)$$

as for the straight elastica with an end moment $M = EI^{\frac{1}{2}}(1)$.

Through the use of $x' \cos v$ and $y' \sin v$ we may write the total potential energy in terms of v as

$$\pi(v) = \int_0^1 \left(\frac{1}{2} EI \frac{y'^2}{1-v'^2} + q(1-v')^{\frac{1}{2}} \right) ds - Pv(1) \quad (2.5)$$

where the admissible y is C^1 and satisfies the fixed end conditions $y(0) = y'(0) = 0$.

We propose a finite element discretization of $\pi(v)$ in (2.1) with a quadratic interpolation of v over each element and a two-point Gauss quadrature of the total potential energy. This minimal integration scheme assures the numerical stability of the finite element method and is sufficiently accurate. The resulting quadratic element is precise, efficient and easily programmable.

Interpolation of v over the three-nodal-point element is compactly expressed by $v^{(e)}_{n,e}$ where $v^{(e)}_{n,e} = [v_1, v_2, v_3]$ is the element nodal values vector, and

$$v^{(e)} = \left\{ \frac{1}{3}(C-1), 1-\frac{2}{3}, \frac{1}{3}(C+1) \right\} \quad (e=1, 2) \quad (2.6)$$

the shape functions vector.

Let the typical element be of size h such that $ds = \frac{1}{2}hd\zeta$ and $\pi_e = 2h^{-1}\zeta$, where $(\cdot) = d/d\zeta$. Two Gauss point integration of $\pi(\zeta)$ in (2.1) over the e th element results in the approximation

$$\pi_e = \frac{1}{2}h \sum_{j=1}^2 4h^{-1}\zeta_j^2 - P \sin \zeta_j + Q \cos \zeta_j \quad (2.7)$$

in which the index $j=1,2$ refers to the Gauss points $\zeta_1 = -\sqrt{3}/3$ and $\zeta_2 = \sqrt{3}/3$. The values of P and Q at the j th Gauss point are computed from $\dot{\zeta}_j = u_e \dot{x}_j$ and $\ddot{\zeta}_j = u_e \ddot{x}_j$, where $\dot{x}_j = \dot{x}(\zeta_j)$ and $\ddot{x}_j = \ddot{x}(\zeta_j)$, and from (2.6) we have that

$$\begin{aligned} \dot{\zeta}_{1,2} &= \frac{1}{6}(1+\sqrt{3}, 4, 1+\sqrt{3}) \\ \dot{\zeta}_{1,2} &= \frac{1}{6}(+2\sqrt{3}-3, +4\sqrt{3}, +2\sqrt{3}+3) \end{aligned} \quad (2.8)$$

where the upper sign of $\sqrt{3}$ belongs to $j=1$ and the lower to $j=2$.

From π_e in (2.7) we derive the element gradient vector

$$g_e = \frac{d\pi_e}{du_e} = \sum_{j=1}^2 2h^{-1}\zeta_j \dot{\zeta}_j + \frac{1}{2}h(P \cos \zeta_j + Q \sin \zeta_j) \ddot{\zeta}_j \quad (2.9)$$

and the element stiffness matrix

$$k_e = \frac{u_e}{m_e} = \frac{2\pi_e}{m_e} = \sum_{j=1}^2 2h^{-1}\zeta_j \dot{\zeta}_j + \frac{1}{2}h(Q \cos \zeta_j - P \sin \zeta_j) \ddot{\zeta}_j \quad (2.10)$$

where

$$i_1 \dot{\zeta}_1 + i_2 \dot{\zeta}_2 = \frac{1}{6} \begin{bmatrix} 7 & -8 & 1 \\ -8 & 16 & -8 \\ 1 & -8 & 7 \end{bmatrix}, \quad i_1 \ddot{\zeta}_1 = \frac{1}{18} \begin{bmatrix} 24\sqrt{3} & 2(1+\sqrt{3}) & -1 \\ 2(1+\sqrt{3}) & 8 & 2(1-\sqrt{3}) \\ -1 & 2(1-\sqrt{3}) & 2-\sqrt{3} \end{bmatrix},$$

$$i_2 \ddot{\zeta}_2 = \frac{1}{18} \begin{bmatrix} 2-\sqrt{3} & 2(1-\sqrt{3}) & 1 \\ 2(1-\sqrt{3}) & 8 & 2(1+\sqrt{3}) \\ -1 & 2(1+\sqrt{3}) & 2+\sqrt{3} \end{bmatrix} \quad (2.11)$$

After \mathbf{g}_e and \mathbf{k}_e are prepared, the finite element assembly and solution procedure follows for the nonlinear case precisely as for the linear. An initial guess \mathbf{u}_0 is made for the global slopes vector \mathbf{u} , all \mathbf{g}_e and \mathbf{k}_e are computed from it and routinely assembled into the global \mathbf{g} and \mathbf{k} ; the essential boundary conditions and boundary work terms are included in \mathbf{g} and \mathbf{k} ; and \mathbf{u}_0 is improved into \mathbf{u}_1 with the Newton-Raphson method
 $\mathbf{u}_1 = \mathbf{u}_0 + \mathbf{E}_0^{-1} \mathbf{g}_0$ until convergence.

To discretize $\pi_e(v)$ in (2.5) we propose a piecewise cubic, C^1 , interpolation of v with two Gauss point quadrature of the element total potential energy,

$$\text{Now } v = u_e^{[j]} \text{ at } s, \text{ where } u_e^{[j]} = (v_1, \dot{v}_1, v_2, \dot{v}_2)^T \text{ and} \\ \{s\} = \{1+3^{-2}i2^{-3}, -2^{-2}+3^{-2}, 3^{-2}-2^{-3}, -2^{-2}+3^{-3}\} \quad (2.12)$$

and the two Gauss points are at $s_1 = (-1+\sqrt{3})/6$ and $s_2 = (1+\sqrt{3})/6$ with equal weights $w_1 = w_2 = \frac{1}{2}$. Consequently the approximate element total potential energy (2.5) becomes

$$\pi_e = \frac{1}{3}h \sum_{j=1}^2 \left[\frac{1}{2}h^{-4} \ddot{y}_j (1-h^{-2}\dot{v}_j^2)^{-1} + q(1-h^{-2}\dot{v}_j^2) \right] \quad (2.13)$$

where $\ddot{y}_j = u_e^{[j]}|_{s_j}$, $\dot{v}_j = u_e^{[j]}|_{s_j}$ and

$$\begin{aligned} t_{1,2}^{[j]} &= (-1, -J/3, 1, +J/3) \\ t_{1,2}^{[1]} &= (\bar{t}/2\sqrt{3}, -1+\bar{t}/3, +2/\bar{t}, 1+\bar{t}/3) \end{aligned} \quad (2.14)$$

From π_e in (2.13) we get

$$\mathbf{g}_e = \frac{\partial \pi_e}{\partial \mathbf{u}_e} = \sum_{j=1}^2 a_j \frac{\ddot{v}_j}{\dot{v}_j^2} + b_j \frac{\dot{v}_j}{\dot{v}_j^2} \quad (2.15)$$

with

$$a_j = \frac{1}{2}h^{-3} \ddot{y}_j (1-h^{-2}\dot{v}_j^2)^{-1}, \quad b_j = \frac{1}{2}h^{-5} \ddot{y}_j \dot{v}_j (1-h^{-2}\dot{v}_j^2)^{-2} \quad (2.16)$$

and

$$\mathbf{k}_e = \frac{\partial \mathbf{g}_e}{\partial \mathbf{u}_e} = \frac{\partial^2 \pi_e}{\partial \mathbf{u}_e^2} = \sum_{j=1}^2 a_j \frac{\ddot{v}_j \ddot{v}_j^2}{\dot{v}_j^4} + b_j \left(\frac{\ddot{v}_j \ddot{v}_j^2}{\dot{v}_j^4} + \frac{\ddot{v}_j^2 \ddot{v}_j^2}{\dot{v}_j^4} \right) \quad (2.17)$$

with

$$\begin{aligned} a_j &= \frac{1}{2} h^{-3} (1-h^{-2} \dot{\psi}_j^2)^{-1}, \quad b_j = h^{-5} \dot{\psi}_j \ddot{\psi}_j (1-h^{-2} \dot{\psi}_j^2)^{-2} \\ c_j &= \frac{1}{2} h^{-5} \dot{\psi}_j (1-h^{-2} \dot{\psi}_j^2)^{-2} + 2h^{-7} \dot{\psi}_j^2 \ddot{\psi}_j (1-h^{-2} \dot{\psi}_j^2)^{-3} \\ &\quad - \frac{1}{2} h^{1-1} (1-h^{-2} \dot{\psi}_j^2)^{-\frac{1}{2}} + h^{-2} \dot{\psi}_j^2 (1-h^{-2} \dot{\psi}_j^2)^{-\frac{3}{2}} \end{aligned} \quad (2.18)$$

To observe the behavior of the discretization method in its computational realization we undertake the calculation of the bent elastica using (2.1) with $Q = 0$. For a tip force $P = 1.5$ the Newton-Raphson method successively computes a tip deflection $y(1) = 0.5000000, 0.437216, 0.4124599, 0.4109994, 0.4109928, 0.4109928$; having started with a zero initial sag.

When P is increased above 1.5 the Newton-Raphson method suddenly fails to converge from a zero initial guess. A better starting shape is needed then for the iterative solution, or the deflection under higher loads can be reached stepwise with the computed solution at the end of the previous step serving as an initial guess for the next iteration with the higher load. One is thus confronted with the choice of small load increments with fewer iterative corrections-an incremental method, or large load increments with more corrections-a global method. In the presence of multiple solutions to the stiffness equation $g(u)=0$, the load history of the incremental method is what determines which one of them will be discovered, while the solution reached with the global method is determined by the initial guess u_0 .

To disclose the discretization accuracy of the element in (2.15)-(2.18) a varying number, N_e , of elements are employed in the computation of cantilever deflected by $P = 5$. For $N_e = 1, 2, 3, \dots, 9$ we, respectively, compute $y(1) = 0.7669329, 0.7183933, 0.7143314, 0.7140374, 0.7139174, 0.7138622, 0.7138340, 0.7138185$ and extrapolation to the limit provides the estimate error in $y(1) = 0.1N_e^{-3.75}$.

Solving the same cantilever problem with the element given in (2.9) and (2.10) we get for $N_e = 3, 4, 5, 6, 7$ the corresponding tip slopes $\dot{y}(1) = 1.2149992, 1.2152510, 1.2153196, 1.2153444, 1.2153549$; and with extrapolation to the limit we reach the estimate error in $\dot{y}(1) = 0.03N_e^{-4}$.

A seven element discretization of the elastica with the element data in (2.9) and (2.10) computes the stable and unstable equilibrium configurations [4] shown in Figs. 2, 3 and 4. Figure

2 shows the shapes the cantilever assumes when the tip is forced by $P = 0.5, 1.0, 1.5, \dots, 9.0$. All eigenvalues of the global stiffness matrix are positive here and the equilibrium configurations shown in Fig. 2 are concluded to be stable. Figure 3 depicts other possible stable equilibrium states for $P = 10.5, 12.0, \dots, 24.0$. The elastica equilibrium configurations shown in Fig. 4 for a tip load $P = 14, 15, \dots, 29$ are unstable; the lowest eigenvalue of K being negative.

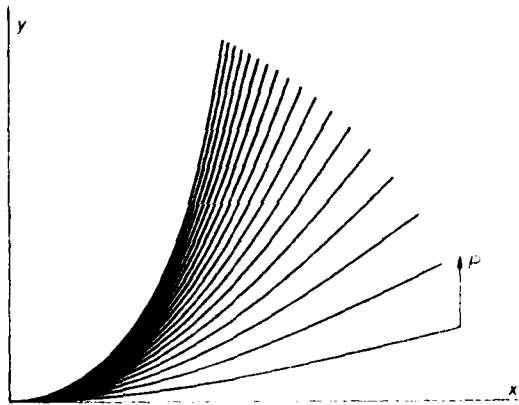


FIG. 2. Stable equilibrium states of elastica.

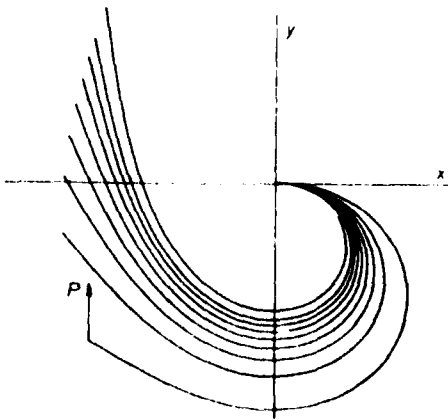


FIG. 3. Other stable equilibrium states of elastica.

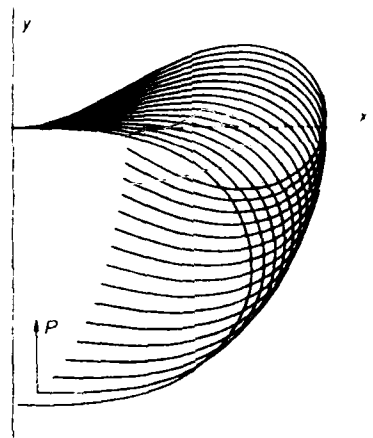


FIG. 4. Unstable equilibrium states of elastica.

Figures 5 and 6 show a similar computation for the circular ring. Figure 5 follows the opening of a C-spring [9] with a force $Q = 1, 2, \dots, 10$; while Fig. 6 follows the compression of a circular ring [5] squeezed by equal and opposite forces P .

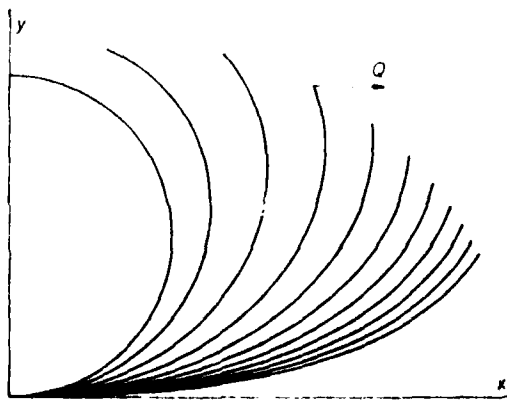


FIG. 5. Forcing of a circular C-spring.

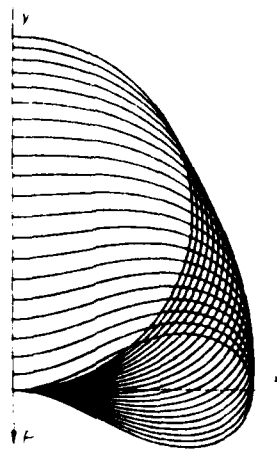


FIG. 6. Squeezing of a circular ring.

3. CIRCULAR PLATE

A unit circular plate ($r < 1$) is highly bent [11] under the action of an axisymmetrically distributed lateral load t and a uniform edge compression p . The total potential energy of this plate reads

$$\begin{aligned} \pi(u, w) = & \frac{1}{2} \int_0^1 \left(\frac{1}{12} (w')^2 + \frac{w'^2}{r^2} \right) + \frac{u^2}{r^2} r dr + \\ & \frac{1}{2} \int_0^1 (u' + \frac{1}{2} w'^2)^2 r dr - \int_0^1 t w r dr + p u(1) \end{aligned} \quad (3.1)$$

where u and w denote the inplane and lateral displacements, respectively, and where $(\cdot)' = d/dr$.

We propose to discretize $\pi(u, w)$ with a C^1 piecewise cubic interpolation of w , a piecewise quadratic interpolation of u , and a two Gauss point integration of the total potential energy over each element. A linear interpolation scheme for u is noticed to produce a decidedly inferior element.

Typically an element extends between $r=r_1$ and $r=r_3$, has three nodal points and is associated with the element nodal values vector $u_e = [u_1, w_1, \dot{w}_1, u_2, u_3, w_3, \dot{w}_3]$. Interpolation of u and w inside the element is formally written as $u = u_e(\cdot)$ and $w = w_e(\cdot)$ with

$$\begin{aligned}\underline{\varphi}^i &= \left\{ \frac{1}{2}\xi(\xi-1), 0, 0, 1-\xi^2, \frac{1}{2}\xi(\xi+1), 0, 0 \right\} \\ \underline{\varphi}^t &= \frac{1}{4}\{0, 2-3\xi+\xi^3, 1-\xi-\xi^2+\xi^3, 0, 0, 2+3\xi-\xi^3, -1-\xi+\xi^2+\xi^3\}\end{aligned}\quad (3.2)$$

where $-1 \leq \xi \leq 1$.

A two point Gauss integration produces from (3.1) the approximate

$$\begin{aligned}\pi_e &= \sum_{j=1}^2 \frac{1}{3} h^{-3} r_j \dot{w}_j^2 + \frac{1}{12} r_j^{-1} h^{-1} \ddot{w}_j^2 + \frac{1}{4} h r_j^{-1} u_j^2 \\ &\quad + h^{-3} (h \dot{u}_j + \dot{w}_j^2)^2 r_j - \frac{1}{2} h r_j f_j w_j\end{aligned}\quad (3.3)$$

for which the values of u_j , w_j , \dot{u}_j , \dot{w}_j and \ddot{w}_j are computed from $u_j = u_e^j$, $w_j = w_e^j$, $\dot{u}_j = \dot{u}_e^j$, $\dot{w}_j = \dot{w}_e^j$, and $\ddot{w}_j = \ddot{w}_e^j$, with the aid of the numerical vectors

$$\begin{aligned}\dot{u}_{1,2}^i &= \frac{1}{6}(1+\sqrt{3}, 0, 0, 4, 1+\sqrt{3}, 0, 0) \\ \dot{u}_{1,2}^t &= \frac{1}{6}(+2\sqrt{3}-3, 0, 0, +4\sqrt{3}, +2\sqrt{3}+3, 0, 0) \\ \dot{w}_{1,2}^i &= \frac{1}{18}(0, 9+4\sqrt{3}, 3+\sqrt{3}, 0, 0, 9+4\sqrt{3}, -3+\sqrt{3}) \\ \dot{w}_{1,2}^t &= \frac{1}{6}(0, -3, +\sqrt{3}, 0, 0, 3, +\sqrt{3}) \\ \ddot{w}_{1,2}^i &= \frac{1}{2}(0, +\sqrt{3}, -1+\sqrt{3}, 0, 0, +\sqrt{3}, 1+\sqrt{3})\end{aligned}\quad (3.4)$$

From (3.3) we produce

$$g_e = \frac{\pi_e}{u_e} = \sum_{j=1}^2 a_j \dot{u}_j + b_j \dot{w}_j + c_j \ddot{w}_j + d_j \dot{u}_j^2 + e_j \dot{w}_j^2 \quad (3.5)$$

with

$$\begin{aligned}a_j &= \frac{2}{3} h^{-3} r_j \dot{w}_j, \quad b_j = \frac{1}{6} h^{-1} r_j^{-1} \dot{w}_j + 4h^{-3} r_j w_j (h \dot{u}_j + \dot{w}_j^2) \\ r_j &= -\frac{1}{2} h r_j f_j, \quad d_j = 2h^{-2} r_j (h \dot{u}_j + \dot{w}_j^2), \quad e_j = \frac{1}{2} h r_j^{-1} u_j\end{aligned}\quad (3.6)$$

and

$$k_e = \frac{\partial g_e}{\partial u_e} = \frac{\partial^2 \pi_e}{\partial^2 u_e} = \sum_{j=1}^2 a_j \dot{\psi}_j \dot{\phi}_j + b_j \ddot{\psi}_j \dot{\phi}_j + c_j (\dot{\psi}_j \ddot{\phi}_j + \ddot{\psi}_j \dot{\phi}_j) + d_j \dot{\phi}_j \dot{\phi}_j + e_j \ddot{\psi}_j \dot{\phi}_j \quad (3.7)$$

with

$$\begin{aligned} a_j &= \frac{2}{3} h^{-3} r_j, \quad b_j = \frac{1}{6} h^{-1} r_j^{-1} + 12 h^{-3} r_j \dot{w}_j^2 + 4 h^{-2} r_j \dot{u}_j \\ c_j &= 4 h^{-2} r_j \dot{w}_j, \quad d_j = 2 h^{-1} r_j, \quad e_j = \frac{1}{2} h r_j^{-1} \end{aligned} \quad (3.8)$$

To assess the performance of our element we use it to compute the deflection of the uniformly loaded (i.e. $f=\text{const.}$), clamped (i.e. $w(l)=w'(l)=0$) plate with an immovable (i.e. $u(l)=0$) edge. For $f = 10$ we compute, with $N_e=2, 3, \dots, 7$, a central deflection $w(0)=1.138993, 1.140754, 1.141714, 1.142070, 1.142220, 1.142293$; meaning a relative error in $w(0)$ equal to $0.068 N_e^{-3.3}$. A Newton-Raphson solution of the nonlinear stiffness equation for $f = 10$ and $N_e = 7$ successively comes up with $w(0)=1.874962, 1.394681, 1.182066, 1.143467, 1.142294, 1.142293$, having started with a zero deflection.

The critical thrust for the plate is given by $p_{cr} = \alpha^2 / 12$ where $\alpha^2 = 3.39$ is the first root of Bessel's function equation $J_1(\alpha) = 0$. Figure 7 traces the computed central deflection of a simply supported plate bent under the combined action [3,10] of a lateral load f and an edge thrust p that exceeds p_{cr} . When $f = 0$ the unstable trivial solution $w = 0$ for $p > p_{cr}$ is absent and a zero initial deflection can be chosen for the Newton-Raphson method. When $f = 0$ the Newton-Raphson method must start with a nonzero initial guess but proceeds otherwise as before to produce the typical bifurcation curve in Fig. 7.

Close to a critical point at which K^{-1} is non computable, the condition of K declines and the Newton-Raphson method slows down. It is our experience, though, that by using higher precision computations and more corrective iterations one can get as close as it is only numerically meaningful to such a point.

4. RUBBER MEMBRANE

Let the generating curve of the undeformed axisymmetric membrane be given in the (r, z) plane through $r=r(s)$ and $z=z(s)$, s being the arc length. Under the action of applied forces and prescribed displacements the point (r, z) moves to the deformed location (x, y) . An arc element ds is stretched thereby to ds'

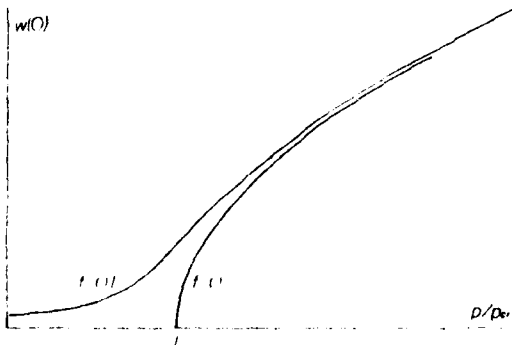


FIG. 7. Face and edge forced circular plate.

and the thickness t of the membrane is reduced to \bar{t} .

The energy density function of the membrane is ultimately expressed in terms of the three principal stretch ratios

$$\lambda_1 = \frac{ds}{ds} , \quad \lambda_2 = \frac{2\pi x}{2\pi r} , \quad \lambda_3 = \frac{t}{\bar{t}} \quad (4.1)$$

and if the deformation is incompressible $\lambda_1 \lambda_2 \lambda_3 = 1$. With $ds = (\sqrt{x'^2 + y'^2})^{1/2}$ the stretch ratios become

$$\lambda_1 = (x'^2 + y'^2)^{1/2} , \quad \lambda_2 = \frac{x}{r} , \quad \lambda_3 = \frac{1}{\sqrt{\lambda_1 \lambda_2}} \quad (4.2)$$

where $(\cdot)' = d/ds$.

Assuming a membrane made of Mooney material its total potential energy acquires the form

$$\pi(x, y) = 2\pi\mu t \int_0^s [(\lambda_1 - 3) + (\lambda_2 - 3)] ds + \frac{1}{2} \frac{p}{\mu t} \int_0^s x^2 y' ds \quad (4.3)$$

where p is the pressure, μ and t material constants, and where λ_1 and λ_2 are the strain invariants

$$\begin{aligned} \lambda_1 &= \lambda_1^2 + \lambda_2^2 + \lambda_3^2 \\ \lambda_2 &= \lambda_1^2 \lambda_2 + \lambda_2^2 \lambda_3 + \lambda_3^2 \lambda_1 \end{aligned} \quad (4.4)$$

with $\lambda_3 = 1/\lambda_1 \lambda_2$. From here on we replace $p/\mu t$ by p and assume that $2\pi\mu t = 1$.

We propose to discretize $\pi(x, y)$ with a quadratic-quadratic interpolation of x and y over the element and a two Gauss point quadrature of the element total potential energy. Inside each element $x = u_e^j$ and $y = v_e^j$, where $u_e^j = [x_1, v_1, x_2, v_2, x_3, v_3]$ and

$$\begin{aligned} \xi &= \left\{ \frac{1}{2}(-1), 0, 1 \right\}^T, 0, \frac{1}{2}(-1), 0 \\ \eta &= \left\{ 0, \frac{1}{2}(-1), 0, 1 \right\}^T, 0, \frac{1}{2}(-1) \end{aligned} \quad (4.5)$$

We shall need the Gauss point values $x_j = u_e^{j,j}$, $v_j = v_e^{j,j}$, $\dot{x}_j = u_e^{j,j+1}$ and $\dot{y}_j = v_e^{j,j+1}$, computed from u_e and

$$\begin{aligned} \xi_{1,2} &= \frac{1}{6} \{1 + \sqrt{3}, 0, 4, 0, 1 - \sqrt{3}, 0\} \\ \xi_{1,2} &= \frac{1}{6} \{+2\sqrt{3}-3, 0, +4\sqrt{3}, 0, +2\sqrt{3}+3, 0\} \\ \xi_{1,2} &= \frac{1}{6} \{0, +2\sqrt{3}-3, 0, +4\sqrt{3}, 0, +2\sqrt{3}+3\} \end{aligned} \quad (4.6)$$

as before.

The element total potential energy is written as the sum

$$\pi_e = J_1 + J_2 + J_3 + (J_4 + J_5 + J_6) + \frac{1}{2} p J_7 \quad (4.7)$$

of the seven approximate integrals

$$\begin{aligned} J_1 &= \int_e \lambda_1^2 r ds = h^{-1} \sum_{j=1}^2 r_j (\dot{x}_j^2 + \dot{y}_j^2) \\ J_2 &= \int_e \lambda_2^2 r ds = h^{-1} \sum_{j=1}^2 r_j^{-1} x_j^2 \\ J_3 &= \int_e \lambda_1^{-2} \lambda_2^{-2} r ds = h^2 \sum_{j=1}^2 r_j^3 x_j^{-2} (\dot{x}_j^2 + \dot{y}_j^2)^{-1} \\ J_4 &= \int_e \lambda_1^2 \lambda_2^2 r ds = h^{-1} \sum_{j=1}^2 r_j^{-1} x_j^2 (\dot{x}_j^2 + \dot{y}_j^2) \end{aligned} \quad (4.8)$$

$$\begin{aligned} I_5 &= \int_{\epsilon}^r r^2 r ds + h^3 \sum_{j=1}^2 r_j (x_j^2 + y_j^2)^{-1} \\ I_6 &= \int_{\epsilon}^r r^2 r ds + h \sum_{j=1}^2 r_j^{3/2} \\ I_7 &= \int_{\epsilon}^r x^2 y' ds - \sum_{j=1}^2 x_j^2 y_j^2 \end{aligned}$$

Repeated differentiation of π_e with respect to u_e furnishes

$$\frac{\partial \pi_e}{\partial u_e} = \sum_{j=1}^2 a_j \left[\frac{1}{j} b_j^{-1} + c_j^{-1} \right] \quad (4.9)$$

with

$$\begin{aligned} a_j &= 2r_j x'_j (1 + \frac{x'^2}{1_j} + \frac{x'^2}{2_j}) (1 + \frac{y'^2}{1_j} + \frac{y'^2}{2_j}) \\ b_j &= 2r_j y'_j (1 + \frac{x'^2}{1_j} + \frac{x'^2}{2_j}) (1 + \frac{y'^2}{1_j} + \frac{y'^2}{2_j}) + \frac{1}{2} p x_j^2 \\ c_j &= 2h \frac{1}{2_j} (1 + \frac{x'^2}{1_j} + \frac{x'^2}{2_j}) (1 + \frac{y'^2}{1_j} + \frac{y'^2}{2_j}) + h p x_j y'_j \end{aligned} \quad (4.10)$$

and

$$\begin{aligned} \frac{\partial^2 \pi_e}{\partial u_e^2} &= \frac{\partial^2 \pi_e}{\partial u_e^2} = \sum_{j=1}^2 a_j \left[\frac{1}{j} b_j^{-1} + c_j^{-1} \right] - \left(\frac{1}{j} b_j^{-1} + c_j^{-1} \right) \\ &\quad + d_j \left(\frac{1}{j} b_j^{-1} + c_j^{-1} \right) + e_j \left(\frac{1}{j} b_j^{-1} + c_j^{-1} \right) \quad (4.11) \\ &\quad + f_j \left(\frac{1}{j} b_j^{-1} + c_j^{-1} \right) \end{aligned}$$

with

$$\begin{aligned}
 a_j &= 2h^{-1}r_j(1 - \frac{x_j^2 + 3y_j^2}{2} + \frac{1}{6})\left(1 + \frac{2}{1-j}\right) \\
 b_j &= 2h^{-1}r_j(1 - \frac{x_j^2 + 3y_j^2}{2} + \frac{1}{6})\left(1 + \frac{2}{1+j}\right) \\
 c_j &= 2hr_j^{-1}(1 + \frac{-2}{1-j} + \frac{-4}{2j})(1 + \frac{2}{1+j}) + hp\psi_j' \quad (4.12) \\
 d_j &= 4x_j^2\frac{1}{2j}(1 + \frac{-4}{1-j} + \frac{-4}{2j}) \\
 e_j &= 4y_j^2\frac{1}{2j}(1 + \frac{-4}{1-j} + \frac{-4}{2j}) + px_j \\
 f_j &= 8h^{-1}r_jx_j^2y_j^2\frac{1}{1-j}\frac{-2}{2j}(1 + \frac{2}{1+j})
 \end{aligned}$$

Our first application of the rubber membrane element is to compute the inflated shape (11) of a unit disc ($\epsilon = 0.1$) for a pressure $p = 5$ and an inplane stretching of the edge to $x(1) = 1.1$. The disc is substantially deformed by this high pressure, and for a uniform layout of N_e finite elements we compute, corresponding to $N_e = 1, 2, 3, 4, 10$, a polar rise $y(0) = 1.2546$, 1.4278, 1.4299, 1.4304, 1.4304. We reach this last value of $y(0)$ with the Newton-Raphson scheme that successively computes $y(0) = 2.31875$, 1.44782, 1.44302, 1.43059, 1.43040, 1.43040.

Figure 8 shows inflated shapes of the disc for a pressure $p = 1, 2, \dots, 7$. Corresponding to these pressures are the polar stretch ratios $\lambda_0 = 1.144, 1.233, 1.375, 1.648, 2.430, 4.625, 6.552$. The global stiffness matrix K is found to be positive definite for the shapes in Fig. 8 and we conclude that the disc is in stable equilibrium.

Figure 9 shows a torus (6) ($\epsilon = 0.25$), generated by $r = 2 + \cos s$, $z = \sin s$ $0 \leq s \leq \pi$, inflated by a pressure that increases in ten equal steps from $p = 0$ to a critical $p = 2.185$. As the pressure approaches this last value of p the lowest eigenvalue of the global stiffness matrix K nears zero indicating a decline in stability.

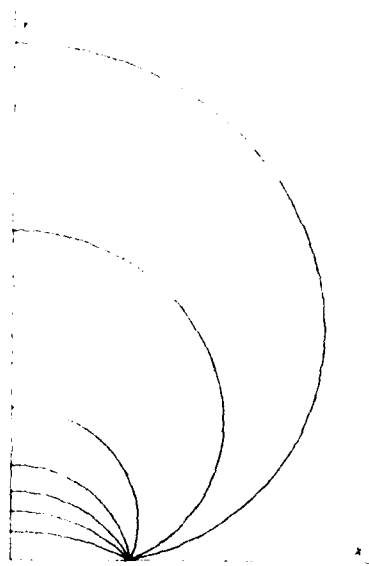


FIG. 8. Stretched and inflated disc.

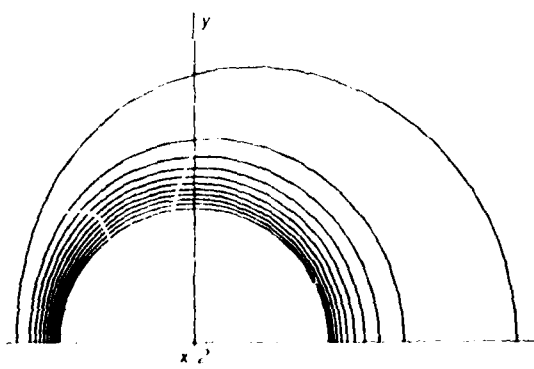


FIG. 9. Inflated torus.

Figure 10 shows bulging [6] of a tube ($C = 0$), stretched both axially and circumferentially, and inflated. The curves in Fig. 10 are for a pressure that increases in ten equal steps from $p = 0$ to the critical $p = 0.95$.

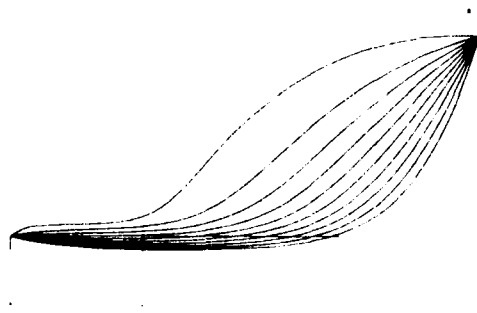


FIG. 10. Bulging of stretched and inflated tube.

ACKNOWLEDGEMENT

The results of this paper were obtained with the support of the Office of Naval Research, under contract: ONR-N0014-76C-036.

REFERENCES

1. ADKINS, J.E., and RIVLIN, R.S., Large Elastic Deformations of Isotropic Materials. II: the Deformation of Thin Shells, *J. Mech. Phys. Solids*, Section A, 30(6):511 (1962).
2. FRIED, I., *Large Elastic Deformations of Isotropic Materials*, Academic Press, New York (1979).
3. FRIEDRICHSS, E.O., and STOKER, J.J., Buckling of the Circular Plate Beyond the Critical Bifurcation, *J. Math. Anal. Appl.*, 9, 47-63 (1965).
4. FRISCH-FAY, R., *Elasticity Theory*, Butterworth, London (1962).
5. FRISCH-FAY, R., The Deformation of Elastic Circular Rings, *Trans. Roy. Inst. Tech. Stockholm*, 11, 329-340 (1960).
6. HYDONIERS, A.D., and SPENCER, A.L.M., The Finite Inflation of an Elastic Toroidal Membrane of Circular Cross Section, *Proc. Roy. Soc. (London)*, 15, 367-391 (1967).

AD-A138 468

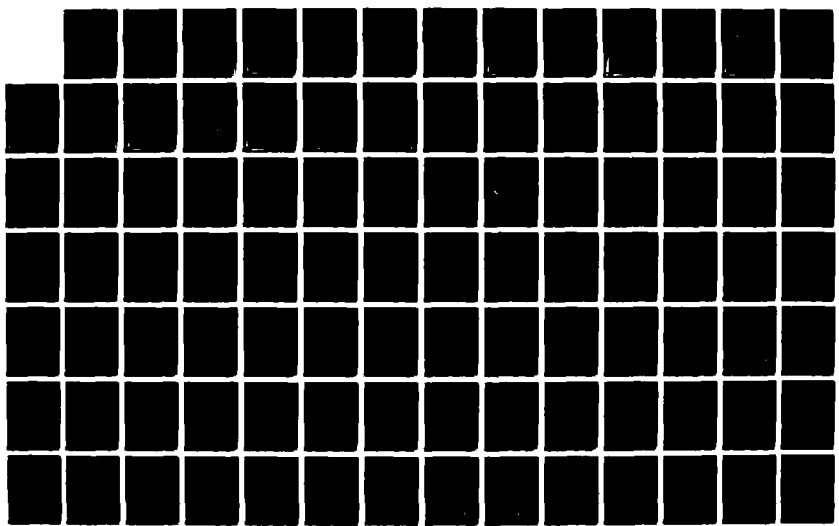
LINEAR AND NONLINEAR FINITE ELEMENTS(U) BOSTON UNIV MA
DEPT OF MATHEMATICS I FRIED DEC 83 BU-1-84
N00014-76-C-0036

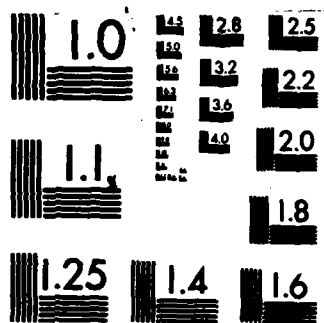
23

UNCLASSIFIED

F/G 12/1

NL





MICROCOPY RESOLUTION TEST CHART
NATIONAL BUREAU OF STANDARDS-1963-A

7. KYDONIADIS, A.D. and SPENCER, A.J.M., Finite Axisymmetric Deformation of an Initially Cylindrical Elastic Membrane. *Quart. J. Mech. Appl. Math.* 20, 88-95 (1969).
8. LOVE, A.E., *A Treatise on the Mathematical Theory of Elasticity*. Chapters 18 and 19, Dover Publications, New York (1944).
9. SHINOHARA, A. and HARA, M. Large Deflection of a Circular C-shaped spring. *Int. J. Nonlinear Mech.* 8, 169-178 (1973).
10. TANI, J., Elastic Instability of an Annular Plate Under Uniform Compression and Lateral Pressure. *J. Appl. Mech.* 47, 591-594 (1980).
11. TIMOSHENKO, S. and WOJNORSKY-KRIEGER, S. *Theory of Plates and Shells*. McGraw-Hill Book Co., New York (1959).

NONLINEAR FINITE ELEMENT COMPUTATION OF THE
EQUILIBRIUM, STABILITY AND MOTION OF THE
EXTENSIONAL BEAM AND RING*

Isaac FRIED

Boston University, Department of Mathematics, Boston, MA 02215, U.S.A.

Received 6 August 1981

Revised manuscript received 11 October 1982

Discrete Gauss integration of the element total potential energy is applied to the formation of a cubic-cubic C^1 extensible completely nonlinear curved beam finite element. The versatility, accuracy, effectiveness, and robustness of the element, and the Newton-Raphson technique used to solve the nonlinear algebraic stiffness equation set up with it is numerically demonstrated by computations of the nonlinear equilibrium stability and motion of beams and rings.

1. Introduction

A nonlinear finite element discretization technique based on the approximate Gauss integration of a nonquadratic energy density function, successful in the nonlinear computation [1] of the straight and curved inextensible elastica, the circular plate, and the axisymmetric rubber membrane, is applied here to nonlinear equilibrium stability and motion analysis of the extensible curved beam.

A cubic-cubic C^1 element is developed in detail (a numerically integrated cubic-cubic beam element for large displacements is available in the MARC program [2]) and is computationally tested for accuracy and effectiveness on the particular large displacement problems of a tip loaded straight beam, a closed ring compressed by two equal and opposite forces, a circular ring under post critical hydrostatic pressure, and the large amplitude vibrations of free and fixed beams and rings.

2. Finite element

With reference to Fig. 1 let a point on the deflected beam be marked by (x, y) , $x = x(s)$ and $y = y(s)$, s being the distance measure along the original curved beam. Let further ϵ denote the axial strain and κ the curvature of deflected beam. Then in terms of x and y

$$\epsilon = (x'^2 + y'^2)^{1/2} - 1 \quad (1)$$

and

$$\kappa = \frac{x'y'' - y'x''}{(x'^2 + y'^2)^{3/2}} \quad (2)$$

*Work supported by the Office of Naval Research with contract N00014-76-C-0036.

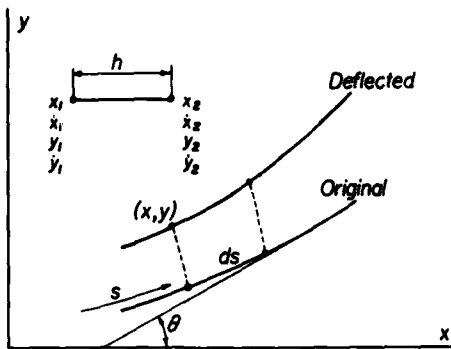


Fig. 1. Geometry and element of a largely bent beam.

with the usual notation $x' = dx/ds$ and $x'' = d^2x/ds^2$. The initial curvature of the beam is expressed in terms of the original slope θ as $\kappa_0 = d\theta/ds$.

A bent and stretched elastic beam of length l that is under the action of distributed forces f and g in the x and y direction, respectively, is in possession of a total potential energy

$$\pi(x, y) = \frac{1}{2} EI \int_0^l (\kappa - \kappa_0)^2 ds + \frac{1}{2} EA \int_0^l \epsilon^2 ds - \int_0^l (fx + gy) ds \quad (3)$$

or when the beam is of thickness t and unit width

$$\pi(x, y) = \frac{1}{12} Et^3 \left[\frac{1}{2} \int_0^l (\kappa - \kappa_0)^2 ds + \frac{1}{2} c \int_0^l \epsilon^2 ds \right] - \int_0^l (fx + gy) ds \quad (4)$$

where $c = 12/t^2$. Hence forward we shall assume, for typographical brevity, that $Et^3/12 = 1$.

For the approximation of $\pi(x, y)$ in (4) we propose a C^1 cubic-cubic finite element and a three Gauss point integration, which appears to be the minimal integration scheme to maintain the full element accuracy inherent in the cubic interpolation, while averting spurious zero energy modes. We shall also consider in the paper the possibility of integrating the axial strain energy part of $\pi(x, y)$ with only two Gauss points, but it appears that an all out three point integration of $\pi(x, y)$ is preferred.

To prepare for the numerical integration the typical finite element is mapped from s to ξ by $s = s_1 + h\xi$, $0 \leq \xi \leq 1$, so that $ds = h d\xi$ and $(\cdot)' = h^{-1}(\cdot')$ and $(\cdot)'' = h^{-1}(\cdot'')$, where the dot means $d/d\xi$. From the element nodal values vector (see Fig. 1)

$$u_e^t = (x_1, \dot{x}_1, y_1, \dot{y}_1, x_2, \dot{x}_2, y_2, \dot{y}_2); \quad (5)$$

x and y are both cubically interpolated inside each element by

$$x = u_e^t \phi \quad \text{and} \quad y = u_e^t \psi, \quad (6)$$

ϕ and ψ being the shape function vectors

$$\phi^t = (\phi_1, \phi_2, 0, 0, \phi_3, \phi_4, 0, 0) \quad \text{and} \quad \psi^t = (0, 0, \phi_1, \phi_2, 0, 0, \phi_3, \phi_4) \quad (7)$$

in which

$$\phi_1 = 1 - 3\xi^2 + 2\xi^3, \quad \phi_2 = \xi - 2\xi^2 + \xi^3, \quad \phi_3 = 3\xi^2 - 2\xi^3, \quad \phi_4 = -\xi^2 + \xi^3. \quad (8)$$

Since the typical element extends between $\xi = 0$ and $\xi = 1$, and since $ds = h d\xi$, the approximate integration of the element total potential energy $\pi_e(x, y)$ is of the form

$$\pi_e = h \sum_{j=1}^3 w_j [\frac{1}{2}(\kappa_j - \kappa_{0j})^2 + \frac{1}{2}c\epsilon_j^2 - f_j x_j - g_j y_j] \quad (9)$$

where here, specifically,

$$w_1 = w_3 = \frac{5}{18}, \quad w_2 = \frac{8}{18} \quad (10)$$

with the three Gauss points G_1, G_2, G_3 being at

$$\xi_{1,3} = \frac{1}{10}(5 \mp \sqrt{15}) \quad \text{and} \quad \xi_2 = \frac{1}{2} \quad (11)$$

the upper sign of $\sqrt{15}$ referring to $j = 1$ and the lower sign of $\sqrt{15}$ referring to $j = 3$.

The integration point values of the curvature κ_j , the strain ϵ_j , and the coordinates x_j and y_j needed in π_e in (9) are obtained from the nodal values vector u_e through

$$\begin{aligned} x_j &= u_e^t \phi_j, & \dot{x}_j &= u_e^t \dot{\phi}_j, & \ddot{x}_j &= u_e^t \ddot{\phi}_j \\ y_j &= u_e^t \psi_j, & \dot{y}_j &= u_e^t \dot{\psi}_j, & \ddot{y}_j &= u_e^t \ddot{\psi}_j \end{aligned} \quad (12)$$

where ϕ_j stands briefly for $\phi(\xi_j)$, etc. Here, for the three-point Gauss integration we have from (6), (7), (8) and (11) that

$$\begin{aligned} \phi_{1,3}^t &= \frac{1}{100}(50 \pm 12\sqrt{15}, 5 \pm \sqrt{15}, 0, 0, 50 \mp 12\sqrt{15}, -5 \pm \sqrt{15}, 0, 0), \\ \phi_2^t &= \frac{1}{8}(4, 1, 0, 0, 4, -1, 0, 0), \\ \dot{\phi}_{1,3}^t &= \frac{1}{10}(-6, 2 \pm \sqrt{15}, 0, 0, 6, 2 \mp \sqrt{15}, 0, 0), \\ \dot{\phi}_2^t &= \frac{1}{4}(-6, -1, 0, 0, 6, -1, 0, 0), \\ \ddot{\phi}_{1,3}^t &= \frac{1}{3}(\mp 6\sqrt{15}, -5 \pm 3\sqrt{15}, 0, 0, \pm 6\sqrt{15}, 5 \mp 3\sqrt{15}, 0, 0), \\ \ddot{\phi}_2^t &= (0, -1, 0, 0, 0, 1, 0, 0) \end{aligned} \quad (13)$$

and

$$\begin{aligned} \psi_{1,3}^t &= \frac{1}{100}(0, 0, 50 \pm 12\sqrt{15}, 5 \pm \sqrt{15}, 0, 0, 50 \mp 12\sqrt{15}, -5 \pm \sqrt{15}), \\ \psi_2^t &= \frac{1}{8}(0, 0, 4, 1, 0, 0, 4, -1), \\ \dot{\psi}_{1,3}^t &= \frac{1}{10}(0, 0, -6, 2 \pm \sqrt{15}, 0, 0, 6, 2 \mp \sqrt{15}), \\ \dot{\psi}_2^t &= \frac{1}{4}(0, 0, -6, -1, 0, 0, 6, -1), \\ \ddot{\psi}_{1,3}^t &= \frac{1}{3}(0, 0, \mp 6\sqrt{15}, -5 \pm 3\sqrt{15}, 0, 0, \pm 6\sqrt{15}, 5 \mp 3\sqrt{15}), \\ \ddot{\psi}_2^t &= (0, 0, 0, -1, 0, 0, 0, 1). \end{aligned} \quad (14)$$

Differentiation of π_e in (9) with respect to the element vector of nodal values u_e creates the element gradient vector g_e . Further differentiation of g_e with respect to u_e generates the nonlinear element stiffness matrix k_e . Before doing that we shall introduce some notational abridgements. First we rewrite the axial strain ϵ and the curvature κ of the beam as

$$\epsilon = h^{-1}\beta^{1/2} - 1 \quad \text{and} \quad \kappa = \alpha\beta^{-3/2} \quad (15)$$

with (in fact for a nearly inextensible beam we may set $\beta = 1$ in κ)

$$\alpha = \dot{x}\ddot{y} - \ddot{x}\dot{y} \quad \text{and} \quad \beta = \dot{x}^2 + \dot{y}^2. \quad (16)$$

Secondly, we wish to employ in this section a prime to denote differentiation with respect to the vector u_e so that ϵ' and κ' are vectors, and ϵ'' , κ'' , $\epsilon'\epsilon''$ and $\kappa'\kappa''$ are matrices. Now, since $x'_j = \phi_j$ and $y'_j = \psi_j$,

$$\pi'_e = g_e = h \sum_{j=1}^3 w_j [(\kappa_j - \kappa_{0j})\kappa'_j + c\epsilon_j\epsilon'_j - f_j\phi_j - g_j\psi_j] \quad (17)$$

in which

$$\alpha'_j = \dot{x}_j\ddot{\psi}_j + \dot{\phi}_j\ddot{y}_j - \ddot{x}_j\dot{\psi}_j - \ddot{\phi}_j\dot{y}_j, \quad \beta_j = 2(\dot{x}_j\dot{\phi}_j + \dot{y}_j\dot{\psi}_j), \quad (18)$$

$$\kappa'_j = \beta_j^{-5/2}(\beta_j\alpha'_j - \frac{3}{2}\alpha_j\beta'_j) \quad (19)$$

and

$$\epsilon'_j = \frac{1}{2}h^{-1}\beta_j^{-1/2}\beta'_j. \quad (20)$$

Next we find that

$$\pi''_e = k_e = h \sum_{j=1}^3 w_j [(\kappa_j - \kappa_{0j})\kappa''_j + \kappa'_j\kappa''_j + c(\epsilon_j\epsilon''_j + \epsilon'_j\epsilon''_j)] \quad (21)$$

where, in terms of α_j and β_j ,

$$\epsilon''_j = \frac{1}{2}h^{-1}\beta_j^{-1/2}(\beta''_j - \frac{1}{2}\beta_j^{-1}\beta'_j\beta''_j) \quad (22)$$

and

$$\kappa''_j = \beta_j^{-7/2}[\beta_j^2\alpha''_j - \frac{3}{2}\alpha_j\beta_j\beta''_j - \frac{3}{2}\beta_j(\beta'_j\alpha''_j + \alpha'_j\beta''_j) + \frac{15}{4}\alpha_j\beta_j\beta'_j]. \quad (23)$$

both computed from

$$\alpha''_j = \dot{\phi}_j\ddot{\psi}_j + \dot{\psi}_j\dot{\phi}_j - \ddot{\phi}_j\dot{\psi}_j - \dot{\psi}_j\ddot{\phi}_j \quad (24)$$

and

$$\beta''_j = 2(\dot{\phi}_j\dot{\phi}'_j + \dot{\psi}_j\dot{\psi}'_j) \quad (25)$$

which are numerical symmetric matrices of dimension 8×8 .

Assembly of g_e and k_e into the global g and K is the same here as for linear finite elements except that an iterative method, say Newton-Raphson, is needed to solve the nonlinear discrete equation of equilibrium $g = 0$. With the Newton-Raphson method an initial guess u_0

is improved into

$$u_1 = u_0 - K_0^{-1} g_0, \quad (26)$$

etc., until convergence.

3. Tests for effectiveness

First to concern us is the accuracy of the element, occurrence of spurious modes devoid of energy, and the performance of the Newton-Raphson method in the presence of a large axial elastic constant c . We perform tests in this respect with two numerical integration schemes: one that integrates the bending part of the element total potential energy with three Gauss points, and the stretching part of π_e with two points (this will be referred to as the 3-2 scheme); and another procedure that integrates the entire π_e with three Gauss points (a 3-3 scheme). To start, we compute the deflection of an originally straight unit cantilever beam with a tip force $P = 5$, shown in Fig. 3, and imposed boundary conditions $x(0) = y(0) = y'(0) = 0$. Standard assembly of all the element stiffness matrices produces a global, displacement dependent, stiffness matrix that can be put in the form

$$K = K_b + cK_s \quad (27)$$

with K_b and K_s constituting the bending and stretching parts of K , respectively.

All subsequent computations are carried out with 7 and 14 element discretizations that give rise to 27 and 57 degrees of freedom, correspondingly. The 3-2 integration scheme is found to produce a K_s matrix with 15 zero eigenvalues for a 7 element discretization, and 29 zero eigenvalues for the 14 element discretization. Imposition of the boundary conditions $x(0) = y(0) = y'(0)$ still leaves the total global stiffness matrix K with one spurious zero eigenvalue in its straight configuration, which disappears with bending, and which does not seem to heap any difficulties upon the working of the Newton-Raphson method even with a straight ($x = s$, $y = 0$) initial guess. Table 1 lists the largest eigenvalue λ_N^k of the global stiffness matrix K as it varies with the number of elements N_e and the axial elastic constant c . Table 2 lists the tip coordinates $x(1)$ and $y(1)$ computed (with some 16 significant digits) with the Newton-Raphson method for different values of c .

Raising the integration scheme to a 3-3 level produces an element stiffness matrix k_e that assembles into a global K with a K_s part that has 14 zero eigenvalues for $N_e = 7$ and 28 zero eigenvalues for $N_e = 14$. No spurious zero eigenvalues occur anymore in the assembled and constrained K , the extremal eigenvalues of which are listed in Table 3 in their dependence upon N_e and c . Table 4 lists the computed tip coordinates $x(1)$ and $y(1)$ of the originally straight beam discretized with 3-3 integration elements and tip loaded with $P = 5$, as they become improved with the Newton-Raphson method, for different values of the axial elastic constant c , and a different number of finite elements N_e .

A remarkably propitious conclusion emerges from Tables 2 and 4: that the Newton-Raphson method is only slightly affected by the large values of c .

Table 1

Largest eigenvalue λ_N^K of K formed with 3-2 integration elements in its dependence upon the number of elements N_e and the axial elastic constant c

λ_N^K	$N_e = 7$			$N_e = 14$	
	$c = 10^3$	$c = 10^4$	$c = 10^5$	$c = 10^3$	$c = 10^5$
	0.27 10^5	0.27 10^6	0.27 10^7	0.55 10^7	

Table 2

Convergence of the tip coordinates $x(1)$ and $y(1)$ with the Newton-Raphson (NR) iterative cycles. Straight beam tip loaded with $P = 5$ and discretized with 3-2 integration elements

	$N_e = 7$				$N_e = 14$			
	$c = 10^3$		$c = 10^4$		$c = 10^5$		$c = 10^5$	
	$x(1)$	$y(1)$	$x(1)$	$y(1)$	$x(1)$	$y(1)$	$x(1)$	$y(1)$
1	1.0000000	1.6830084	1.0000000	1.6830084	1.0000000	1.6830084	1.0000000	1.6924615
2	0.55703212	0.77655095	0.55205671	0.77962496	0.55134776	0.78051978	0.54965834	0.78171462
3	0.61384381	0.72384822	0.61361089	0.72184756	0.61276418	0.72211633	0.61403859	0.72174536
4	0.61061737	0.71912615	0.60820549	0.71735096	0.60713127	0.71758132	0.60799521	0.71731317
5	0.61180749	0.71817148	0.61099979	0.71498461	0.61090756	0.71467798	0.61042256	0.71501707
6	0.61180735	0.71816995	0.61099710	0.71497673	0.61091337	0.71465933	0.61041886	0.71501085
7	0.61180735	0.71816995	0.61099714	0.71497671	0.61091606	0.71465766	0.61041902	0.71501073
8			0.61099714	0.71497671	0.61091606	0.71465766	0.61041902	0.71501073

Table 3

Lowest (1st) and highest (N th) eigenvalues λ_F^K and λ_N^K of the assembled global stiffness matrix K for the straight beam discretized with N_e 3-3 integration elements

λ_F^K	$N_e = 7$				$N_e = 14$			
	$c = 10^3$		$c = 10^4$		$c = 10^5$		$c = 10^5$	
	λ_N^K							
1.25	0.32 10^5	1.25	0.32 10^6	1.25	0.32 10^7	0.75	0.66 10^7	

Table 4

Convergence of the tip coordinates $x(1)$ and $y(1)$ with the Newton-Raphson (NR) iterative cycles. Straight beam tip loaded with $P = 5$, and discretized with 3-3 integration elements

	$N_e = 7$				$N_e = 14$			
	$c = 10^3$		$c = 10^4$		$c = 10^5$		$c = 10^6$	
	$x(1)$	$y(1)$	$x(1)$	$y(1)$	$x(1)$	$y(1)$	$x(1)$	$y(1)$
1	1.0000000	1.6651444	1.0000000	1.6651444	1.0000000	1.6651444	1.0000000	1.6636502
2	0.56022070	0.77453293	0.55526060	0.77770589	0.55452073	0.77870079	0.55478261	0.77847397
3	0.61529505	0.72278893	0.61557099	0.72053522	0.61541080	0.72053192	0.61594304	0.72015670
4	0.61221822	0.71820317	0.61007604	0.71628612	0.60969777	0.71624185	0.61019765	0.71596357
5	0.61335240	0.71729088	0.61260781	0.71402538	0.61297276	0.71312999	0.61251874	0.71374747
6	0.61335228	0.71728948	0.61260543	0.71401851	0.61296877	0.71311681	0.61261565	0.71374152
7	0.61335228	0.71728948	0.61260545	0.71401850	0.61296970	0.71311611	0.61251582	0.71374140
8			0.61260545	0.71401850	0.61296970	0.71311611	0.61251582	0.71374140
9							0.61237501	0.71378936

The (stable) equilibrium configuration computed for the tip loaded beam with the 3-2 integration scheme is shown in Fig. 2. Fig. 3 shows the computed curvature distribution $\kappa(s)$ for the same beam, and Fig. 4 shows the tension p along this beam computed from equilibrium considerations ($p = Py'$) and from Hook's law ($p = ce$). We remark in Fig. 3 that even though the elastically computed tension oscillates violently inside each element, at the two Gauss points G_1 and G_2 , at which the stretching energy is sampled, the statically and elastically computed tensions agree and are accurate to a degree that is sure to satisfy any practical requirement.

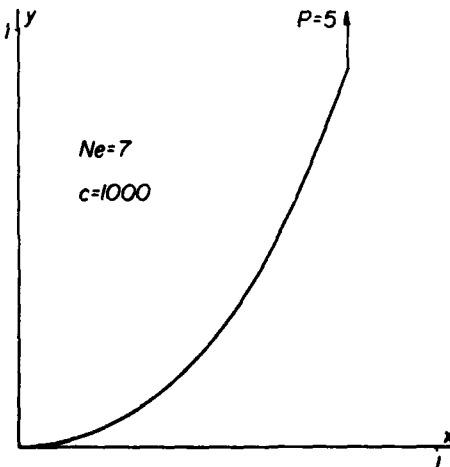


Fig. 2. Deep bending of a tip loaded beam computed with 3-2 integration elements.

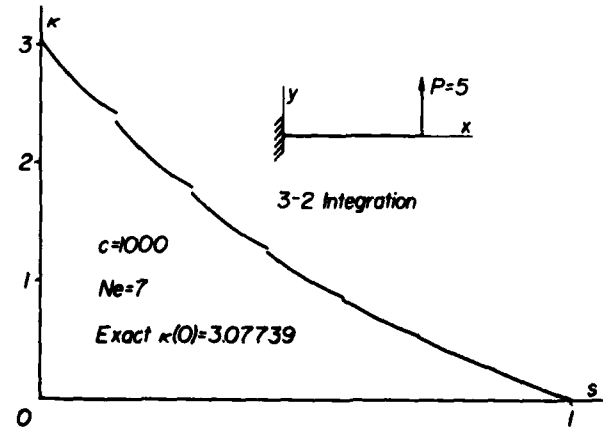


Fig. 3. Curvature distribution for the beam of Fig. 2.

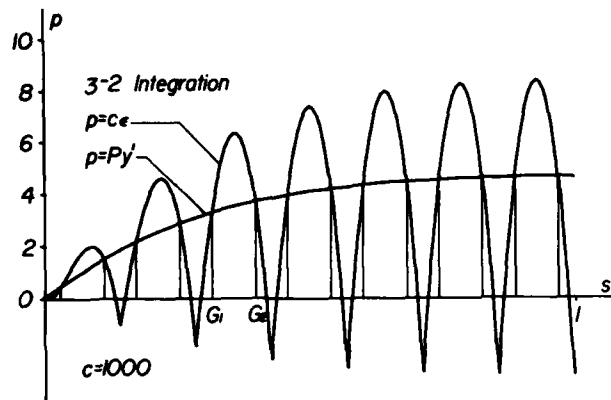


Fig. 4. Tension distribution for the beam of Fig. 2.

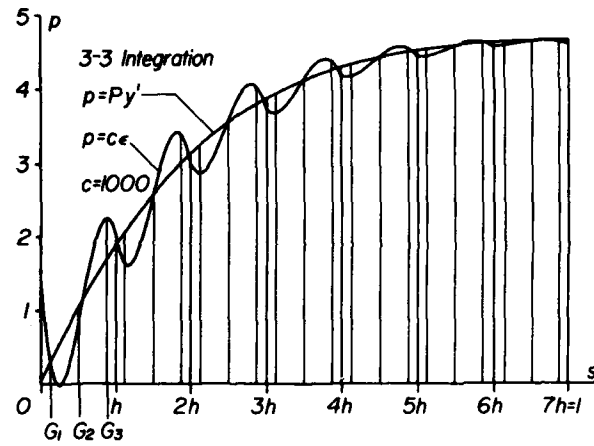


Fig. 5. Tension distribution for the beam of Fig. 2.

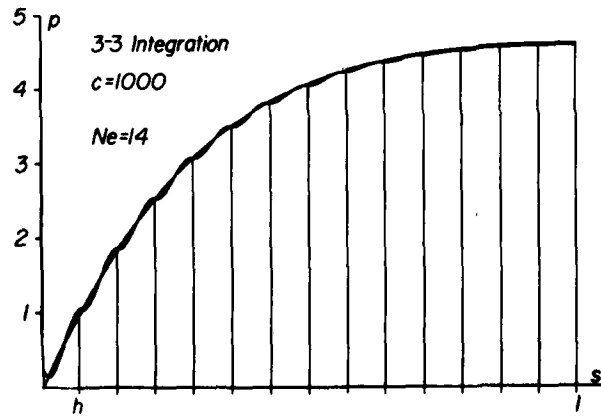


Fig. 6. As in Fig. 5 but with 14 elements.

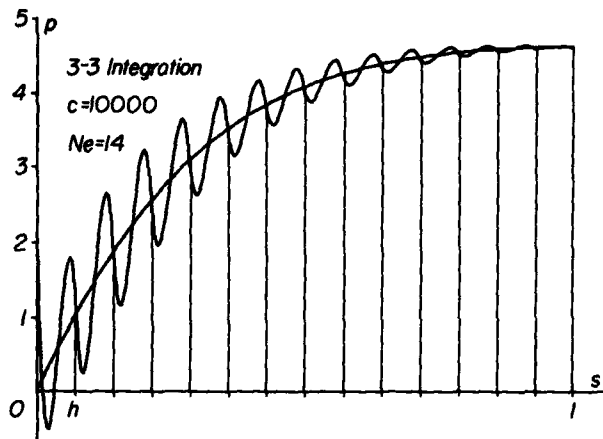
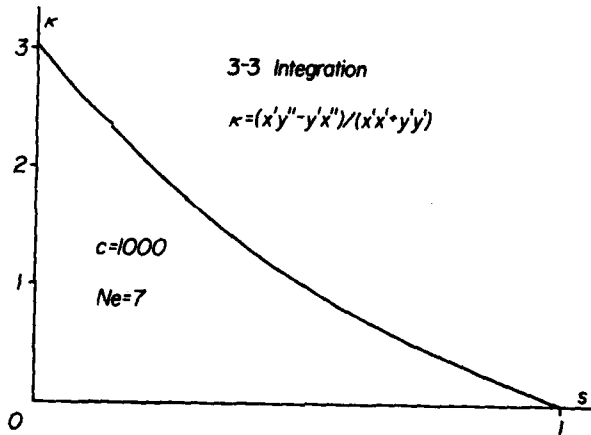
Fig. 7. As in Fig. 6 but with $c = 10^4$.

Fig. 8. Curvature distribution for the beam of Fig. 2 discretized with 3-3 integration elements.

Figs. 5, 6 and 7 trace the computed tensions for the tip loaded beam discretized with 3-3 integration elements. Fig. 8 shows the, here smoother looking, computed curvature distribution for the same beam.

4. Pressed ring

The elastic deflection of a thin inextensible circular ring pressed by two equal and opposite forces has been previously computed [1] with quadratic C^0 finite elements. In this section we present similar results obtained with the cubic-cubic C^1 element. Fig. 9 shows the equilibrium configurations that the ring assumes when pressed by a force P that increases in steps of 2 from 0 to 38. Fig. 10 follows the closing of the gap along the diameter of the ring with the

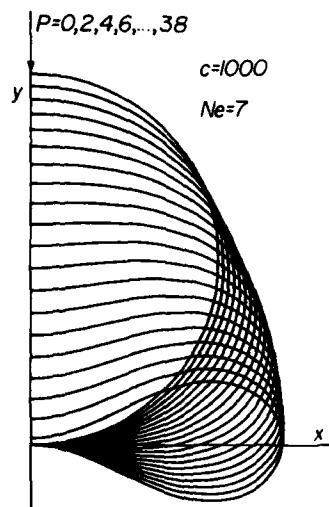
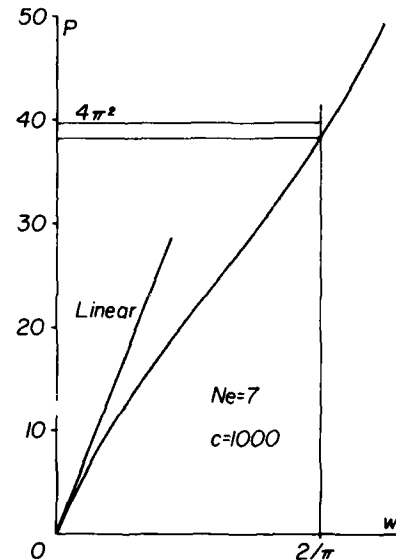


Fig. 9. Point pressed circular ring.

Fig. 10. Computed sinking of ring's top point with the top force P .

increase of P . We see in Fig. 10 that our extensible element has a slight extra flexibility to it; contact of the pressed points is reached with a force P that is somewhat less than the theoretical [3-5] $P = 4\pi^2$ for a ring of radius $1/\pi$.

5. Ring under hydrostatic pressure

To account for the action of an external uniform pressure (nonuniform is actually as easy) q we have to add to $\pi(x, y)$ in (3) the pressure's potential

$$\pi(x, y) = q \int_0^l xy' ds \quad (28)$$

or approximately, for the typical element,

$$\pi_e = q \sum_{j=1}^3 w_j x_j \dot{y}_j \quad (29)$$

that leads to

$$g_e = \pi'_e = q \sum_{j=1}^3 w_j (\phi_j \dot{y}_j + \dot{\psi}_j x_j) \quad (30)$$

and then to

$$k_e = \pi''_e = q \sum_{j=1}^3 w_j (\phi_j \dot{\psi}'_j + \dot{\psi}_j \phi'_j) \quad (31)$$

which are added to g_e and k_e in (17) and (21).

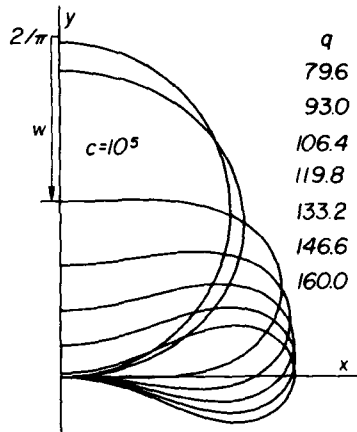


Fig. 11. Deformation of a circular ring under the action of an external pressure q .

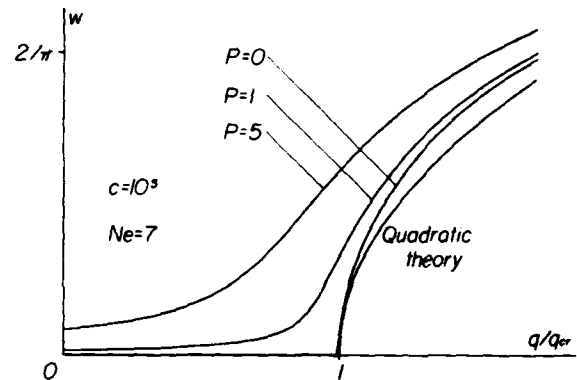


Fig. 12. Displacement of the ring's top point under the action of an external pressure q and a top force P .

The critical pressure on a closed circular inextensible ring is at $q_{cr} = 3/r^2$, or in our case where $r = 1/\pi$, $q_{cr} = 3\pi^2 = 29.609$. Fig. 11 shows the collapse of the ring, discretized with seven elements, under the action of an increasing, as listed, pressure. Fig. 12 compares the variation of the maximal deflection w caused by the external hydrostatic pressure q and a point force P , computed with our element, with results obtained from an analytic quadratic theory [6-9]. A high c value is chosen here to make the comparison with the inextensible theory more meaningful.

6. Vibrating beams

If $g(u)$ denotes, as before, the global gradient of the total potential energy and M the beam's global mass matrix, then its equation of motion is written as

$$g(u) + M\ddot{u} = 0 \quad (32)$$

where \dot{u} denotes velocity and \ddot{u} acceleration, that we propose to numerically solve with the Newmark scheme [10]

$$u_1 = u_0 + \tau\dot{u}_0 + \frac{1}{2}\tau^2\ddot{u}_0, \quad \dot{u}_1 = \dot{u}_0 + \frac{1}{2}\tau(\ddot{u}_0 + \ddot{u}_1) \quad (33)$$

for a time step size τ . By virtue of (32), (33) becomes

$$u_1 = u_0 + \tau\dot{u}_0 - \frac{1}{2}\tau^2M^{-1}g_0, \quad \dot{u}_1 = \dot{u}_0 - \frac{1}{2}\tau M^{-1}(g_0 + g_1). \quad (34)$$

In our subsequent dynamic computations we shall exclusively use the consistent [10] beam mass matrix.

We can foresee the possibility of a simply supported beam with free axial motion executing very large amplitude vibrations even when nearly inextensional. To numerically study such motions we impart the originally straight ($x = s, y = 0$) beam an initial velocity

$$\dot{x}_0 = 0, \quad \dot{y}_0 = \frac{a}{\pi} \sin \pi s \quad (35)$$

with magnitude determined by the factor a . Fig. 13 shows the appearance of the beam at time intervals of $\frac{1}{100}$ as it hurls up towards its ultimate flexed position. In Fig. 14 the beam's central elevation is traced against time for different values of a in (35). When the vibration amplitude is small, say for $a < 2$, the computed time it takes the crest of the beam to rise and fall back to zero is close to the theoretical half period value of $1/\pi$. A growing amplitude is predicted by our computations to cause a hardening of the beam and a shorter period of vibration. This does not sit well with other published results [11, 12], but meaningful comparisons are anyway not easy here. First, the approximations of the analytic approaches are sensitive [11] to very large displacements; and also, one must bear in mind that for a periodic solution to exist in the nonlinear range, particular, not easy to come by, initial conditions must be at hand.

To study the large movements of a free-free beam we set it in motion with the initial velocities

$$\dot{x}_0 = 0 \quad \text{and} \quad \dot{y}_0 = a[\cos \lambda s + \cosh \lambda s + \alpha(\sin \lambda s + \sinh \lambda s)] \quad (36)$$

where $\lambda = 4.7300408$ and where

$$\alpha = \frac{\sin \frac{1}{2}\lambda - \sinh \frac{1}{2}\lambda}{\cos \frac{1}{2}\lambda + \cosh \frac{1}{2}\lambda} = -1.018. \quad (37)$$

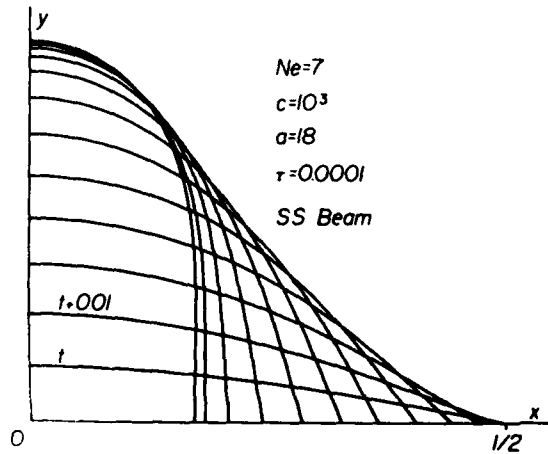


Fig. 13. Movement of a simply supported axially unconstrained beam.

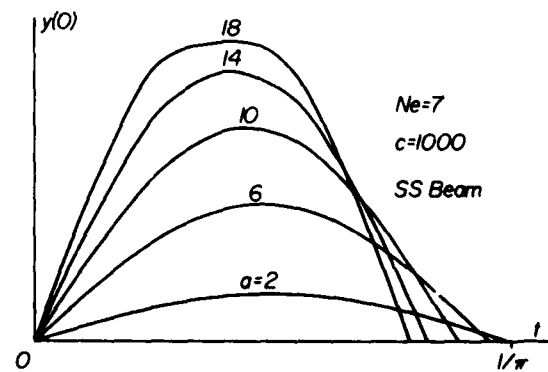


Fig. 14. Movement of the beam's central point for different magnitudes of the initial velocity in equation (35).

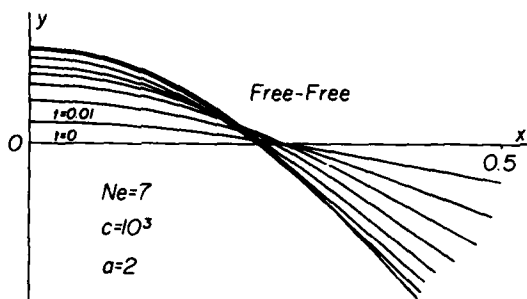


Fig. 15. Movement of a free-free beam.

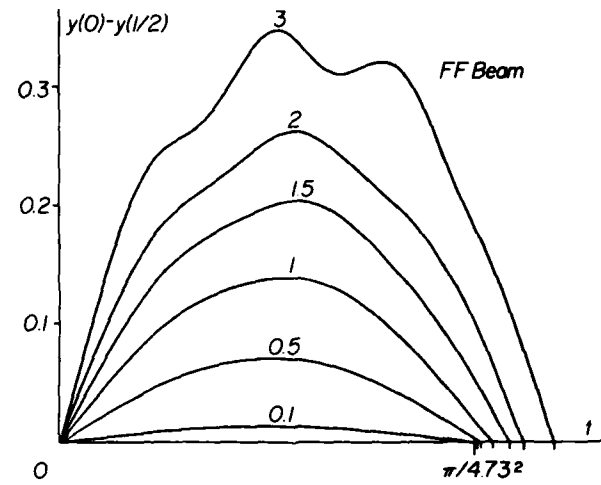
Fig. 16. Progress of the total bend in a free-free beam for different values of a in equation (36).

Fig. 15 shows a sequence of still pictures computationally taken of the beam between its first and second rest positions for a velocity factor $a = 2$. Fig. 16 traces the total bend $y(0) - y(\frac{l}{2})$ of the beam as it progresses with time. Again, for small amplitudes the free-free beam's computed half period is near π/λ^2 predicted by the inextensible small displacements theory, but as a , and with it the amplitude, keeps growing the beam becomes softer with longer periods, in agreement with the computations of Takahashi [13] but opposite those of Wagner [14].

7. Vibrating ring

For the circular ring it is more convenient to deal with the normal displacement w and the tangential displacement v , that are related to x and y (see Fig. 17) by

$$x = (r + w)\cos \theta - v \sin \theta \quad \text{and} \quad y = (r + w)\sin \theta + v \cos \theta, \quad (38)$$

θ being an angle measured from the positive x -axis. A time dependent displacement

$$w = \frac{1}{\omega} a \cos 2\theta \sin \omega t \quad \text{and} \quad v = -\frac{1}{\omega} \cdot \frac{1}{2} a \sin 2\theta \sin \omega t \quad (39)$$

constitutes an inextensional (i.e. $x'^2 + y'^2 = 1$) deformation for any value of a , and for all time t . We choose, therefore, to send the ring moving with the initial velocities

$$\dot{w}_0 = a \cos 2\theta \quad \text{and} \quad \dot{v}_0 = -\frac{1}{2} a \sin 2\theta \quad (40)$$

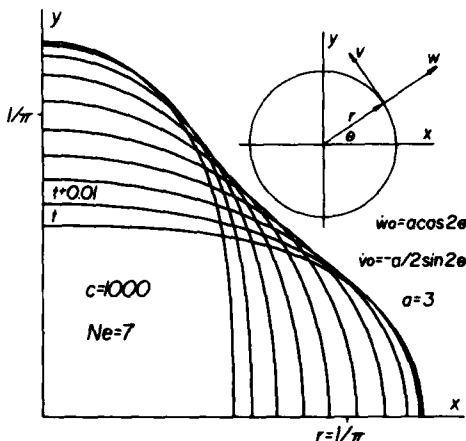
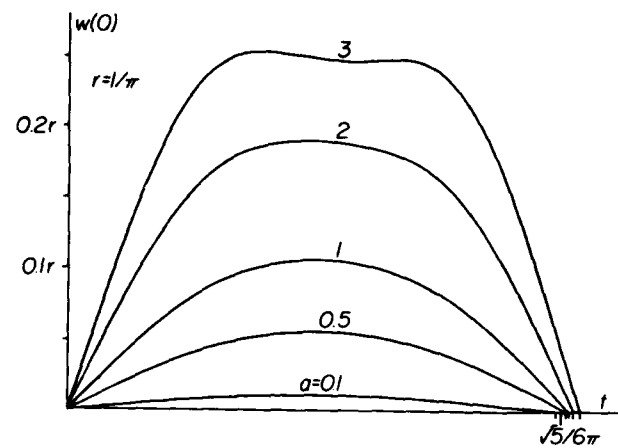


Fig. 17. Vibrating ring.

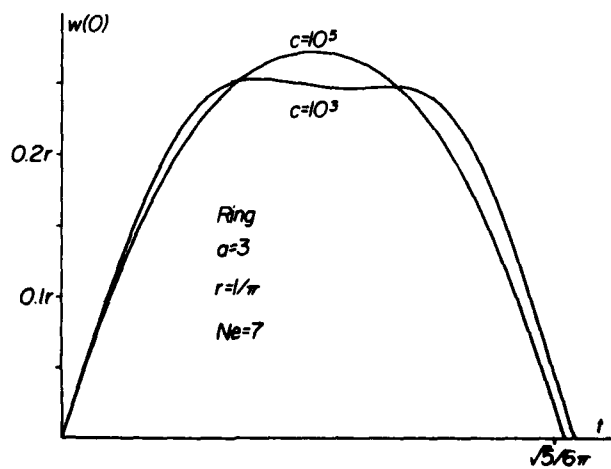
Fig. 18. Movement of $w(0)$ of the ring in Fig. 17.

or in terms of the Cartesian coordinates

$$\dot{x}_0 = \dot{w}_0 \cos \theta - \dot{v}_0 \sin \theta, \quad \dot{y}_0 = \dot{w}_0 \sin \theta + \dot{v}_0 \cos \theta \quad (41)$$

with $0 \leq \theta \leq \frac{1}{2}\pi$.

Fig. 17 shows a train of snapshots computationally taken of the beam at $\frac{1}{100}$ time intervals. Fig. 18 traces $w(0)$ with time for different magnitudes of the initial velocity. When a , and with it the displacement amplitude, is small the ring executes half a period in a time nearly equal to the theoretical inextensible $\sqrt{5}/6\pi$, but as the amplitude grows a slight softening is computationally detected for the ring in agreement with Evensen's [15] reporting. Fig. 19 shows the influence of c on the motion of the ring started with \dot{w}_0 and \dot{v}_0 in (40).

Fig. 19. Influence of c on the movement of $w(0)$ for the ring in Fig. 17.

8. Nonconservative loads

Beck's problem of a slender cantilever loaded by tip follower forces [16] is perhaps of little practical value as its real occurrence is somewhat farfetched but it will serve as a good example to describe the application of finite elements to problems with no potential for the load. Fig. 20 shows the arrangement of the tip forces that consist of a tangential follower force P and a normal follower force Q . When the load cannot be derived from a potential, as here, we are forced to forego the addition of appropriate work terms to the total potential energy and must introduce instead the forces directly into the gradient and consequently into the (nonlinear) equations of equilibrium. For our present beam element this operation is straightforward. Indeed, since the gradient entries that correspond to the x and y nodal values express the force sums in these directions, all we have to do here is to add the negative horizontal

$$H = P \cos \theta + Q \sin \theta \quad (42)$$

component, and the negative vertical

$$V = P \sin \theta - Q \cos \theta \quad (43)$$

component of the tip forces to the entries of g that correspond to the tip x and y , say g_{N-3} and g_{N-1} if the tip node is the last.

When we know the beam to be nearly inextensible the substitutions

$$\sin \theta = h^{-1} \dot{y}(1) \quad \text{and} \quad \cos \theta = h^{-1} \dot{x}(1) \quad (44)$$

can be made, with which H and V become

$$H = h^{-1}(Pu_{N-2} + Qu_N) \quad \text{and} \quad V = h^{-1}(Pu_N - Qu_{N-2}) \quad (45)$$

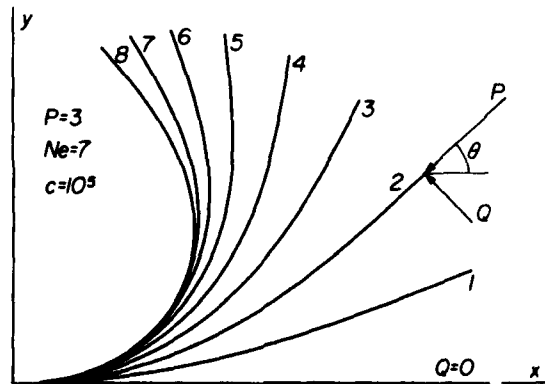


Fig. 20. Cantilever bent by large follower forces.

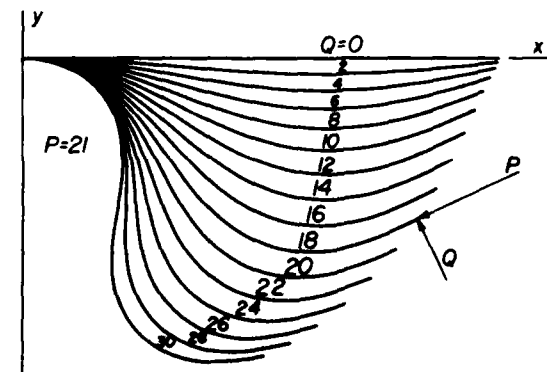


Fig. 21. Same as Fig. 20 but with $P = 21$.

that we add to g_{N-3} and g_{N-1} , respectively. To prepare for the Newton-Raphson solution of $g(u) = 0$ the four terms

$$\frac{\partial g_{N-3}}{\partial u_{N-2}} = h^{-1}P, \quad \frac{\partial g_{N-3}}{\partial u_N} = h^{-1}Q, \quad \frac{\partial g_{N-1}}{\partial u_{N-3}} = h^{-1}Q, \quad \frac{\partial g_{N-1}}{\partial u_N} = h^{-1}P \quad (46)$$

have to be added, nonsymmetrically, to the global stiffness matrix K at the addresses $(N-3, N-3)$, $(N-3, N)$, $(N-1, N-3)$ and $(N-1, N)$, respectively. Fig. 20 and 21 show computed equilibrium configurations for the elastic column bent by the follower forces P and Q . No nontrivial equilibrium configuration is found for $Q = 0$.

References

- [1] I. Fried, Finite element computation of large elastic deformations, in: J.R. Whiteman, ed., Proceedings of MAFELAP IV, Brunel University, April 27-May 1, 1981 (Academic Press, New York, 1982) 143-159.
- [2] A.K. Noor, Survey of computer programs for solution of nonlinear structural and solid mechanics problems, *Comput. & Structures* 13 (1981) 425-465.
- [3] R. Sonntag, Die Kreisringfeder. Zur Theorie des geschlossenen Kreisringes mit grosser Formänderung, *Ing.-Arch.* 13 (1943) 380-397.
- [4] R. Frisch-Fay, Flexible Bars (Butterworth, London, 1962).
- [5] P. Seide, Postbuckling behavior of circular rings with two or four concentrated loads, *Internat J. Non-Linear Mech.* 8 (1973) 169-178.
- [6] G.F. Carrier, On the buckling of elastic rings, *J. Math. Phys.* 26 (1947) 94-103.
- [7] M.S. El Naschie, The initial post-buckling of an extensional ring under extremal pressure, *Internat. J. Mech. Sci.* 17 (1975) 387-388.
- [8] M.S. El Naschie, Influence of loading behavior on the post buckling of circular rings, *J. Appl. Mech.* 44 (1976) 266-267.
- [9] L.B. Sills and B. Budiansky, Postbuckling ring analysis, *J. Appl. Mech.* 45 (1978) 208-210.
- [10] I. Fried, Numerical Solution of Differential Equations (Academic Press, New York, 1979).
- [11] S.R. Woodall, On the large amplitude oscillations of a thin elastic beam, *Internat. J. Non-Linear Mech.* 1 (1966) 217-238.
- [12] S. Atluri, Nonlinear vibration of a hinged beam including nonlinear inertia effects, *J. Appl. Mech.* 40 (1973) 121-126.
- [13] K. Takahashi, Nonlinear free vibrations of inextensible beams, *J. Sound Vibration* 64 (1979) 31-34.
- [14] H. Wagner, Large-amplitude free vibrations of a beam, *J. Appl. Mech.* 32 (1965) 887-892.
- [15] D.A. Evensen, Nonlinear flexural vibrations of thin circular rings, *J. Appl. Mech.* 33 (1966) 553-560.
- [16] Y.G. Panovko and I.I. Gubanova, Stability and Oscillations of Elastic Systems (Consultants Bureau, New York, 1965).

REFLECTIONS ON THE COMPUTATIONAL APPROXIMATION OF ELASTIC INCOMPRESSIBILITY†

ISAAC PRUD*

Boston University, Department of Mathematics, Boston, MA 02215, U.S.A.

(Received 7 December 1981; revised for publication 8 June 1982)

Abstract—Gradual diminution of compressibility tied with mesh refinement is shown to be an effective and practical way to numerically cope with near incompressibility of elastic solids. It is remarked that (low order) numerical integration is a side issue in this technique and that (high order) exact integration of high order finite elements can be safely used with the correct minimal variation principle of classical elasticity, including a high Poisson ratio.

1. INTRODUCTION

In 1974 the author wrote a paper [1] on the finite element analysis of nearly incompressible elastic solids in which he advocated the gradual introduction of incompressibility by way of a bulk modulus that is allowed to increase only when accompanied by a proper mesh reduction in such a way as to balance the discretization errors with the compressibility errors. Progressive imposition of incompressibility is called for in the finite element displacement method because for any given mesh a too large bulk modulus can either cause a dangerously ill conditioned stiffness equation or an overly stiff (locked) finite element model. Exact enforcement of incompressibility via a minimum variational principle and polynomial shape functions is often possible only at the trivial state of zero displacements. And if the computational model is rough why should one use anyway a large bulk modulus and disproportionately small compressibility errors?

The paper, which included computations of an elastic sphere came upon the additional observation that numerical integration, not necessarily reduced, can remove utter locking.

Since then the subject of finite element analysis of incompressible materials both solid [2] and fluid [3-7] has kept central stage in computational continuum mechanics research and many thoughtful papers [8, 9] regularly appear on this subject in the open literature. Nevertheless, the author dares believe that no significant improvement has yet been offered over his original technique, which he sees as the most practically satisfying and theoretically safe method to computationally deal with solid nearincompressibility.

His technique is not a penalty (the author has not yet reconciled himself to this ugly term) method [9-12], nor does it require reduced (not to be confused with numerical) integration. It is a standard application of the displacement finite element method to classical elasticity including a wise limit on the bulk modulus in order to produce a reasonably conditioned stiffness matrix and balanced discretization-computational errors.

The main purpose of this paper is to reconsider in

greater detail the, so often misquoted, arguments of Ref. [1] and to clearly point out that unlike the penalty methods that rely on huge, machine dependent, bulk modulus and reduced integration that supposedly release volume preserving modes, the present technique does not need them.

2. INCOMPRESSIBLE SPHERE

In order to make our arguments as explicit as possible we shall pay close attention to the simple problem of an elastic unit hollow sphere, as in Fig. 1 stressed by a unit internal pressure, but free of stress on its outer skin. Here, when the shear modulus equals one

$$u(r, v) = p \left[\frac{1}{4r^2} + \frac{1-2v}{2(1+v)} r \right], P = \frac{a^3}{1-a^2} \quad (1)$$

a being the internal radius and v the Poisson ratio. With

$$z = \frac{2v}{1-2v} \quad (2)$$

Equation (1) becomes

$$u(r, z) = u(r, w) + \frac{p}{3z+2} r. \quad (3)$$

Subsequently we will use an overbar to denote values at $v = 1/2$, as $\bar{u} = u(r, w)$.

A radial displacement u causes the elastic strains

$$\epsilon_r = u', \epsilon_\theta = \frac{u}{r}, \epsilon_z = \frac{u}{r} \quad (4)$$

and a dilatation

$$\epsilon = \epsilon_r + \epsilon_\theta + \epsilon_z = u' + \frac{2u}{r} \quad (5)$$

where prime means differentiation with respect to r . With u in eqn (1) we have then that

$$\epsilon(r, z) = \frac{3}{3z+2} p \quad (6)$$

and

$$\bar{\epsilon}(r, z) = \bar{\epsilon}(r, w) = p \quad (7)$$

*Research supported by the Office of Naval Research through contract N00014-75C-0306.
†Professor.

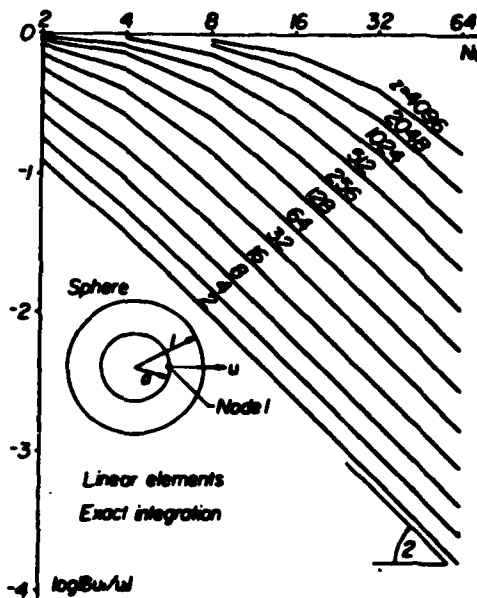


Fig. 1. Convergence of u_1 with Ne for different z values.

K being the bulk modulus which is equal to $z + 2/3$. Also, the stresses

$$\sigma_r(r, z) = p \left(1 - \frac{1}{r^2}\right) \text{ and } \sigma_\theta(r, z) = p \left(1 + \frac{1}{2r^2}\right) \quad (8)$$

are both independent of z .

Equation (3) can be written as

$$u(r, z) = u(r, \infty) + pr \left(\frac{1}{32} - \frac{2}{9z^2} + \frac{4}{27z^4} + \dots\right) \quad (9)$$

or

$$u(r, z) = u(r, \infty) + O(z^{-1}) \quad (10)$$

in agreement with the general prediction of Ref. [1].

3. LINEAR FINITE ELEMENTS

Our sphere has stored elastic energy

$$E = \int_0^1 \left(\frac{1}{2} 2r^2 + e_r^2 + e_\theta^2 + e_\phi^2 \right) r^2 dr \quad (11)$$

and throughout this paper we shall assume that $a = 1/2$. For a single element that extends between $\xi = -1$ and $\xi = 1$ (or $r = r_1$ and $r = r_1 + h$)

$$E_e = \frac{h}{2} \int_{-1}^1 \left[\frac{1}{2} \dot{x}(q\dot{u} + 2u)^2 + (q^2 \dot{u}^2 + 2u^2) \right] d\xi \quad (12)$$

where dot denotes differentiation with respect to ξ , and where $q = 2r/h$.

An exact stiffness matrix for a two nodal point element is readily derived from eqn (12) in the form

$$k = h \begin{pmatrix} 14a^2 + 3 & 4a\beta - 3 \\ 4a\beta - 3 & 4\beta^2 + 3 \end{pmatrix} + \frac{13 - 12a\beta}{6} \begin{pmatrix} 1 & -1 \\ -1 & 1 \end{pmatrix} + \frac{2}{3} \begin{pmatrix} 2 & 1 \\ 1 & 2 \end{pmatrix} \quad (13)$$

in which $a = 1/2 + r_1/h$ and $\beta = 1/2 + r_1/h$, $a + \beta = 2$.

To understand in what way this element locks when $z \rightarrow \infty$ observe first that linear shape function produce a dilatation

$$e = \frac{3}{h} (u_2 - u_1) + \frac{2}{rh} (u_1 r_2 - u_2 r_1) \quad (14)$$

so that $e = 0$ is possible only with $u_1 r_2 - u_2 r_1 = 0$ and $u_2 - u_1 = 0$, or $u_1 = u_2 = 0$. On the other hand the energy error in the finite element computed ℓ , ℓ , and ℓ_0 is

$$\begin{aligned} E(u - \ell) &= \frac{1}{2} z \int_0^1 (e - \ell)^2 r^2 dr \\ &\quad + \int_0^1 [(e - \ell)^2 + (e_0 - \ell_0)^2] r^2 dr \end{aligned} \quad (15)$$

As $z \rightarrow \infty$, the exact $e \rightarrow 0$, and because of the large z in the dilatation energy expression, ℓ is forced down too and locking ensues. Choosing the two parameter interpolation

$$u = \frac{1}{3} c_1 r + \frac{c_2}{r} \quad (16)$$

for the element displacements allows a constant dilatation without locking but we forgo this restricted possibility here.

We now employ the linear element to compute the elastic displacements of the radially deforming sphere of Section 1. Since we use the exact variational principle we are assured an $O(h^3)$ convergence in the displacements for any chosen value of z because of the factor z in $E(u - \ell)$ in eqn (15) we must also be resigned to a factor z in the displacements error, and a locking mechanism. Figure 1 shows the error in $u_1 = u(a = 1/2, z)$ for different values of z , and indeed for a number of elements Ne sufficiently large $|du_1/u_1|$ is proportional to Ne^{-2} . Figure 2 shows the error growth in u_1 as z is increased, for different values of Ne , and truly when $z < Ne^2$ the computed error in, the z the dependent, u_1 is proportional to z . Precisely

$$\left| \frac{\delta u_1}{u_1} \right| = 0.32z Ne^{-2} \quad (17)$$

and we conclude that for any fixed value of z any desired

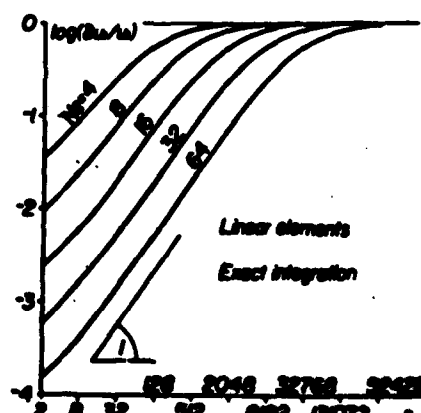


Fig. 2. Reduced accuracy in u_1 with increased z for different mesh refinements.

displacement discretization accuracy can be secured with a sufficiently large number of elements, but the larger z the more elements needed for any given accuracy. A limit of $z = 1000$ can be safely assumed for the available elastic materials. At this value of z , $\nu = 0.4995$, and according to eqn (3)

$$\mathbf{u}\left(\frac{1}{2}, 10^3\right) = \mathbf{u}\left(\frac{1}{2}, \infty\right) + 2.38 \cdot 10^{-5}. \quad (18)$$

Even if the elastic material is practically incompressible it would be unwise to substitute a large z value in the finite element stiffness matrix. It is computationally more sensible to equate the relative compressibility error, which for \mathbf{u}_1 is about $1/6z$, with the discretization error, for a smaller, mesh dependent z . Our linear element invites the choice

$$0.32z Ne^{-2} = 0.167z^{-1} \quad (19)$$

that leads to

$$z = 0.72 Ne \quad (20)$$

and a balanced error of

$$\left| \frac{\delta u_1}{u_1} \right| = 0.23 Ne^{-1} \quad (21)$$

where u_1 is a function of z and consequently Ne .

At this point many a reader will raise the objection that the optimal z/Ne ratio is not only element dependent but also problem dependent and is possible here only with the aid of the exact solution. This is true but we must bear in mind that the computational analyst is regularly confronted with the question of choosing discretization parameters without ever being able to select the optimal ones. Does he ever know what number of elements or which mesh layout is optimal? All we can do, for a given element, is settle for a reasonable z/Ne ratio and either incorporate it in a finite element computer code or instruct the user as to the proper limit on z depending on the number of elements. What is important here is that a constant z/Ne ratio assures a simultaneous, $z \rightarrow \infty$, $h \rightarrow 0$, energy convergence $O(Ne^{-1})$ to the incompressible solution. One order of Ne^{-1} is lost in this process but we are for that on theoretically safe ground.

When the stiffness matrix for the linear element is created with a one point Gauss integration rule one global finite element mode escapes locking and the dilatational part of the global stiffness matrix is reduced from being positive definite to being positive semidefinite with one zero eigenvalue. It happens for the sphere that this mode is just the right one for the approximation of the incompressible solution and finite elements produce now accurate nodal values independent of z . This is the trick of reduced integration; to save (good) approximation modes from getting locked. The success of this convenient device appears however to be only conditional and a very large z can leave at our disposition faulty approximation modes. Counting degrees of freedom may disclose the number of locking free modes in the discretization but foretells nothing about their quality. Here is the weak point of penalty methods: they insist on using only computationally pure incompressible modes.

4. HIGHER ORDER ELEMENTS

We conclude from the previous section that for nearly incompressible solids it is worthwhile to step up the

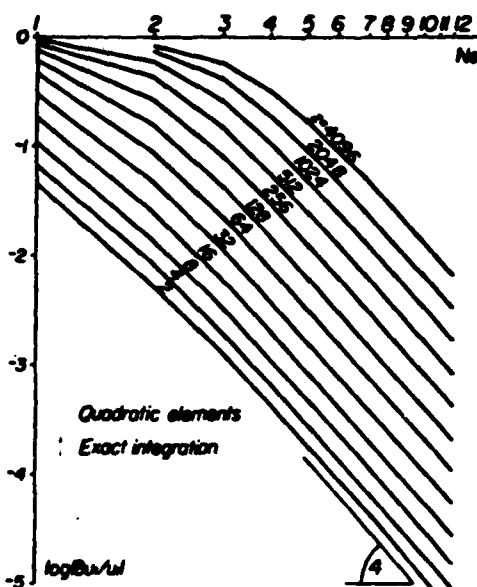


Fig. 3. Same as Fig. 1 but for exact quadratic elements.

order of the element for better computational efficiency. When exact quadratic elements are used to discretize the elastic sphere the relative error in \mathbf{u}_1 is, according to Figs. 3 and 4

$$\left| \frac{\delta u_1}{u_1} \right| = 0.0344 z Ne^{-4} \quad (22)$$

provided that $z < Ne^4$. The compressibility error stays the same $1/6z$, and therefore incompressibility is best approached with

$$z = 2.2 Ne^2 \quad (23)$$

resulting in

$$\left| \frac{\delta u_1}{u_1} \right| = 0.076 Ne^{-2} \quad (24)$$

where u_1 is still a function of z or Ne .

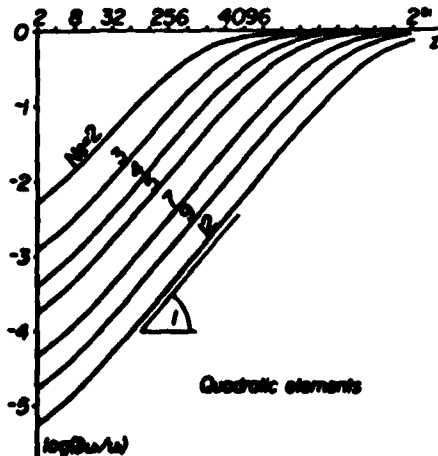


Fig. 4. Same as Fig. 2 but for exact quadratic elements.

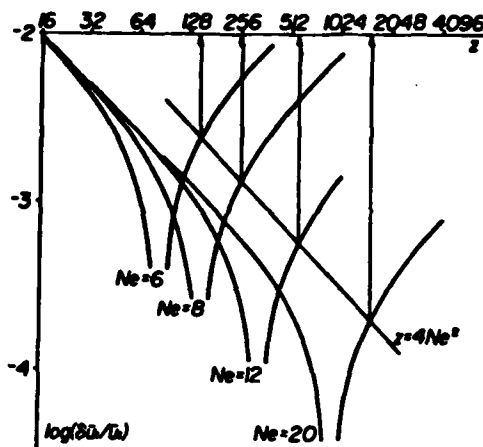


Fig. 5. Error in the incompressible \bar{u} , as depending on z for different number of finite elements Ne in the discretization.

Figure 5 clearly shows the convergence process to the totally incompressible solution \bar{u}_1 . For a fixed number of elements as z is increased the approximation is first improved as the compressibility error declines. An exact value happens to be crossed, but further increase of z brings only a decline in accuracy as the element stiffness and ultimately locks. Figure 5 shows also the error reduction in \bar{u} , for the choice $z = 4 Ne^2$. Notice that with $Ne = 20$ we can go here as high as $z = 1600$ or $v = 0.4997$, and get a relative error $|\delta\bar{u}/\bar{u}| = 10^{-3.66}$.

5. ROUND-OFF ERRORS

We infer from the elastic energy expression (11) that the global stiffness matrix is with a spectral condition number [13] proportional to z and Ne^2 . Direct computations reveal that the quadratic element leads to

$$C_2(K) = 6.6 z Ne^2 \quad (25)$$

or with $z = 4 Ne^2$ to

$$C_2(K) = 26.4 Ne^4 \quad (26)$$

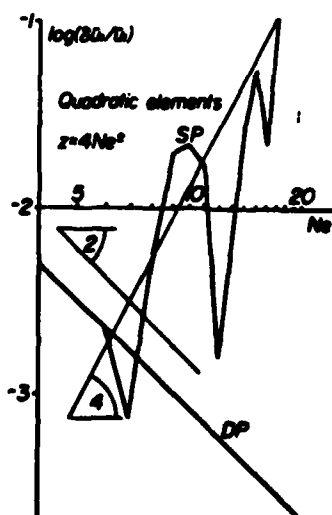


Fig. 6. Effect of round off-error on the computed approximation to \bar{u} . Single precision (SP) machine accuracy is $0.5 \cdot 10^{-2}$, and double precision (DP) is 10^{-16} .

calling for round-off precautions [14, 15]. Our IBM computer has a single precision relative accuracy of $0.5 \cdot 10^{-2}$ and a double precision relative accuracy of 10^{-16} . On this machine, when using single precision, all accuracy is lost, as soon as the number of elements reaches 17. Double precision saves the day for nearly incompressible solid computations by banishing this unhappy episode to $Ne = 4500$! As Fig. 6 shows available higher computer accuracy permits the achievement of any reasonable discretization accuracy practically free of round-off error.

6. EXTRAPOLATIONS TO THE LIMIT

Simultaneous extrapolation to the limits of z and Ne can desist the need for their large values. Let \bar{u} denote the incompressible solution and u the finite element computed displacement. Since the compressibility and discretization errors are proportional to z^{-1} and z , respectively, we may write

$$u = \bar{u} + \frac{\alpha}{z} + \beta z \quad (27)$$

and three u values for three z values will determine α , β , and \bar{u} . Suppose that u_1 , u_2 and u_3 are the three u values computed for z_1 , $z_2 = 2z_1$ and $z_3 = 4z_1$, then

$$\bar{u} = -2u_1 + 5u_2 - 2u_3 \quad (28)$$

$$\beta z_1 = \frac{1}{3}(u_1 - 3u_2 + u_3) \quad (29)$$

and

$$\alpha/z_1 = \frac{4}{3}(2u_1 - 3u_2 + u_3). \quad (30)$$

For example, the quadratic element of Section 4 computes

$$\begin{aligned} u_1 &= 0.14234053 & \text{for } z_1 = 512 \\ u_2 &= 0.14176086 & \text{for } z_2 = 1024 \\ u_3 &= 0.14064927 & \text{for } z_3 = 2048 \end{aligned} \quad (31)$$

with which eqn (28) yields $\bar{u} = 0.1428247$ as compared with the exact $\bar{u} = 0.1428571$, or a relative error of $10^{-3.44}$. Knowing βz_1 in eqn (26) allows for a better approximation for the compressible u at z_1 ,

$$u = \frac{1}{3}(2u_1 + 3u_2 - 2u_3). \quad (32)$$

Using the data in eqn (28) we compute with eqn (32) a $u(1/2, 512) = 0.1428837$ as compared with the exact $u(1/2, 512) = 0.14290359$, a relative error of $10^{-3.07}$. The corresponding $u_1 = u(1/2, 512) = 0.14234053$ from eqn (28) is with a relative error of $10^{-3.4}$.

7. PRESSURE COMPUTATION

We foresee difficulties in the computation of the pressure $p = K\varepsilon$ as we have to multiply a small ε by a large K , and still expect an accurate p . Figures 7 and 8 show the computed pressure $p = K\varepsilon$ over a mesh of 32 linear finite elements. The change of sign in p that takes place inside each element can be explained with reference to the energy error in eqn (15) and its minimization by the finite element solution. We expect also a good average p computed with respect to a weight r^2 , or good sampling

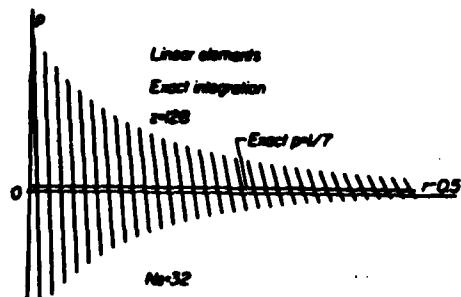


Fig. 7. Computed pressure distribution in exact linear elements.

points at the optimal integration nodes for a weight distribution r^2 .

For the linear element optimal integration point is at the root of the equation $r - b_0 = 0$ where b_0 minimizes

$$I_0 = \int_{r_1}^{r_2} (b_0 - r)r^2 dr. \quad (33)$$

Denoting

$$A_1 = \frac{1}{3}(r_2^3 - r_1^3) \quad (34)$$

we have that in the interval $-1 \leq \xi \leq 1$ this point is at

$$\xi = \frac{2}{h} \left(\frac{A_1}{A_2} - r_1 \right) - 1 \quad (35)$$

which means that in a 32 element mesh, in the first element $\xi = 0.01025562$, while in the last element $\xi = 0.00524924$. Figure 9 describes the convergence of the average pressure

$$p' = \frac{1}{A_2} \int_{r_1}^{r_2} pr^2 dr \quad (36)$$

in the first element for both the exact and approximate integration.

Quadratic elements are more interesting. Figure 10 shows the computed pressure distribution over an 8 element mesh of quadratic elements. Change of sign in the pressure error distribution occurs now twice in each

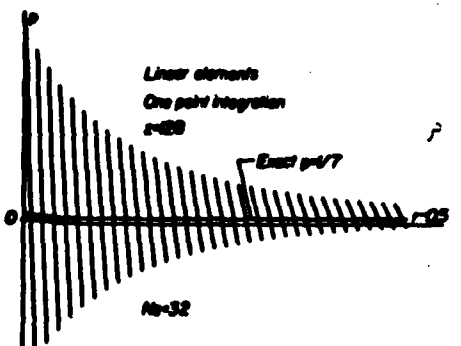
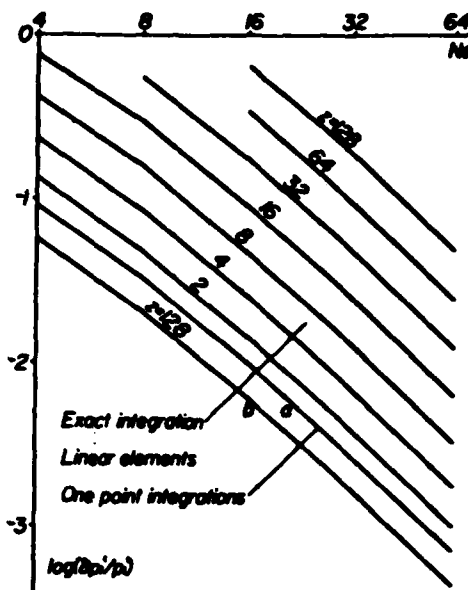


Fig. 8. Computed pressure distribution in one point integrated, linear elements.

Fig. 9. Convergence of average pressure in the first element (between $r_1 = 1/2$ and $r_2 = 1/2 + h$) with N_e , as depending on z . Curve a is for exact integration of the deviatoric part, and one point integration of dilatonic part of the total potential energy. Curve b is for a one point throughout integration.

element. To locate the optimal integration points for this element we minimize

$$L_1 = \int_{r_1}^{r_2} (b_0 + b_1 r - r^2)^2 r^2 dr \quad (37)$$

with respect to b_0 and b_1 and find the roots of the equation $b_0 + b_1 r - r^2 = 0$. Doing this we have for the first element, between $r_1 = 1/2$ and $r_2 = 1/2 + 1/16$,

$$\xi_1 = -0.561056 \text{ and } \xi_2 = 0.592478 \quad (38)$$

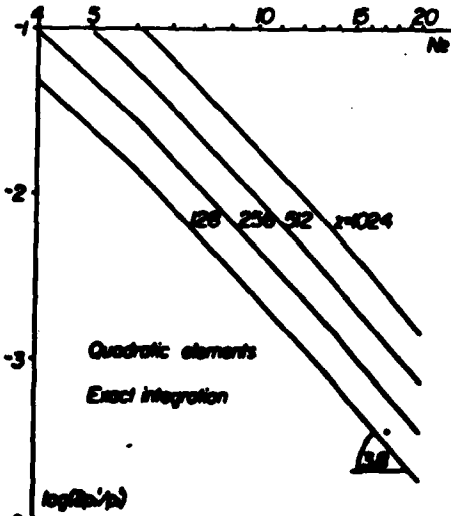


Fig. 10. Computed pressure distribution over 8 exact quadratic elements.

1. FORM

Table 1. Computed average pressure p' , and the pressures at the Gauss points G_1 and G_2 , as well as at the optimal points F_1 and F_2 , for an 8 element discretization with $z = 256$. Exact $p = 0.14285714$

element	p	$p(G_1)$	$p(G_2)$	$p(F_1)$	$p(F_2)$
1	0.14434	0.19356	0.10137	0.14341	0.14369
2	0.14340	0.16846	0.12120	0.14298	0.14309
3	0.14280	0.15666	0.13075	0.14279	0.14284
4	0.14280	0.15068	0.13568	0.14270	0.14272
5	0.14271	0.14747	0.13837	0.14265	0.14266
6	0.14266	0.14565	0.13992	0.14263	0.14263
7	0.14263	0.14457	0.14004	0.14261	0.14262
8	0.14262	0.14391	0.14141	0.14261	0.14261

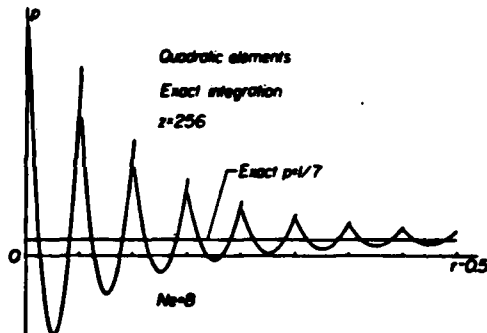


Fig. 11. Convergence of average pressure in the first element of Fig. 10.

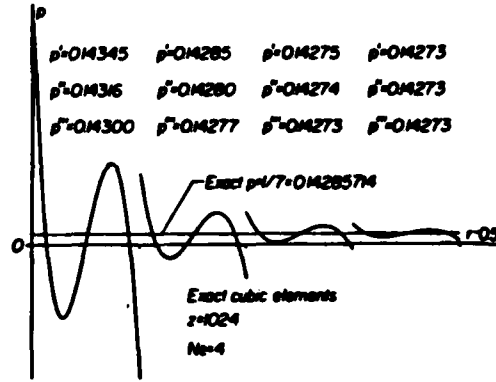


Fig. 12. Pressure distribution over 4 exact cubic elements, for p' , p'' , and p''' see eqn (39).

as compared with the two Gauss points $\xi_{1,2} = \pm 0.577350$. Table 1 lists the computed pressures at the two Gauss points G_1 and G_2 , at the optimal points F_1 and F_2 , and also the average pressure inside each element for the mesh and z of Fig. 10. Figure 11 shows the convergence with N_e of the average pressure in the first element of Fig. 10.

Figure 12 shows the computed pressure distribution in a four cubic element discretization of the sphere, together with

$$p' = \frac{1}{A_1} \int_{r_1}^{r_2} pr^2 dr, \quad p'' = \frac{1}{A_2} \int_{r_1}^{r_2} pr^2 dr, \quad p''' = \frac{1}{A_3} \int_{r_1}^{r_2} pr^2 dr \quad (39)$$

where A_i is given in eqn (34). In the first cubic element of Fig. 12 the three optimal points are at

$$\begin{aligned} \xi_1 &= -0.76076448 \\ \xi_2 &= 0.03173087 \\ \xi_3 &= 0.76037818 \end{aligned} \quad (40)$$

whereas the Gauss points are of $\xi_{1,2} = \mp 0.77459667$, $\xi_3 = 0$. At the optimal integration points we find, for $z = 1024$,

the three corresponding computed pressure values $p = 0.129513$, 0.161753 , 0.127681 . At the three Gauss points we compute the less accurate $p = 0.237300$, 0.053148 , 0.199470 , that we compare with the exact $p = 0.142857$.

2. REVOLVING SPHERE

Our present discussion will be wanting without a multidimensional example. Let's consider for that purpose the problem of a hollow sphere revolving around an axis that passes through its center [16]. Both the inner radius $r = 1/2$, and the outer radius $r = 1$ of the sphere are assumed free of surface forces. Symmetry permits the reduction of the problem to the portion shown in Fig. 13. Discretization of the sphere is accomplished with 6×6 biquadratic elements numerically integrated. Also with reference to Fig. 13 we assume $\theta = 0$ to be the axis of revolution, and suppose for this example $z = 256$. Table 2 lists the computed average pressure

$$p' = \int_{r_1}^{r_2} \int_{\theta_1}^{\theta_2} pr^2 \sin \theta dr d\theta / \int_{r_1}^{r_2} \int_{\theta_1}^{\theta_2} r^2 \sin \theta dr d\theta \quad (41)$$

Table 2. Pressure at the finite elements of Fig. 12. Values are, from top to bottom in each square: exact pressure at the center of the element, average over element with a 3×3 integration rule, and average over element with a 2×2 integration rule. Square at bottom left is for element 1, while at top right it is for element 36

0.600032	0.403300	0.256938	0.133459	0.019543	-0.091800
0.500531	0.390253	0.247000	0.127514	0.017415	-0.091066
0.503598	0.391603	0.248830	0.129064	0.016352	-0.093078
0.534409	0.370445	0.245900	0.138760	0.030362	-0.060892
0.531703	0.368236	0.245330	0.139609	0.040411	-0.057486
0.520862	0.360984	0.239209	0.134179	0.035537	-0.062085
0.420747	0.313538	0.226779	0.147942	0.070958	-0.007360
0.418307	0.311750	0.226071	0.148148	0.071935	-0.00556
0.410849	0.306350	0.221624	0.143981	0.068147	-0.009103
0.288501	0.247827	0.204700	0.158545	0.108586	0.054453
0.288306	0.246727	0.203838	0.157902	0.108157	0.054234
0.283923	0.243268	0.200007	0.155269	0.109756	0.051987
0.175838	0.190920	0.185500	0.167727	0.141191	0.107985
0.176042	0.190585	0.184664	0.166374	0.139496	0.109962
0.174047	0.188652	0.183072	0.165038	0.138316	0.104871
0.110216	0.158064	0.174508	0.173028	0.160010	0.138892
0.111306	0.158218	0.173617	0.171271	0.157587	0.135812
0.110619	0.157124	0.172800	0.170676	0.157111	0.135400

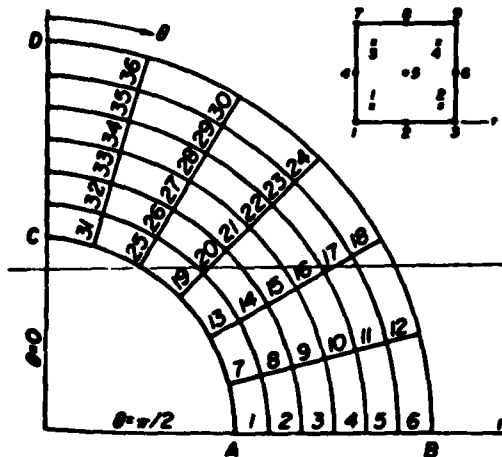


Fig. 13. Mesh layout on revolving sphere. Also element nodes and integration points numbering.

In all 36 elements of the discretization, for a 3×3 and a 2×2 Gauss integration rules.

The maximum pressure occurs at point C in element 31 in Fig. 13 and we plan to pay closer attention to this element. Minimization of

$$L = \int_{r_1}^{r_2} (a_0 + a_1 r - r^2)^2 r^2 dr \text{ and}$$

$$L = \int_{\theta_1}^{\theta_2} (b_0 + b_1 r - r^2)^2 \sin \theta d\theta \quad (42)$$

locates the optimal integration points

$$\xi_1 = -0.555786, \xi_2 = 0.596906$$

in the element that lies between $r_1 = 1/2$ and $r_2 = 1/2 + 1/12$, and

$$\eta_1 = -0.2906565, \eta_2 = 0.6892173 \quad (44)$$

in the same element that is between $\theta_1 = 0$ and $\theta_2 = \pi/12$.

At these four integration points, numbered as in Fig. 13, we compute $p = 0.6185, 0.7719, 0.4360, 0.7439$, as compared with the exact $p = 0.7080, 0.7123, 0.6300, 0.6335$. Computation being done with 3×3 Gauss integrated elements and $z = 256$.

As for the displacements we have at point A

$$\begin{aligned} u_{\text{exact}} &= 0.1089531 \quad (z = 256) \\ \delta_{\text{exact}} &= 0.1087581 \quad (z = \infty) \\ u_{\text{comp}} &= 0.1131709 \quad (2 \times 2 \text{ error} = 3.87\%) \\ u_{\text{comp}} &= 0.1069682 \quad (3 \times 3 \text{ error} = 1.82\%) \end{aligned} \quad (45)$$

We may attempt to approximate the pressure at point C through a bilinear extrapolation over elements 25, 26, 31 and 32. Let p_{25} , etc. denote the average pressure at element 26 assigned to its center. Extrapolation from the four center values furnishes the pressure approximation for point C

$$p = \frac{1}{4}(-3p_{25} + p_{26} + 9p_{31} - 3p_{32}) \quad (46)$$

or

$$\begin{aligned} p_{\text{comp}} &= 0.72479 \quad (3 \times 3) \\ p_{\text{exact}} &= 0.74613 \quad (z = 256) \\ p_{\text{exact}} &= 0.74867 \quad (z = \infty) \end{aligned} \quad (47)$$

which means a discretization error of about 3%.

REFERENCES

1. I. Fried, Finite element analysis of incompressible material by residual energy balancing. *Int. J. Solids Structures* 10, 993-1002 (1974).
2. D. S. Malkus, A finite element displacement model valid for any value of the compressibility. *Int. J. Solids Structures* 12, 731-736 (1976).
3. T. J. R. Hughes, W. K. Liu and A. Brooks, Finite element analysis of incompressible viscous flows by the penalty function formulation. *J. Comp. Phys.* 30, 1-60 (1979).
4. M. S. Engelman, R. L. Sani, P. M. Gresho and M. Bercovier, Consistent vs reduced integration penalty methods for incompressible media using several old and new elements. *Int. J. Num. Meth. Fluids* (1980).
5. R. L. Sani, P. M. Gresho, R. L. Lee and D. F. Griffith, The cause and cure(?) of the spurious pressures generated by certain FEM solutions of the incompressible Navier-Stokes equations—1. *Int. J. Num. Meth. Fluids* 1, 17 (1981).
6. R. L. Sani, P. M. Gresho, R. L. Lee, D. F. Griffiths and M. S. Engelman, The cause and cure(?) of the spurious pressures generated by certain FEM solutions of the incompressible Navier-Stokes equations—2. *Int. J. Num. Meth. Fluids* 1, 171 (1981).
7. O. C. Zienkiewicz, R. L. Taylor and J. M. W. Baynham, Mixed and irreducible formulations in finite element analysis: some general comments and applications to the incompressibility problem. *Proc. Int. Symp. on Mixed and Hybrid FEM*, Atlanta, Georgia, 8-10 April 1981.
8. D. S. Malkus, Eigenproblems associated with the discrete LBB condition for incompressible finite elements. *Int. J. Engng Sci.* 19, 1299-1310 (1981).
9. J. T. Oden and N. Kikuchi, Finite element methods for constrained problems in elasticity. *Proc. Symp. on the Unification of Finite Elements, Finite Differences and the Calculus of Variations* (Edited by H. Kardestuncer), pp. 8-45. (1980).
10. J. T. Oden, N. Kikuchi and Y. J. Song, Penalty-finite element methods for the analysis of stokesian flows. To appear.
11. J. T. Oden, RIP Methods for stokesian flows. TICOM Rep. 80-11, 1980.
12. M. Bercovier, Y. Haasani, Y. Gilon and K. J. Bathe, On a finite element procedure for nonlinear incompressible elasticity. *Proc. Int. Symp. on Mixed and Hybrid FEM*, Atlanta, Georgia, 8-10 April 1981.
13. I. Fried, Influence of Poisson's ratio on the condition of the finite element stiffness matrix. *Int. J. Solids Structures* 9, 323-329 (1973).
14. J. H. Argyris, P. C. Dunne, Th. L. Johnsen and H. P. Meijneke, A new iterative solution for structures and continua with very stiff or rigid parts. *Comp. Meth. Appl. Mech. Engng* 24, 215-248 (1980).
15. I. Fried and J. A. Metzler, Conjugate gradient solution of a finite element elastic problem with high Poisson ratio. *Comp. Meth. Appl. Mech. Engng* 15, 83-84 (1978).
16. M. A. Goldberg, V. L. Salerno and M. A. Sadowsky, Stress distribution in a rotating spherical shell of arbitrary thickness. *J. Appl. Mech.*, 127-131 (1961).

On Unconditionally Stable Explicit Time Integration

Methods in Elastodynamics and Heat Transfer

by

Isaac Fried*

Boston University

Department of Mathematics

Boston, Mass. 02215

* Professor

1. Introduction

Unconditionally stable (semi) explicit integration schemes for stiff systems of equations as generated by finite element analysis of elastodynamics and non-stationary heat transfer are shown to suffer from the DuFort-Frankle-Saul'ev [1] syndrome whereby coupling between the space and time discretizations may have a ruinous effect on the accuracy of the computations.

2. Elastodynamics

To integrate the discrete equation of motion

$$M\ddot{y} + Ky = 0 \quad (1)$$

in which M is the global mass matrix and K the stiffness matrix, a (semi) explicit method has been introduced [2] in recent years into the engineering literature (see also Refs. [3,4]) based on the symmetric splitting of K into

$$K = L + L^T \quad (2)$$

where L is lower triangular. Then for time step τ

$$\begin{aligned} (M + \frac{\tau^2}{8}L)\dot{y}_{\frac{1}{2}} &= (M - \frac{\tau^2}{8}L)\dot{y}_0 - \frac{\tau}{2}Ky_0 \\ \dot{y}_{\frac{1}{2}} &= y_0 + \frac{\tau}{4}(\dot{y}_0 + \dot{y}_{\frac{1}{2}}) \\ (M + \frac{\tau^2}{8}L^T)\dot{y}_1 &= (M - \frac{\tau^2}{8}L^T)\dot{y}_{\frac{1}{2}} - \frac{\tau}{2}Ky_{\frac{1}{2}} \\ \dot{y}_1 &= \dot{y}_{\frac{1}{2}} + \frac{\tau}{4}(\dot{y}_{\frac{1}{2}} + \dot{y}_1) \end{aligned} \quad (3)$$

$$\begin{bmatrix} M - \frac{\tau^2}{8}L & \frac{\tau}{2}K \\ -\frac{\tau}{2}M & M - \frac{\tau^2}{8}L^T \end{bmatrix} \begin{bmatrix} \dot{y}_1 \\ y_1 \end{bmatrix} = \begin{bmatrix} M - \frac{\tau^2}{8}L & -\frac{\tau}{2}K \\ \frac{\tau}{2}M & M - \frac{\tau^2}{8}L^T \end{bmatrix} \begin{bmatrix} \dot{y}_0 \\ y_0 \end{bmatrix} \quad (4)$$

If M is diagonal passage from time level 0 to time level 1 requires back substitutions only and hence the appeal of scheme (3).

It is shown [5] that this method is energy conserving and unconditionally stable. It is also shown in Ref. [5] that for any fixed τ , spacial mesh refinement, done with the hope of improving the discretization accuracy, will eventually sabotage the quality of the displacements computed with eqns (3) or (4). We reconsider here the singular behavior of the computational errors.

Consider the string problem

$$\begin{aligned} -y'' + \ddot{y} &= 0 & y(0, t) &= y(1, t) = 0 \\ y(x, 0) &= \sin 2\pi x \end{aligned} \quad (5)$$

for which we know that $u(x, t) = \sin 2\pi x \sin 2\pi t$. According to the analysis of Ref. [4] when eqn (5) is discretized with first order elements of size h and a lumped mass matrix, the first mode excitation causes the string to vibrate with the computed frequency ω given by

$$\cos \omega \tau = \frac{1 - \frac{1}{32}(1 - \cos 2\pi h)\psi^2(24 - \psi^2)}{1 + \frac{1}{32}(1 - \cos 2\pi h)\psi^2(8 + \psi^2)} \quad (6)$$

where $\psi = \tau/h$. Power series expansion yields

$$\omega = 2\pi \left[1 + \pi^2 \left(\frac{1}{3} h^2 + \frac{1}{2} \tau^2 + \frac{1}{16} \frac{\tau^4}{h^2} \right) \right]^{\frac{1}{2}} \quad (7)$$

or

$$\frac{\delta\omega}{2\pi} = \frac{\omega}{2\pi} - 1 = \frac{\pi^2}{2} \left(\frac{1}{3} h^2 + \frac{1}{2} \tau^2 + \frac{1}{16} \frac{\tau^4}{h^2} \right) \quad (8)$$

This error estimate for the computed frequency includes the expected $O(h^2)$ from the spacial discretization, $O(\tau^2)$ from the time discretization, and also the coupled $O(\tau^4/h^2)$. Holding τ constant and reducing h lowers $\delta\omega$ until a critical $\psi^* = (\tau/h)^*$ is reached, beyond which $\delta\omega$ increases and accuracy is lost. This behavior of $\delta\omega$ is clearly seen in Fig. 1 directly computed from eqn (6).

The critical ψ^* is found from $d\omega/dh = 0$, and we find that

$$\psi^* = 3^{-\frac{1}{4}} 2 \left(1 + \frac{\sqrt{3}\pi^2}{24} \tau^2 \right) \quad (9)$$

One would not want to exceed this ψ^* even for the stable method. Going beyond ψ^* does not produce the computational bang typical of instability but its effects could be as insidious.

Figure 2 shows the computed motion of the central point of a string discretized with linear finite elements. With $h = 0.05$ and $\tau = 0.1$ the computed solution can barely be distinguished from the exact, but small elements cause a hefty error in the period.

3. Heat Transfer

For the solution of the system of first order equations

$$\dot{y} = f(y) \quad (10)$$

the unconditionally stable, explicit scheme

$$\begin{aligned} g_1 &= \tau f(y_0) \\ g_2 &= \tau f(y_0 + \frac{1}{2}g_1) \\ g &= 2g_1 - g_2 \\ y_1 &= y_0 + \frac{2g_1(g_1^T g) - g(g_1^T g_1)}{g^T g} \end{aligned} \quad (11)$$

has been advanced [7,8] recently.

To analyze the scheme in eqn (11) we consider the linear system

$$\dot{y} + Ky = 0 \quad (12)$$

with positive definite and symmetric K . Let v_1 and v_2 be two eigenvectors of K and $0 < \lambda_1 < \lambda_2$ the corresponding eigenvalues. The initial value

$$y_0 = a v_1 + b v_2 \quad (13)$$

produces the evolution

$$y(t) = a(t)\psi_1 + b(t)\psi_2$$

$$a(t) = e^{-\lambda_1 t}, \quad b(t) = e^{-\lambda_2 t} \quad (14)$$

Or with $t = j\tau$, $j = 0, 1, 2, \dots$, $\psi_1 = \lambda_1 \tau$ and $\psi_2 = \lambda_2 \tau$

$$a_j = a e^{-j\psi_1}, \quad b_j = b e^{-j\psi_2} \quad (15)$$

Starting with y_0 in eqn (13) we have that

$$g_1 = - (a\psi_1 v_1 + b\psi_2 v_2)$$

$$g_2 = a\psi_1 (-1 + \frac{1}{2}\psi_1) v_1 + b\psi_2 (-1 + \frac{1}{2}\psi_2) v_2 \quad (16)$$

$$g = -a\psi_1 (1 + \frac{1}{2}\psi_1) v_1 - b\psi_2 (1 + \frac{1}{2}\psi_2) v_2$$

and eqn (11) produces

$$a_{j+1} = a_j \left(1 - \frac{a_j^2 \psi_1^2 (1 + \frac{1}{2}\psi_1) + b_j^2 \psi_2^2 (1 - \frac{1}{2}\psi_1 + \psi_2)}{a_j^2 \psi_1^2 (1 + \frac{1}{2}\psi_1)^2 + b_j^2 \psi_2^2 (1 + \frac{1}{2}\psi_2)^2} \psi_1 \right) \quad (17)$$

$$b_{j+1} = b_j \left(1 - \frac{a_j^2 \psi_1^2 (1 + \psi_1 - \frac{1}{2}\psi_2) + b_j^2 \psi_2^2 (1 + \frac{1}{2}\psi_2)}{a_j^2 \psi_1^2 (1 + \frac{1}{2}\psi_1)^2 + b_j^2 \psi_2^2 (1 + \frac{1}{2}\psi_2)^2} \psi_2 \right)$$

Figures 3, 4, 5 and 6 describe the behavior of eqn (17).

Starting with $a = b = 1$ in eqn (13), Fig. 3 shows the error δa in $a(t)$ at $t = 1$ as a function of ψ_2 . It is clearly seen in Fig. 3 that $\psi_2^* \approx 2$ constitutes a critical value; below it the error in $a(1)$ is nearly independent of ψ_2 but as $\psi_2 = 2$ is crossed the accuracy of $a(t)$ suffers a sudden loss. A

smaller ψ_1 and more steps to reach $t = 1$ produces a more accurate solution for $\psi_2 < 2$, as can be seen in Fig. 4 but as soon as $\psi_2 = 2$ is crossed the same sudden loss of accuracy reoccurs.

In Figs. 5 and 6 we examine the errors in $a(t = 1)$ and $b(t = 1)$ as a function of the initial b , when the initial $a = 1$. It is readily concluded from Figs. 5 and 6 that high machine accuracy is of little help in avoiding the sudden error jump in a . Only when $b = 0$, is

$$a_{j+1} = \frac{1 - \frac{1}{2}\psi_1}{1 + \frac{1}{2}\psi_1} a_j \quad (18)$$

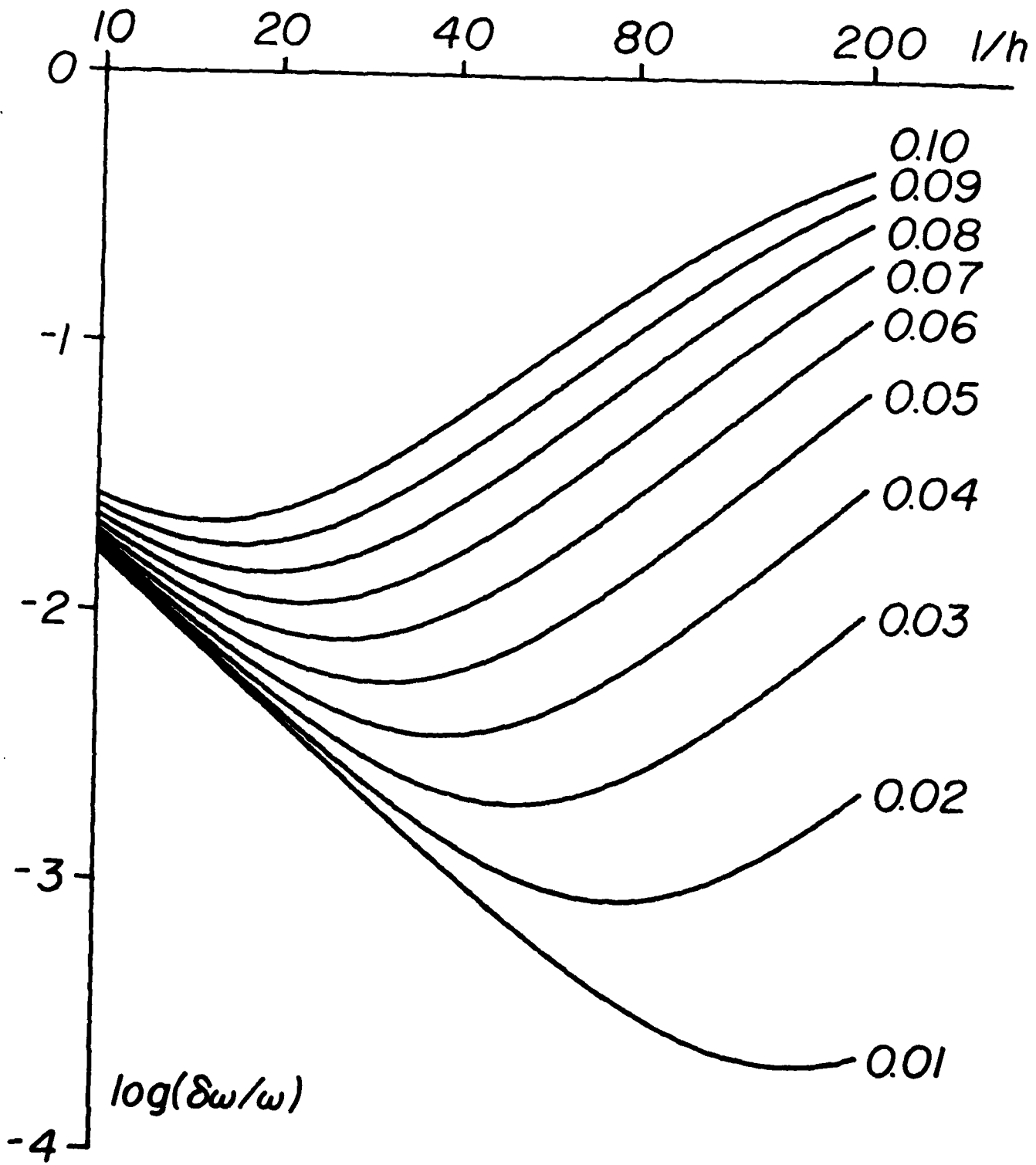
REFERENCES

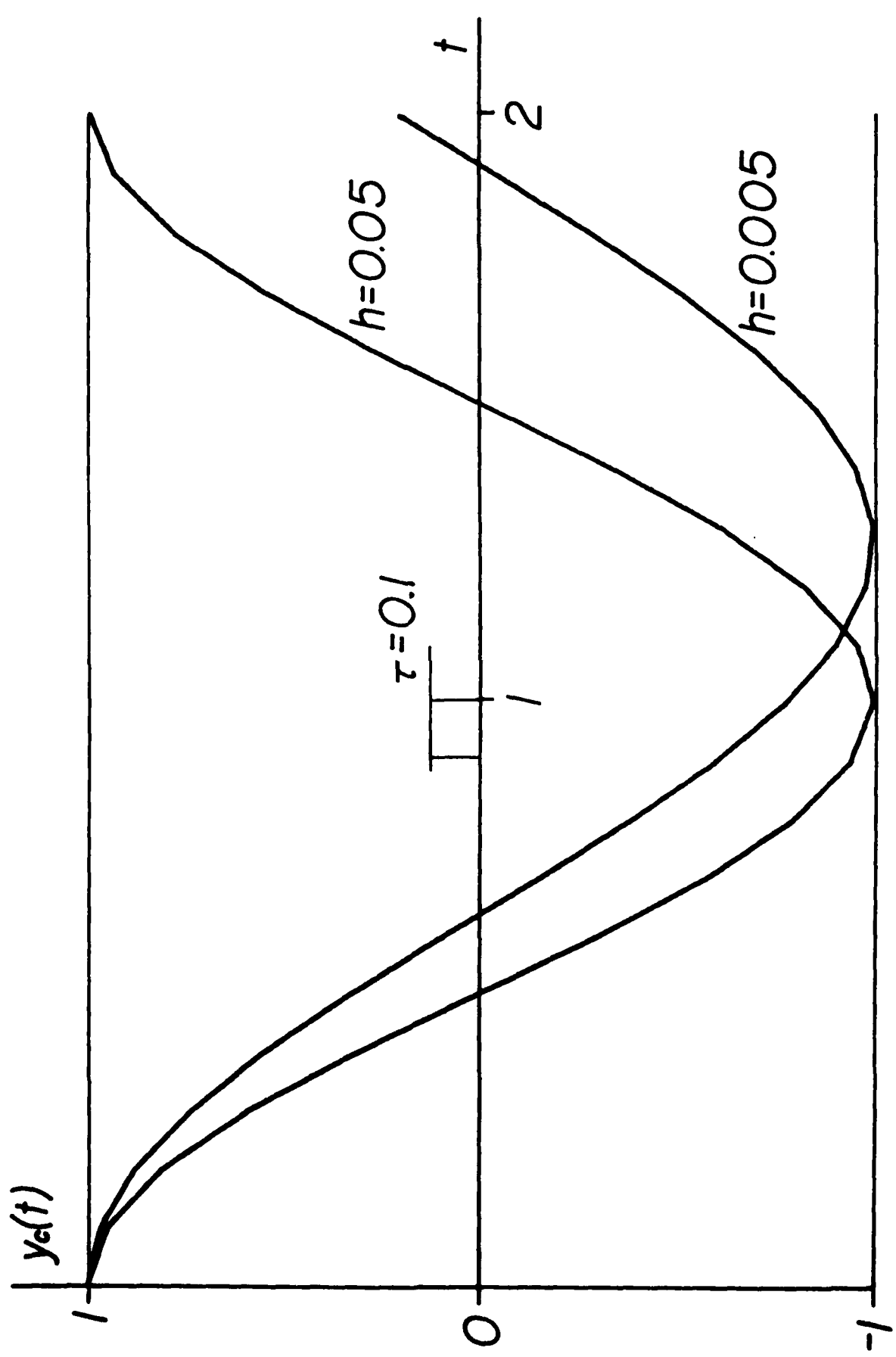
- [1] R.D. Richtmyer and K.W. Morton, Difference Methods for Initial-Value Problems. Interscience Publishers, New York, 2nd Edition 1967.
- [2] D.M. Trujillo, An unconditionally stable explicit algorithm for structural dynamics. Int. J. Num. Math. Engng. 11, 1579-1592 (1977).
- [3] H.Z. Barakat and J.A. Clark, On the solution of the diffusion equation by numerical methods. J. Heat Transfer, 421-427 (Nov. 1966).
- [4] D.M. Trujillo, An unconditionally stable explicit algorithm for finite-element heat conduction analysis. Nucl. Eng. Design 41, 175-180 (1977).
- [5] I. Fried, Numerical Solution of Differential Equations, Academic Press, New York, 1979.
- [6] R. Mullen and T. Belytschko, An analysis of an unconditionally stable explicit method. Computers & Structures 16, 691-696 (1983).
- [7] A. Wambecq, Rational Runge-Kutta methods for solving systems of ordinary differential equations. Computing 20, 333-342 (1978).
- [8] E. Hairer, Unconditionally stable explicit methods for parabolic equations. Numer. Math. 35, 56-68 (1980).

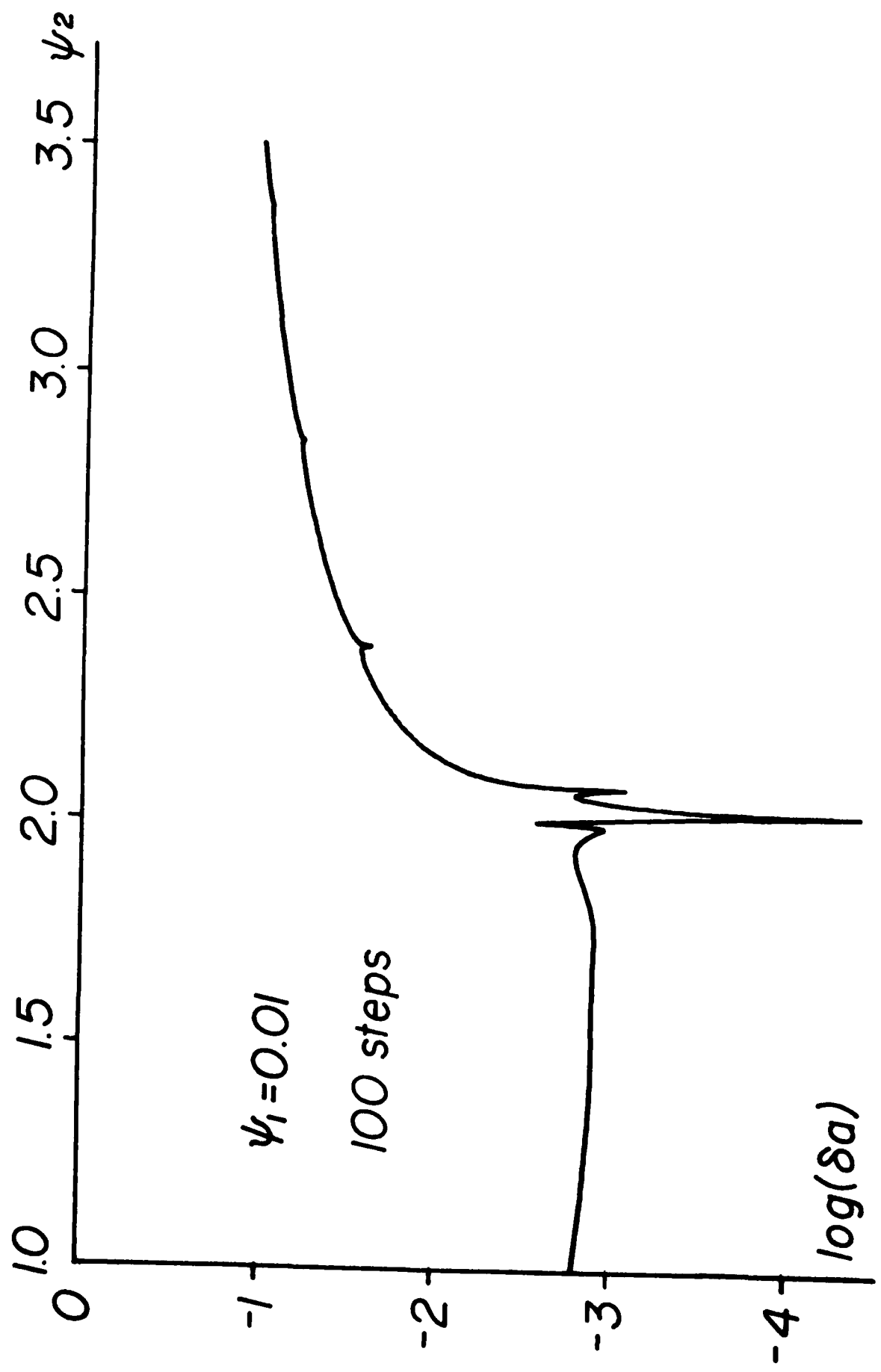
Figures

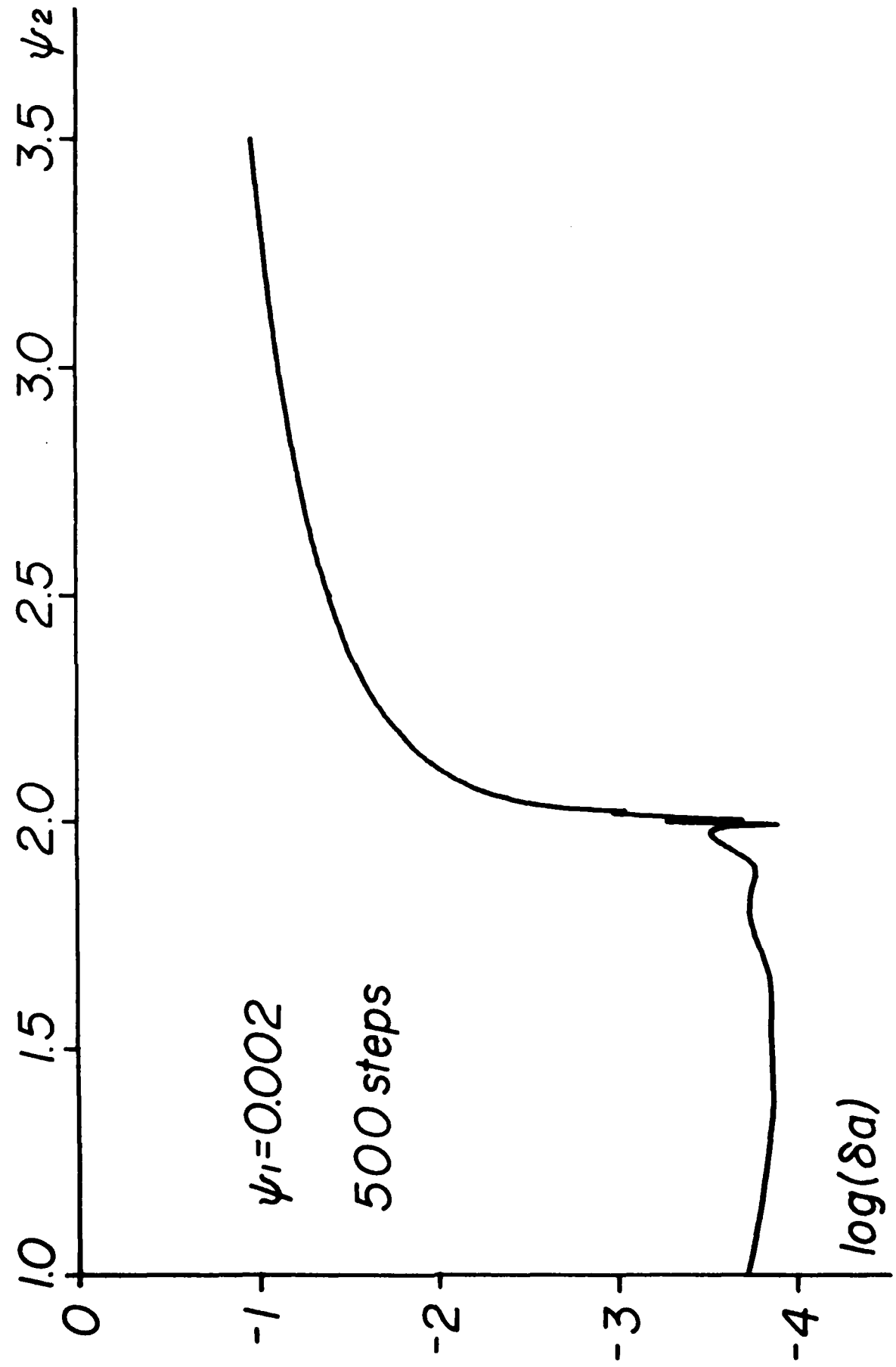
1. Frequency error of the integration formula (3) as a function of the mesh size h for time steps between $\tau = 0.01$ and $\tau = 0.10$.
2. Vibrating string solved with eqn (3). Accuracy declines as h decreases.
3. Accuracy of integration formula (11) with initial value in eqn (13).
4. Same as 3 but different ψ_1 .
5. Accuracy of $a(t = 1)$ and $b(t = 1)$ for different initial b . Initial $a = 1$.
6. Same as 5 but higher ψ_2 .

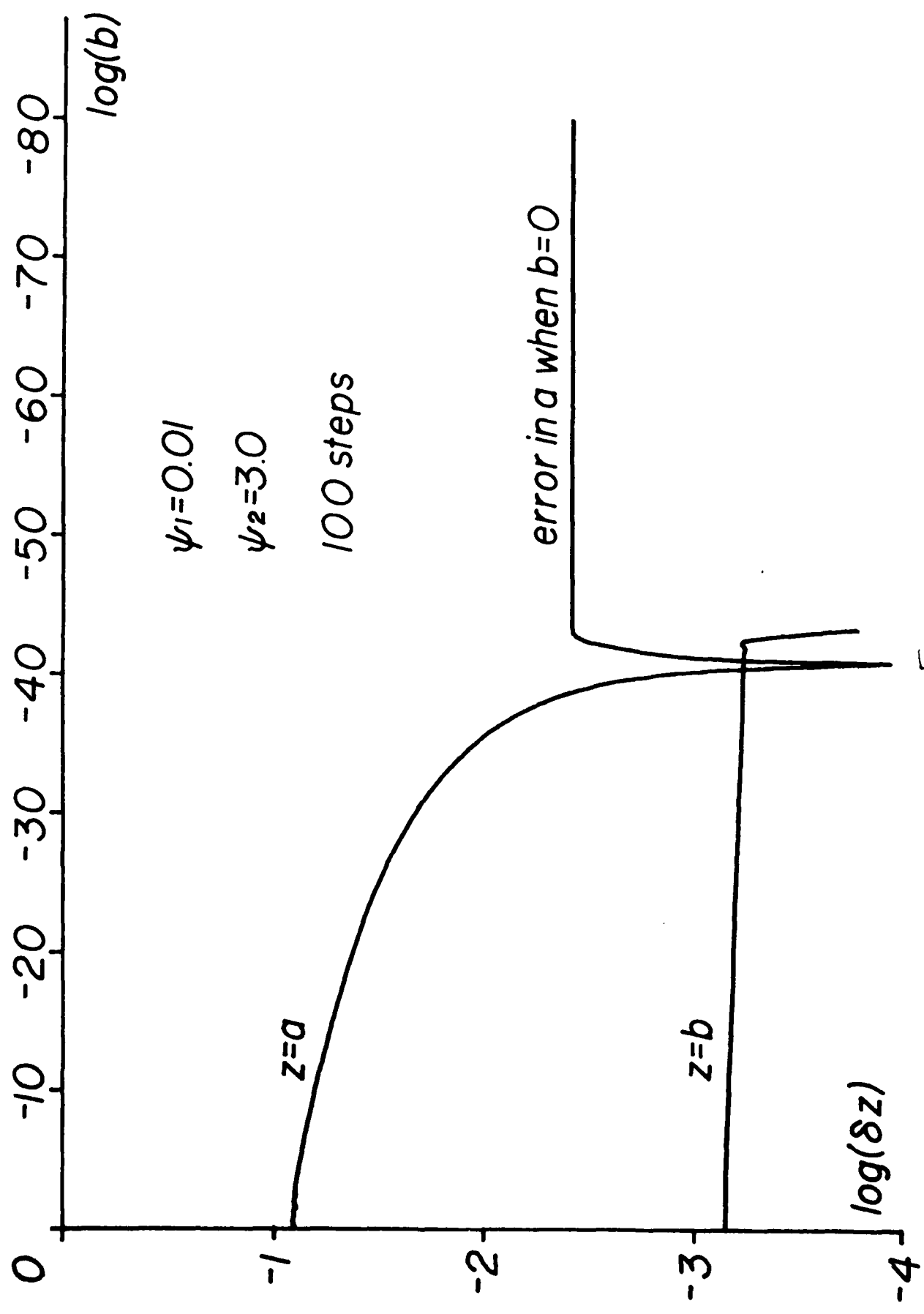
Fig. 1

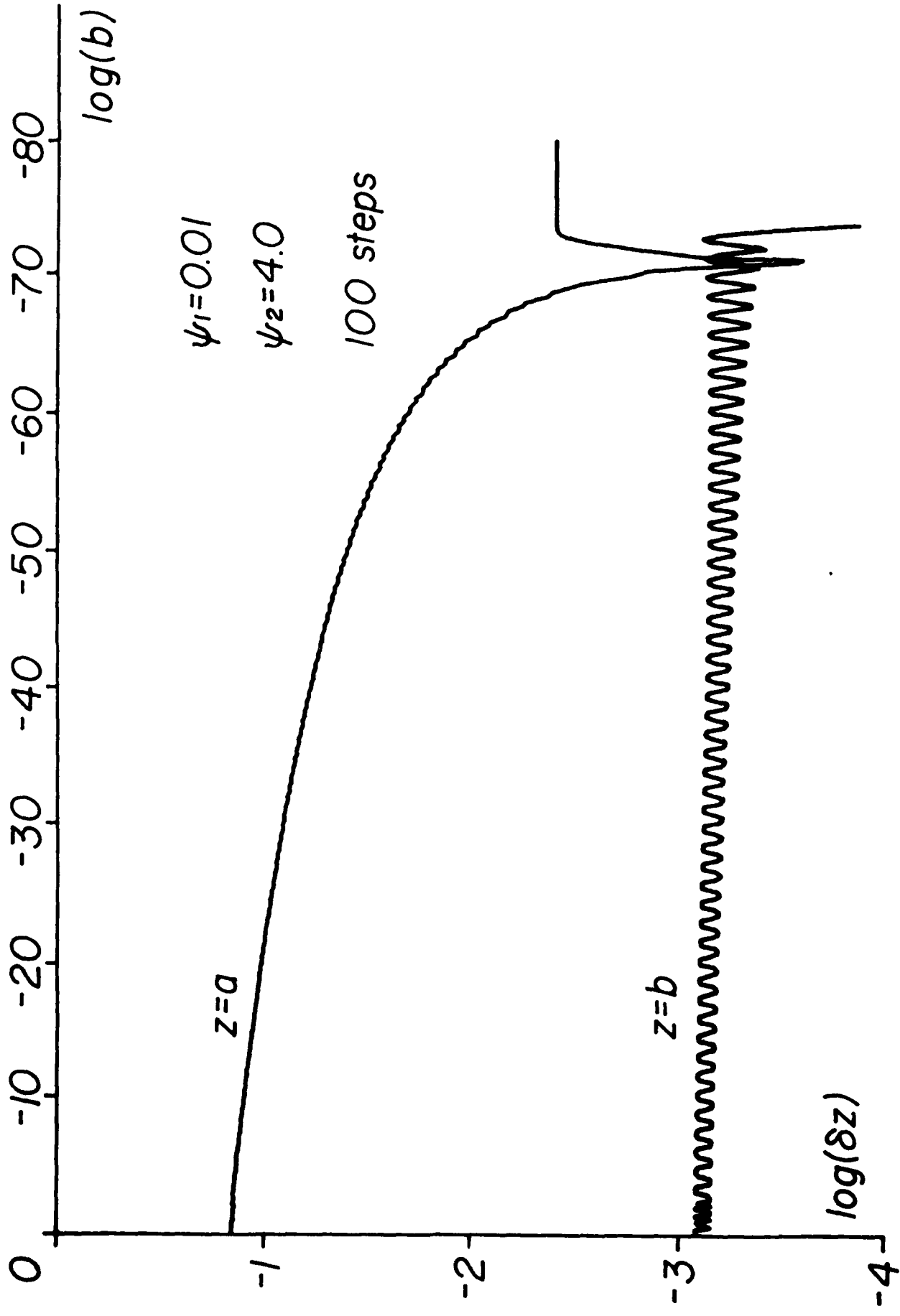












F. 1.6

Orthogonal Trajectory Accession to the
Nonlinear Equilibrium Curve

by

Isaac Fried^{*}
Boston University
Department of Mathematics
Boston, Mass. 02215 USA

* Professor

Abstract

An alternative to the Riks-Wempner-Crisfield iterative correction scheme is presented that does not require an explicit displacement-load accession path to the nonlinear equilibrium curve, nor a known equilibrium point. Its symmetry with respect to the displacement and load assures success in rounding limit points as well as turning points.

1. Introduction

Consider the single, implicit equilibrium curve

$$r(x, \lambda) = 0 \quad (1)$$

in which x is the displacement and λ the load. To trace λ versus x we shall have to compute close root pairs (x, λ) to eqn (1).

Since iterative methods must invariably be used to solve the nonlinear $r(x, \lambda) = 0$, two strategy decisions concerning the solution procedure have to be made: (i) how to advance from an established equilibrium point, say (x_0, λ_0) , to a next initial guess say (x_1, λ_1) ; and (ii) what corrective method to use if $r(x_1, \lambda_1)$ is untolerably large.

The simplest and cheapest tracking, or continuation, procedure for $r(x, \lambda) = 0$ consists of increasing λ_0 to λ_1 for a new initial guess $(x_1 = x_0, \lambda_1)$ and a (modified) Newton-Raphson iterative solution of $r(x, \lambda_1)$, with a constant load λ_1 .

That a monotonic λ sequence can miss sections of the equilibrium curve has long been pointed out [1,2]. To remedy this Riks [3,5], Wempner [4], Crisfield [6,7] and others [8,9] suggest an iterative approach to the equilibrium curve on a variable $\lambda = \lambda(x)$ load-displacement constraint. The difference between the different methods being that while Riks and Wempner advocate a linear (planar) constraint, Crisfield promotes a spherical one.

Continuation [10-11] of the equilibrium curve is invariably based on linearization. Let (x_n, λ_n) be a point in the (x, λ) plane not necessarily satisfying the equilibrium equation, $r(x_n, \lambda_n) \neq 0$. Let further $\delta x = x_{n+1} - x_n$ and $\delta \lambda = \lambda_{n+1} - \lambda_n$ denote the displacement and load corrections. Linearization of $r(x_n + \delta x, \lambda_n + \delta \lambda) = 0$ yields

$$r_n + r'_n \delta x + \dot{r}_n \delta \lambda = 0 \quad (2)$$

where $r' = dr/dx$ and $\dot{r} = dr/d\lambda$. Henceforth we shall omit the subscript n when referring to the current n th point.

As for the prediction, that is for the move from the already computed equilibrium point (x_0, λ_0) to the next initial guess (x_1, λ_1) , it is commonly agreed to supplement eqn. (2) with the elliptical constraint

$$\alpha^2 \delta x^2 + \beta^2 \delta \lambda^2 = s^2 \quad (3)$$

where α and β are scaling parameters and s the step size. Combining eqns. (2) and (3) we get

$$\delta \lambda_0 = \lambda_1 - \lambda_0 = \pm \frac{s r'}{(\alpha^2 r'^2 + \beta^2 r'^2)^{1/2}}, \quad \delta x_0 = x_1 - x_0 = \mp \frac{s \dot{r}}{(\alpha^2 r'^2 + \beta^2 r'^2)^{1/2}} \quad (4)$$

since $r(x_0, \lambda_0) = 0$. The choice of sign in eqn. (4) determines the direction of travel.

In this note we present and experiment with a correction procedure, based on the Newton-Raphson method as expressed in eqn. (2), whereby the initial guess (x_1, λ_1) is iteratively improved on an orthogonal trajectory to the equilibrium

curve, but with no analytical expression for it and without the involvement of the previously computed (x_0, λ_0) .

2. The Riks-Wempner method

The cleverness of this method lies in the replacement of the constant λ correction by the linear relationship

$$\alpha x + \beta \lambda = f \quad (5)$$

so that $\alpha \delta x + \beta \delta \lambda = 0$. Adding this constraint to eqn. (2) yields

$$\delta \lambda = \frac{\alpha r}{\beta r' - \alpha \dot{r}}, \quad \delta x = - \frac{\beta r}{\beta r' - \alpha \dot{r}} \quad (6)$$

or if the constraint line in eqn. (5) is chosen to be orthogonal to the tangent vector $(\delta x_0, \delta \lambda_0)$, as Riks and Wempner suggest, then

$$\delta \lambda = \frac{r}{r' \frac{\delta \lambda_0}{\delta x_0} - \dot{r}}, \quad \delta x = - \frac{r}{r' - \dot{r} \frac{\delta x_0}{\delta \lambda_0}} \quad (7)$$

In preparation for things to come we further observe that since $r'_0 \delta x_0 + \dot{r}_0 \delta \lambda_0 = 0$, eqn. (7) may be rewritten as

$$\delta \lambda = - \frac{r \dot{r}_0}{r' r'_0 + \dot{r} \dot{r}_0}, \quad \delta x = - \frac{r r'_0}{r' r'_0 + \dot{r} \dot{r}_0} \quad (8)$$

If $r(x, \lambda) = f(x) - \lambda$, then $r' = f'$, $\dot{r} = -1$, and eqn. (8) becomes

$$\delta \lambda = \frac{r}{1 + f' f'_0}, \quad \delta x = - \frac{r f'_0}{1 + f' f'_0} \quad (9)$$

that is shown to be directly obtainable from the Newton-Raphson method applied to the intersection of $r = r(x, \lambda)$ and $\lambda = -x/f'_o + s$. Indeed, since $\delta x = r/r'$, we have that $\delta x = -r/(f' - \lambda')$, but $\lambda' = -1/f'_o$ and hence eqn (9).

For the success and failure of the Riks-Wempner method in turning a limit point see Fig. 1.

3. The Crisfield method

Crisfield replaces the linear constraint in eqn (5) by the circular (elliptical)

$$(x - x_o)^2 + (\lambda - \lambda_o)^2 = s^2 \quad (10)$$

Using the linearization $r + r' \delta x + \dot{r} \delta \lambda = 0$ and the constraint $(x + \delta x - x_o)^2 + (\lambda + \delta \lambda - \lambda_o)^2 = s^2$, $\delta \lambda$ is eliminated and we are left with the quadratic equation [12]

$$\begin{aligned} \delta x^2(r'^2 + \dot{r}^2) + 2\delta x[r\dot{r}' + (x-x_o)\dot{r}^2 - (\lambda-\lambda_o)\dot{r}\dot{r}'] \\ + r^2 - 2(\lambda-\lambda_o)r\dot{r} = 0 \end{aligned} \quad (11)$$

for δx . The load increment $\delta \lambda$ is obtained either from $r + r' \delta x + \dot{r} \delta \lambda = 0$ or directly from the circular constraint.

A direct Newton-Raphson application to $r = r(x, \lambda)$, $(x - x_o)^2 + (\lambda - \lambda_o)^2 = s^2$ produces $\delta x = -r/dr/dx$, $dr/dx = r' - \dot{r}d\lambda/dx$, $(x - x_o)dx + (\lambda - \lambda_o)d\lambda = 0$, and

$$\delta x = -\frac{r}{r' - \dot{r} \frac{x - x_o}{\lambda - \lambda_o}} \quad (12)$$

or alternatively

$$\delta\lambda = - \frac{r}{\dot{r} - r' \frac{\lambda - \lambda_0}{x - x_0}} \quad (13)$$

It is interesting to compare eqns. (12), (13) with eqn. (7).

For the success and failure of the Crisfield method in rounding limit and turning points see Fig. 2.

4. Orthogonal trajectory

What we consider now is an orthogonal trajectory approach to the equilibrium curve without the need for an explicit constraint, and without the involvement of an equilibrium point (x_0, λ_0) . All we have to do for that is apply the Newton-Raphson method to $r = r(x, \lambda) = 0$ so as to have $\delta x = -r/dr/dx$, add to this $dr = r'dr + \dot{r}d\lambda$, and impose the orthogonality condition

$$\frac{d\lambda}{dx} \frac{r'}{\dot{r}} = 1 \quad (14)$$

and we get

$$\delta\lambda = - \frac{r\dot{r}}{r^2 + \dot{r}^2}, \quad \delta x = - \frac{rr'}{r^2 + \dot{r}^2} \quad (15)$$

which is symmetric in x and λ . Comparing this with eqn. (8) for the Riks-Wempner method reveals how the orthogonal constraint is updated here.

In fact, Ramm [13] has suggested a correction method that includes updated normals. When applied to $r(x, \lambda) = 0$, Ramm's method produces the load increment

$$\delta\lambda = - \frac{r}{\dot{r} - r' \frac{\lambda - \lambda_0}{x - x_0}} \quad (16)$$

involving not only the previous equilibrium point (x_0, λ_0) but also the new initial guess (x_1, λ_1) . It is interesting to compare eqn. (16) with eqns. (7) and (13).

5. The vector form

Our main interest is systems of nonlinear stiffness equation as produced by finite elements applied to elastic problems, and we turn our attention in this section to the application of the orthogonal trajectory method to problems with many degrees of freedom.

Let $\pi(x, \lambda)$ be the total potential energy of the discretization, with x being the displacement vector and λ the scalar load. Here $r(x, \lambda) = \partial\pi/\partial x$ is the gradient vector of π . If (x_0, λ_0) is, again, an equilibrium point so that $r(x_0, \lambda_0) = 0$, then a linear expansion around it is written as

$$\frac{\partial r}{\partial x} (x - x_0) + \frac{\partial r}{\partial \lambda} (\lambda - \lambda_0) = 0 \quad (17)$$

where $\partial r/\partial x$ is the stiffness matrix, say K , and where $\partial r/\partial \lambda$ is the load vector, say p . For how to compute K and p see [14-19].

A prediction with step size s subject to the constraint

$$(x_1 - x_0)^T (x_1 - x_0) + (\lambda_1 - \lambda_0)^2 = s^2 \quad (18)$$

together with the linearization

$$K_0 (x_1 - x_0) + (\lambda_1 - \lambda_0) p_0 = 0 \quad (19)$$

leads to the initial guess

$$\lambda_1 = \lambda_0 + s \left(1 + \mathbf{P}_0^T \mathbf{K}_0^{-1} \mathbf{K}_0^{-1} \mathbf{P}_0 \right)^{-\frac{1}{2}}, \quad x_1 = x_0 - \delta \lambda_0 \mathbf{K}_0^{-1} \mathbf{P}_0 \quad (20)$$

where $\delta \lambda_0 = \lambda_1 - \lambda_0$.

Newton-Raphson's correction applied to the system of linear equations

$r(x, \lambda) = 0$ becomes

$$\delta x = -\mathbf{K}^{-1} (\mathbf{r} + \delta \lambda \mathbf{p}) \quad (21)$$

A constant load iteration with $\delta \lambda = 0$ reduces eqn. (21) to $\delta x = -\mathbf{K}^{-1} \mathbf{r}$. A linear load-displacement constraint that relates $\delta \lambda$ to δx by

$$\delta \lambda = \mathbf{a}^T \delta x \quad (22)$$

with the given vector \mathbf{a} produces the correction

$$\delta \lambda = -\frac{\mathbf{a}^T \mathbf{K}^{-1} \mathbf{r}}{1 + \mathbf{a}^T \mathbf{K}^{-1} \mathbf{p}}, \quad \delta x = -\mathbf{K}^{-1} (\mathbf{r} + \delta \lambda \mathbf{p}) \quad (23)$$

For orthogonal trajectory accession we set $\mathbf{a} = \mathbf{K}^{-1} \mathbf{p}$, and have

$$\delta \lambda = -\frac{\mathbf{P}^T \mathbf{K}^{-1} \mathbf{K}^{-1} \mathbf{r}}{1 + \mathbf{P}^T \mathbf{K}^{-1} \mathbf{K}^{-1} \mathbf{P}}, \quad \delta x = -\mathbf{K}^{-1} (\mathbf{r} + \delta \lambda \mathbf{p}) \quad (24)$$

Observe that both the Riks-Wempner method and the present one call for the computation of $\mathbf{K}^{-1} \mathbf{r}$ and $\mathbf{K}^{-1} \mathbf{p}$, and otherwise entail comparable computational effort.

6. Midpoint correction

A Runge-Kutta type correction in the form of a midpoint reevaluation of the stiffness matrix and load vector is also often used [20] in nonlinear computational elasticity. In this method an initial guess is predicted along the tangent to the equilibrium curve with eqn. (20) but then K and p are reformed at $x = x_0 + \delta x/2$ and $\lambda = \lambda_0 + \delta\lambda/2$, and the new data is resubstituted into eqn. (20). Each step requires in this way two assemblies and two inversions.

An alternative of equal computational effort would be a linear prediction with one Newton-Raphson correction. It happens that this procedure is considerably more accurate than a midpoint correction.

It is sufficient that we analyze the methods on the parabolic stiffness equation $\lambda = \alpha x^2$, where $\alpha = \lambda''/2$, with the circular constraint $x^2 + \lambda^2 = s^2$. Their exact intersection point (x_e, λ_e) is at

$$x_e = \frac{1}{\alpha} \left[-\frac{1}{2} + \frac{1}{2} \left(1 + 4\alpha^2 s^2 \right)^{\frac{1}{2}} \right]^{\frac{1}{2}}, \quad \lambda_e = \frac{1}{2\alpha} \left[-1 + \left(1 + 4\alpha^2 s^2 \right)^{\frac{1}{2}} \right] \quad (25)$$

Without correction point p in Fig. 3, $(x = s, \lambda = 0)$ constitutes the approximation to equilibrium. Since both the exact solution (x_e, λ_e) and all other approximations are at an equal distance s from the origin we prefer to use the directional error

$$\varphi = \cos^{-1} \left(\frac{x x_e + \lambda \lambda_e}{s^2} \right) \quad (26)$$

of (x, λ) . For point p we have that $\varphi = \cos^{-1}(x_p/s)$, or the ^{w, M, M_e} expansions

$$x_e = s \left(1 - \frac{1}{2} \alpha^2 s^2 + \frac{1}{8} \alpha^4 s^4 - \dots \right), \quad \lambda_e = \alpha s^2 \left(1 - \alpha^2 s^2 + 2\alpha^4 s^4 - \dots \right) \quad (27)$$

we get that for tangent prediction only

$$\varphi = \alpha s \quad (28)$$

if s is small.

Midpoint correction reaches point m of Fig. 3 with

$$x = \frac{s}{(1+\alpha^2 s^2)^{\frac{1}{2}}} , \lambda = \frac{\alpha^2 s^2}{(1+\alpha^2 s^2)^{\frac{1}{2}}} \quad (29)$$

Using eqn. (27), and with similar expansions in powers of s of x and λ in eqn. (29) we have for small s that

$$\varphi = \frac{1}{2} \alpha^3 s^3 \quad (30)$$

which is a substantial improvement over eqn. (28).

One Newton-Raphson correction with a circular constraint leads to

$$\delta x = \frac{-2\alpha s^3 - s + s(1+3\alpha^2 s^2)^{\frac{1}{2}}}{1+4\alpha^2 s^2} , x = x + \delta x , \lambda = \alpha s^2 + 2\alpha s \delta x \quad (31)$$

and a directional error

$$\varphi = \frac{1}{4} \alpha^5 s^5 \quad (32)$$

which is two orders better than eqn. (30).

7. Numerical examples

The ability of orthogonal trajectory accession to succeed around limit points, bifurcation points, turning points, snap-throughs and detachments is numerically

demonstrated on two simple structural elastic problems.

First to be considered is the two member hinged truss shown in Fig. 5 in its original undeformed state. As the load λ is increased the two elastic bars shorten symmetrically until a snap-through occurs and the triangle is inverted.

A displacement x causes the strain

$$e = 1 - (1 + \frac{x^2}{2} - \frac{h}{2})^{\frac{1}{2}} \quad (33)$$

in the bars. With each bar being of the stiffness $k/2$ the total potential energy of the two bar system is $\pi(x) = ke^2 - \lambda x$, and hence

$$r(x, \lambda) = keee' - \lambda, \quad \dot{r} = -1, \quad \ddot{r} = k(e'^2 + ee'') \quad (34)$$

where

$$e' = \frac{h-x}{1-e}, \quad e'' = \frac{-1+e'^2}{1-e} \quad (35)$$

The exact equilibrium curve $r(x, \lambda) = 0$ is shown in Fig. 4.

Figure 4 shows also the convergence paths of orthogonal trajectory accession given by eqn. (15), for different starting points that are far from equilibrium. To observe the orthogonal trajectory one must look close to the end of the iterative approach. A starting point on the normal to a limit point converges in one step. Notice also the special attraction of the limit points.

Figure 5 shows the point by point continuation of the equilibrium curve of Fig. 4 with the predictor of eqn. (4) and the corrector of eqn. (15), with 3 Newton-Raphson corrections per step.

The two member truss shown in Fig. 5 is flat when $\lambda = 0$. Its behavior under load includes bifurcation, turning points, and detachment. Two degrees of freedom, x and ϕ , determine the configuration of the deformed system, whose total potential energy reads now

$$\pi(x, \phi) = 2k_2\phi^2 + k_1e^2 - \lambda x \quad (36)$$

where k_1 is the stiffness of each bar, k_2 the stiffness of the torsional spring at the vertex, and e the strain in the bars:

$$e = 1 - \frac{1-x}{\cos \phi} \quad (37)$$

The two stiffness equations are obtained from $\pi(x, \phi)$ through differentiation

$$\begin{aligned} \frac{\partial \pi}{\partial \phi} &= 4k_2\phi + e \frac{\partial e}{\partial \phi} = 0 \\ \frac{\partial \pi}{\partial x} &= 2k_1 \frac{\partial e}{\partial x} - \lambda = 0 \end{aligned} \quad (38)$$

If $k_1 = 1/2$ and $k_2 = \epsilon/16$, then after eliminating x between the pair of eqns. (38) we are left with

$$\phi \left(\lambda^2 \frac{\sin 2\phi}{2\phi} - \lambda \frac{\sin \phi}{\phi} + \frac{\epsilon}{4} \right) = 0 \quad (39)$$

When $\phi = 0$ we have either $\lambda = x$ or

$$\lambda = \frac{1}{2} [1 \pm (1-\epsilon)^{\frac{1}{2}}] \quad (40)$$

so that for $\epsilon < 1$ two bifurcation points occur on the λ -axis, and they coalesce for $\epsilon = 1$. As ϵ surpasses 1 the nonlinear bifurcation curve detaches from the

λ axis and a turning point (i.e. $d\lambda/dx = \infty$) is created. The critical φ^* and λ^* at which turning occurs are given by

$$\frac{\tan \phi^*}{\phi^*} = \epsilon, \quad \lambda^* = \frac{1}{2\cos \phi^*} \quad (41)$$

For a given $\epsilon > 1$ no nonlinear solution exists for $\varphi < \varphi^*$ whatever λ .

Tangential prediction plus orthogonal trajectory accession has no difficulty following the equilibrium curves past the turning points, as can be seen in Fig. 6. The two values of $\epsilon = 1.0235$ and $\epsilon = 1.1027$ in Fig. 6 correspond to $\varphi^* = \pi/12$ and $\varphi^* = \pi/6$, respectively.

Figure 7 uses ϕ and λ from Fig. 6 to trace λ res. x using

$$x = 1 + \cos \phi (\lambda \cos \phi - 1) \quad (42)$$

Finally, we compare the performance of the various continuation methods discussed in this paper in rounding a limit point ($d\lambda/dx = 0$) and a turning point ($d\lambda/dx = \infty$). The parabolic $r = \alpha x(1-x) - \lambda = 0$ has a limit point at $x = 1/2$, $\lambda = \alpha/4$ and is of the shape of Fig. 1. We choose $\alpha = 8$, $x_0 = 0.4375$ (at which $r' = 1$), and $\lambda_0 = 1.96875$. A tangential predictor of step size $s = 0.2$ lands us at $x_1 = 0.57892136$ and $\lambda_1 = 2.1101714$. This is approximately the situation shown in Fig. 1(b) and Fig. 2(a). Both the linear constraint method and Ramm's method fail to find an equilibrium point starting with these x_1 and λ_1 . Only the circular constraint method and the orthogonal trajectory method converge here - to different points, though, as can be seen in Table 1.

Reversing the roles of λ and x : $r = \alpha \lambda(1-\lambda) - x$ creates an equilibrium curve as in Fig. 2(b) with a turning point. Starting from the reversed $\lambda_1 = 0.57892136$

and $x_1 = 2.1101714$, the circular constraint method fails, but the orthogonal trajectory method, because of its inherent symmetry to x and λ , converges to the reversed values of x and λ in Table 1.

step	Circular constraint $s = 0.2$		orthogonal trajectory	
	x	λ	x	λ
0	0.57892136	2.1101714	0.57892136	2.1101714
1	0.62723680	1.8891614	0.50104992	2.0485029
2	0.62287506	1.8793660	0.50023522	2.0000049
3.	0.62283738	1.8792878	0.50023520	1.9999996
4	0.62283737	1.8792878	0.50023520	1.9999996

Table 1: Convergence of the circular constraint and orthogonal trajectory methods upon $r = 8x(1-x) - \lambda$.

References

- [1] J.H. Argyris, Continua and discontinua in matrix methods of structural analysis. AFFDL-TR-66-80, 11 (1966).
- [2] G.A. Thurston, Continuation of Newton's method through bifurcation points. J. Appl. Mech. 36, 425-430 (1969).
- [3] E. Riks, The application of Newton's method to the problem of elastic stability. J. Appl. Mech. 39, 1060-1066 (1972).
- [4] G.A. Wempner, Discrete approximations related to nonlinear theories of solids. Int. J. Solids Structures 7, 1581-1599 (1971).
- [5] E. Riks, An incremental approach to the solution of snapping and buckling problems. Int. J. Solids Structures 15, 329-551 (1979).
- [6] M.A. Crisfield, A fast incremental/iterative solution procedure that handles "snap-through." Computers & Structures 13, 55-62 (1981).
- [7] M.A. Crisfield, An arc-length method including line searches and accelerations. IJNME 19, 1269-1289 (1983).
- [8] J. Padorean and S. Tovichakchaikul, Self adaptive predictor-corrector algorithms for static nonlinear structural analysis. Computers & Structures 15, 365-377 (1982).
- [9] J. Padorean and S. Tovichakchaikul, Operating characteristics of hyperbolically and elliptically constrained self-adaptive incremental Newton-Raphson algorithms. J. of the Franklin Institute 316, 197-223 (1983).
- [10] E.L. Allgower and K. George, Simplicial and continuation methods for approximating fixed points and solutions to systems of equations. SIAM Reviews 22, 28-85 (1980).
- [11] E.L. Allgower, A survey of homotopy methods for smooth mappings in Numerical Solution of Nonlinear Equations (Edited by E.L. Allgower et al.) Springer-Verlag, Berlin (1981).
- [12] L.T. Watson and S.M. Holzer, Quadratic convergence of Crisfield's method. Computers and Structures 17, 69-72 (1983).
- [13] E. Ramm, Strategies for tracing the nonlinear response near limit points in Non-linear Finite Element Analysis in Structural Mechanics (Edited by W. Wunderlich et al.) Springer-Verlag, Berlin (1981).
- [14] I. Fried, Numerical Solution of Differential Equations, Academic Press, New York (1979).
- [15] I. Fried, Stability and equilibrium of the straight and curved elasto-finite element computation. CMAME 28, 49-61 (1981).

- [16] I. Fried, Nonlinear finite element computation of the equilibrium and stability of the circular plate. IJNME 17, 1427-1440 (1981).
- [17] I. Fried, Finite element computation of large rubber membrane deformations. IJNME 18, 653-660 (1982).
- [18] I. Fried, Nonlinear finite element computation of the equilibrium, stability and motion of the extensional beam and ring. CMAME 38, 29-44 (1983).
- [19] I. Fried, Large deformation static and dynamic finite element analysis of extensible cables. Computers and Structures 15, 315-319 (1982).
- [20] T.Y. Yang, Matrix displacement solution to elastica problems of beams and frames. Int. J. Solids structures 9, 829-842 (1973).

Figures

- 1) Success (a) and failure (b) of the linear constraint method.
- 2) Success (a) and failure (b) of the circular constraint method.
- 3) Midpoint and Newton-Raphson corrections with circular constraint.
- 4) Orthogonal trajectory convergence to the equilibrium curve of the truss in Fig. 5 from different starting points.
- 5) Pointwise tracking of the equilibrium curve with a tangential corrector and orthogonal trajectory corrections.
- 6) Computed equilibrium points for the two member truss.
- 7) As in Fig. 6 but x vs. λ .

Fig. 1

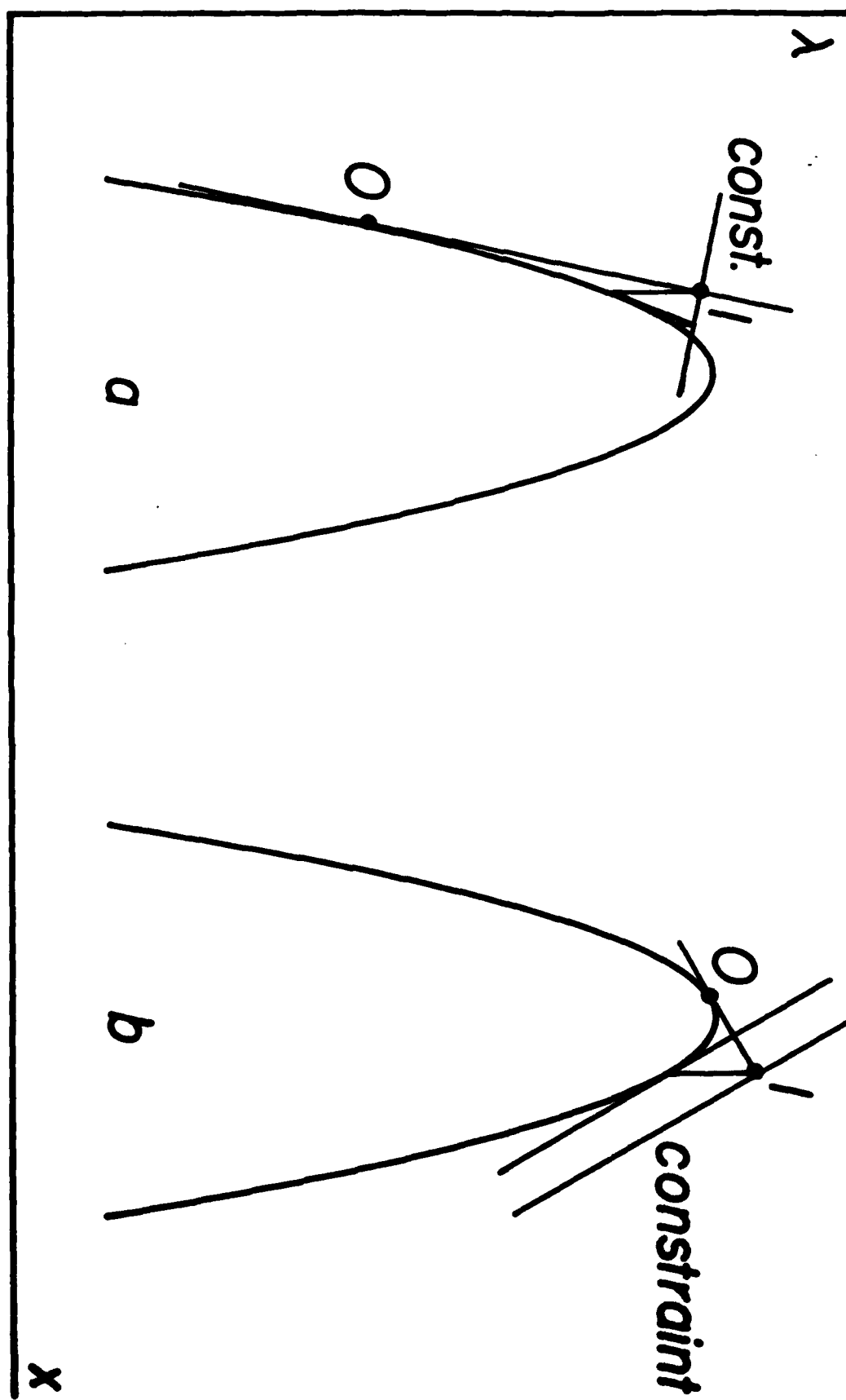


Fig. 2

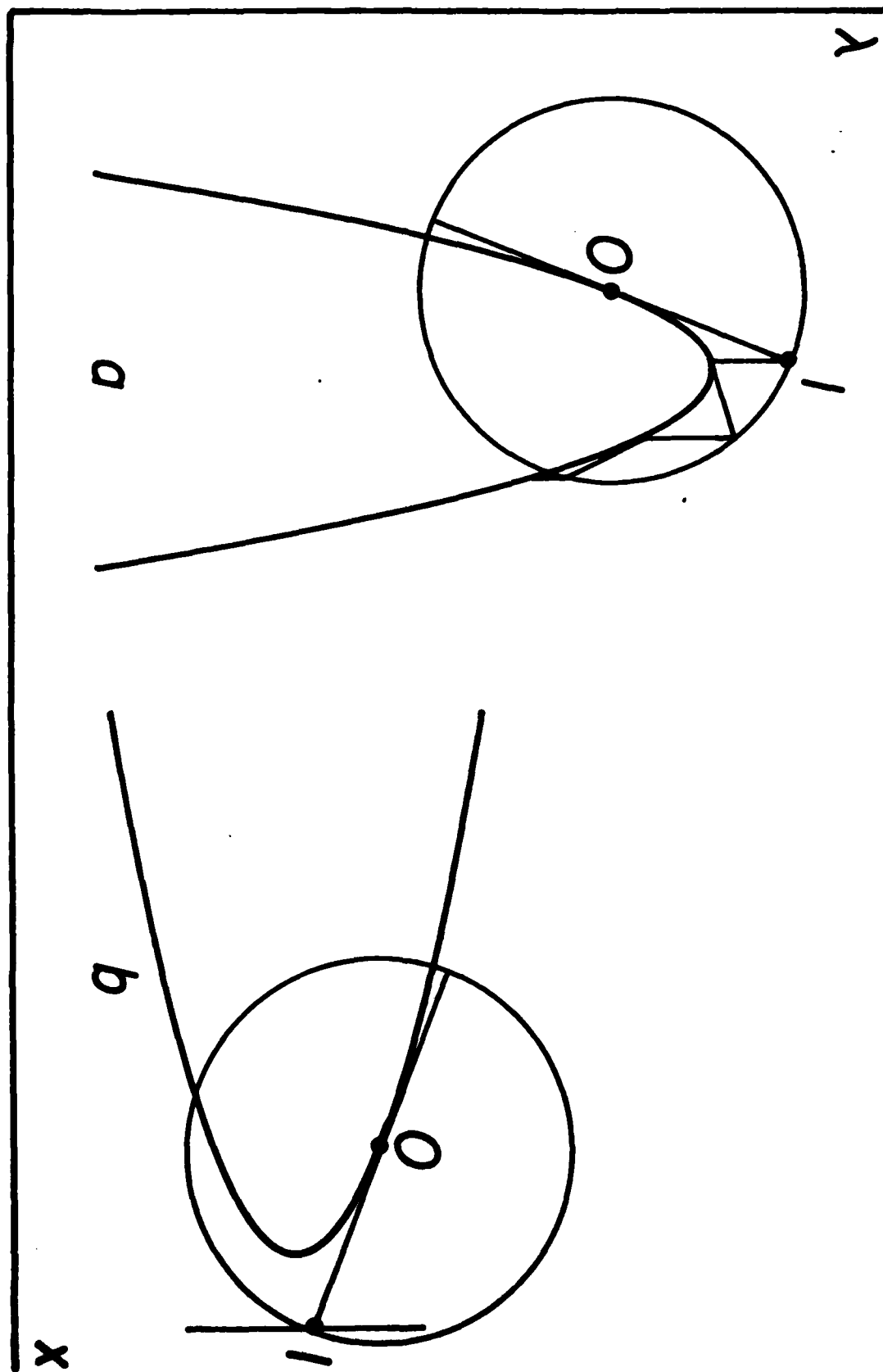


Fig.3

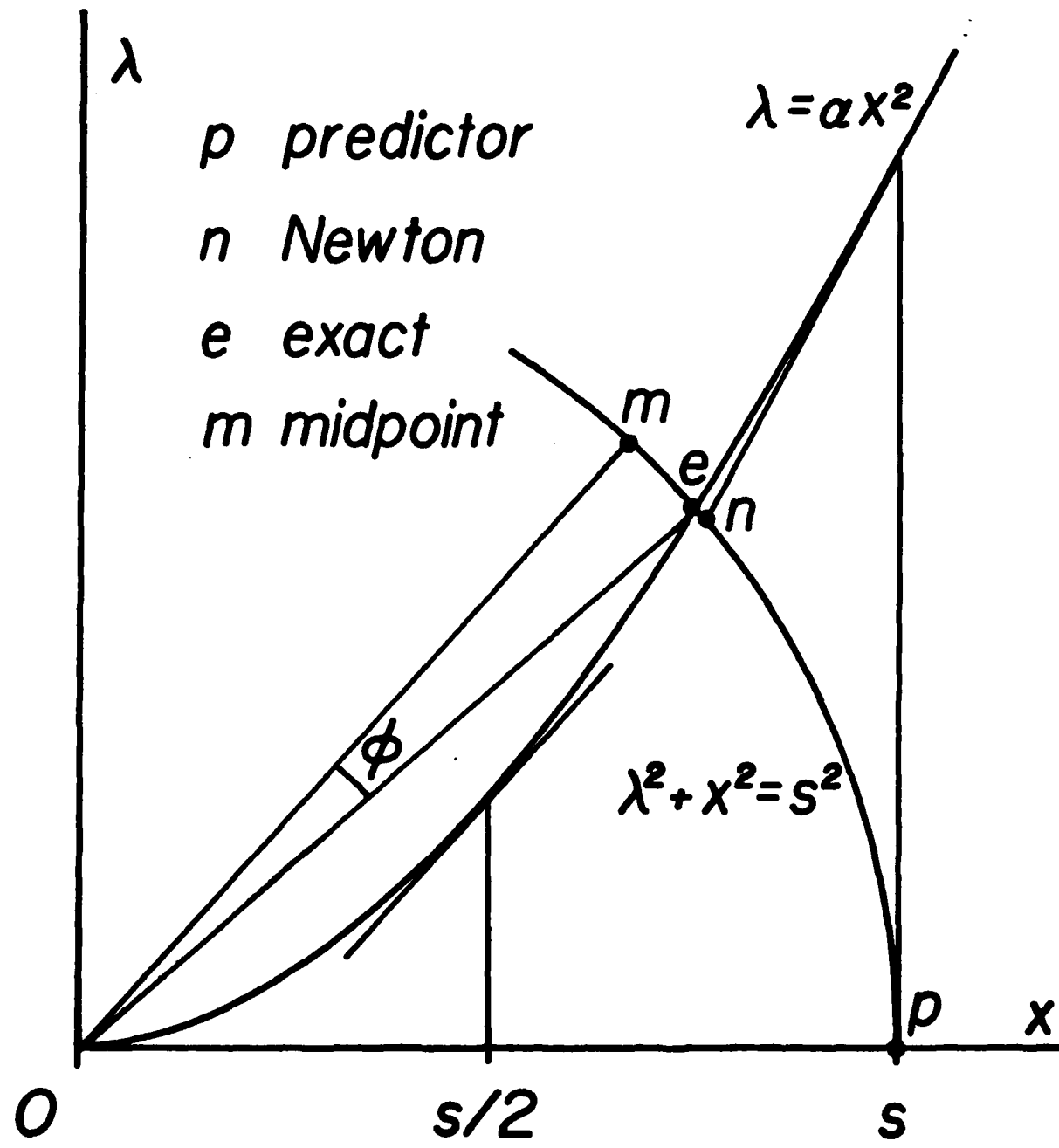


Fig. 4

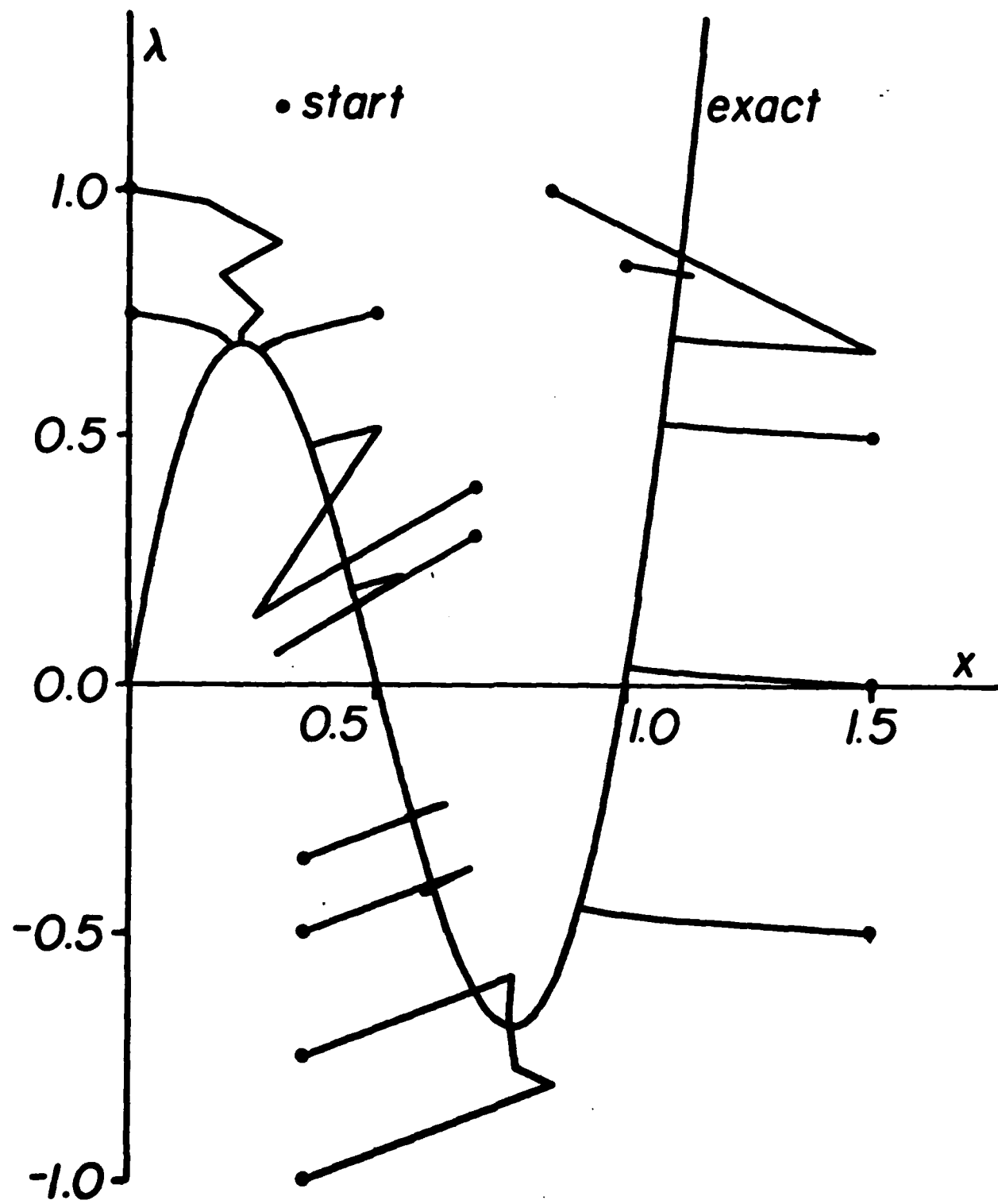


Fig.5

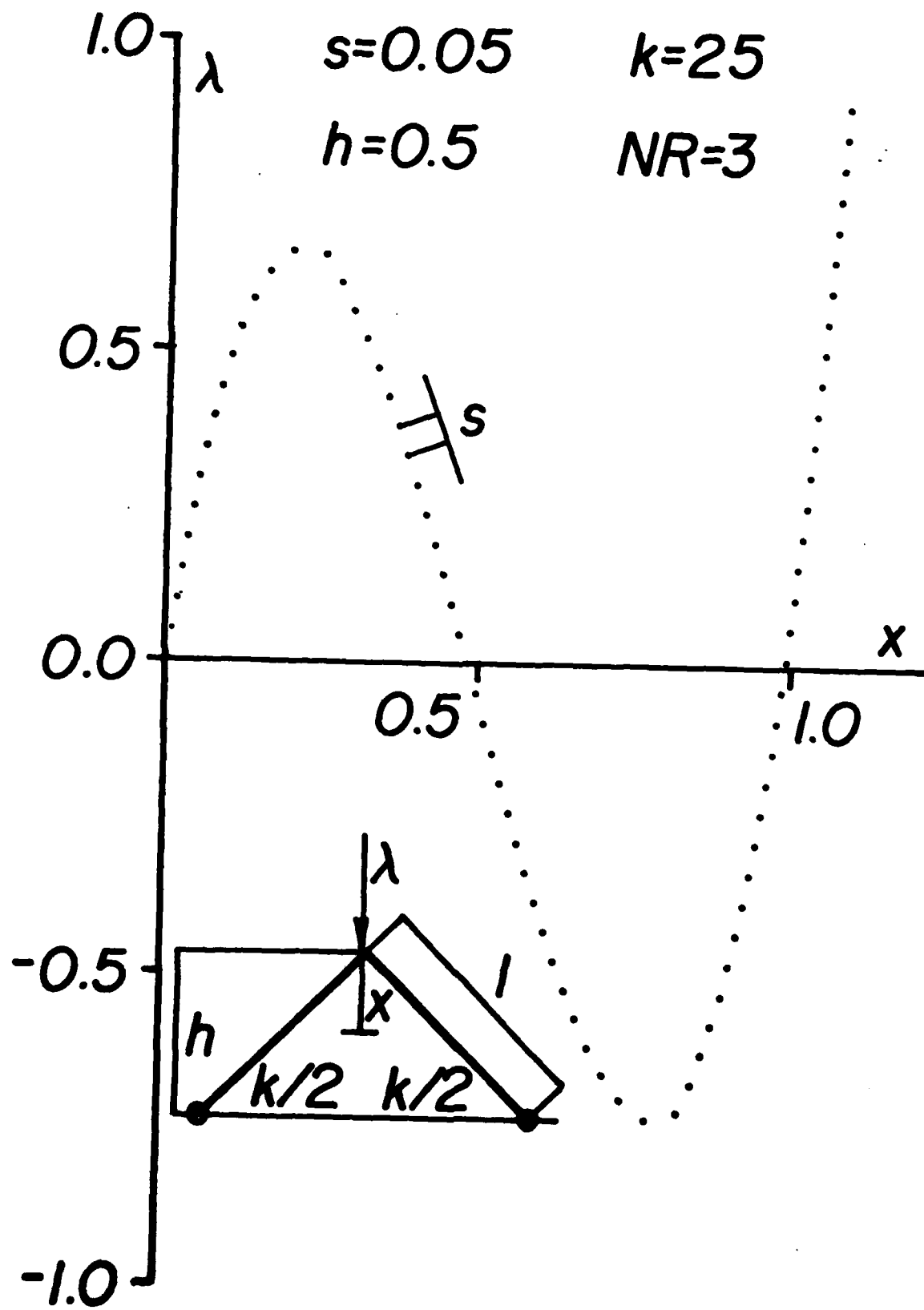


Fig. 6

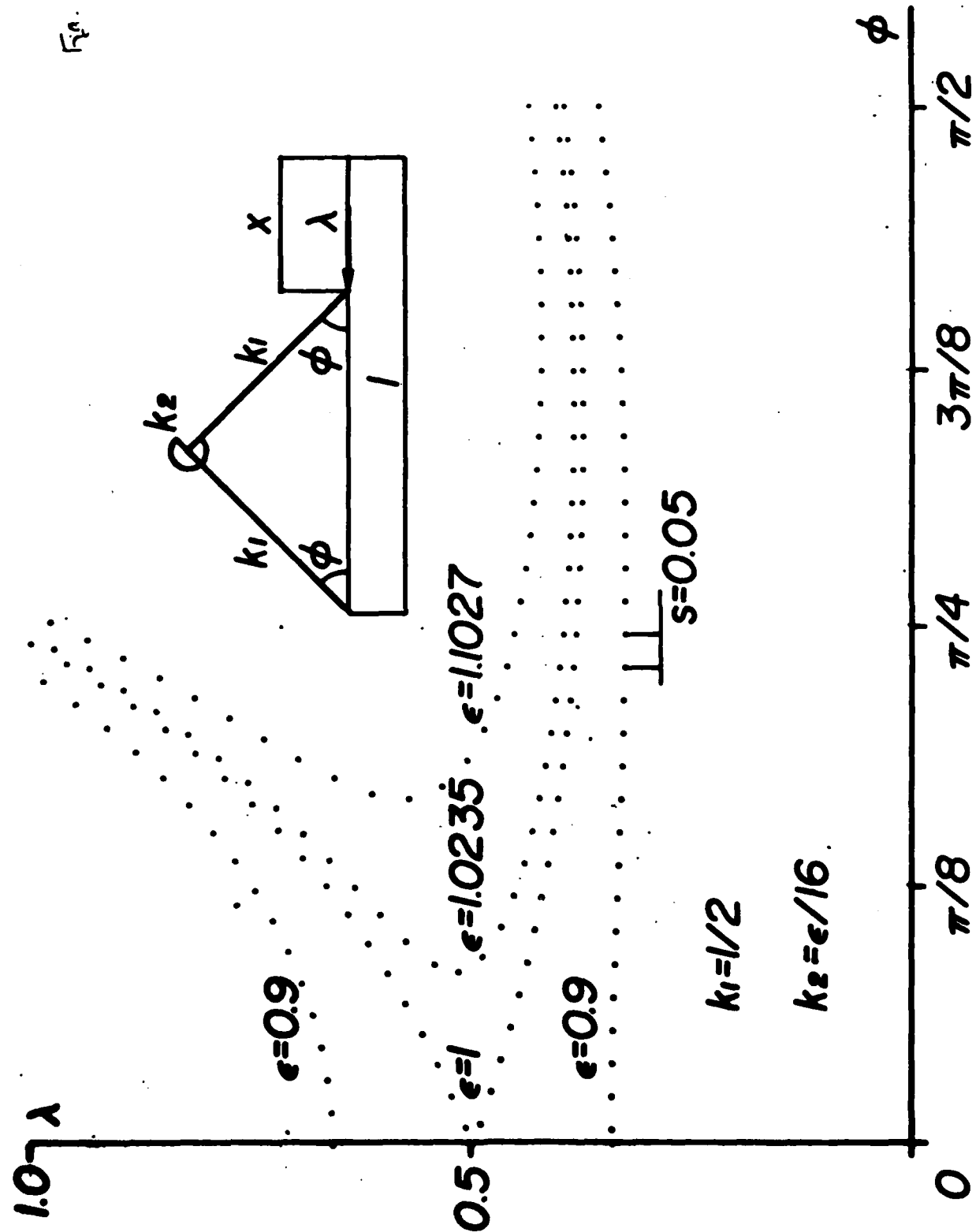
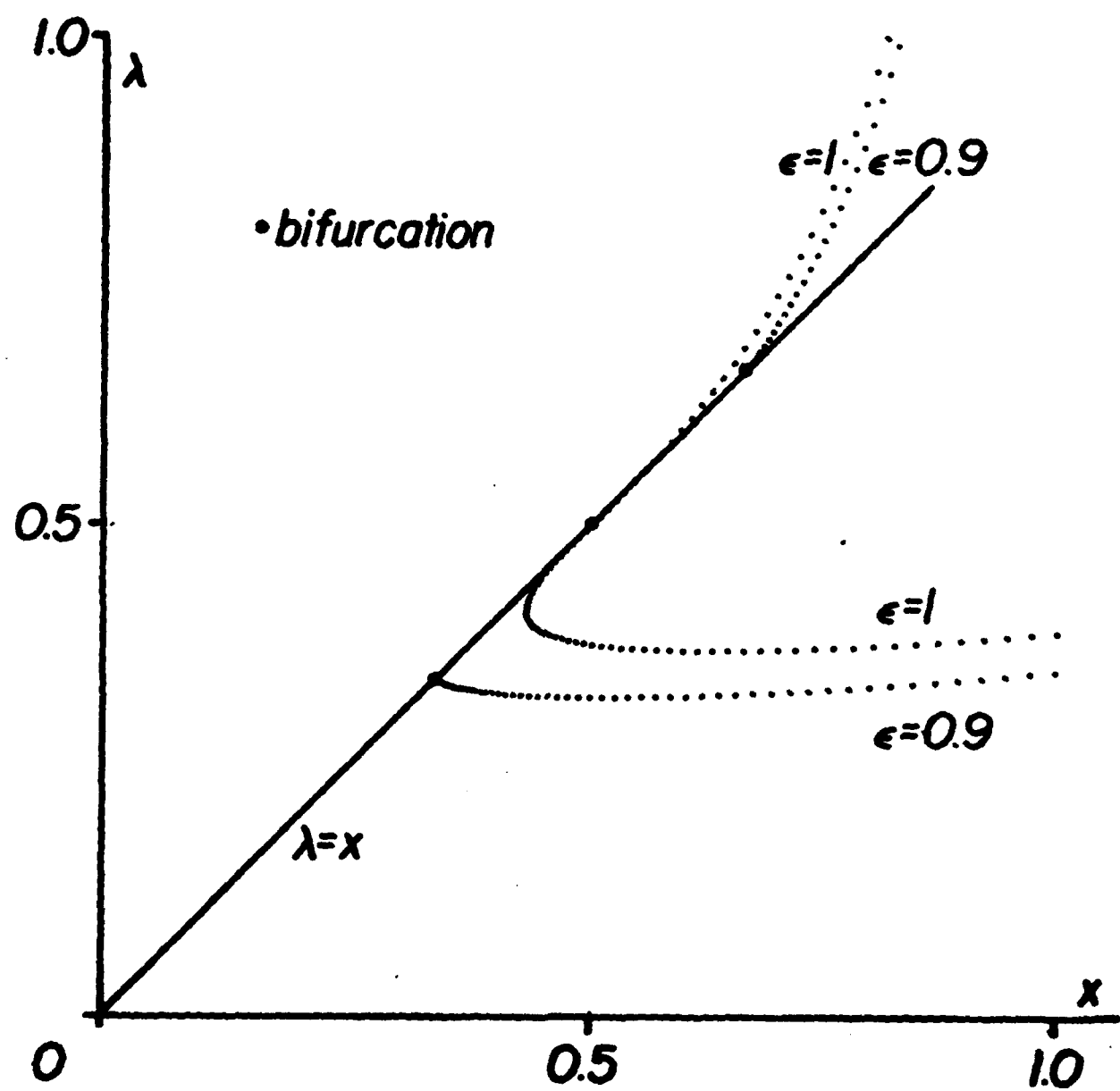


Fig. 1



Nonlinear Finite Element Analysis of
the Thin Elastic Shell of Revolution

by

Isaac Fried*
Boston University
Department of Mathematics
Boston, Mass. 02215

*Professor

Abstract

A cubic-cubic element stiffness matrix and element gradient are derived for the thin shell of revolution undergoing large axisymmetrical Kirchhoff deformation. Application is made to follow the nonlinear elastic distortion of a spherical shell under surface pressure and polar forces.

FOLLOWING
Reproduced from
best available copy.
PAGE'S

1. Introduction

Discrete integration of the total potential energy is used to derive the stiffness matrix and gradient of a cubic-cubic element for the thin shell of revolution that may undergo large elastic deformation. This element need not be small in the sense of approximating arc length and is routinely assembled for a Newton-Raphson solution. The same technique has been previously applied with success to study the large deformation of the circular plate [1], the cable [2], the elastica [3], the rubber membrane [4], and the curved extensible rod [5].

An example is made whereby a thin spherical shell is deformed under the combined action of polar forces and a surface pressure.

2. Elastic energy

Considering axisymmetric Kirchhoff deformation, shear is absent and the elastic energy of the stressed shell reduces to

$$\mathcal{E} = \frac{1}{2} \iiint_V (\sigma_1 \epsilon_1 + \sigma_2 \epsilon_2 + \sigma_3 \epsilon_3) dV \quad (1)$$

where σ_1 , σ_2 and σ_3 are the normal stresses, and ϵ_1 , ϵ_2 , ϵ_3 the corresponding strains. By V we denote the original, undeformed, volume of the elastic solid. We further assume that the elastic material obeys Hook's law so that stress is linearly related to strain by

$$\begin{aligned} \sigma_1 &= \frac{E}{1+\nu} \left(\epsilon_1 + \frac{\nu}{1-2\nu} e \right) \\ \sigma_2 &= \frac{E}{1+\nu} \left(\epsilon_2 + \frac{\nu}{1-2\nu} e \right) \\ \sigma_3 &= \frac{E}{1+\nu} \left(\epsilon_3 + \frac{\nu}{1-2\nu} e \right) \end{aligned} \quad (2)$$

where E is the elastic modulus, ν Poisson's ratio, and $\epsilon = \epsilon_1 + \epsilon_2 + \epsilon_3$. Following the common assumption that $\epsilon_3 = 0$ we have that

$$\epsilon_3 = -\frac{\nu}{1-\nu} (\epsilon_1 + \epsilon_2) \quad (3)$$

and

$$\sigma_1 = \frac{E}{1-\nu^2} (\epsilon_1 + \nu \epsilon_2) \quad (4)$$

$$\sigma_2 = \frac{E}{1-\nu^2} (\epsilon_2 + \nu \epsilon_1)$$

so that

$$E = \frac{1}{2} \frac{E}{1-\nu^2} \iiint_V (\epsilon_1^2 + 2\nu \epsilon_1 \epsilon_2 + \epsilon_2^2) dV \quad (5)$$

In case of a rod we add the stress assumption $\sigma_2 = 0$ and have that

$$\epsilon_2 = -\nu \epsilon_1, \quad \epsilon_3 = -\nu \epsilon_1 \quad (6)$$

and Eq. (2) reduces to $\sigma_1 = E \epsilon_1$. The elastic energy (5) becomes

$$E = \frac{1}{2} E \iiint_V \epsilon_1^2 dV \quad (7)$$

or

$$E = \frac{1}{2} E \int_S A(s) \epsilon_1^2 ds \quad (8)$$

where s denotes arc length and A the area of the cross section.

3. Displacements and strains

Let (x, y, z) be a point on the middle surface of the deformed shell of revolution so that

$$\begin{aligned}x &= r(\eta) \cos \theta \\y &= r(\eta) \sin \theta \\z &= z(\eta)\end{aligned}\tag{9}$$

Obviously $x^2 + y^2 = r^2$. It is helpful to introduce the angle ϕ measured between \vec{r} and the tangent to the generating curve. With this the position vector \vec{r} and unit normal to the middle surface, \vec{n} are written as

$$\vec{r} = (r \cos \theta, r \sin \theta, z), \vec{n} = (\sin \phi \cos \theta, \sin \phi \sin \theta, -\cos \phi) \tag{10}$$

The position vector of a point on \vec{n} at a distance ζ from the middle surface is

$$\vec{R} = \vec{r} + \zeta \vec{n} \tag{11}$$

and

$$d\vec{R} = d\vec{r} + d\zeta \vec{n} + \zeta d\vec{n} \tag{12}$$

Since $d\vec{r}$ is in the tangent plane and $\vec{n} \cdot \vec{n} = 1$, we have that $\vec{n} \cdot d\vec{r} = 0$, $\vec{n} \cdot d\vec{n} = 0$, and $ds^2 = d\vec{R} \cdot d\vec{R}$ becomes

$$ds^2 = d\vec{r} \cdot d\vec{r} + \zeta^2 d\vec{n} \cdot d\vec{n} + d\zeta^2 + 2\zeta d\vec{r} \cdot d\vec{n} \tag{13}$$

where

$$\begin{aligned} d\vec{r} &= \frac{\partial \vec{r}}{\partial \eta} d\eta + \frac{\partial \vec{r}}{\partial \theta} d\theta \\ d\vec{n} &= \frac{\partial \vec{n}}{\partial \phi} d\phi + \frac{\partial \vec{n}}{\partial \theta} d\theta \end{aligned} \quad (14)$$

Because η and θ are orthogonal

$$\begin{aligned} \frac{\partial \vec{r}}{\partial \eta} \cdot \frac{\partial \vec{r}}{\partial \theta} &= 0, \quad \frac{\partial \vec{n}}{\partial \phi} \cdot \frac{\partial \vec{n}}{\partial \theta} = 0 \\ \frac{\partial \vec{r}}{\partial \eta} \cdot \frac{\partial \vec{n}}{\partial \theta} &= 0, \quad \frac{\partial \vec{n}}{\partial \phi} \cdot \frac{\partial \vec{r}}{\partial \theta} = 0 \end{aligned} \quad (15)$$

we are left with

$$\begin{aligned} d\vec{r} \cdot d\vec{r} &= \alpha^2 d\eta^2 + r^2 d\theta^2 \\ d\vec{n} \cdot d\vec{n} &= \phi'^2 d\eta^2 + \sin^2 \phi d\theta^2 \\ d\vec{r} \cdot d\vec{n} &= \alpha \phi' d\eta^2 + r \sin \phi d\theta^2 \end{aligned} \quad (16)$$

where prime denotes differentiation with respect to η and

$$\begin{aligned} \alpha &= (r'^2 + z'^2)^{\frac{1}{2}}, \quad \sin \phi = \frac{z'}{\alpha}, \quad \cos \phi = \frac{r'}{\alpha} \\ \phi' &= \frac{z'' r' - z' r''}{\alpha^2} \end{aligned} \quad (17)$$

Finally

$$ds^2 = (\alpha + \zeta \phi')^2 d\eta^2 + (r + \zeta \sin \phi)^2 d\theta^2 + dz^2 \quad (18)$$

as compared to the original

$$ds^2 = (\alpha_0 + \zeta\phi'_0)^2 dy^2 + (r_0 + \zeta \sin\phi'_0)^2 d\theta^2 + d\zeta^2 \quad (19)$$

Notice that no distinction is made between r_0 and α_0 . Hence the strains are here

$$\epsilon_1(\zeta) = \frac{\alpha - \alpha_0 + \zeta(\phi' - \phi'_0)}{\alpha_0 + \zeta\phi'_0} \quad (20)$$

and

$$\epsilon_2(\zeta) = \frac{r - r_0 + \zeta(\sin\phi - \sin\phi'_0)}{r_0 + \zeta \sin\phi'_0} \quad (21)$$

4. Integration with respect to ζ

From Eq. (19) we get the element of volume

$$dV = r_0 \alpha_0 (1 + \zeta \beta_0) (1 + \zeta \gamma_0) d\zeta dy d\theta \quad (22)$$

in which $\beta_0 = \phi'_0 / \alpha'_0$ and $\gamma_0 = \sin\phi'_0 / r_0$. Substituting dV in Eq. (22) and the strains $\epsilon_1(\zeta)$ and $\epsilon_2(\zeta)$ in Eqs. (20) and (21) into the elastic energy expression in Eq. (5) we integrate it analytically with respect to ζ between $-t/2$ and $t/2$, where t denotes the thickness of the shell.

In doing this we encounter integrals of the form

$$\int_{-\frac{t}{2}}^{\frac{t}{2}} \frac{mx^3 + nx^2 + px + q}{ax + 1} = \frac{m}{3a}x^3 + \frac{an - m}{2a^2}x^2 + \frac{a^2p - an + m}{a^3}x + \left. \frac{a^2(aq - p) + an - m}{a^4} \ln(ax + 1) \right|_{-\frac{t}{2}}^{\frac{t}{2}} \quad (23)$$

or if $|ax| < < 1$

$$\ln(ax + 1) = ax - \frac{1}{2}a^2x^2 + \frac{1}{3}a^3x^3 - \frac{1}{4}a^4x^4 + O(a^5x^5) \quad (24)$$

and

$$\int_{-\frac{t}{2}}^{\frac{t}{2}} \frac{mx^3 + nx^2 + px + q}{ax + 1} = tq + \frac{t^3}{12}(a^2q - ap + n) \quad (25)$$

Now

$$\begin{aligned} E &= \frac{2\pi E}{1-\nu^2} \frac{1}{2} \int \alpha_0 r_0 \left\{ t (\epsilon_1^2 + 2\nu \epsilon_1 \epsilon_2 + \epsilon_2^2) \right. \\ &\quad \left. + \frac{t^3}{12} [(\kappa_1 - \epsilon_1 \beta_0)^2 + (\kappa_2 - \epsilon_2 \beta_0)^2 + \epsilon_1 \beta_0 (2\kappa_1 - \epsilon_1 \beta_0) + \epsilon_2 \beta_0 (2\kappa_2 - \epsilon_2 \beta_0) \right. \\ &\quad \left. + 2\nu \kappa_1 \kappa_2] \right\} d\theta \end{aligned}$$

where

$$\epsilon_1 = \frac{\alpha}{\alpha_0} - 1, \quad \epsilon_2 = \frac{r}{r_0} - 1, \quad \kappa_1 = \frac{\phi' - \phi'_0}{\alpha_0}$$

$$\kappa_2 = \frac{\sin \phi - \sin \phi_0}{r_0}, \quad \beta_0 = \frac{\phi'_0}{\alpha_0}, \quad \beta_0' = \frac{\sin \phi_0}{r_0} \quad (27)$$

If $|t \beta_0/2|$ and $|t r_0/2|$ are ignored relative to 1 the elastic energy of the shell simplifies into

$$\begin{aligned} E = & \frac{2\pi E}{1-\nu^2} \frac{1}{2} \int \alpha_0 r_0 \left[t (\epsilon_1^2 + 2\nu \epsilon_1 \epsilon_2 + \epsilon_2^2) \right. \\ & \left. + \frac{t^3}{12} (K_1 + 2\nu K_1 K_2 + K_2^2) \right] dy \end{aligned} \quad (28)$$

For the spherical shell Eq. (28) is obtained without simplification but because $\epsilon_0 = \gamma_0$.

5. The plate and beam

When the shell of revolution is a flat circular plate

$$\begin{aligned} \phi_0 &= 0, \sin \phi_0 = 0, z_0 = 0, z'_0 = 0 \\ r_0 &= 2, r'_0 = 1, \alpha_0 = 1 \end{aligned} \quad (29)$$

and

$$\begin{aligned} E = & \frac{2\pi E}{1-\nu^2} \frac{1}{2} \int r_0 \left[t (\epsilon_1^2 + 2\nu \epsilon_1 \epsilon_2 + \epsilon_2^2) \right. \\ & \left. + \frac{t^3}{12} \left(\phi'^2 + \frac{\sin^2 \phi}{2^2} + 2\nu \phi' \frac{\sin \phi}{2} \right) \right] dy \end{aligned} \quad (30)$$

where $\epsilon_1 = (r'^2 + z'^2)^{1/2} - 1$ and $\epsilon_2 = r/r_0 - 1$.

For the beam we set in Eq. (26)

$$\epsilon_2 = K_2 = \gamma_0 = \nu = 0, 2\pi r_0 = 1 \quad (31)$$

and have that

$$\mathcal{E} = \frac{1}{2} E \int [t \epsilon_1^2 + \frac{t^3}{12} (\phi' - \alpha \phi'_0)^2] \alpha_0 dy \quad (32)$$

If the axial extension is small we may set $\alpha = \alpha_0 = 1$, and

$$\mathcal{E} = \frac{1}{2} E \int [t \epsilon_1^2 + \frac{t^3}{12} (\phi' - \phi'_0)^2] ds \quad (33)$$

with

$$\epsilon_1 = (z'^2 + r'^2)^{\frac{1}{2}} - 1, \quad \phi' = z''r' - z'r'' \quad (34)$$

6. Stress resultants

These are defined as

$$N_1 = \frac{\partial \mathcal{E}}{\partial \epsilon_1}, \quad N_2 = \frac{\partial \mathcal{E}}{\partial \epsilon_2}$$

$$M_1 = \frac{\partial \mathcal{E}}{\partial \kappa_1}, \quad M_2 = \frac{\partial \mathcal{E}}{\partial \kappa_2} \quad (35)$$

and from Eq. (26) we have them as

$$N_1 = \frac{Et}{1-\nu^2} [\epsilon_1 + \nu \epsilon_2 - \frac{t^2}{12} (\beta_0 - \gamma_0)(\kappa_1 - \epsilon_1 \beta_0)] \quad (36)$$

$$N_2 = \frac{Et}{1-\nu^2} [\epsilon_2 + \nu \epsilon_1 - \frac{t^2}{12} (\gamma_0 - \beta_0)(\kappa_2 - \epsilon_2 \gamma_0)]$$

and

$$M_1 = \frac{Et^3}{12(1-\nu^2)} [K_1 + \nu K_2 - \epsilon_1 (\beta_0 - \gamma_0)] \quad (37)$$

$$M_2 = \frac{Et^3}{12(1-\nu^2)} [K_2 + \nu K_1 - \epsilon_2 (\delta_0 - \beta_0)]$$

7. Differentiation with respect to a vector

Let $f(x) = f(x_1, x_2, \dots, x_n)$ be a scalar function of the vector argument x .

We define the differentiation of f with respect to the vector x as

$$\frac{\partial f}{\partial x} = f' = \frac{\partial f}{\partial x_i}, \quad \frac{\partial^2 f}{\partial x^2} = f'' = \frac{\partial^2 f}{\partial x_i \partial x_j}. \quad (38)$$

Notice that f' is a vector and f'' is a symmetric matrix.

Obviously

$$(f+g)' = f' + g', \quad (cf)' = cf', \quad (fg)' = gf' + fg' \quad (39)$$

but

$$(gf')' = g f'' + f' g'^T \quad (40)$$

where

$$f' g'^T = \frac{\partial f}{\partial x_i} \frac{\partial g}{\partial x_j} \quad (41)$$

is a nonsymmetric matrix. The matrix

$$(fg)'' = gf'' + fg'' + f'g'^T + g'f'^T \quad (42)$$

is symmetric.

8. Cubic-Cubic shell element

Let η in Eq. (26) measure arc along the generator so that $\eta_0 = 1$ and $d\eta = ds$. The finite element extends between s_1 and $s_1 + h$ so that $s = s_1 + h\xi$, $0 \leq \xi \leq 1$, and $ds = h d\xi$, $()' = h^{-1}(\xi)$, $()'' = h^{-2}(\xi)$. To have a cubic-cubic element we choose the nodal values vector

$$u_e^T = (r_1, \dot{r}_1, z_1, \dot{z}_1, r_2, \dot{r}_2, z_2, \dot{z}_2) \quad (43)$$

and interpolate r and z with

$$r = u_e^T \phi, \quad z = u_e^T \psi \quad (44)$$

where ϕ and ψ are shape function vectors

$$\phi^T = (\phi_1, \phi_2, 0, 0, \phi_3, \phi_4, 0, 0), \quad \psi^T = (0, 0, \phi_1, \phi_2, 0, 0, \phi_3, \phi_4) \quad (45)$$

with

$$\phi_1 = 1 - 3\xi^2 + 2\xi^3, \quad \phi_2 = \xi - 2\xi^2 + \xi^3, \quad \phi_3 = 3\xi^2 - 2\xi^3, \quad \phi_4 = -\xi^2 + \xi^3 \quad (46)$$

We integrate the total potential energy by sampling at the three Gauss points

$$\xi_1 = \frac{1}{10}(5 - \sqrt{15}), \quad \xi_2 = \frac{1}{2}, \quad \xi_3 = \frac{1}{10}(5 + \sqrt{15}) \quad (47)$$

with weights

$$w_1 = w_3 = \frac{5}{18} \quad , \quad w_2 = \frac{8}{18} \quad (48)$$

The values of $r, z, \dot{r}, \dot{z}, \ddot{r}, \ddot{z}$ at the three integration points ξ_j , $j = 1, 2, 3$ are given by

$$\begin{aligned} r_j &= \mathbf{U}_e^T \phi_j, \quad \dot{r}_j = \mathbf{U}_e^T \dot{\phi}_j, \quad \ddot{r}_j = \mathbf{U}_e^T \ddot{\phi}_j \\ z_j &= \mathbf{U}_e^T \psi_j, \quad \dot{z}_j = \mathbf{U}_e^T \dot{\psi}_j, \quad \ddot{z}_j = \mathbf{U}_e^T \ddot{\psi}_j \end{aligned} \quad (49)$$

where ϕ_j and ψ_j shortly stand for $\phi(\xi_j)$ and $\psi(\xi_j)$, and

$$\begin{aligned} \phi_{1,1}^1 &= \frac{1}{100}(50 + 12\sqrt{15}, 5 + \sqrt{15}, 0, 0, 50 + 12\sqrt{15}, -5 + \sqrt{15}, 0, 0) \\ \phi_{2,1}^1 &= \frac{1}{8}(4, 1, 0, 0, -4, -1, 0, 0), \\ \dot{\phi}_{1,1}^1 &= \frac{1}{10}(-6, 2 + \sqrt{15}, 0, 0, 6, 2\sqrt{15}, 0, 0), \\ \dot{\phi}_{2,1}^1 &= \frac{1}{8}(-6, -1, 0, 0, 6, -1, 0, 0), \\ \ddot{\phi}_{1,1}^1 &= \frac{1}{10}(76\sqrt{15}, -5 + 3\sqrt{15}, 0, 0, -6\sqrt{15}, 5 + 3\sqrt{15}, 0, 0), \\ \ddot{\phi}_{2,1}^1 &= (0, -1, 0, 0, 0, 1, 0, 0) \\ \phi_{1,3}^1 &= \frac{1}{100}(0, 0, 50 + 12\sqrt{15}, 5 \pm \sqrt{15}, 0, 0, 50 + 12\sqrt{15}, -5 \pm \sqrt{15}), \\ \phi_{2,3}^1 &= \frac{1}{8}(0, 0, 4, 1, 0, 0, 4, -1), \\ \dot{\phi}_{1,3}^1 &= \frac{1}{10}(0, 0, -6, 2 + \sqrt{15}, 0, 0, 6, 2\sqrt{15}), \\ \dot{\phi}_{2,3}^1 &= \frac{1}{8}(0, 0, -6, -1, 0, 0, 6, -1), \\ \ddot{\phi}_{1,3}^1 &= \frac{1}{10}(0, 0, -6\sqrt{15}, -5 + 3\sqrt{15}, 0, 0, -6\sqrt{15}, 5 + 3\sqrt{15}), \\ \ddot{\phi}_{2,3}^1 &= (0, 0, 0, -1, 0, 0, 0, 1), \end{aligned} \quad (50)$$

where the upper sign of $\sqrt{15}$ is for Gauss point 1 and the lower for Gauss point 3.

We choose to derive the element data from the simpler energy expression (28)

and write for the e th element

$$\begin{aligned} \mathcal{E}_e^* &= \frac{1}{2} h \sum_{j=1}^3 w_j r_{0j} \left[c (\epsilon_{1j}^2 + 2\nu \epsilon_{1j} \epsilon_{2j} + \epsilon_{2j}^2) \right. \\ &\quad \left. + (K_{1j}^2 + 2\nu K_{1j} K_{2j} + K_{2j}^2) \right] \end{aligned} \quad (51)$$

where j refers to the j th Gauss sampling point, and where

$$c = \frac{12}{t^2}, \quad \varepsilon^* = \frac{12(1-\nu^2)}{2\pi E t^3} \varepsilon \quad (52)$$

From

$$g_e = \frac{\partial \varepsilon_e^*}{\partial u_e}, \quad k_e = \frac{\partial^2 \varepsilon_e^*}{\partial u_e^2} \quad (53)$$

we have that

$$g_e = h \sum_{j=1}^3 w_j r_{0j} \left\{ c \left[\epsilon_{1j} \epsilon'_{1j} + \nu (\epsilon_{1j} \epsilon'_{2j} + \epsilon'_{1j} \epsilon_{2j}) + \epsilon_{2j} \epsilon'_{2j} \right] + K_{1j} K'_{1j} + \nu (K_{1j} K'_{2j} + K_{2j} K'_{1j}) + K_{2j} K'_{2j} \right\} \quad (54)$$

and

$$k_e = h \sum_{j=1}^3 w_j r_{0j} \left\{ \epsilon'_{1j} \epsilon'^T_{1j} + \epsilon'_{1j} \epsilon''_{1j} + \nu (\epsilon'_{1j} \epsilon'^T_{2j} + \epsilon'_{1j} \epsilon''_{2j} + \epsilon'_{2j} \epsilon'^T_{1j} + \epsilon'_{2j} \epsilon''_{1j}) \right\} + K'_1 K'^T_1 + K'_1 K''_1 + K'_2 K'^T_2 + K'_2 K''_2 + \nu (K'^T_1 K'^T_2 + K'_1 K''_2 + K'_2 K''_1 + K'^T_2 K'^T_1) \quad (55)$$

where $(\cdot)' = \partial / \partial u_e$.

To shorten the notation we introduce

$$f = \ddot{z} \dot{r} - \dot{z} \ddot{r}, \quad g = \dot{r}^2 + \dot{z}^2 \quad (56)$$

so that

$$\epsilon_1 = h^{-1} g^{\frac{1}{2}} - 1 \quad , \quad \kappa_1 = h^{-1} g^{-1} f - \beta_0 \quad (57)$$

$$\epsilon_2 = r_0 r - 1 \quad , \quad \kappa_2 = r_0^{-1} g^{-\frac{1}{2}} z - \gamma_0$$

and

$$f' = \dot{r}\ddot{\psi} + \dot{\phi}\ddot{z} - \ddot{r}\dot{\psi} - \dot{z}\dot{\phi} \quad , \quad g' = 2(\dot{r}\dot{\phi} + \dot{z}\dot{\psi}) \\ f'' = \ddot{\psi}\dot{\phi}^T + \dot{\phi}\ddot{\psi}^T - \dot{\psi}\dot{\phi}^T - \dot{\phi}\dot{\psi}^T \quad , \quad g'' = 2(\dot{\phi}\dot{\phi}^T + \dot{\psi}\dot{\psi}^T) \quad (58)$$

Next we write

$$\epsilon'_1 = \frac{1}{2} h^{-1} g^{-\frac{1}{2}} g' \quad , \quad \kappa'_1 = h^{-1} (g^{-1} f' - g^{-2} f g') \\ \epsilon'_2 = r_0^{-1} \phi \quad , \quad \kappa'_2 = r_0^{-1} (g^{-\frac{1}{2}} \dot{\psi} - \frac{1}{2} g^{-\frac{3}{2}} \dot{z} g') \quad (59)$$

$$\epsilon''_1 = \frac{1}{2} h^{-1} (g^{-\frac{1}{2}} g'' - \frac{1}{2} g^{-\frac{3}{2}} g' g'^T) \quad , \quad \epsilon''_2 = 0 \\ \kappa''_1 = h^{-1} [2g^{-3} f g' g'^T + g^{-1} f'' - g^{-2} f g'' - g^{-2} (f' g'^T + g' f'^T)] \\ \kappa''_2 = r_0^{-1} \left[\frac{3}{4} g^{-\frac{5}{2}} \dot{z} g' g'^T - \frac{1}{2} g^{-\frac{3}{2}} (g' \dot{\psi}^T + \dot{\psi} g'^T) - \frac{1}{2} g^{-\frac{3}{2}} \dot{z} g'' \right] \quad (60)$$

which is all we need to program the element gradient and matrix.

9. Potential of pressure and point force

If p denotes external pressure and F an apex ($r=0$) force then to ξ
we add

$$\pi^* = p^* \frac{1}{t} \int r^2 z' ds - F^* z \quad (61)$$

where

$$P^* = \frac{6(1-\nu^2)}{Et^2} P, \quad F^* = \frac{6(1-\nu^2)}{\pi Et^3} F \quad (62)$$

and have that

$$g_e = P^* \frac{1}{t} \sum_{j=1}^3 w_j (2r_j \dot{z}_j \phi_j + r_j^2 \dot{\psi}_j) \quad (63)$$

and

$$k_e = \frac{2P^*}{t} \sum_{j=1}^3 w_j [\dot{z}_j \phi_j \phi_j^T + r_j (\phi_j \dot{\psi}_j^T + \dot{\psi}_j \phi_j^T)] \quad (64)$$

which need be added to g_e and k_e in Eqs. (54) and (55).

10. Bending of a spherical shell

As an example to the usefulness of the shell element we compute the large deformation of a thin spherical shell of radius 1 and $\nu = 0.3$ acted upon by a surface pressure p (negative is internal) and an apex force F (negative is inward). For typographical neatness we ignore the asterisks on p and F . The geometry and loads on the shell are shown in Fig. 3. Because of symmetry we consider only the upper half of the sphere.

Figure 1 shows the deformation of the shell discretized with 14 elements, under a succession of polar forces $F = 0, -2.5, -5.0, \dots, -30$ with no internal pressure. Figure 2 shows the same shell under the same loading but discretized with 24 elements.

Tables 1 and 2, referring to Figs. 1 and 2, respectively, list $\|g\|_2$ as it changes with the Newton-Raphson (NR) iteration, for the different loadings. Evidently the computation of large shell deformations can become expensive.

Figure 3 shows the shell of Fig. 2 but with an internal pressure $p = -1.0$. Figures 4 and 5 show the creation of a dimple in a thinner ($t = 0.001$) shell. The solutions for $F = 10$ and $F = 20$ in Fig. 5 are not well convergent.

F

NR	-2.5	-5.0	-7.5	-10.0	-12.5	-15.0	-17.5	-20.0	-22.5	-25.0	-27.5	-30.0
1	.25E1	.25E1	.25E1									
2	.62E1	.75E2	.11E4	.13E4	.12E4	.11E5	.96E4	.13E5	.78E4	.12E5	.34E4	.30E4
3	.20E1	.22E2	.73E2	.71E2	.52E2	.67E3	.56E3	.87E3	.16E3	.27E3	.38E2	.24E2
4	.24E0	.20E2	.31E2	.14E2	.38E2	.42E3	.16E3	.56E3	.93E2	.12E3	.21E4	.57E2
5	.30E-2	.67E1	.16E1	.22E2	.15E2	.57E2	.22E2	.73E2	.32E2	.24E1	.25E2	.41E1
6	.59E-6	.52E1	.45E0	.71E1	.49E2	.13E2	.15E2	.13E2	.23E3	.27E3	.34E5	.16E2
7	.13E-9	.46E0	.42E-2	.10E2	.35E1	.46E2	.44E2	.93E1	.68E1	.70E0	.17E4	.16E0
8		.45E-1	.63E-5	.11E1	.80E2	.12E0	.55E1	.11E0	.72E4	.52E-1	.18E4	.86E-1
9		.39E-4	.19E-9	.77E0	.25E0	.52E1	.14E3	.13E0	.20E3	.76E-4	.22E3	.26E-5
10		.37E-9		.70E-2	.19E2	.64E-3	.10E1	.22E-4	.16E3	.82E-9	.70E2	.25E-9
11			.39E-4	.13E-1	.30E-5	.24E3	.48E-8	.33E1		.22E1		
12			.34E-9	.62E-1	.12E-9	.17E1	.35E-9	.33E2		.51E0		
13			.95E-6		.11E1		.13E0		.14E-1			
14			.24E-9		.54E-1		.27E1		.17E-4			
15					.26E-2		.46E-4		.27E-9			
16					.42E-6		.13E-5					
17						.29E-9		.15E-9				

Table 1: Values of the ℓ_2 norm of the global gradient $\|g\|_2$ for different apex force F, as they diminish with the Newton-Raphson (NR) iteration. This table refers to Fig. 1.

F

NR	-2.5	-5.0	-7.5	-10.0	-12.5	-15.0	-17.5	-20.0	-22.5	-25.0	-27.50	-30.0
1	.25E1	.25E1										
2	.62E1	.86E2	.76E3	.15E4	.32E4	.69E4	.14E5	.21E5	.28E5	.46E5	.67E5	.82E5
3	.23E1	.18E2	.63E2	.93E2	.19E3	.45E3	.91E3	.97E3	.13E4	.22E4	.21E4	.24E4
4	.29E0	.27E2	.21E2	.53E2	.16E3	.32E3	.43E3	.82E3	.16E4	.22E4	.21E4	.44E4
5	.33E-2	.42E1	.86E1	.96E1	.14E2	.30E2	.45E2	.69E2	.10E3	.14E3	.17E3	.19E3
6	.43E-6	.58E1	.31E1	.12E2	.26E2	.31E2	.29E2	.21E2	.49E2	.11E3	.90E2	.17E3
7	.34E-9	.20E0	.53E0	.25E1	.41E1	.94E1	.26E2	.45E2	.45E2	.61E2	.10E3	.11E3
8		.22E-1	.31E-1	.27E1	.21E2	.35E2	.13E2	.85E1	.15E2	.12E2	.54E1	.63E1
9		.42E-5	.60E-4	.12E0	.52E0	.20E1	.27E2	.10E3	.84E2	.18E3	.78E3	.11E4
10		.55E-9	.59E-9	.94E-2	.36E1	.39E2	.46E1	.88E0	.27E1	.11E1	.24E1	.44E1
11			.16E-5	.10E-1	.13E0	.38E2	.27E3	.45E3	.14E4	.11E4	.15E4	
12			.44E-9	.22E-2	.36E1	.46E0	.91E0	.17E1	.66E1	.51E1	.61E1	
13				.53E-8	.12E-2	.23E2	.78E1	.14E3	.21E2	.12E3	.22E3	
14				.50E-9	.34E-3	.18E-1	.31E-1	.18E0	.13E1	.22E0	.33E0	
15					.53E-9	.14E0	.10E0	.19E2	.30E2	.18E3	.41E3	
16						.19E-5	.59E-5	.45E-2	.54E-1	.20E0	.54E0	
17						.13E-8	.33E-8	.31E-1	.45E1	.35E0	.31E1	
18						.38E-9	.34E-9	.65E-7	.41E-3	.65E-3	.18E-1	
19							.29E-9	.56E-3	.11E-4	.23E-1		
20								.44E-9	.73E-4	.11E-5		
21										.40E-9		

Table 2. Same as Table 1 but Ne = 24. Refers to Fig. 2.

References

1. I. Fried, Nonlinear finite element computation of the equilibrium and stability of the circular plate. IJNME 17, 1427-1440 (1981).
2. I. Fried, Large deformation static and dynamic finite element analysis of extensible cables. Computers & structures 15, 315-319 (1982).
3. I. Fried, Stability and equilibrium of the straight and curved elastica-finite element computation. CMAME 28, 49-61 (1981).
4. I. Fried, Finite element computation of large rubber membrane deformations. IJNME 18, 653-660 (1982).
5. I. Fried, Nonlinear finite element computation of the equilibrium stability and motion of the extensional beam and ring. CMAME 38, 24-44 (1983).

Figures

1. Thin spherical shell bent under inwardly directed forces F. Discretization done with 14 elements. No internal pressure.
2. Same as Fig. 1 but discretization done with 24 elements.
3. Same as Fig. 2 but with unit internal pressure.
4. A dimple in a thin spherical shell.
5. Same as Fig. 4 but with a unit internal pressure.

Fig. 1

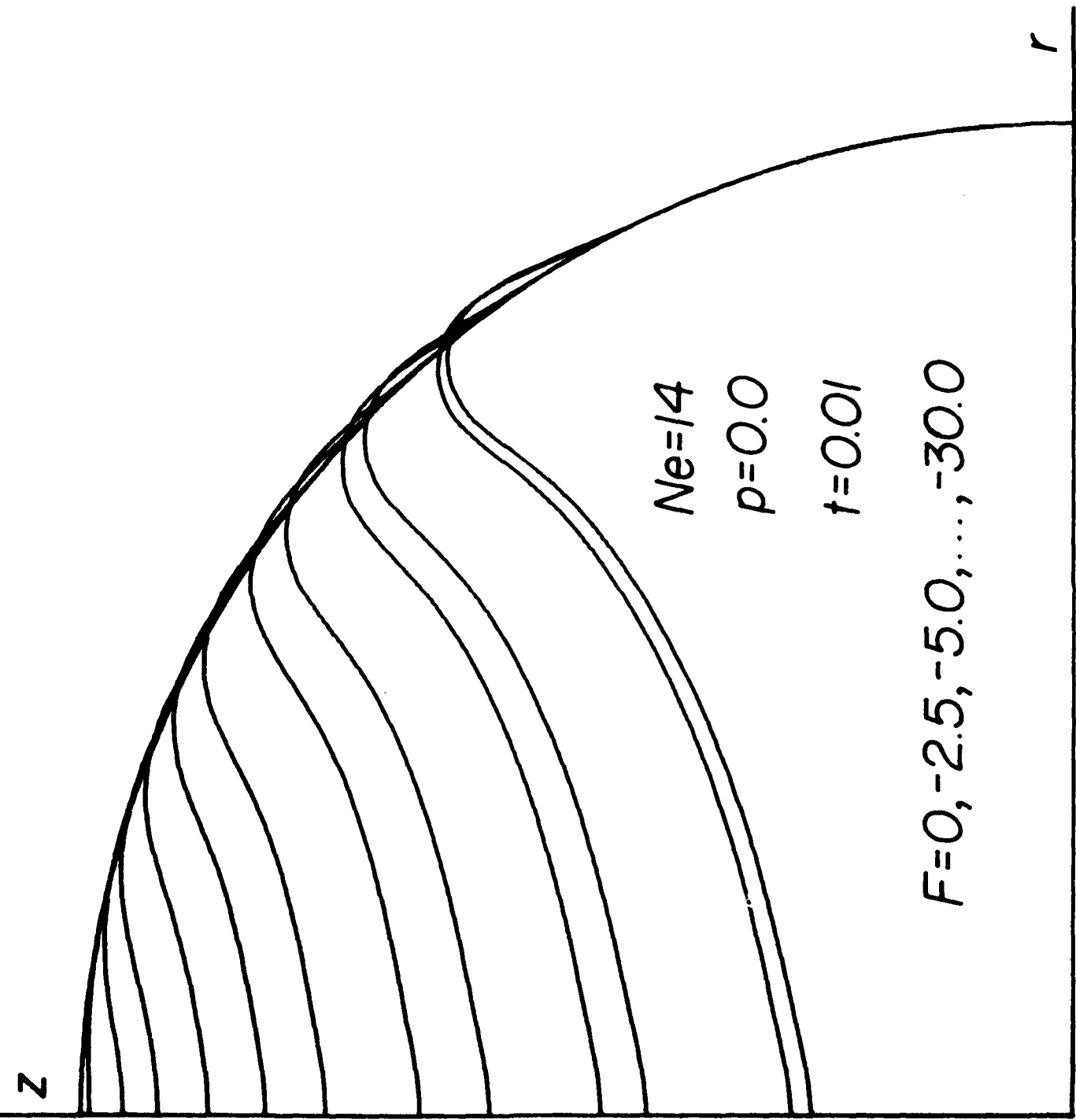


Fig.2

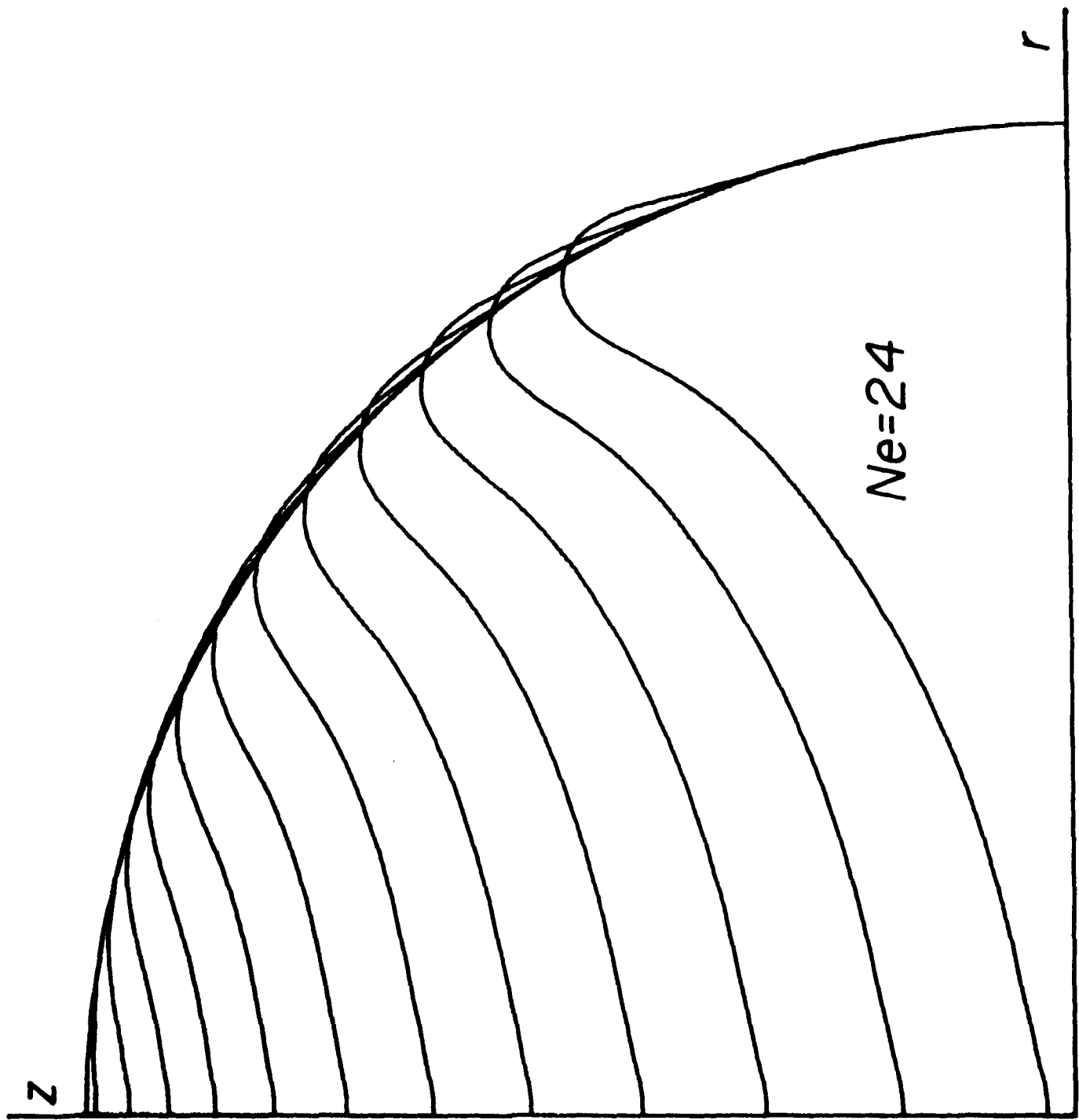
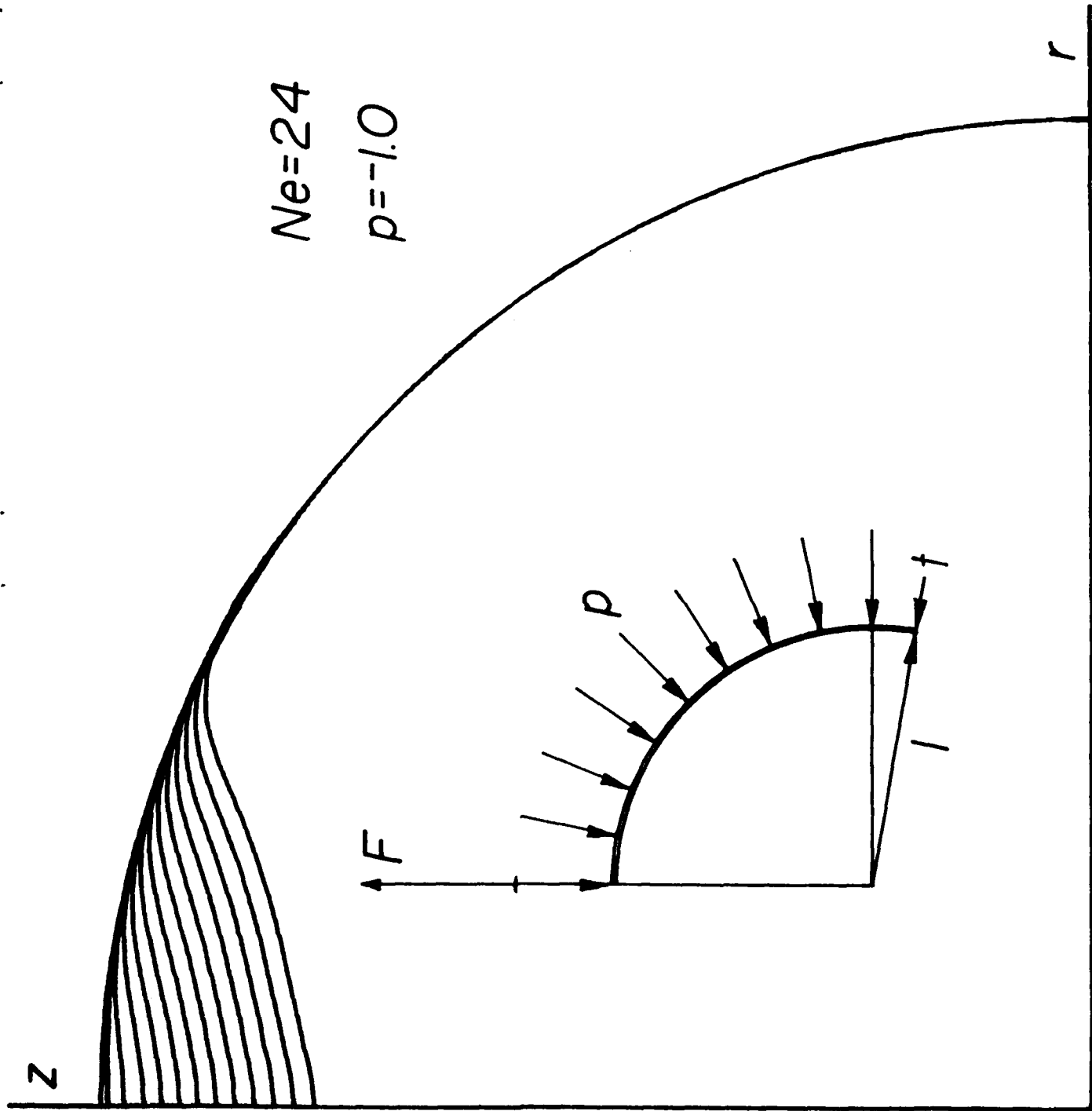


Fig. 3



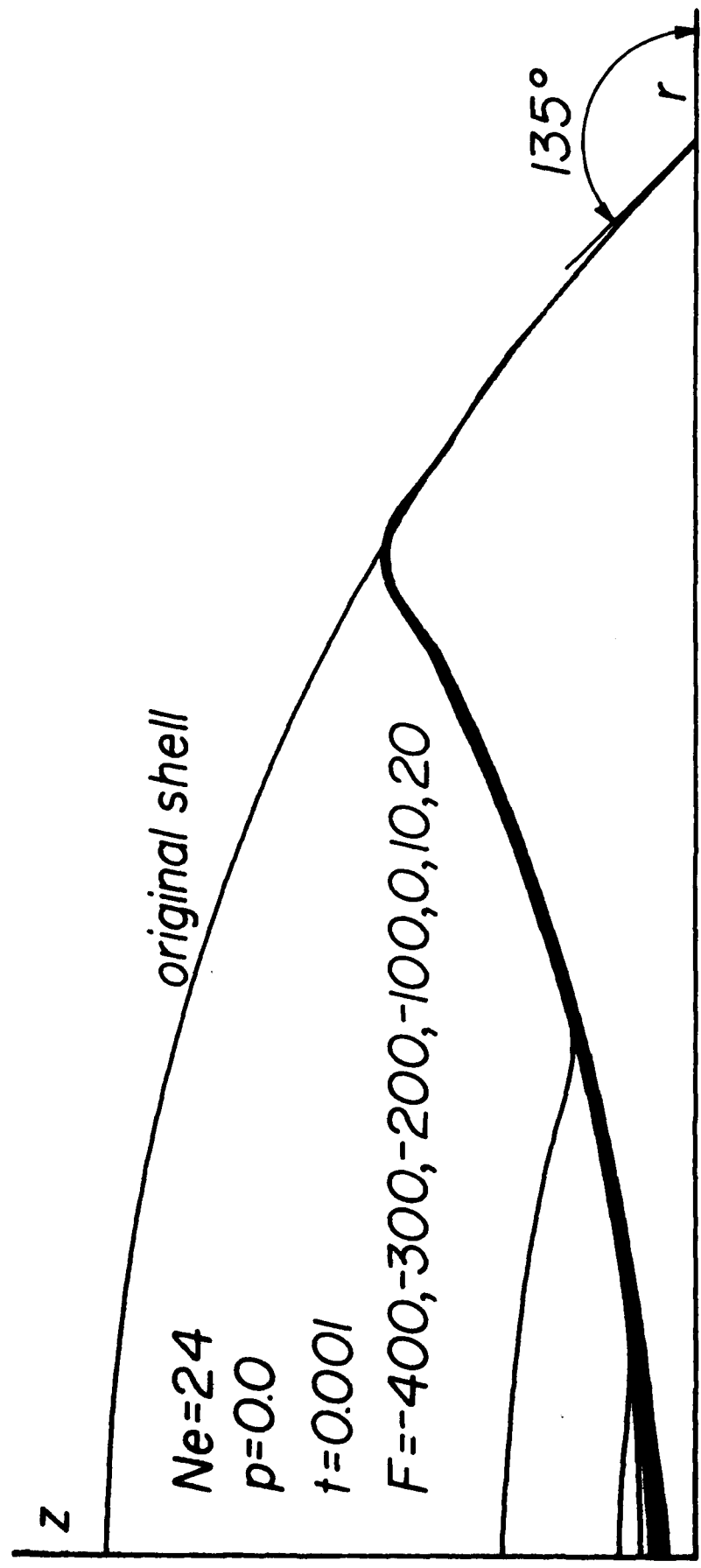
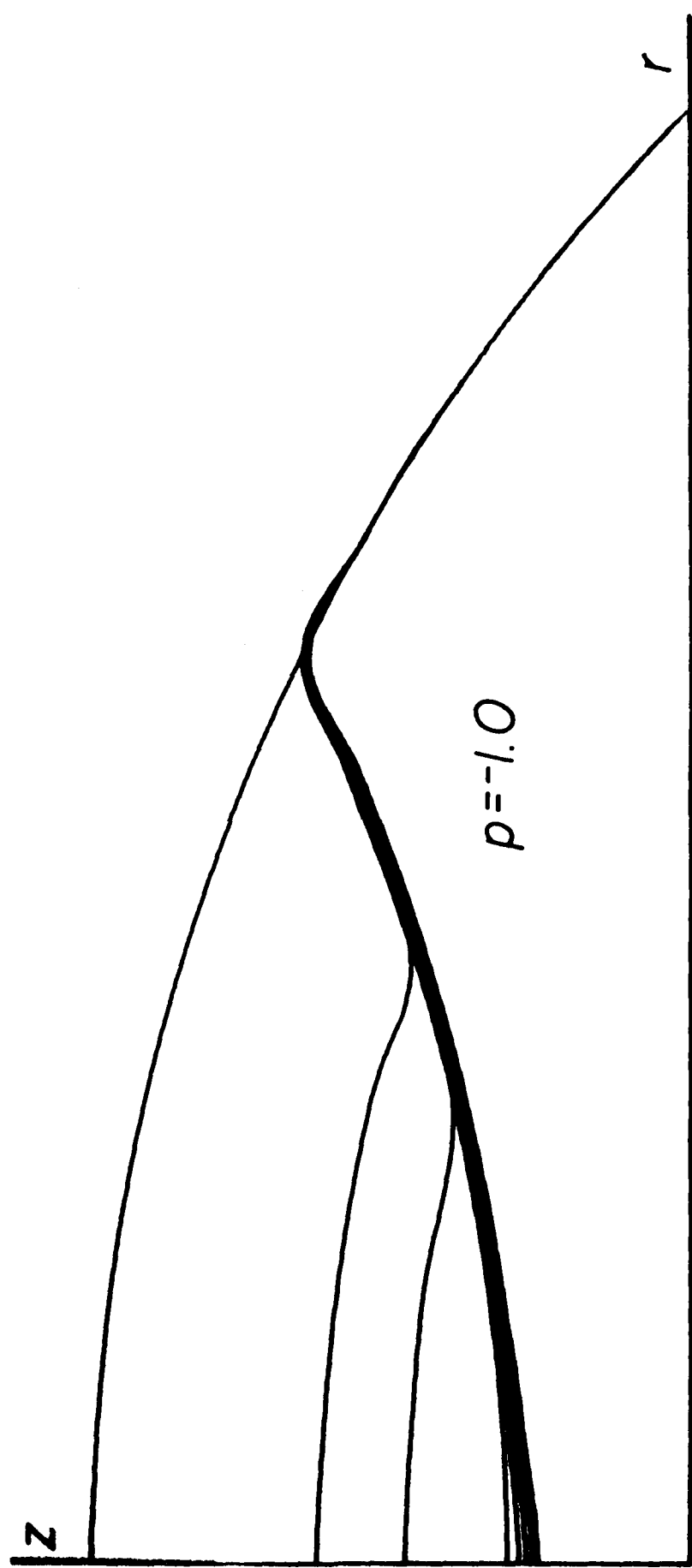


Fig. 4

Fig. 5



4. List of Publications

Papers in Professional Journals

Published

1. J.H. Argyris and I. Fried: The LUMINA element for the matrix displacement method. J. of the Royal Aero. Soc., 514-517, June (1968).
2. J.H. Argyris, I. Fried and D.W. Scharpf: The TET 20 and TEA 8 element for matrix displacement method. J. of the Royal Aero. Soc. July (1968).
3. J.H. Argyris, I. Fried and D.W. Scharpf: The HERMES 8 element for the matrix displacement method. J. of Royal Aero. Soc., 613-617, July (1968).
4. I. Fried: Finite element analysis of time dependent phenomena. AIAA Journal 7, 6, (1969).
5. J.H. Argyris, I. Fried and D.W. Scharpf: The TUBA family of plate elements for the matrix displacement method. J. of the Royal Aero. Soc., August (1968).
6. I. Fried: More on gradient iterative methods in finite element analysis, AIAA Journal, 7, 3, March (1969).
7. I. Fried: Gradient iterative methods for eigenproblems in the finite element analysis. AIAA Journal, 7, 4 (1969).
8. I. Fried: Some aspects of the natural coordinate system in the finite element method. AIAA Journal, 7, 7, July (1969).
9. I. Fried: A computational procedure for the solution of large problems arising from the finite element method. Int. J. for Numer. Methods in Engineering, 2, 477-494 (1970).
10. I. Fried: Basic computational problems in the finite element analysis of shells. Int. J. Solids Structures, Dec. (1971).
11. I. Fried: Accuracy of finite element eigenproblems. J. Sound and Vibration, 5, 2, (1971).
12. I. Fried: Discretization and computational errors in high order finite elements. AIAA Journal, 9, 10, (1971).
13. I. Fried: N-step conjugate gradient minimization scheme for non-quadratic functions. AIAA Journal, 9, 2286-2287 (1971).
14. I. Fried: Optimal gradient minimization scheme for finite element eigenproblems. Journal Sound and Vibration, 20, 3, 333-342 (1972).

15. I. Fried: Accuracy of complex finite elements. AIAA Journal, 10, 3, 347-349 (1972).
16. I. Fried: Condition of finite element matrices generated from non-uniform meshes. AIAA Journal, 10, 2, 219-221 (1972).
17. I. Fried: Bounds on the extremal eigenvalues of the finite element matrices and their spectral condition number. J. Sound and Vibration, 22, 4, 407-418.
18. I. Fried and Shok Keng Yang: Best finite element distribution around a singularity. AIAA Journal, 10, 3, 1244-1246 (1972).
19. I. Fried: Possible loss of accuracy in curved (isoparametric) finite elements. Journal of Sound and Vibration, 23, 4, 507-513 (1972).
20. I. Fried: Perturbation errors in the finite element method. J. Appl. Mech., 629-631, June (1972).
21. I. Fried: Condensation of finite element eigenproblems. AIAA Journal, 10, 11, 1529-1530, November (1972).
22. I. Fried: Shape functions and the accuracy of arch finite elements. AIAA Journal, 11, 3, 287-291 (1973).
23. I. Fried: Influence of Poisson's ratio on the condition of the stiffness matrix. Int. J. Solids Structures, 9, 323-329 (1973).
24. I. Fried: Shear in C^0 and C^1 bending finite elements. Int. J. Solids and Structures, 9, 449-460 (1973).
25. I. Fried and Shok Keng Yang: Triangular nine-degrees-of-freedom, C^0 , plate bending element of quadratic accuracy. Quart. of App. Math., 303-312, Oct. (1973).
26. I. Fried: Finite element methods; accuracy at a point. Quart. of App. Math., 149-161, July (1974).
27. I. Fried: Accuracy and condition of curved (isoparametric) finite elements. Journal of Sound and Vibration, 31, 345-357 (1973).
28. I. Fried: Boundary and interior approximation errors in the finite element method. J. App. Mech. Paper No. 73-APM-AIA (1973).
29. I. Fried: Bounds on the spectral and maximum norms of the finite element stiffness, flexibility and mass matrices. Int. J. Solids and Structures, 9, 1013-1034 (1973),
30. I. Fried: Residual energy balancing technique in the generation of plate bending finite elements. Computers and Structures, 2, 771-778 (1974).

31. I. Fried: Numerical integration in the finite element method. Computers and Structures, 4, 921-932 (1974).
32. I. Fried: Note on the finite element analysis of the axisymmetric elastic solid. Int. J. Solids and Structures, 10, 383-386 (1974).
33. I. Fried: Finite element analysis of incompressible material by residual energy balancing. Int. J. Solids and Structures, 10, 993-1002 (1974).
34. I. Fried and D.S. Malkus: Finite element mass matrix lumping by numerical integration with no convergence loss. Int. J. Solids and Structures, 11, 461-466 (1975).
35. I. Fried: Monoton finite element matrices and their computed condition numbers. Computers and Structures, 5, 317-319 (1975).
36. I. Fried: Finite element analysis of thin elastic shells with residual energy balancing and the role fo rigid body modes. J. App. Mech. paper No. 75-APM-6 (1975).
37. I. Fried and J. Metzler: SOR vs. conjugate gradients in a finite element discretization. Int. J. Numer. Methods in Eng. 12, 1329-1342 (1978).
38. I. Fried and J. Metzler: Displacement, strain and stress error nodal lines in finite elements. Computers and Structures, 9, 335-339 (1978).
39. I. Fried and J. Metzler: Conjugate gradient solution of a finite element elastic problem with high Poisson ratio. Comp. Meth. App. Mech., Eng. 15, 1, 83-84 (1978).
40. I. Fried: Accuracy of string element man matrix. Comp. Meth. App. Mech. Eng. 20, 317-321 (1979).
41. I. Fried: On the optimality of the pointwise accuracy of the finite element solution, IJNME 15, 451-476 (1980).
42. I. Fried: Irregular finite element meshes in elastodynamics, IJNME 15, 626-628 (1980).
43. I. Fried: Meaningful existance of finite element solutions to off-limit problems, CMAME, 22, 229-240 (1980).
44. I. Fried: Nonlinear finite element computations of the equilibrium and stability of the circular plate, IJNME, 17, 1427-1440 (1981).
45. I. Fried: Large deformation static and dynamic finite element analysis of extensible cables, Computers and Structures, 15, 315-319 (1982).
46. I. Fried: Stability and equilibrium of the straight and curved elastica-finite element computation. CMAME, 28, 49-61 (1981).

47. I. Fried: Finite element computation of large rubber membrane deformations. IJNME 18, 653-660 (1982).
48. I. Fried: Finite element computation of large elastic deformations: Proceedings of the Brunel Conference of the mathematics of finite elements and applications, MEF LAP IV, J.R. Whiteman Editor, Academic Press, 143-159 (1982).
49. I. Fried: Nonlinear finite element computation of the equilibrium stability and motion of the extensional beam and ring. CMAME 38, 29-44 (1983).
50. I. Fried: Reflections on the computational approximation of elastic incompressibility. Computers and Structures 17, 161-168 (1983).

In Print

51. I. Fried: Observations on stiffness and flexibility modal identification techniques. CMAME (1982).
52. I. Fried: Orthogonal accession to the equilibrium curve. CMAME (1983).
53. I. Fried: On conditionally stable explicit time integration methods in elastodynamics and heat transfer. CMAME (1984).
54. I. Fried: Nonlinear finite element analysis of the thin shell of revolution. CMAME (1984).

Theses

1. Etude de flambage d'une coque conique sous l'effet combine d'une force axiale et torsion en presence d'une pression interne; Travail elabore dans le cadre d'un program d'obtention de diplome de Maitre es-science Aeronautique (M.Sc.Ae.), Ecole National Superieure de l'Aeronautique, Paris, Dec. (1965).
2. Discretization and round-off errors in the finite element analysis of elliptic boundary value problems; Ph.D. Massachusetts Institute of Technology, June (1971).

Books

- I. Fried: Numerical Solution of Differential Equations, Academic Press, London, New York (1979).

Papers in Professional Conferences

1. J.B. Spooner, O.E. Brönlund, I. Fried, J.H. Argyris: The change in the (two dimensional) stress distribution round a rectangular hole with rounded corners, caused by a varying internal pressure and temperature. Proc. XVII International Aeronautical Congress, Belgrad, 24-29 Sept. (1967).
2. I. Fried: A computational procedure for gradient iterative techniques in the finite element method. EUROMECH II Conference, Stuttgart, 8-10 April (1968).
3. J.H. Argyris, K.E. Buck, I. Fried, H.M. Hilbert, G. Mareczek and D.W. Scharpf: Some new elements for the matrix displacement method. 2nd Conference on Matrix Methods in Structural Mechanics, Wright-Patterson Air Force Base, Ohio, 15-17 October (1968).
4. I. Fried: The L_2 and L_∞ condition numbers of the finite element matrices and the pointwise convergence of the method. Proc. Conference on the Mathematics of the Finite Element Method, Edited by J.R. Whiteman, Academic Press, Brunel University, 18 April (1972).
5. I. Fried: Finite element analysis of eigenproblems - theory and practice. National Symposium on Computerized Structural Analysis and Design, The George Washington University, Washington, D.C. 27-29, March (1972).
6. I. Fried and D.S. Malkus: Energy error in the elastic solution when an incompressible solid is assumed compressible. Proceedings of the U.S.-Germany Seminar on the Finite Element Method, Edited by K.J. Bathe, J.T. Oden and W. Wunderlich, MIT Press, August (1976).
7. I. Fried, J. Carson and Y. Park: Nonlinear finite element analysis of gas flow in a contact bed reactor. Proc. Conference on Finite Element Analysis in Flow Problems, Portofino, Italy, 16-18 June (1976).
8. J.A. Metzler and I. Fried: The conjugate gradient method with finite elements. 2nd IMACS (AICA) International Symposium on Computer Methods for Partial Differential Equations, Lehigh University, June 22-24 (1977).
9. I. Fried and J. Metzler: Successive overrelaxation parameters for general finite element meshes, 1978 ACM Computer Science Conference, February 21-23, Detroit, Michigan.
10. I. Fried: High order nonlinear tangent element data by discrete integration, Proc. of the 5th Invitational symposium on Finite Elements, Finite Differences and Calculus of Variations, 81-118, H. Kardestuncer Editor, University of Connecticut, May 2 (1980).

AD-A138 468 LINEAR AND NONLINEAR FINITE ELEMENTS(U) BOSTON UNIV MA
DEPT OF MATHEMATICS I FRIED DEC 83 BU-1-84
N00014-76-C-0036

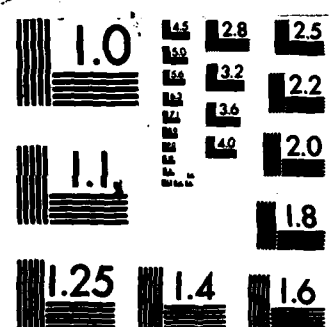
3/3

UNCLASSIFIED

F/G 12/1

NL





MICROCOPY RESOLUTION TEST CHART
NATIONAL BUREAU OF STANDARDS-1963-A

Reports

1. I. Fried: Finite element method in fluid dynamics and heat transfer. Report No. 38, Institut für statik und Dynamik der Luft-und Raumfahrtkonstruktionen, April (1967).
2. J.H. Argyris, W. Bossard, I. Fried and H.M. Hilbert: A fully compatible plate bending element. ISD Report No. 42, Universität Stuttgart, December (1967).
3. I. Fried and D.S. Malkus: A finite element displacement model valid for any value of the compressibility. Report to the US Office of Naval Research (1976).
4. A. Johnson and I. Fried: High order nonlinear finite element analysis of the axisymmetric rubber membrane, Report 6-80 to the Office of Naval Research (1980).

Symposia

1. The 17th International Aeronautical Congress. Belgrad, 24-29 September, 1967.
2. EUROMECH 11, Experience in Computer-Based Analysis of Three-Dimensional Media. University of Stuttgart, 8-10 April 1968. Invited.
3. Second Conference on Matrix Methods in Structural Mechanics. Wright-Patterson Air Force Base, Ohio, 15-17 October, 1968.
4. Seminar, McGill University, Department of Electrical Engineering. Montreal, December 1971. Invited.
5. Seminar on the Role of Computers in Structural Analysis, Design and Optimization. Indian Institute of Technology, Madras, December 11-13, 1972.
6. National Symposium on Computerized Structural Analysis and Design. George Washington University, March 27-29, 1972.
7. Boston Numerical Mathematics Seminar. Harvard University, April 12, 1972. Invited.
8. Seminar on the Mathematical Theory of Finite Elements Approximations. The University of Alabama in Huntsville, June 6-8, 1972. Invited.
9. New England Bioengineering Conference. The University of Vermont, April 19-20, 1973. Invited.
10. US-Japan Symposium on the Mathematics of Finite Elements with Emphasis on Nonlinear Problems. Lake Hakone, August, 1975. Invited.
11. Applied Mechanics Conference. Rensselaer Polytechnic Institute, Troy, New York, June 23-25, 1975.

12. The Mathematics of Finite Elements and Applications. Brunel University, April 15-17, 1975.
13. National Bureau of Standards Mathematics Colloquium on Deformation and Mechanical Failures. Gaithersburg, May 16, 1975. Invited.
14. ICAD-International Computer Analysis and Design, Second Symposium on the Finite Element Analysis of Fluid Flow, Santa Margherita Ligure, Italy, June 14-18, 1975.
15. US-Germany Symposium on Finite Element Analysis. Massachusetts Institute of Technology, 9-13 August 1976.
16. Second IMACS (AICA) International symposium on Computer Methods for Partial Differential Equations, Lehigh University, June 22-24, 1977.
17. Fifth Invitational symposium on Finite Elements, Finite Differences and calculus of Variations, University of Connecticut, May 2 (1980). Invited.
18. Fourth conference on the Mathematics of Finite Elements and Applications, MEFLAP IV, Brunel University, May 1, 1981. Invited.
19. Cambridge symposium on optical and Electro-optical Engineering, Nov. 6-10 (1983). Invited.

Unclassified

SECURITY CLASSIFICATION OF THIS PAGE (When Data Entered)

REPORT DOCUMENTATION PAGE		READ INSTRUCTIONS BEFORE COMPLETING FORM
1. REPORT NUMBER BU - 1 - 84	2. GOVT ACCESSION NO. AD-A138 46V	3. RECIPIENT'S CATALOG NUMBER
4. TITLE (and Subtitle) Linear and Nonlinear Finite Elements	5. TYPE OF REPORT & PERIOD COVERED Final	
7. AUTHOR(s) Isaac Fried	8. CONTRACT OR GRANT NUMBER ONR-N00014-76-C-036	
9. PERFORMING ORGANIZATION NAME AND ADDRESS Department of Mathematics Boston University Boston, MA 02115	10. PROGRAM ELEMENT, PROJECT, TASK AREA & WORK UNIT NUMBERS	
11. CONTROLLING OFFICE NAME AND ADDRESS Dept. of the Navy, Office of Naval Research Structural Mechanics Program Arlington, VA 22217	12. REPORT DATE Dec. 1983	
14. MONITORING AGENCY NAME & ADDRESS (if different from Controlling Office)	13. NUMBER OF PAGES	
	15. SECURITY CLASS. (of this report) Unclassified	
	16a. DECLASSIFICATION/DOWNGRADING SCHEDULE	
16. DISTRIBUTION STATEMENT (of this Report) Approved for public release; distribution unlimited		
17. DISTRIBUTION STATEMENT (of the abstract entered in Block 20, if different from Report)		
18. SUPPLEMENTARY NOTES		
19. KEY WORDS (Continue on reverse side if necessary and identify by block number) Finite elements, Nonlinear elasticity, plate, cable, Rod, Rubber membrane, shell of Revolution, Incompressible, Orthogonal accession.		
20. ABSTRACT (Continue on reverse side if necessary and identify by block number) A general procedure is presented for the setting up of the element tangent stiffness matrix and element gradient through the discrete sampling of the nonquadratic total potential energy. Computations are done for the plate, the bent rod, the cable, the rubber membrane, and the thin shell of revolution.		